A Pc-scale study of radio-loud AGN : The Fanaroff–Riley Divide and Unification

A thesis
submitted for the degree of

Doctor of Philosophy

in
The Faculty of Science

Bangalore University

by

PREETI KHARB

Indian Institute of Astrophysics

Bangalore 560 034, India

2004

Contents

List of Tables

List of Figures

List of symbols and abbreviations

α	:	Spectral index defined as $S_\nu \propto \nu^{-\alpha}$
β	:	v/c, bulk velocity in units of the speed of light
χ	:	Polarization electric vector, EVPA
δ	:	Doppler factor, $\quad \frac{1}{\gamma(1-\beta cos\theta)}$
γ	:	Lorentz factor, $\quad \frac{1}{\sqrt{1-\beta^2}}$
λ	:	Emission wavelength
ν	:	Emission frequency
θ	:	Angle between AGN axis/radio axis and line of sight
ADAF	:	Advection Dominated Accretion Flow
AIPS	:	Astronomical Image Processing System
AU	:	Astronomical Unit $\sim 1.5 \times 10^{13}$ cm
B	:	Magnetic field
c	:	Speed of light in vacuum, $\sim 3 \times 10^{10}$ cm sec^{-1}
CDQs	:	Core-dominated quasars
CSS	:	Compact Steep-spectrum source
EVN	:	European VLBI Network
EVPA	:	Electric Vector Position Angle
FR	:	Fanaroff–Riley
H_0	:	Hubble constant,
		assumed to be 71 km s^{-1} Mpc^{-1} unless otherwise stated
HBLs	:	High-energy peaked BL Lacs
HPQs	:	Highly polarized quasars

$L_\odot$	:	Solar luminosity, $\sim 4 \times 10^{33}$ erg sec^{-1}
LBLs	:	Low-energy peaked BL Lacs
LDQs	:	Lobe-dominated quasars
LPRQs	:	Low-optically polarized radio-loud quasars
ly	:	Light year, $\sim 9.5 \times 10^{17}$ cm
mas	:	Milliarcsecond
$M_\odot$	:	Solar mass, $\sim 2 \times 10^{33}$ g
MERLIN	:	Multi-Element Radio-Linked Interferometer Network, UK
MHD	:	Magneto Hydrodyanamic
OVVs	:	Optically Violently Variable quasars
PA	:	Position Angle
pc	:	Parsec, $\sim 3 \times 10^{18}$ cm
kpc	:	Kiloparsec, 10^3 pc
Mpc	:	Megaparsec, 10^6 pc
q_0	:	Cosmological deceleration parameter,
		assumed to be –0.6 unless otherwise stated
RLQs	:	Radio-loud quasars
RM	:	Rotation Measure
R_c	:	Ratio of radio emission from the core to that from the lobes
SMBH	:	Supermassive black hole
S_ν	:	Flux density
US	:	Unified Scheme
VLA	:	Very Large Array, New Mexico
VLBA	:	Very Long Baseline Array, USA
VLBI	:	Very Long Baseline Interferometry
VLBP	:	Very Long Baseline Polarimetry
WSRT	:	Westerbork Synthesis Radio Telescope
z	:	Redshift

Abstract

In this thesis an attempt is made to address the Fanaroff-Riley (FR) dichotomy observed in radio-powerful active galactic nuclei (AGNs) within the framework of the "Unification Scheme" for radio-loud AGNs, using high angular resolution total intensity and polarization observations in the radio and optical wavebands. We describe the technique of Very Long Baseline Interferometry (VLBI) and VLBI polarimetry (VLBP) which were made use of in order to study the magnetic (B) field structure and orientation in AGN jets on parsec-scales. In this thesis we present the first VLBP images of four relatively low-luminosity FRI radio galaxies with detected polarized emission on parsec-scales. We further present the results from our multi-frequency, multi-epoch VLBP observations of the broad-line FRII radio galaxy – 3C111. We compare and contrast our VLBP results in the light of the Fanaroff-Riley dichotomy and the Unified Scheme that relates the FRI and FRII radio galaxies to BL Lac objects and quasars, respectively. We find that the B-field geometry in FRIs and FRII(s) is similar to radio-powerful BL Lacs and quasars respectively, in accordance with the Unified Scheme. We present VLBP images of the relatively poorly studied subclass of BL Lacertae objects, the high-energy peaked BL Lacs (HBLs). We find that they tend to exhibit a predominantly longitudinal B-field geometry in their VLBI jets, similar to the radio-loud quasars but different from the low-energy peaked BL Lacs (LBLs) which show a predominantly transverse B-field geometry in their jets. We examine the nature of the unresolved optical nuclei discovered by the Hubble Space Telescope in the centres of a majority of FR radio galaxies by fitting simple models to the optical and radio data. We conclude that the nature of the optical nuclei in the FRI population (FRI radio galaxies and BL Lac objects) and the FRII population (FRII radio galaxies and radio-loud quasars) differs in a significant manner. FRI sources probably lack the optically thick obscuring tori around their central engines while FRII sources do not. Further, the contribution to the nuclear optical luminosity from the accretion disk is much more significant in the FRII population.

Chapter 1

Introduction

1.1 Active Galactic Nuclei

Galaxies are the building blocks of the Universe. They are gravitationally bound systems consisting of a billion to a hundred billion stars and copious amounts of gas and dust. Although most galaxies show bright centres due to increased star density, a small fraction $(1 - 10\%)$ of galaxies are distinguished by their overwhelmingly brilliant nuclei (luminosity $\sim 10^{46}$ erg s^{-1}), the emission from which can even swamp the stellar emission from the host galaxies. These nuclei exhibit rapid variability which can be of the order of weeks or days and sometimes even hours at X-ray wavelengths. The dimensions of the source can at most be comparable with $c \times$ the 'time-scale' of the variations, c being the speed of light. The sizes turn out to be of the order of a few tens of AU. Thus these solar-system-sized nuclei emit radiation equivalent or up to a hundred times the emission from all the stars of the galaxy combined. The continuum emission from these nuclei extends over an extraordinarily broad range of frequencies – from the lowest energy radio waves to the highest energy gamma-rays. Their line spectra often display emission lines whose total flux is several percent of the continuum flux and whose widths suggest velocities ranging up to $\sim 10^4$ km s^{-1}. These exotic phenomena in the centres of galaxies are called Active Galactic Nuclei (AGNs).

Unlike any ordinary galaxy or star, the ratio of X-ray flux to optical flux in AGNs, approaches unity. In order to produce the enormous energy output of AGNs from very small radii, and in some cases hundreds of kiloparsec-scale collimated jets and radio lobes, emission by conventional nuclear-fusion-powered sources like stars, falls far too short and is unfeasible in view of the central engine being tiny. 10^{10} stars in a volume of ~ 1 pc^3 would collide and dissipate in much less time than the typical AGN lifetimes

of 10^8 years derived from the radiative lifetimes of radio-emitting electrons (e.g., Eilek *et al.*, 1997). Even a cluster of neutron stars and black holes would evolve in a relatively short time to form larger black holes through mergers, until the core would collapse into a single massive black hole (Shapiro & Teukolsky, 1993). At present, the near-consensus view of AGNs therefore is that they are powered by the release of gravitational potential energy due to the accretion of matter onto a super-massive black hole (SMBH). However, the details of the physical processes involved are still not well understood and we do not yet have a comprehensive theory of AGN that can predict the whole range and variety of observed AGN properties from a minimal set of well-defined parameters. Taxonomy as a substitute for quantification of parameters still plays a major role in the investigation of AGN physics.

1.2   Discovery and classification

It all began in the 1940s. In 1943, Carl Seyfert discovered spiral galaxies with a bright 'star-like' nucleus which exhibited strong emission lines, generally absent in normal galaxies. These emission lines had Doppler widths corresponding to gas velocities of several thousand km s^{-1}. These galaxies are now known as 'Seyfert galaxies'. By 1964, Hey had discovered discrete luminous radio sources which were soon identified to be external galaxies (e.g., Cygnus A). The spectacular jet in the nearest radio galaxy M 87 had been identified to be synchrotron emission by Baade & Minkowski (1954). In the 1960s, radio interferometers were able to provide positional accuracies of a few arcseconds, critical to the optical identification of many radio sources, which turned out to be low redshift galaxies (e.g., Minkowski, 1960).

In 1963, Maarten Schmidt discovered that the quasi-stellar radio source 3C 273 which showed strong emission lines, was in fact a peculiar galaxy at a redshift of 0.16. These objects were later called quasars. However many of these 'star-like' objects did not have appreciable radio emission and were termed quasi-stellar objects or QSOs.

In the 1970s, another exotic class of AGNs was discovered – the BL Lac objects, named after the prototype BL Lacertae in the Lacerta constellation. These objects are extremely variable 'star-like' objects with a non-thermal spectrum devoid of emission lines.

Kellermann *et al.* (1989) found from the arcsecond-scale observations of objects from the Palomar Bright Quasar Survey (BQS) that the BQS quasars fell in two classes – while the majority were 'radio-quiet' *i.e.*, they had a radio flux density close to that of the optical flux density, $15 - 20\%$ were 'radio-loud' *i.e.*, they were much brighter at radio

than at optical wavelengths. The formal definition of a 'radio-loud' AGN (Kellermann *et al.*, 1989) was an object with $S_{5GHz}/S_{B-\text{band}} \geq 10$, S_{ν} being the flux density at frequency ν.
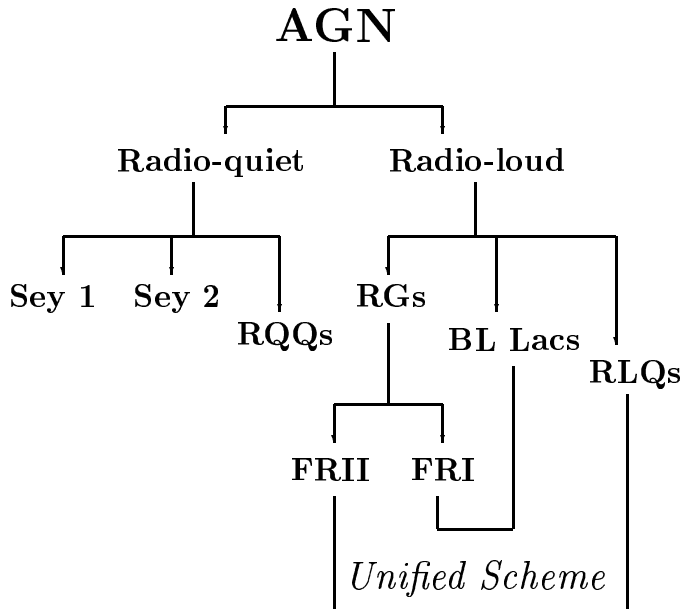
Figure 1.1: A tree chart showing AGN classification. 'Sey 1' (and 2) stand for Seyfert 1 (and 2) galaxies, RQQs = radio-quiet quasars, RGs = Radio galaxies, RLQs = radio-loud quasars, FRI (and II) = Fanaroff-Riley type I (and II) radio galaxies.

1.2.1 Radio-quiet AGNs

Following the definition by Kellermann *et al.* (1989), the ratio of the radio (5 GHz) to optical (B–band) flux density in radio-quiet AGNs is $S_{5GHz}/S_{B-\text{band}} \leq 10$. Seyfert galaxies and radio-quiet quasars fall under this class. The emission line spectrum of Seyfert galaxies falls broadly in two categories. Seyfert type 1 display broad permitted lines and narrow forbidden lines in their emission line spectrum, while Seyfert type 2 display only narrow forbidden lines. Similar to the Seyfert 1s, radio-quiet quasars display broad emission lines in their spectra. However, they differ from Seyfert 1s in having higher nuclear luminosities (see Antonucci, 1993). Spectropolarimetric observations of the Seyfert 2 NGC 1068 by Antonucci & Miller (1985) revealed the presence of very highly polarized, very broad symmetric Balmer lines, closely resembling the spectra of Seyfert type 1 nuclei. A Unified Scheme has emerged, according to which Seyfert 1s and 2s are essentially the same class of objects differing in properties primarily on the basis of their orientation with respect to us. The *Hubble Space Telescope* (*HST*) and ground-based observations of host galaxies of AGNs have revealed that radio-quiet

AGNs are found in both elliptical and disk galaxies (Taylor *et al.*, 1996; Bahcall *et al.*, 1997; McLure *et al.*, 1999).

1.2.2   Radio-loud AGNs

The 'radio-loud' AGNs by definition have radio power exceeding the optical power by an order of magnitude or more. Radio galaxies, BL Lac objects and radio-loud quasars fall in the 'radio-loud' AGN class. These AGNs can have radio jets spanning hundreds of kiloparsecs and even a megaparsec, extending way beyond the extent of their host galaxies. The radio emission from AGNs is conventionally interpreted as incoherent synchrotron radiation from a non-thermal distribution of relativistic electrons (e.g., Jones *et al.*, 1974).

For a self-absorbed synchrotron source, the brightness temperatures, T_B, cannot exceed 10^{12} K, called the 'Compton limit' (also see Singal, 1986). This limit exists because at higher values of T_B, the inverse Compton scattering by the relativistic electrons upscatters their own synchrotron photons to higher energies, which readily escape the optically thin medium and the source cools down (Kellermann & Pauliny-Toth, 1969). However the source sizes inferred from the rapid variations in the flux densities from some quasars at centimeter wavelengths were so small that these sources seemed to violate the Compton limit.

Many theoretical models were propounded to explain the extreme properties of radio-loud AGNs. Rees (1967) postulated bulk relativistic motion in compact radio sources to explain the rapid variability. He also predicted that the apparent speeds of emitted blobs of plasma in these sources could exceed the speed of light ('superluminal motion') due to their bulk relativistic motion, close to our line of sight. This superluminal motion was detected in compact radio sources with the advent of Very Long Baseline Interferometry (VLBI) (e.g., Cohen *et al.*, 1971; Whitney *et al.*, 1971).

Blandford & Rees (1974) proposed the 'twin-exhaust' model for radio-loud AGNs wherein the relativistic plasma generated in the AGN could not escape isotropically due to the presence of too much dense thermal gas surrounding the nucleus. However, an equilibrium flow in which plasma escaped along two oppositely-directed channels, was possible. Blandford & Konigl (1979) proposed that radio emission in compact radio sources originated from a collimated relativistic jet and with their model could explain the flat radio spectra, the superluminal expansion and the flux variability of AGNs, among other properties.

HST and ground-based observations have revealed that radio-loud AGNs are almost always found in elliptical host galaxies, often luminous ellipticals comparable to the

brightest cluster galaxies (Smith & Heckman, 1986; Hutchings *et al.*, 1989; Taylor *et al.*, 1996; Zirm *et al.*, 1998). However, for high redshift quasars it has been shown that the *HST* may only be sampling the bulge and thereby misclassifying the host galaxy as an elliptical (Hutchings *et al.*, 2002).

In radio-loud AGNs, there is compelling evidence that bulk relativistic motion is ubiquitous, which leads to relativistic aberration effects, so that the angle to the line of sight plays a dominant role in the appearance of these objects (see review by Urry & Padovani, 1995). For every Doppler-boosted object, there are intrinsically similar objects whose jets are not directed toward us – the "parent" population. By comparing properties that are known to be independent of orientation, for objects that are known to be boosted and not boosted, we can attempt to identify a given class of Doppler-beamed objects with their plane-of-sky counterparts or "parent objects". A simple Unified Scheme (US) has thus emerged (Barthel, 1989; Antonucci, 1993; Urry & Padovani, 1995), according to which the BL Lacs and radio-loud quasars are the relativistically beamed counterparts of FRI and FRII radio galaxies, respectively (but see Singal, 1993). We will discuss the Unified Scheme in greater detail in subsequent sections.

1.3 The current paradigm for radio-powerful AGNs

By the late 1970s, a zeroth-order model of a radio-loud AGN had emerged. We give here a simplified picture of the model (see Figure 1.2), followed by sub-sections on each of the model components and observational evidence supporting its validity. At the heart of this model of an AGN is a supermassive black hole. Matter falls into the gravitational potential well of this SMBH. However, in order to release excess angular momentum, the matter first falls onto and through an accretion disk. The matter in the differentially rotating disk slowly loses momentum and falls into the event horizon of the black hole.

The accretion disk itself can puff up due to radiation or gas pressure. The matter around the SMBH and in the inner accretion disk is heavily ionised and dust sublimates at the high temperatures. Further away, on scales of a parsec, the gas is molecular and the dust survives in a torus or warped disk kind of structure. From certain lines of sight, this torus hides the central engine from direct view. Somewhere in the interface of the black hole-accretion disk, jets of plasma are ejected at relativistic speeds. Magnetic fields are thought to play a crucial role in the formation and collimation of these jets. The jets themselves emit synchrotron radiation due to relativistically moving charged particles (basically electrons) around magnetic field lines. The jets stay relativistic for distances of the order of a few kiloparsecs and then decelerate to sub-relativistic speeds

in some sources while in others they may stay relativistic and collimated to hundreds of kiloparsecs and even a megaparsec. Some jets (like in FRIs) flare out on scales of a kpc while some jets (like in FRIIs) hit the intergalactic medium, terminate in regions of high surface brightness called "hot spots" and then create a backflow of plasma, forming a radio lobe.

1.3.1   Supermassive black holes

Direct observational evidence for the presence of supermassive black holes is difficult with the present day telescopes – even the *Hubble Space Telescope* cannot directly image the < 0.1 pc accretion disk expected for a $\sim 10^8$ M$_\odot$ SMBH. Therefore we must rely on indirect observational evidence for the presence of black holes as well as to estimate their masses.

Indirect estimates of black hole masses for AGNs and galaxies include the following results :

1. Observations of the parsec-scale gas disk in the centre of the nearby AGN M 87 with the Faint Object Spectrograph on the *Hubble Space Telescope* showed that the gas was rotating in a Keplerian state about a central mass of $\sim 2 \times 10^9$ M$_\odot$ (Macchetto *et al.*, 1997).

2. Stellar kinematics of the nearby (less than a Mpc away) 'non-active' galaxies M 31 and M 32, using ground-based telescopes revealed the presence of a $> 10^7$ M$_\odot$ object in the centre of them (Kormendy, 1988).

3. Water vapour maser emission imaged by the VLBI in the parsec-scale disk of the nearby AGN NGC 4258, has revealed their Keplerian motion around a $\sim 3 \times 10^7$ M$_\odot$ object, within a distance of < 0.1 pc (Miyoshi *et al.*, 1995).

4. The X-ray line of Fe Kα at ~ 6.4 keV seen in the Seyfert 1, MCG-6-30-15 is very asymmetric and has a velocity width of $\sim 10^5$ km s^{-1}. It fits with a model of the gas suffering a gravitational redshift in the field of a supermassive black hole (Tanaka *et al.*, 1995). However, a controversy currently exists concerning the interpretation of this line. Lee *et al.* (2001) interpret this feature as an absorption edge produced by a dusty, partially ionized ("warm") absorber.

5. The measurements of stellar dynamics have established that the nucleus of the Milky Way harbors a supermassive black hole with a mass $\sim 2.6 \times 10^6$ M$_\odot$ (Genzel *et al.*, 1997; Ghez *et al.*, 2000).

HST observations have revealed that supermassive black holes having masses in the range $10^6 - 10^9$ M$_\odot$ are ubiquitous in the universe. They reside in the centres of (almost) all the galaxies and accretion of matter onto the black hole and the accretion-

rate is crucial in the galaxies being 'active' or 'non-active'. Urry *et al.* (2002) find that a comparison of AGN and normal galaxies in the luminosity-black hole mass plane, yields no gap between them, suggesting that AGN activity decreases smoothly towards the non-active state.

From studies of nearby inactive galaxies, it has been established that the mass of the SMBH scales roughly linearly with the luminosity (or mass) of the bulge component of the host galaxy (Kormendy & Richstone, 1995; Magorrian *et al.*, 1998; Ho, 1999; Kormendy & Gebhardt, 2001). Further, the masses of supermassive black holes correlate even better with the velocity dispersions of their host bulges and the relation is much tighter than the relation between black hole masses and the bulge luminosity (Ferrarese & Merritt, 2000; Gebhardt *et al.*, 2000). There are many strong arguments in favour of the SMBH as against the best alternative of AGNs being powered by starbursts (e.g., Terlevich & Melnick, 1985; Heckman *et al.*, 1991; Filippenko, 1992). However, some radio-quiet AGNs could be powered partly by starbursts.

1.3.2   Accretion Disks

Accretion of matter into the supermassive black hole in the galactic center is thought to be the source of all AGN activity. Frictional interaction of gas clouds which are attracted by the gravitational field of the SMBH leads to the formation of a rotating disk of material or an accretion disk (see review by Shlosman *et al.*, 1990). One possible mechanism for accretion disks to transfer angular momentum and dissipate binding energy is via magneto-rotational instability which inevitably produces magnetically active coronae. Accretion disks are likely to generate outflows that are further boosted by centrifugal force (e.g., Blandford & Payne, 1982; Begelman, 2001). One possible origin of the optical-UV feature referred to as the "big blue bump" in quasar SEDs is suggested to be thermal emission from an accretion disk (Shields, 1978; Malkan, 1983).

Accretion disks have complicated structures for different accretion rates $\dot{m}$, and the viscosity α (Chen, 1995). For a disk with a low accretion rate, three possible solutions have been suggested: optically thin advection-dominated accretion flows or ADAF (Narayan & Yi, 1994), advection-dominated inflow-outflows (ADIOs) (Blandford & Begelman, 1999) and convection-dominated accretion flows (CDAF) (Narayan *et al.*, 2000; Quataert & Gruzinov, 2000). When $\alpha^2 < \dot{m} < 1$, the disk has a standard optically thick, geometrically thin structure (Shakura & Sunyaev, 1973), which has been extensively studied.

1.3.3   Obscuring tori

Rees *et al.* (1982) had proposed that at the center of each radio-loud AGN there is a spinning black hole, which is surrounded by a torus of gas. This torus anchors magnetic fields which extract rotational energy from the SMBH in the form of two collimated beams of relativistic particles and fields. The central regions of many AGNs do appear to contain obscuring material, probably in the form of gas and dust, that prevents IR through UV light from passing through in some lines of sight (Rowan-Robinson, 1977). The most direct evidence for circumnuclear obscuration has come from the spectropolarimetry of Seyferts 2s (e.g., NGC 1068, Antonucci & Miller, 1985) and the radio galaxy 3C 234 (Antonucci, 1984). The polarized spectra of these objects show strong broad lines like type I objects (*i.e.*, which are at $\theta \sim 0°$). The polarization is probably caused by electron scattering because it is wavelength-independent; some polarization can also be caused by dust (Miller *et al.*, 1991; di Serego Alighieri *et al.*, 1994). In 3C 234, the plane of polarization is perpendicular to the radio jet axis, as expected if a type I nucleus is partially obscured by a wall of gas and dust whose axis coincides with the radio jet axis. Like 3C 264, the radio galaxy IC 5063 has polarized broad lines, indicative of scattered light from a hidden broad-line region (Inglis *et al.*, 1993). Other polarization observations also support the picture of scattered light from a luminous, hidden continuum source in narrow line radio galaxies (NLRGs) (di Serego Alighieri *et al.*, 1994; Goodrich, 1992). Jackson & Browne (1990); Hes *et al.* (1996) found significant differences in the [OIII] line luminosities of FRII radio galaxies and quasars, while the difference in the [OII] line luminosity was marginal. This result could be explained by the presence of an obscuring torus which affects the [OIII] line more than [OII] because it comes from regions closer to the central engine.

Since optical depths are much smaller at infrared wavelengths as compared to optical, IR observations probe deeper into the nuclear regions of type II AGNs (*i.e.*, which are relatively plane-of-sky objects). Bright IR cores and perpendicular polarization like in 3C 234 have been observed in many NLRGs (e.g., Bailey *et al.*, 1986; Fabbiano *et al.*, 1986; Antonucci & Barvainis, 1990). The hardness of the X-ray continuum from type II AGNs relative to the type Is, possibly due to higher absorbing column densities, is also consistent with the idea of an obscured nucleus (e.g., Cygnus A, Ward *et al.*, 1991).

There is no spectropolarimetric evidence from obscuration in low-luminosity FRI radio galaxies. Even though apparent differences in [OIII] luminosities for a small sample of BL Lacs and FRIs (Stickel *et al.*, 1993; Tadhunter *et al.*, 1993) could rise from obscuration in FRIs, the case for obscuring tori in FRIs is far from being settled (Urry & Padovani, 1995).

1.3.4 The emission line region

Observational evidence points to the central kiloparsec of AGNs being photoionized by the intensely luminous central source (Davidson & Netzer, 1979; Netzer & Maoz, 1990), which results in the highly ionized emission lines in their optical, UV, and even X-ray spectra. Only the BL Lacs have either no lines or their line equivalent widths are very small (Stickel *et al.*, 1989). Celotti *et al.* (1997) have proposed that emission line regions in quasars, especially close to the black hole, are likely to be photoionized by the thermal emission from the accretion disk.

The gas clouds associated with the broad-line region (BLR) are located close to the central engine, within $\sim$ 2–20 $\times 10^{16}$ cm (*i.e.*, 0.006–0.06 pc) of the black hole (Urry & Padovani, 1995). The BLR is associated with broad and strong emission lines with velocity widths of atleast 1000–2000 km s^{-1} and even up to 10,000 km s^{-1}. The emission lines comprise of the Lyman, Balmer, Paschen and Brackett series of atomic hydrogen (e.g., Lyα, Hα, Hβ, Paα, Paβ, Brα), helium (e.g., HeI, HeII), carbon (e.g., CIII], CIV), and oxygen (e.g., OI, OIV, OVI) lines among others. The fraction of the thermal disk emission reprocessed by the BLR clouds is roughly equal to the cloud covering factor which is ≈ 0.1 (Netzer & Maoz, 1990). From the presence of the semi-forbidden CIII] line and the absence of the broad component of the [OIII] doublet, the electron density in the BLR has been estimated to be $\sim 10^8 - 10^{10}$ cm^{-3}.

The narrow line region (NLR) extends approximately from $10^{18} - 10^{20}$ cm (*i.e.*, 0.3–33 pc) from the central engine (Urry & Padovani, 1995). The NLR has emission from many forbidden lines like oxygen [OIII], [OII], [NII], [SII] among other lines which include the HI Lyman and the Balmer series. The densities within the NLR are believed to be $\sim 10^4 - 10^6$ cm^{-3} from the measurements of [SII] and [OIII] lines.

1.3.5 The jets

The jets in AGNs are beams of plasma which transport particles and energy to the extended radio lobes from the central engine. The jet emission is synchrotron radiation (Schwinger, 1949) emitted from charged particles that are gyrating at relativistic speeds around magnetic field lines (e.g., Shklovsky, 1958). It was proposed that jets are emitted in the form of bipolar outflows from the black hole-accretion disk interface (Blandford & Rees, 1974; Wiita, 1978). The synchrotron emission is mostly emitted at radio wavelengths due to the longer lifetimes of the radio-emitting electrons. Optical synchrotron emitting electrons may be short-lived due to higher energies in which case the optical emission in AGN jets must come from electrons that are re-accelerated *in situ*, possibly due to transverse shocks propagating in the jets (e.g., Hughes *et al.*, 1985;

Marscher & Gear, 1985). However, relativistic beaming in jets could result in longer lifetimes for the optical emitting electrons and *in situ* acceleration may then not be needed (e.g., Fraix-Burnet *et al.*, 1991).

It has also been speculated that the relativistic jets associated with radio-loud AGNs are powered electromagnetically by a spinning black hole and that they are collimated by an encircling magneto hydrodyanamic (MHD) wind leaving the accretion disk at a slower speed (Blandford & Levinson, 1995). The MHD simulations of Ustyugova *et al.* (2000) have established that a quasi-stationary collimated Poynting jet (*i.e.*, in which the mass flux is negligible and the energy and angular momentum are carried predominantly by the electromagnetic field) arises from the inner part of the disk while a steady uncollimated hydromagnetic outflow arises in the outer part of the accretion disk.

Due to the absence of emission lines from AGN jets, the jet composition is still a matter of debate. Celotti (1997) have suggested that the jet composition differs among AGNs, with the low-luminosity FRIs having electron-positron and the high-luminosity FRIIs having primarily electron-proton jets (eg., Wardle *et al.*, 1998).

Two processes have been widely advocated for jet formation in AGNs : (1) energy extraction from the spin of the SMBH (Blandford & Znajek, 1977) and (2) energy extraction from a disk wind (Blandford & Payne, 1982). Several variants of these two models have been proposed. The strong correlation found between the luminosity of the extended radio emission and the accretion rate supports the notion that radio jets are directly coupled to the accretion disk (Wang *et al.*, 2003). In their investigation of the process (1) in the regime of the standard optically thin, geometrically thick disk, Livio *et al.* (1999) conclude that power from both the processes, even for rotating black holes, are negligible compared with the radiative output from the accretion disk itself. This is because geometrically thin disks cannot produce a strong enough poloidal magnetic field for the energy extraction to be effective.

Relativistic beaming in AGN jets

There are many strong arguments in support of bulk relativistic motion in the jets of AGNs.

1. Synchrotron photons can be inverse Compton scattered to higher energies by the relativistic electrons, which is known as the synchrotron self-Compton (SSC) process. The synchrotron radiation density inferred from the observed radio power and angular size predicts SSC X-rays, much greater than observed X-ray flux densities (e.g., Marscher *et al.*, 1979), which is called the "Compton catastrophe".

It follows that the true synchrotron photon density must be lower than what is inferred from assuming isotropy, meaning the emission is beamed.

2. The highly variable flux densities of BL Lacs and OVV quasars (e.g., Quirrenbach, 1992) can be explained by shortened time scales (over and above the 'time dilation' effect) due to relativistic beaming (Rees, 1967).

3. The one-sidedness of kiloparsec-scale jets in the high-luminosity FRIIs and parsec-scale jets in the low-luminosity FRI AGNs can be accounted for by Doppler boosting of the approaching jet and Doppler dimming of the receding jet (e.g., Parma *et al.*, 1994).

4. The 'Laing-Garrington' effect (Garrington *et al.*, 1988; Laing, 1988) *i.e.*, depolarization asymmetry observed in high-luminosity FRIIs shows that the observed jet is on the same side as the less depolarized lobe, indicating that it is nearer to the observer. Depolarization asymmetry has also been observed (though it is much less conspicuous) for the low-luminosity FRIs (Parma *et al.*, 1993, 1994) which have slower moving jets on kpc-scales (Bicknell *et al.*, 1990) but still have mildly relativistic pc-scale jets (Venturi *et al.*, 1993; Feretti *et al.*, 1993; Laing, 1994).

The jet-to-counter-jet ratio R_j, is an indicator of relativistic beaming. It is given by

$$R_j = \left[\frac{1 + \beta\cos\theta}{1 - \beta\cos\theta} \right]^p \tag{1.1}$$

where $p = 3 + \alpha$ for a moving, isotropic source and $p = 2 + \alpha$ for a continuous jet (e.g., Urry & Padovani, 1995).

Superluminal motion of jet components, which has been observed with VLBI, is a consequence of bulk relativistic motion in the AGN jet, close to our line of sight. The apparent velocity/c is given by :

$$\beta_{app} = \frac{\beta\sin\theta}{1 - \beta\cos\theta} \ . \tag{1.2}$$

Therefore, if the jet is oriented such that, for example, $\theta = 11°$ and β of the jet $= 0.999$, then the $\beta_{app} = 10c$.

The kinematic Doppler factor of a moving source is defined as

$$\delta \equiv [\gamma(1 - \beta\cos\theta)]^{-1} \tag{1.3}$$

where β is its bulk velocity in units of the speed of light, $\gamma = (1 - \beta^2)^{-1/2}$ is the corresponding Lorentz factor, and θ is the angle between the velocity vector and the

line of sight. The Doppler factor has a strong dependence on the viewing angle, which gets stronger for larger Lorentz factors.

A consequence of bulk relativistic motion is the intensity enhancement or "Doppler boosting" effect.

$$I_\nu(\nu) = \delta^3 I'_{\nu'}(\nu') \qquad (1.4)$$

(Rybicki & Lightman, 1979) where I_ν is the specific intensity and primed quantities refer to the rest frame of the source. If the emission is isotropic in the source rest frame, the flux density, S_ν is given as

$$S_\nu(\nu) = \delta^{3+\alpha} S'_{\nu'}(\nu') \ . \qquad (1.5)$$

The observed luminosity of a relativistic jet, L_j^{obs} is related to its intrinsic luminosity L_j^{int}, via

$$L_j^{obs} = \delta^p L_j^{int} \ , \qquad (1.6)$$

where p is the jet structural parameter described above.

1.4   The Fanaroff-Riley dichotomy in radio galaxies

Fanaroff & Riley (1974) recognised that the radio morphology and total radio power of radio galaxies fell in two distinct sub-classes : the low-power Fanaroff-Riley type I (FRI) galaxies showed extended plumes and tails with no distinct termination of the jet while the high-power type II (FRII) radio galaxies showed narrow, well-collimated jets with clear termination points called "hot spots". The total radio luminosity break at 178 MHz occurred at $L_{178} = 2 \times 10^{26}$ WHz^{-1} although at higher frequencies the break is less sharp (Urry & Padovani, 1995). Later studies revealed further systematic differences, *viz.*, that FRII radio galaxies have systematically more luminous optical emission lines (Zirbel & Baum, 1995) and greater far-infrared flux densities (O'Dea *et al.*, 1994), while FRI radio galaxies inhabit richer environments (Prestage & Peacock, 1988).

A useful diagnostic for radio galaxies, as first shown by Ledlow & Owen (1996), is the plot of extended radio luminosity versus optical absolute magnitude. A diagonal line separates the two radio populations: at a given optical luminosity (which in the case of radio galaxies is dominated by the host galaxy), FRIIs have much higher radio powers than FRIs. There is an alternate interpretation of the plot, *viz.*, only a 'high-enough' powered radio jet can punch through a high-mass (greater interstellar density) galaxy to produce non-decelerating (or near non-decelerating) jets (Urry, 2003). However, it has been shown by Scarpa & Urry (2001) that radio galaxies are a luminosity-biased but otherwise random sample of elliptical galaxies. They state that the well-known difference

of ~ 0.5 mag in average optical luminosity between FRI and FRII radio galaxies is a simple selection effect.

Bicknell (1995) and Gopal-Krishna & Wiita (2001) suggest that the division in the Owen–Ledlow plot may arise from the interaction of the jet with the interstellar or intracluster medium. Other suggested possibilities to explain the FR divide include differences in the spin of the SMBH, resulting in different jet kinetic powers (Wilson & Colbert, 1995; Meier, 1999), different galaxy environments (Smith & Heckman, 1990), and varying accretion rates (Baum *et al.*, 1995). Ghisellini & Celotti (2001) have suggested that the dividing line corresponds to a transition in the accretion mode, from an optically thick, geometrically thin disk (Shakura & Sunyaev, 1973) in FRIIs to an optically thin advection dominated accretion flow (ADAF) in FRIs. The work of Bicknell *et al.* (1990) supports the notion that the transition from FRI to FRII radio sources represents, in large part, a transition from low- to high-Mach number jets. It has also been speculated that FRIIs evolve into FRI radio sources (e.g., Maraschi & Rovetti, 1994; Jackson & Wall, 1999).

Some radio sources however, show both FRI and FRII characteristics, *viz.*, narrow jets and hotspots along with diffuse large-scale radio lobes (e.g., Capetti *et al.*, 1995) raising questions about the bimodality of the dichotomy and hinting at the possibility of FRIs smoothly merging into FRIIs. It has also been suggested that FRI jets are electron-positron dominated, while the FRII jets are electron-proton dominated (e.g., Celotti, 1997).

1.5 The BL Lacertae objects

The BL Lacertae objects are named after the prototype BL Lacertae which was considered at first to be a variable star in the Lacerta constellation. Strittmatter *et al.* (1972) soon identified it to be an AGN. As a class, BL Lac objects are characterized by a predominantly non-thermal, highly polarized continuum which is highly variable. The bulk of their radiation is thought to be highly relativistically beamed synchrotron emission from plasma outflows in the form of jets. Its optical spectra have only weak or no emission lines. The radio morphology of BL Lacs is similar to that seen in FRI radio galaxies, *viz.*, diffuse jets and lobes which have no distinct termination. Based on orientation-independent properties like extended radio emission, host galaxy types and magnitudes, galaxy environments, the FRI radio galaxies are thought to be the "parent population" of the BL Lac objects (Orr & Browne, 1982; Wardle *et al.*, 1984; Antonucci & Ulvestad, 1985). However, there exists a small subset of BL Lac objects which have radio morphologies more consistent with FRIIs than FRIs (e.g., Kollgaard *et al.*, 1992).

1.5.1 The BL Lac sub-classes

The BL Lacs that have been detected through radio searches (e.g., Ledden & Odell, 1985; Burbidge & Hewitt, 1987) show systematic differences from those that have been discovered through space-based X-ray surveys (e.g., Giommi *et al.*, 1989; Stocke *et al.*, 1989). The radio-selected BL Lacs (RBLs) are typically more core-dominated on arcsec-scales (Perlman & Stocke, 1993; Kollgaard *et al.*, 1996), they show higher average optical polarization and greater variability (Schwartz *et al.*, 1989; Jannuzi *et al.*, 1994), and have more powerful radio lobes than the X-ray selected BL Lacs (XBLs) (Kollgaard *et al.*, 1992; Laurent-Muehleisen *et al.*, 1993). RBLs therefore appear to be more "extreme" than XBLs.

Based on the nuclear trends, the spectral energy distribution (SEDs) of XBLs were expected to be different from RBLs due to their inferred, less extreme orientations, but the SEDs showed that the synchrotron emission in RBLs typically peaks in the near infrared (*i.e.*, they are low–energy peaked BL Lacs or LBLs), whereas the XBL synchrotron emission typically peaks in the soft X-ray regime (the high–energy peaked BL Lacs or HBLs) (see Figure 1.4). LBLs and HBLs are sometimes referred to as 'red' and 'blue' BL Lacs. Most, though not all, RBLs are LBLs and most, though not all, XBLs are HBLs. We will deal with these two sub-classes of BL Lac objects in more detail in Chapter 5.

1.6   Radio-loud quasars

The quasi-stellar radio sources or quasars have been a subject of intense study ever since their discovery by Schmidt (1963). These objects show a non-thermal spectrum along with strong and broad emission lines. Their radio morphology is similar to that seen in FRII radio galaxies *viz.*, jets terminating in regions of high surface brightness called "hot spots".

BL Lac objects and optically violently variable (OVVs) quasars together are sometimes referred to as 'blazars'. The separation of BL Lacs and quasars is still a matter of some debate, since the original classification criterion for BL Lac objects (strongest rest-frame emission line width narrower than 5 $\mathring{A}$; e.g., Stickel *et al.*, 1991) does not appear to reflect any natural division in the observed line-width distribution of blazars (Scarpa & Falomo, 1997). A further complication arises in that the emission line widths of many blazars (including BL Lac itself; Vermeulen *et al.*, 1995) are known to vary with time.

1.7 Radio-loud Unified Scheme

The twin relativistic jets in radio-loud AGNs, exhibit Doppler beaming effects, making intrinsically similar objects appear different based on orientation. Based on orientation-independent properties like extended radio emission, narrow emission lines, host galaxy type and galaxy environments, a simple Unified Scheme has emerged (Barthel, 1989; Antonucci, 1993; Urry & Padovani, 1995), according to which BL Lacs and radio-loud quasars are the relativistically beamed counterparts of FRI and FRII radio galaxies, respectively. However, it has also been proposed that the FRIs are not the parent population of *all* the BL Lac objects (Kollgaard *et al.*, 1992; Murphy *et al.*, 1993). Weak-lined FRIIs may be the parent population for some BL Lac objects (Jackson & Wall, 1999).

1.8 The study of magnetic fields in AGN jets by polarimetry

The incoherent synchrotron emission from relativistic electrons in magnetic fields observed in AGNs can be as much as 75% linearly polarized for optically thin plasma (Pacholczyk, 1970). However, polarization up to only $30 - 40\%$ is observed in the kiloparsec-scale jets of BL Lacs and quasars (Bridle & Perley, 1984). This depolarization from the theoretical maximum polarization could be a result of magnetic fields which are not ordered on kpc-scales and other factors described in the next section.

Magnetic field configurations in kiloparsec jets of radio-powerful AGNs have been well studied (Bridle & Perley, 1984; Morganti *et al.*, 1997). There are primarily three configurations common to jets :

1. $B_{\parallel}$, *i.e.*, apparent B is predominantly parallel to the jet axis all across it.

2. $B_{\perp}$, *i.e.*, apparent B is predominantly perpendicular to the jet axis all across it.

3. $B_{\perp-\parallel}$, *i.e.*, apparent B is predominantly perpendicular to the jet axis at the center of the jet ('spine'), but becomes parallel to the axis near one or both of its edges ('sheath').

The weak FRI sources have two-sided $B_{\perp}$ or $B_{\perp-\parallel}$ - dominated jets, while the powerful FRII sources have one-sided $B_{\parallel}$ - dominated jets. We must keep in mind that the above B-field geometry applies only to the ordered component of the magnetic field, which is significant, but there exists also a random B-field component, as we discuss later.

Studies on arcsecond-scales have demonstrated that the cores of FRII radio galaxies typically have low fractional polarization ($< 0.6\%$) (e.g., Rudnick *et al.*, 1986; Rusk, 1988). This is in contrast to the properties of quasar cores which are generally more highly polarized on arcsecond-scales ($2 - 5\%$). Rudnick *et al.* (1986) have speculated that the low polarization of radio galaxy cores could be due to optical depth effects of self-absorbed emission, highly randomized internal magnetic fields, or Faraday depolarization by a highly tangled screen.

1.8.1   The parsec-scale B-field geometry

VLBI observations have shown that the B-field configuration seen on kpc-scales may extend down to parsec-scale jets (for e.g., Gabuzda *et al.*, 1992; Attridge *et al.*, 1999). There is a systematic difference seen in the orientation of the polarization electric vector (χ) with respect to the position of the local VLBI jet direction in quasars and BL Lacs. Assuming optically thin jet emission, the B-fields inferred from the χ vectors are predominantly longitudinal to the jet directions in quasars while they are predominantly transverse in the BL Lac jets (Cawthorne *et al.*, 1993; Gabuzda, 1997).

The orientation of the polarization electric vectors in the VLBI cores of quasars had not shown a systematic trend until the recent work of Pollack *et al.* (2003), which shows quasar cores to preferentially have χ's which are transverse to the jet direction. The observations of BL Lac cores by Gabuzda *et al.* (2000) have demonstrated a bimodal χ distribution, with χ either aligned with or perpendicular to the VLBI jet; it has recently been suggested that this bimodality may be associated with bimodality in the optical depth of the polarized regions within the observed VLBI core (Gabuzda, 2003).

Multifrequency polarimetry with the VLBA has recently revealed absolute Faraday rotation measures (RM) in excess of 1000 rad m^{-2} in the central regions of a majority of the quasars studied (Taylor, 1998, 2000). Beyond a projected distance of 20 parsec in the jets, however, the RM reduce to < 100 rad m^{-2}. Such sharp RM gradients must be the result of magnetic fields organized over the central 1–100 pc. Taylor (2000) postulates that the cores and inner jets of quasars are viewed through ionized gas associated with the nuclear region. According to the Unified scheme linking quasars to FRII radio galaxies, one then expects that the jet components of FRII radio galaxies within 100 parsec of the cores will be viewed through a deep 'Faraday screen' *i.e.*, the unobservable distribution of thermal magnetoionic plasma which results in the Faraday rotation of the electric vector of the electromagnetic waves traversing the medium. This would explain the low fractional polarization of radio galaxy cores.

With the high resolution afforded by VLBI observations it might be possible to

resolve the Faraday screen and recover some polarized flux density. Furthermore, once the jet components move farther from the nuclear environment the Faraday depth (the physical extent of the Faraday screen through which the electromagnetic waves traverse) should drop, and it may be possible to measure both significant polarization from the jet and still high RMs.

Lister (2003) have observed AGN jets with the VLBA, to investigate structural and polarization changes. Linearly polarized emission is detected in a majority of jets which have been imaged, with the exception of a few sources which are likely to be heavily depolarized by intervening gas in the host galaxy (e.g., Vermeulen, 2002). The unresolved cores (located close to the base of the jet) are weakly polarized, with the majority having fractional polarizations under 4%. In most cases, the magnetic field order increases with distance down the jet, with features in the jets being appreciably more polarized than the cores. In many sources, the field appears highly ordered on the outside edge where the jet bends, suggesting a compression of the field from interaction with the external medium. A Kolmogorov-Smirnov test on the distributions of fractional polarization for the polarized features in the jets of BL Lacs and radio-loud quasars indicates only a 0.1% probability that the two are from the same parent distribution.

1.8.2 Faraday Rotation and depolarization mechanisms

Faraday rotation is the rotation of the plane of linear polarization during propagation of an electromagnetic wave through a magnetized plasma. The intrinsic polarization angle χ_0 is related to the observed polarization angle χ by

$$\chi = \chi_0 + RM\lambda^2 \tag{1.7}$$

where λ is the observing wavelength. RM is the rotation measure, which is given by

$$RM = \frac{e^3}{2\pi m^2 c^4} \int n_e B_\parallel dl \tag{1.8}$$

where e and m are the charge and mass of the plasma particles, respectively. Because of the inverse square dependence on the mass of the charged particles which are accelerated by the passing electromagetic wave, Faraday rotation by protons will be negligible compared to that of electrons. n_e refers to the electron density, $B_\parallel$ is the net line-of-sight magnetic field and dl is the path length traversed by the electromagetic wave through the plasma. Using units of cm^{-3}, milligauss, and parsecs, the RM is given by

$$RM = 812 \int n_e B_\parallel dl \ \ \text{rad m}^{-2} \tag{1.9}$$

The RM thus measures the density-weighted magnetic field along the line of sight.

Tangled magnetic fields can cause depolarization to occur. If the magnetic field in the source is composed of a uniform component B_0 and a random component B_r, and the scale of the random component is less than the dimensions of the source, then the intrinsic polarization (p_i) over the whole source will reduce to

$$p_i = p(\gamma)(B_0{}^2)/(B_0{}^2 + B_r{}^2) \tag{1.10}$$

(Burn, 1966), where γ is the power law index of the electrons and

$$p(\gamma) = (3\gamma + 3)/(3\gamma + 7) \tag{1.11}$$

(Le Roux, 1961). For the random component to dominate, the jets would have to be turbulent, and very little ordering of the magnetic fields would occur by the jet motion itself. When the source is optically thick, the maximum intrinsic degree of polarization is 10 to 12% (theoretically derived limit, Pacholczyk, 1970).

Internal Faraday rotation can also cause depolarization of the emission. Polarized emission coming from various depths in the source along the line of sight are Faraday rotated by the source itself, the degree of rotation depending on the depth of the emitting region.

$$P(\lambda^2) = p_i \frac{1 - e^{-S}}{S} \tag{1.12}$$

where

$$S = (K n_e B_r)^2 dL\lambda^4 - 2iK n_e B_\parallel^0 L\lambda^2 \tag{1.13}$$

(Burn, 1966), $P(\lambda^2)$ is the observed polarization of the integrated emission from a source, K is a constant, n_e is the free electron density, d is the scale of the fluctuations in the magnetic field, L is the linear depth of the line-of-sight through the source and $B_\parallel$ is the line-of-sight magnetic field. Internal Faraday rotation can also be significant in the transition region between optically thick and optically thin plasma possibly due to the formation of shocks (Hughes *et al.*, 1985).

Bandwidth depolarization may occur due to the presence of a foreground screen. The electromagnetic waves received in different frequency channels of the detector have suffered different Faraday rotations along their journey from the source to the telescope, and when the emission from the different channels is combined, the net polarization decreases. Beam depolarization happens when the beam of the radio telescope is larger than the scales on which magnetic field orientations vary in the emitting region. If the magnetic field in a foreground Faraday screen is tangled on scales much smaller than the observing beam, regions with similar degrees of polarization but opposite signs will average out and the observed degree of polarization will be decreased.

1.9   Motivation for the thesis

In this thesis, we attempt to explore the Fanaroff-Riley dichotomy issue in radio galaxies. We attempt to examine the problem within the framework of the radio-loud Unified Scheme, by which we in turn endeavour to test the tenets and predictions of the Unified Scheme.

If the Unified Scheme holds well, it has wide implications not only for the understanding of AGNs but in fact all astrophysical jet sources. It would basically imply that jet formation is remarkably similar over a wide range in luminosities (~ 5 orders of magnitude spanning FRIs and FRIIs) and perhaps even down to jets in stellar systems like microquasars and young stellar objects (YSOs) where, similar to AGN jets, the inflow of matter onto the blackhole is thought to occur through an accretion disk and the jet acceleration mechanism is associated with magnetic fields (e.g., Livio *et al.*, 2003; Price *et al.*, 2003).

There appears to be a dichotomy in radio galaxies, as first reported by Fanaroff & Riley (1974). Many suggestions have been made to explain the FR dichotomy; we discussed these in § 1.4. Striking differences seen in the parsec-scale magnetic-field geometry of BL Lacs and core-dominated quasars suggest that the Fanaroff-Riley dichotomy probably *arises close to the central engine*, if as the Unified Scheme postulates, BL Lacs and quasars are the beamed counterparts of FRI and FRII radio galaxies, respectively. The magnetic-field geometry in BL Lac and quasar jets shows a clear tendency to be transverse and longitudinal to the local jet direction, respectively (e.g., Gabuzda *et al.*, 1992; Cawthorne *et al.*, 1993; Gabuzda *et al.*, 1994).

It is now well-known that when the HST imaged the central regions of the FR host galaxies on $0.''05$ scales, it discovered unresolved optical nuclei in the centres of a majority of them (Capetti & Celotti, 1999; Chiaberge *et al.*, 1999, 2002; Verdoes Kleijn *et al.*, 2002). It has been suggested in the literature that the optical nuclei emission is synchrotron emission from the base of the relativistic jet.

We ask the questions : What do the optical nuclei tell us about the nuclear regions of FRIs and FRIIs ? Is there really a dichotomy manifesting itself on parsec-scales in terms of differences in the nuclear structures of FRIs and FRIIs ? For instance, are the optical nuclei the bases of relativistic jets seen in optical wavelengths or is the emission coming from a thermal accretion disk ? Is there an obscuring torus in FRIs and FRIIs ? The Unified Scheme requires one for the FRIIs but not for the FRIs (Urry & Padovani, 1995).

Do the parsec-scale magnetic-field geometry show differences in the FRIs and FRIIs ? Do the B-fields of FRIs and FRIIs resemble those seen in their beamed counterparts,

the BL Lacs and quasars, as predicted by the Unified Scheme ?

Most of the BL Lac objects which had been observed for parsec-scale polarization were (naturally) the radio-powerful ones, which were discovered in radio surveys. Subsequent X-ray surveys with the *HEAO-1* and *Einstein* space observatories discovered an even larger number of radio-weak but X-ray powerful BL Lacs. These were assumed to be different from RBLs due to their less extreme orientations but the SEDs of these showed that these differed in other crucial ways from the earlier studied BL Lacs. The X-ray selected BL Lacs (XBLs) were high-energy peaked BL Lacs (HBLs) while the earlier discovered radio-selected BL Lacs were mostly low-energy peaked (LBLs). Thus it was important to determine how these new HBLs looked in polarized emission on parsec-scales – did they also show the B-field trend seen in LBLs ? Did the dichotomy observed between BL Lacs (LBLs) and quasar B-field geometry disappear or was it reinforced ?

In order to probe the conditions in the centres of radio galaxies in terms of the presence of ordered B-fields, depolarizing ionized circumnuclear material and dusty obscuring tori in the context of the FR divide, *we have constructed a rigorously matched sample* of FRIs and FRIIs from among those showing an unresolved optical nucleus in the high resolution images of the *Hubble Space Telescope.* We attempt to address the FR dichotomy issue following two approaches – through published HST nuclear data of FRIs and FRIIs and through new parsec-scale radio polarimetry observations of FR radio galaxies.

1.10   Thesis outline

In this thesis, we try to address the questions regarding the origin and validity of the Fanaroff-Riley dichotomy. The thesis is sectioned into the following chapters. Chapter 2 describes the technique of Very Long Baseline Interferometry and VLBI polarimetry which was used in this thesis to study magnetic-field order and orientation in radio sources on parsec-scales. In the next two chapters, we discuss the results of the parsec-scale polarimetric study of FRI and FRII radio galaxies. Chapter 3 describes our observations of the parsec-scale B-field geometry in four FRI radio galaxies. Chapter 4 describes the results of VLBP studies of FRII radio galaxies taken from the literature, and our new multi-frequency, multi-epoch observations of the parsec-scale B-fields in the FRII radio galaxy – 3C111. We also examine the effects of depolarizing matter on the B-fields in the nuclear regions of this broad-line radio galaxy. Chapter 5 describes the parsec-scale magnetic-field orientation of high-energy peaked BL Lac objects discovered by the *HEAO-1* observatory. Chapter 6 discusses the nature of the unresolved optical

nuclei discovered by the *Hubble Space Telescope* in the centres of a majority of radio galaxies in the context of the FR divide. We present our results from simple model-fitting of the data. Finally, Chapter 7 summarises the main conclusions of this thesis. We further attempt a synthesis of all the work done so far and arrive at a general view of the subject we started to address. We also present a brief outline of the work to be done in the future.

Some definitions, units and adopted cosmology

Througout this thesis, we define spectral indices α such that $S_\nu \propto \nu^{-\alpha}$. The unit of flux density, $S_\nu = 1$ Jansky $= 10^{-23}$ erg sec^{-1} cm^{-2} Hz^{-1}.

θ denotes the angle between the radio jet axis of the AGN and the line of sight with $\theta \sim 0°$ defining objects which have their radio jets pointing directly towards us.

We assume a universe with $\Omega_M = 0.24$, $\Omega_\Lambda = 0.76$ and Hubble's constant $= 71$ km s^{-1} Mpc^{-1} (unless otherwise stated). The corresponding deceleration parameter, $q_0 \sim -0.6$, implying an accelerating universe.
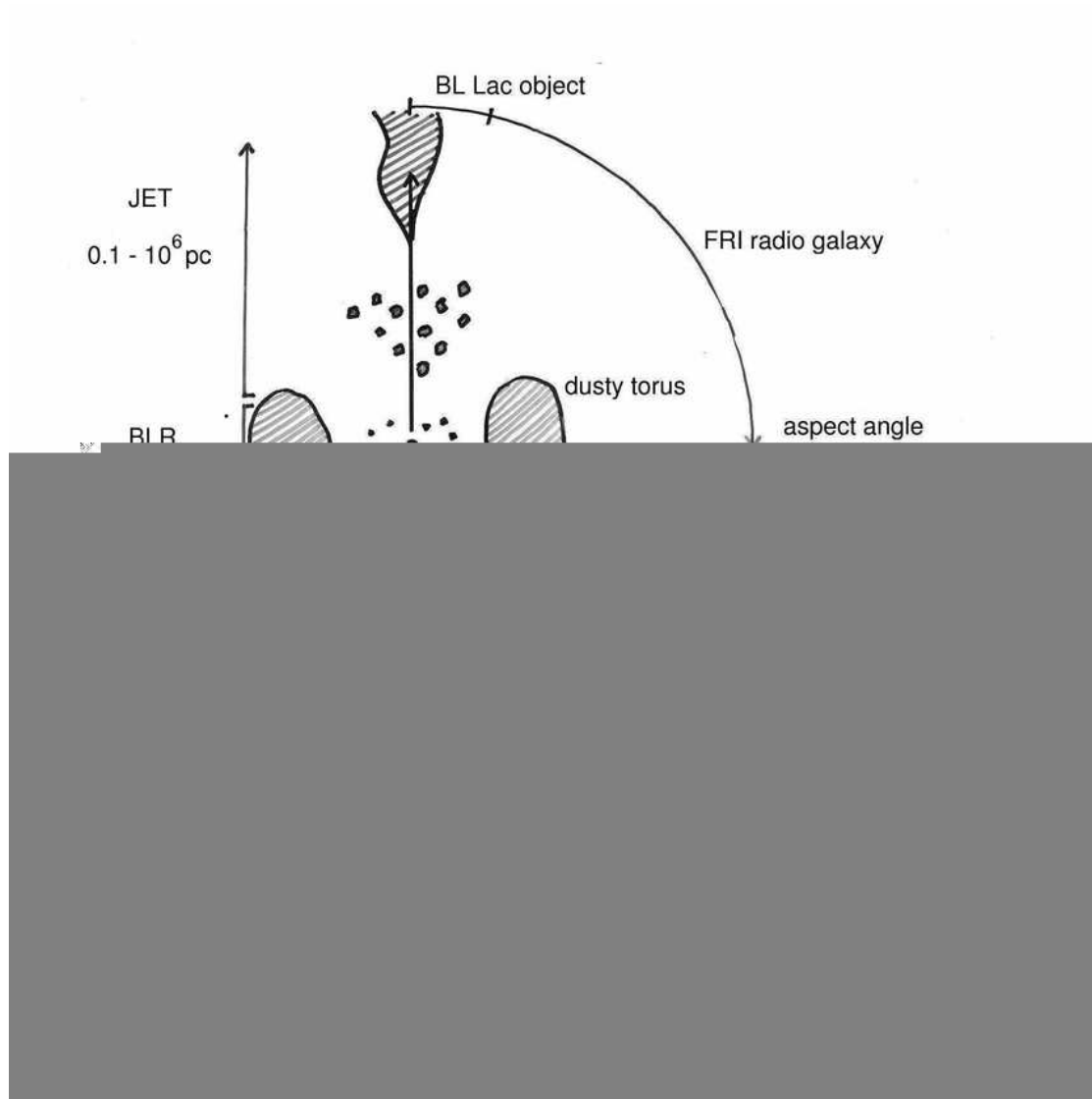
Figure 1.2: Schematic showing the current paradigm for radio-loud AGNs. For the purpose of illustration, an FRI-type flaring, bending jet and an FRII-type collimated jet with a hotspot, have been spliced into one. When the relatively plane-of-sky FRI or FRII radio galaxies are oriented such that their radio jet points towards the Earth, one observes a BL Lac object or a radio-loud quasar respectively. In the centre of the AGN model is the SMBH with an accretion disk. 'l.o.s.' stands for line of sight.

A MODEL FOR THE INNER JET
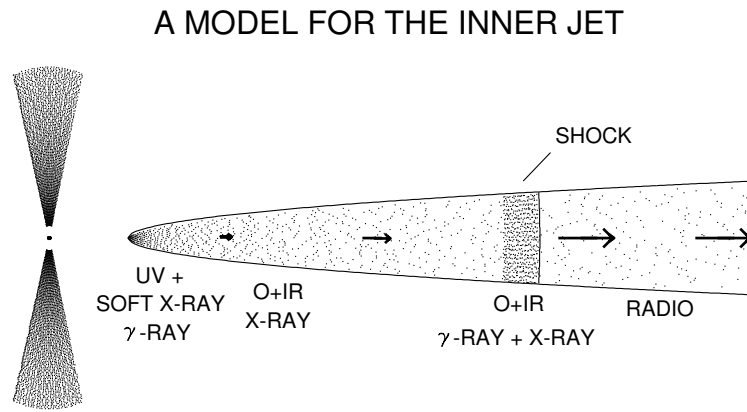
Figure 1.3: Diagram showing a model for the inner jet in AGNs as it is emitted from close to the black hole-accretion disk interface; 'O' stands for optical emission while other symbols have their usual meanings.
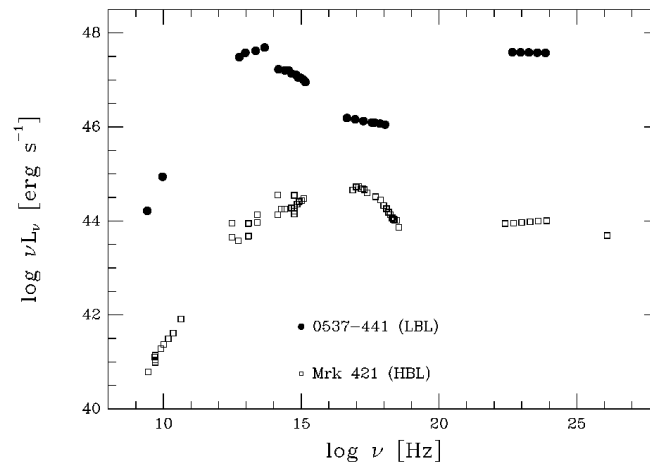
Figure 1.4: Spectral Energy Distributions show that the synchrotron peaks for the LBLs lie in the NIR/optical regime and for HBLs in the EUV/soft-X-ray regime. Taken from Urry and Padovani (1995).

Chapter 2

Observational Techniques : Aperture synthesis and Very Long Baseline Polarimetry

2.1 Introduction

In this chapter, we describe the technique of Very Long Baseline Interferometry (VLBI) and VLBI polarimetry (VLBP) which has been used to study magnetic-field order and orientation in radio sources on parsec-scales. We begin with a brief overview of observations at radio wavelengths and move on to the technique of aperture synthesis.

The radio band in the electromagnetic spectrum extends in frequency from ~ 10 MHz to ~ 300 GHz (*i.e.*, λ 1 mm to 30 m). The earth's ionosphere reflects longer wavelengths back into space while the shorter wavelengths that are allowed through by the ionosphere get absorbed by the water vapour and CO_2 in the atmosphere. The spatial resolution achievable by a telescope is given by Rayleigh's criterion, $\theta \sim \lambda/D$, where λ is the observing wavelength and D is the diameter of the reflecting surface of the telescope. Therefore, at radio wavelengths, the diameter of the telescope needs to be impractically large in order to achieve resolution comparable to, say, optical telescopes (for e.g., ~ 1 arcsecond resolution requires a 60 km radio dish observing at 1 GHz). However, based on radio interferometry, much larger apertures can be 'synthesized' from two or more radio telescopes, resulting in spatial resolution as fine as a milliarcsecond.

Synchrotron radiation emitted from the astrophysical sources can be highly linearly polarized – upto 75% assuming the magnetic field is uniform and the pitch angles of

the radiating charged particles are randomly distributed (e.g., Pacholczyk, 1970). The radio detectors (historically called 'feeds') can be designed to detect circular or linearly polarized radiation. With the development of arrays of radio telescopes having well-calibrated instruments, it is now possible to measure polarization from astrophysical sources on mas-scales.

2.2 Aperture synthesis

Radio interferometry is a technique wherein arrays of two or more radio telescopes observe a radio source simultaneously and the signal of each pair of antennas in the array is combined interferometrically to provide a measure of the brightness distribution of the source. The interferometer obtains measurements at a number of discrete points in the Fourier (or $u - v$) plane of the source intensity distribution. The radio waves from the distant astrophysical source reaching the reflecting surface of a radio telescope, have undergone a Fourier transformation, due to propagation. For example, the plane wave which reaches the telescope is the Fourier transform of the point source of emission. A two-element interferometer measures a single spatial frequency (a *visibility* or a (u, v) component, assuming that the measurement is confined to a plane) of the Fourier transform of the source brightness distribution. Put differently, each (u, v) number denotes the projected baseline coordinates, measured in wavelengths as seen from the source. The visibility is a complex quantity having an amplitude and a phase.

Due to Earth's rotation, the source sees different projections of the baseline vector, resulting in different (u, v) points in the Fourier plane. The Fourier transform of the 'sampled' $u - v$ plane, if sufficiently densely sampled, can give a faithful reconstruction of the image of the source. In this manner, an 'aperture' can be 'synthesized' by a two-element interferometer with the Earth's rotation increasing the $u - v$ coverage – this is referred to as 'Earth-rotation aperture synthesis' or simply 'aperture synthesis'. An 'aperture synthesis' can also be achieved by a collection of such two-element interferometers which make a radio interferometer array and measure many more *visibilities* instantaneously in the Fourier plane. One example of such an array is the Very Large Array (VLA) in New Mexico.
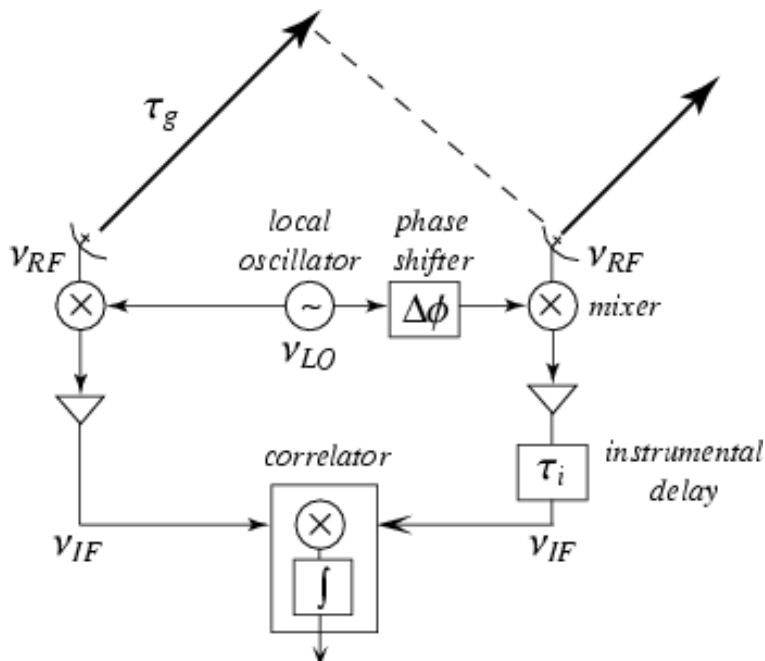
Figure 2.1: Schematic drawing of a two-element interferometer. In order to compensate for the *geometric delay* in the wavefront reaching the two antennas, *instrumental delay* τ_i is introduced in the signal path and its continuous adjustment is called *delay tracking*. The phase shifter in the figure, introduces a time-varying phase, which corrects for the delay tracking being done at a frequency different from the radio frequency ν_{RF}. The introduction of the time-varying phase is called *fringe stopping*.

2.2.1   Principle of radio interferometry :
the van-Zittert Zernicke theorem

If $I_\nu(l, m)$ represents the intensity distribution of the source, and the l, m are the direction cosines with respect to the phase-tracking center, ν is the frequency of radiation, then according to van-Zittert Zernicke theorem, the *spatial coherence function* is given by the Fourier transform relation

$$V_\nu(u, v) = \int_{-\infty}^{\infty} \int_{-\infty}^{\infty} I_\nu(l, m) e^{-i2\pi(ul+vm)} dl \ dm \qquad (2.1)$$

The inverse Fourier transform of the spatial coherence function therefore results in $I_\nu(l, m)$. An interferometer is a device which measures this spatial correlation function. A two-element interferometer measures one (u, v) component of the Fourier plane of the radio source intensity distribution. The use of many such two-element interferometers or observation with one interferometer but taking into account Earth's rotation, is needed to sample the entire Fourier plane.

In practice, the spatial coherence function V_ν is not known everywhere but is sampled at particular places in the $u - v$ plane. The sampling function $S(u, v)$ is such that it has a value of one where data is present and zero elsewhere. Therefore the quantity which is obtained by the observer is :

$$I_\nu^D(l, m) = \int_{-\infty}^{\infty} \int_{-\infty}^{\infty} V_\nu(u, v)S(u, v)e^{i2\pi(ul+vm)}du\ dv \qquad (2.2)$$

where $I_\nu^D(l, m)$ is referred to as the *dirty image* or *dirty map* and is related to the desired $I_\nu(l, m)$ by the convolution

$$I_\nu^D = I_\nu * DB \qquad (2.3)$$

where the asterisk denotes convolution. DB is the inverse Fourier transform of the sampling function $S(u, v)$, and is referred to as the *dirty beam*. It is basically the point spread function (PSF) of the synthesis array, corresponding to the sampling function.

2.2.2 Deconvolution

In order to get the true intensity distribution I, one needs to undo the convolution represented in Eqn. 2.3. Nonlinear deconvolution is required to correct the defects in the image resulting from simply Fourier transforming the observed, sampled visibilities, due to the limited sampling of the $u - v$ plane. The two primary algorithms used for deconvolution of radio synthesis images are 'CLEAN' (e.g., Högbom, 1974) and the Maximum Entropy Method (MEM) (e.g., Cornwell & Evans, 1985; Narayan & Nityananda, 1986). MEM functions by minimizing a smoothness function ("entropy") in an image. 'CLEAN' is an iterative algorithm which deconvolves a sampling function (the *dirty beam*) from an observed brightness (*dirty map*) of a radio source and we discuss this algorithm in detail, below.

The 'CLEAN' algorithm

The 'CLEAN' algorithm provides a solution to the convolution equation (Eqn. 2.3) by representing a radio source by a number of point sources. It works in an iterative manner which is described assuming a simple (but rather unrealistic) model for the source : If there were many point sources which are observed by the interferometric array, the inverse Fourier transform of the $u - v$ plane would give a *dirty map* which will have all these point sources convolved with the *dirty beam*. The relative strengths of the point sources would give relatively stronger side-lobes which would interfere with the other weaker point sources and their side-lobes, resulting in these sources not being seen at all.

With 'CLEAN', the strongest point source which would have been least corrupted by other weaker point sources and would have in turn corrupted them the most by virtue of its stronger sidelobes, is removed along with the *dirty beam*. This then leaves the next stronger peak noticeable, so that all the previous steps can be repeated till all the CLEAN components are got and only noise remains in the *dirty map*. Finally all the CLEAN components are put back convolved with a *synthesized beam*, which is an elliptical Gaussian fitted to the main lobe of the *dirty beam*. The residuals of the *dirty image* are finally added to the 'CLEAN' image.

For the more realistic sources with extended emission and the maxima varying slowly and smoothly, subtracting a narrow maximum completely, leaves sidelobes with the opposite sign, resulting in images of new maxima, which the 'CLEAN' algorithm chooses as the next point source. In order to avoid this, the strongest component is not completely subtracted from the *dirty map* but only 10 to 20% of it is removed. In this way one gets many CLEAN components from the smoothly varying maximum in the source structure. The percentage of the peak to be removed is decided by the *loop gain* parameter in the AIPS task 'IMAGR' and is most useful for extended radio sources. Other related 'CLEAN' algorithms have been developed by Clark (1980); Schwab (1984) and Steer *et al.* (1984).

2.3   Very Long Baseline Interferometry

Connected element interferometers give at best $1''$ to $0.''1$ spatial resolution. This translates to kiloparsec-scales at the distance of nearby radio sources (say, $z < 1$). In order to obtain higher resolution, it is impratical to make larger and larger connected element arrays. The use of atomic clocks and global positioning system (GPS) however, have made it possible to *simultaneously* observe a radio source at telescopes which are not connected by cables (like the VLA) or microwave links (like the MERLIN), record the date on magnetic tapes, bring all the tapes to a central processing location, play the tapes back and correlate the data. This is also called Very Long Baseline Interferometry (VLBI) (e.g., Schilizzi, 1986). VLBI is radio interferometry using intercontinental baselines with baselines varying from a few 100 kms to a few 10,000 kms. This results in a resolution of the order of milliarcsecs which translates for nearby radio sources to a resolution of a few parsecs.

Before moving on to the calibration of radio interferometric data, we digress a little to discuss some details which were specific to the observations described in this thesis. An array may also be used as a *phased array*, where the outputs from the array elements (voltage signals) are combined with appropriate delay and phase shifts, to obtain a

single, total power signal from the array. In order to increase the sensitivity of our observations described in Chapter 3, we used the Westerbork Synthesis Radio telescope (WSRT) as a phased-array, which acted effectively as a single antenna with a collecting area equal to $\sqrt{12} \times 25$ m ≈ 85 m, 12 being the number of antennas in the array. Further, since we were interested in observing faint FRI radio galaxies for polarized emission (typically a few percent of the total intensity), long sensitive baselines (like VLBA and Effelsberg, VLBA and WSRT) and short sensitive baselines (like Effelsberg and WSRT) were needed. Baselines with large collecting area telescopes are crucial to observe the weak FRI radio galaxies. The experiments described in Chapter 4 and Chapter 5 concern relatively stronger radio sources, and therefore our chosen VLBI array was the VLBA.

2.3.1 Calibration

Because the cosmic signals must traverse the ionosphere, the atmosphere, and a complicated train of electronics, the observed visibilities often bear little resemblance to the desired Fourier transform of the source. Calibration is required in order to make corrections for changes that occur in the visibilities due to the atmosphere and the electronics associated with a telescope. Such changes may be on the time scales of minutes to hours. 'Gain' refers to the instrumental as well as atmospheric contributions to corrupting the true amplitude and phase of the incoming radio waves. Calibration involves the determination of the amplitude and the phase of the complex gain in order to get the true visibility distribution.

Ordinary calibration relies upon the observations of a calibrator source of known or assumed structure, usually unresolved, of known strength and position. The relationship between the observed and the true visibility can be written in a very general way as, for one intermediate frequency (IF),

$$V_{ij,obs} = (G_i G_j^*)(G_{ij} V_{ij,true}) + a_{ij} + \epsilon_{ij} . \tag{2.4}$$

The first term on the right hand side is the product of the complex gains of antennas i and j, the second term, G_{ij} represents the gain of the baseline made by antennas i and j, and is mainly due to the correlator gain errors, a_{ij} is an offset term while ϵ_{ij} is the system noise term. G_{ij} and a_{ij} can be eliminated to a satisfactory degree by clever design (Cornwell, 1982). The above relationship simplifies to

$$V_{ij,obs} = (G_i G_j^*)V_{ij,true} + \epsilon_{ij} . \tag{2.5}$$

For simplicity, the effects of time averaging and finite bandwidth have been neglected. Given a calibrator source near the source of interest, whose $V_{ij,true}$ is known, due to the

properties of a calibrator listed above, the antenna gains can be solved as a function of time. Interpolation of these gain solutions then provides approximate values for use in the correction of the source visibility data. If more than N–2 baselines are correlated (N being the number of antennas) then a least squares technique can be utilised to overcome the errors embodied in ϵ_{ij}.

However, the problem with ordinary calibration is that, due to temporal and spatial variations in the atmosphere, the inferred values of G_i from a calibrator, may not apply to the source observed at a different time, and in a different part of the sky. Another obstacle is that on VLBI scales, there are no unresolved sources with stable flux (in fact, the most compact sources on VLBI scales are also the most variable ones) which can be used straightaway to supply the gain amplitudes and phases. Although the random frequency dependent phase delays can be largely removed either by the "fringe-fitting" process (Schwab & Cotton, 1983), and/or by using the phase-cal tones (the set of low-level monochromatic signals ("tones") of known phase embedded in the VLBI data stream to calibrate instrumental phase errors), alternate calibration methods must be used to circumvent the need for stable flux calibrators on VLBI scales. One technique which allows the antenna gains to be degrees of freedom in the determination of the source brightness distribution, is called 'self-calibration'.

2.3.2   *A priori* flux calibration

To avoid the need of flux calibrators that are stable on VLBI scales, the following relationship between the correlation coefficient (ρ_{ij}) and the calibrated visibility amplitude (V_{jk} in e.g. Janskys) is used (e.g., Perley *et al.*, 1989) :

$$V_{jk} = \rho_{ij} S_T \sqrt{\frac{T_{sys,j} T_{sys,k}}{T_{ant,j} T_{ant,k}}} \ , \tag{2.6}$$

where S_T is the total flux density, T_{sys} is the system temperature and T_{ant} is the antenna temperature. The system temperature is the response of the antenna to the source including noise contributions and is normally measured at frequent intervals throughout the experiment. The antenna temperature is the contribution to the system temperature from the source alone. T_{ant} is difficult to measure as it is generally much smaller than T_{sys} except for the brightest sources. Thus T_{ant} and S_T are usually replaced in the equation above with a predetermined "antenna gain". Gravity-induced antenna surface deformations, which are a function of elevation, introduce an elevation-dependent loss of gain for which astronomical observations must be corrected. A gain curve for the participating antennas is usually provided which gives the antenna gain as a function of elevation.

2.3.3   Polarization calibration

For polarization mapping, two additional steps are needed in the calibration procedure. Since the instrumental polarization of typical antennas is $\sim 2-5\%$ which is comparable to the source polarization, the instrumental polarization must be removed. The second step is to calibrate the polarization position angle, χ. But before we describe these two steps in detail, we will digress a little to discuss the Stokes parameters.

Stokes parameters

The Stokes parameters provide a useful description of the polarization state of an electromagnetic wave. The Stokes parameters are related to the amplitudes of the components of the electric field, E_x and E_y, resolved in two perpendicular directions normal to the direction of propogation. If $E_x = e_x(t)\cos(\omega t + \delta_x)$ and $E_y = e_y(t)\cos(\omega t + \delta_y)$ then the Stokes parameters are defined as :

$$I = \left\langle e_x^2(t) \right\rangle + \left\langle e_y^2(t) \right\rangle \tag{2.7}$$

$$Q = \left\langle e_x^2(t) \right\rangle - \left\langle e_y^2(t) \right\rangle \tag{2.8}$$

$$U = 2 \left\langle e_x(t)e_y(t)\cos[\delta_x - \delta_y] \right\rangle \tag{2.9}$$

$$V = 2 \left\langle e_x(t)e_y(t)\sin[\delta_x - \delta_y] \right\rangle \tag{2.10}$$

where the angle brackets denote a time average. The parameter I is a measure of the total power in the wave, Q and U represent the linearly polarized component, and V represents the circularly polarized component. The linear polarization is given by $P = Q + iU = mIe^{2i\chi}$, where m is the degree of linear polarization and χ is the position angle of the plane of polarization, also called the electric vector position angle (EVPA). The polarized flux density $(p = mI)$ and χ are given by

$$p = \sqrt{Q^2 + U^2} \tag{2.11}$$

$$\chi = \frac{1}{2}tan^{-1}\left(\frac{U}{Q}\right) \tag{2.12}$$

In general, the response of an interferometer is a linear combination of two Stokes parameters, the combination determined by the polarization each antenna measures (e.g., the circular feeds of the VLBA antennas measure circular polarization). By observing with different combinations of polarizations, all the Stokes parameters can be determined, and the complete state of the polarization of the wave found. For the interferometer, each Stokes parameter has a corresponding complex visibility. Therefore,

the variation of each of the Stokes parameters over the source can be imaged individually, and the polarization of the radiation emitted from the source at any location determined. In the image plane, I is always positive (ignoring noise, errors and beam sidelobes), whereas Q, U, and V may be positive or negative depending on the polarization position angle, or sense of rotation.

Any linearly polarized electromagnetic wave can be decomposed in two circularly polarized waves – left-circular polarization (LCP) and right-circular polarization (RCP). The correlations from an interferometer with circularly polarized feeds and identical gains are related to the Stokes parameters as follows (e.g., Pacholczyk, 1970):

$$R_j R_k^* = I_{jk} + V_{jk} \tag{2.13}$$

$$L_j L_k^* = I_{jk} - V_{jk} \tag{2.14}$$

$$R_j L_k^* = Q_{jk} + iU_{jk} \tag{2.15}$$

$$L_j R_k^* = Q_{jk} - iU_{jk} \tag{2.16}$$

where j and k refer to the jth and k^{th} antennas in the array that form the baseline under consideration, R and L refer to RCP and LCP, respectively.

Instrumental polarization

Most antennas are equipped with two circularly polarized feeds that respond to the RCP and LCP components of the incoming radiation. However, any feed responds not only to the intended circular polarization but also the 'other' component. That is, the signal measured on one polarization is corrupted by "*leakage*" from the orthogonal sense. These *leakage* terms in the equations above are referred to as *instrumental polarization* or *D-terms*. The instrumental response of an antenna to the radiation field can be written as

$$R = G_R[E_R e^{-i\phi} + D_R E_L e^{i\phi}] \tag{2.17}$$

$$L = G_L[E_L e^{i\phi} + D_L E_R e^{-i\phi}] \tag{2.18}$$

where G_R and G_L are the antenna gains in RCP and LCP respectively, E_R and E_L are the true RCP and LCP electric fields from the source respectively, D_R and D_L are the fraction of the orthogonal polarization that leaks through to RCP and LCP respectively, and ϕ is the parallactic angle. The parallactic angle is the angle between the lines on the celestial sphere joining the source to the north celestial pole and to the antenna's zenith, which measures the orientation of the feed with respect to the source.

The correlations in equations 2.13 to 2.16 can then be rewritten in terms of the R and L instrumental responses. Ignoring terms of higher powers of D and cross-hand

terms (*i.e.*, LR, RL) and assuming $V = 0$, the ratio of the cross to parallel hand terms can be written as,

$$\frac{R_j L_k^*}{L_j L_k^*} = \frac{G_{Rj} G_{Lk}^*}{G_{Lj} G_{Lk}^*} \left[\frac{\langle E_{Rj} E_{Lk}^* \rangle}{\langle E_{Lj} E_{Rk}^* \rangle} e^{-2i\phi_j} + D_{Rj} + D_{Lk}^* e^{2i(\phi_k - \phi_j)} \right] \qquad (2.19)$$

where the angle brackets denote quantities which have been time averaged by the correlator. The first term in the square brackets is the source polarization and can be set to zero if unpolarized sources are observed. If a source is observed over a range of parallactic angles then the equations describing the cross to parallel hand ratios can be solved for the D-terms of each antenna. In order for this method to work, the R and L antenna gains must be aligned. One way to do this is by using the self-calibration technique.

Polarization position angle calibration

The amplitudes and phases of the complex gains are determined during the self-calibration process used for mapping the total intensity structure of the source. This is done relative to a reference antenna whose gain phases are arbitrarily set to zero. This results in the introduction of an arbitrary phase offset (equal to the $R - L$ phase difference at the reference antenna) to the RL and LR correlations which produces a corresponding rotation of χ in the final map.

The polarization PA of connected element interferometers like the VLA can easily be calibrated by observations of sources with known integrated EVPA. Unfortunately, no such sources are known on VLBI scales. Therefore, the approach adopted is to observe a source with compact polarization structure simultaneously with the VLBI array and with a single dish/connected element interferometer. If the source has sufficiently compact polarization structure, then all the polarized flux detected by the low-resolution instrument (e.g., the VLA) should also be present in the VLBI observation. Thus, the integrated polarization PA in the VLBI observation should be the same as that of the VLA. It is important that the time between the two observations be as short as possible because many compact polarized sources are variable on timescales of days or less.

2.3.4 Self-calibration

After the initial calibration, residual amplitude and phase errors remain. Self-calibration or 'selfcal' takes care of antenna-based corrections (e.g., Cornwell, 1982). It is similar to 'hybrid mapping' (Readhead *et al.*, 1980), and it is effectively the same as the adaptive optics used in optical telescopes, where the surface of the telescope is distorted to remove

the effects of the phase changes introduced by the atmosphere. In selfcal, the same is done *after* the observations.

Self-calibration is a process which makes use of the closure phase of a triangle of baselines (3 antennas); in summing the visibility phases around the triangle, the error terms for each individual antenna cancel out. Selfcal uses the difference between the closure phases of the models and the closure phases of the visibilities, to estimate the antenna gains. A similar amplitude closure around a rectangle of baselines (4 antennas) can be used to correct errors in the *a priori* flux calibration. For an N element interferometer, there are $1/2N(N-1) - (N-1)$ constraints on the phase and $1/2N(N-1) - N$ constraints on the amplitude. For large N, the following iterative scheme is adopted :
1. A starting model for the brightness distribution is chosen and the visibilities are computed.
2. Using this model, subject to the closure constraints, the antenna gains are solved for.
3. These gain corrections are applied to the visibility data and the corrected data is used as a fresh model of the brightness distribution.
The iterative deconvolution algorithm 'CLEAN' is used to get components which provide the model for the next iteration of self-calibration. For arrays with large N, the covergence for the selfcal process is fairly rapid and this technique of determining antenna gains is very efficient.

2.3.5   AIPS tasks

We list below some tasks in the Astronomical Image Processing System (AIPS) used for the calibration and data-reduction. The tasks ANTAB and APCAL are used for the *a priori* amplitude calibration using system temperature (TY) and gain (GC) tables for the antennas. For observations at 43 GHz (λ 7 mm), which are described in Chapter 4, "opacity corrections" are needed. This is done using the system temperatures of the antennas in APCAL. The task CLCOR performs the parallactic angle correction. The task FRING performs the global fringe-fitting and determines the phase, rates (variation of phase with time) and delays (variation of phase with frequency).

The task IMAGR performs a Fourier transform and uses the CLEAN deconvolution algorithm on the $u-v$ data. The Briggs' robustness parameter used in IMAGR defines the weight given to different baselines. The parameter varies from –4 (greatest weight given to longer baselines or *uniform weighting*) to +4 (greatest weight given to shorter baselines or *natural Weighting*). The task CALIB performs the self-calibration and a Fourier transform. Tasks IMAGR and CALIB are used in conjunction to perform many iterations (around 10 to 15) on the $u-v$ data for the self-calibration process to converge

and to result in the source image. The task LPCAL is used for the *D-term* calibration.

Chapter 3

The magnetic field geometry on pc-scales in FRI radio galaxies

3.1 Introduction

In this chapter, we present the results of our investigation of the Fanaroff-Riley dichotomy through Very Long Baseline Polarimetry observations of FR radio galaxies. We probe the parsec-scale radio jets, their environments and their magnetic field geometry in FRI radio galaxies through parsec-scale polarimetric observations. It is clear that magnetic field is critical to AGN jet production mechanisms (e.g., Blandford & Konigl, 1979; Bicknell & Henriksen, 1980). The magnetic field is also a tracer of the underlying hydrodynamics of the jets, showing the effects of oblique shocks, boundary layer interactions, instabilities, shear, confinement, turbulence, and cloud interactions. The technique of VLBI polarimetry provides information about the ordering of parsec-scale magnetic fields, their orientation and the Faraday depth along the line of sight to, and possibly within, the jets. B denotes the direction of the *apparent* (synchrotron emissivity weighted) magnetic field inferred from observations of the linear polarization. For optically thin emission as observed in radio jets, the inferred B-field is at right angles to the electric vector of polarized emission (EVPA or χ) while for optically thick emission, the inferred B-field is aligned with the χ vectors (e.g., Pacholczyk, 1970).

3.1.1 Magnetic field orientation in AGNs on kiloparsec-scales

Linear polarization gives a measure of the ordered component of the magnetic field along the line of sight, projected onto the plane of the sky, in the absence of Faraday

rotation. However the interpretation of polarization patterns in jets is complicated by the fact that more than one three-dimensional B-field model could give rise to a similar two-dimensional polarization structure. For example, a toroidal field as well as shocking and shearing of magnetic fields can give rise to similar parallel or transverse polarization or a 'spine-sheath' (Laing, 1980) structure described below. However, definite B-field patterns have resulted from the polarimetric observations of a large number of AGNs.

In Chapter 1, we had discussed the three primary B-field configurations which have been observed in kiloparsec-scale jets of radio-powerful AGNs (Bridle & Perley, 1984) *viz.*, $B_{\parallel}$, $B_{\perp}$ and $B_{\perp-\parallel}$. The FRI radio galaxies studied so far, tend to have two-sided $B_{\perp}$ or $B_{\perp-\parallel}$ - dominated jets, while the FRII radio galaxies tend to have one-sided $B_{\parallel}$ - dominated jets. The narrow, bright 'spine' has a higher Lorentz factor compared to the dimmer, broader 'sheath' layer (e.g., Laing *et al.*, 1999).

3.1.2 Magnetic field orientation in AGNs on parsec-scales

VLBI observations have shown that this B-field configuration extends down to parsec-scales (for e.g., Gabuzda *et al.*, 1992; Attridge *et al.*, 1999). The study of the parsec-scale magnetic-field geometry has revealed that there are differences in the B-field geometry of BL Lacs and core-dominated quasars, with the B-field being longitudinal and transverse to the local jet direction in quasar and BL Lac jets, respectively (e.g., Gabuzda *et al.*, 1992; Cawthorne *et al.*, 1993; Gabuzda *et al.*, 1994,and references therein). Wardle (1998) have shown that the B-field dichotomy holds even when BL Lac objects with high redshifts comparable to quasars, and therefore similar physical scales, are considered.

It has been suggested that an underlying parallel B-field component is stronger in the quasars compared to BL Lacs (Cawthorne *et al.*, 1993; Wardle, 1998; Gabuzda, 1997). It has been suggested that this may be a consequence of different jet flow speeds on parsec-scales, with higher jet Lorentz factors in quasars stretching magnetic field lines along the plasma flow, while the lower velocities in the BL Lac jets cause the field lines to stay more tangled. This along with transverse shocks which compress the field lines perpendicular to the jet more easily in the slower-moving BL Lac jets and not much in the faster-moving quasar jets, give rise to the B-field dichotomy seen in the 'beamed' radio-loud AGNs. Alternatively, the jets may contain a significant toroidal component of magnetic field that is visible in the form of transverse Faraday rotation measure gradients. Such suggestions have come from the recent works of Asada *et al.* (2002); Gabuzda *et al.* (2003).

The orientation of the polarization electric vectors in the VLBI cores of quasars had not shown a systematic trend until the recent work of Pollack *et al.* (2003), which shows

quasar cores to preferentially have χ's which are transverse to the jet direction. The observations of BL Lac cores by Gabuzda *et al.* (2000) have demonstrated a bimodal χ distribution, with χ either aligned with or perpendicular to the VLBI jet; it has recently been suggested that this bimodality may be associated with bimodality in the optical depth of the polarized regions within the observed VLBI core (Gabuzda, 2003).

The fractional polarization in the cores at 5 GHz is typically lower in quasars ($m_c <$ 2%) than that found in BL Lacs ($m_c \sim 2 - 5\%$) (e.g., Gabuzda *et al.*, 1992; Cawthorne *et al.*, 1993; Gabuzda, 1997; Pollack *et al.*, 2003). Most of these quasars are core-dominated quasars. However Lister (2001) find no significant difference in the fractional core polarization at 43 GHz.

There are no systematic differences in the fractional polarization of the VLBI jets in quasars and BL Lacs, however. Fractional polarization of the VLBI jets m_j, range from $0 - 65\%$ in both quasars and BL Lacs (Cawthorne *et al.*, 1993; Gabuzda, 1997).

If indeed BL Lacs and quasars are the beamed counterparts of FRI and FRII radio galaxies, this strongly suggests that the Fanaroff-Riley dichotomy must *arise right at the core*. Simplistically one would predict that in the FRIIs the *B*-field would align along the jet axis while in the FRIs it would be transverse. We note that Pollack *et al.* (2003) have recently reported from a sample of 73 quasars that the jet EVPAs are almost uniformly distributed from 0 to 90°. However, Pollack *et al.* have not taken into account the rotation in polarization vectors due to Faraday rotation which could be very high in quasars (Zavala & Taylor, 2003). Homan *et al.* (2002) have observed 12 blazars at 15 and 22 GHz, where the effects of Faraday rotation would be negligible, and they still find that the seven quasar jets tend to have transverse polarization in their jets. Lister (2001) also find similar differences in the 25 quasar and 9 BL Lac jets observed at an even higher frequency of 43 GHz. Therefore multi-frequency VLBP observations are needed to derive rotation measures on parsec-scales and the corrections made to the EVPAs derived from the 5 GHz observations of Pollack *et al.* (2003) in order to arrive at more robust conclusions.

3.2   Sample selection for a VLBP study

A rigorously selected sample is needed to provide a meaningful comparison of the nuclear properties of the FRI and FRII radio galaxies. This is because we want to avoid the effects of parameters which affect both types of objects (like evolution) and which might be hiding the effects of the more intrinsic parameters that give rise to a dichotomy. We have constructed such a rigorous sample of FRIs and FRIIs from among those

showing an unresolved optical nucleus when observed with the *Hubble Space Telescope*. This was because of our interest in obtaining spectral index and optical polarization observations of these nuclei to ascertain their nature. It is now well-known that when the *HST* imaged the central regions of the FR host galaxies on 0.″05 scales, it discovered unresolved optical cores in the centres of a majority of them (Capetti & Celotti, 1999; Chiaberge *et al.*, 1999, 2002; Verdoes Kleijn *et al.*, 2002). It has been suggested in the literature that the optical core emission is dominantly synchrotron emission from the base of the relativistic jet (e.g., Chiaberge *et al.*, 1999). The observations of optical polarization and spectral index of these *HST* nuclei could determine if the emission is synchrotron radiation or whether it is thermal emission from an accretion disk or a stellar cluster. Therefore starting with the radio galaxies which showed unresolved optical nuclei and applying the selection criteria outlined below, we came up with a sample for our proposed VLBP observations. With VLBP and optical observations we could probe the conditions in the centres of radio galaxies in terms of the presence of ordered B-fields, depolarizing ionized circumnuclear material which could be associated with an accretion disk or be present as gas in the broad-line region, and dusty obscuring tori which could hide the optical emission as well depolarize radio emission from its inner ionized edge, in the context of the Fanaroff-Riley divide. The selection criteria follow :

Restricting the redshifts : We restricted the redshifts of the FRIs and FRIIs to $z < 0.1$ in order to reduce possible effects of evolution (e.g., Baum *et al.*, 1995; Jackson & Wall, 1999). The sample objects have redshifts in the range $0.003 < z < 0.1$. A Kolmogorov-Smirnov test gives a $< 0.1\%$ probability that the redshift distribution comes from the same population.

Matching the host galaxy magnitudes : We constrained the host galaxy magnitudes (M_V) to a narrow range, in view of the dependence of the FRI/FRII luminosity divide on this parameter. Owen & Ledlow (1994) found that the FRIs and FRIIs lie in distinct regions in the total radio luminosity versus host galaxy magnitude plane. Given the correlation between the mass of the black hole and the mass of the host galaxy (e.g., Magorrian *et al.*, 1998), the restriction on M_V essentially implies that we were confining our sample to a small range in black hole mass. A Kolmogorov-Smirnov test gives a > 0.1 probability that the host galaxy magnitude distribution comes from the same population. The broad line radio galaxy 3C 111, which is described in Chapter 4, was excluded as its M_V (~ -18) was out of the chosen range.

Choosing unambiguous FRIs and FRIIs : We chose only *unambiguous* FRIs and FRIIs, *i.e.*, those that conformed to the morphological *and* luminosity criteria (*i.e.*, below and above the Ledlow-Owen fiducial break line, respectively). Objects which
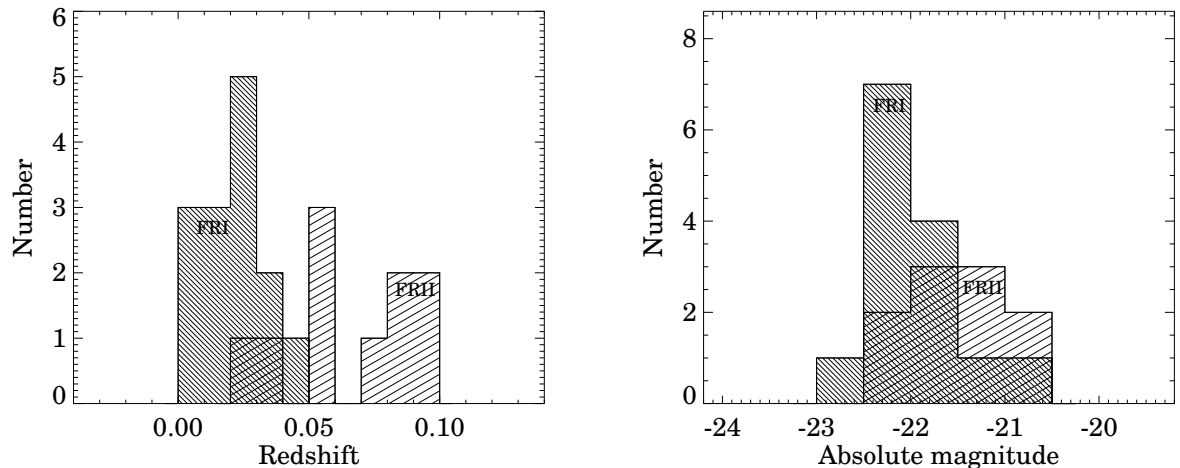
Figure 3.1: Histograms showing the redshits and the host galaxy absolute V-band magnitudes for the FRI and FRII samples.

showed both FRI and FRII characteristics in their radio morphology, *viz.*, narrow jets and "hot spots" along with diffuse large-scale radio lobes (e.g., Capetti *et al.*, 1995) were excluded.

In this manner, four morphological FRIs that have FRII-type radio luminosities and one morphological FRII with a FRI-type radio luminosity were excluded. We excluded 3C 338, since most of its radio emission is likely to be a relic and the AGN is more akin to a Compact Steep Spectrum (CSS) source, and 3C 84, which is complex and quite atypical of the rest of the sample.

The VLBI flux density cutoff : To ensure the feasibility of VLBP observations, we chose sources with total VLBI-scale flux densities to be greater than 30 mJy. We applied this cutoff on the basis of (a) the expectation that $\geq 80\%$ of the arcsec-scale radio core flux density would be detectable by VLBI (e.g., Giovannini *et al.*, 1990), (b) the detectability of polarization from VLBI components with total flux densities of 25–40 mJy and moderate polarization ($\leq 20\%$) as well as polarization from VLBI components with flux densities as low as 10–20 mJy and comparatively high ($\geq 20\%$) polarizations (e.g., Kollgaard *et al.*, 1996; Gabuzda *et al.*, 1999, 2001).

Thus the objects in the sample have :

1. Optical nuclei discovered by the *HST* for which there are detections or upper limits;

2. $z < 0.1$;

3. $-23 \pm 0.5 \leq M_V \leq -21 \pm 0.5$;

4. Unambiguous FRIs and FRIIs in terms of morphology and luminosity;

5. Measured or inferred total radio flux densities on VLBI-scales ≥ 30 mJy;

This yielded a sample of 14 FRI and 10 FRII radio galaxies. Table 3.1 lists the sample objects and their properties.

We applied for observing time on the global VLBI network to observe this sample of objects. We were granted time for a pilot study in order to determine the detectability of parsec-scale polarization in radio galaxies. We included four FRI radio galaxies in this study. These were selected based on the following properties :

1. They had been observed with VLBI and were detectable on parsec-scales. They are also well-studied at different resolutions and wavelengths.

2. They had detectable VLA core polarization.

3. They had well-defined core-jet VLBI structures. So we hoped to detect at least some polarization in the optically thin jet if not in the optically thick cores where Faraday depolarization effects are expected to be higher.

3.3   Observations

We observed the four FRI radio galaxies *viz*., 3C 66B, 3C 78, 3C 264 and 3C 270, at 8.4 GHz (λ 3.6 cm) with a global VLBI array in dual-polarization mode. Ideally one would want to minimize Faraday depth effects and thereby observe at the highest possible frequency. But given that we expect the polarized flux density to be at the instrument detection limits, we would also like to use the radio band with the highest sensitivity. The 5 GHz and 8 GHz bands are the ones with the lowest system temperatures and we chose the higher frequency band (8 GHz) over 5 GHz at a small cost of loss of sensitivity. We observed with the Effelsberg 100 m antenna and the WSRT as a phased-array (which acted effectively as a single antenna with a collecting area equal to $\sqrt{12} \times 25$ m ≈ 85 m) to increase the sensitivity of our observations. We then hoped to have long sensitive baselines (VLBA and Effelsberg, VLBA and WSRT) and a short sensitive baseline (Effelsberg and WSRT) to observe faint structures on small and large scales in the relatively weak FRI radio galaxies. The details of the EVN and VLBA antennas which formed the global array as well as those of the observing run are given in Table 3.3.

The program SCHED (by Craig Walker, NRAO) was used for scheduling the global VLBP observations. The 28 hours of observation which began on 1st March, 2002, were divided into scans of 10 and 20 mins duration (keeping in mind that one pass on the

Table 3.1: The sample of FRIs and FRIIs.

Source Name	IAU Name	RA J2000.0	DEC J2000.0	Redshift	FR type	S^C_{kpc} (5 GHz)	S^T_{pc} (5 GHz)
		h m s	d m s	z		mJy	mJy
3C 15†	0034–01	00 37 04.1	–01 09 08	0.0730	II	299	239*
3C 29	0055–01	00 57 34.9	–01 23 28	0.0448	I	93	74*
3C 31	0104+32	01 07 24.9	+32 24 45	0.0169	I	92	115
3C 66B	0220+43	02 23 11.4	+42 59 31	0.0215	I	182	200
3C 78	0305+03	03 08 26.2	+04 06 39	0.0288	I	964	400
3C 88	0325+02	03 27 54.2	+02 33 42	0.0300	II	159	127*
3C 227	0945+07	09 47 45.1	+07 25 21	0.0862	II	32	26*
3C 236†	1003+35	10 06 01.7	+34 54 10	0.0990	II	84	84
3C 264	1142+19	11 45 05.0	+19 36 23	0.0206	I	200	180
3C 270	1216+06	12 19 23.2	+05 49 31	0.0074	I	308	101‡
3C 272.1	1222+13	12 25 03.7	+12 53 13	0.0037	I	180	180$^\oplus$
3C 274	1228+12	12 30 49.4	+12 23 28	0.0037	I	4000	364$^\oplus$
3C 296	1414+11	14 16 53.1	+10 48 25	0.0237	I	77	62*
3C 317	1514+07	15 16 44.5	+07 01 17	0.0342	I	391	313*
NGC 6251	1637+82	16 32 32.0	+82 32 16	0.0240	I	850	350
3C 382	1833+32	18 35 03.4	+32 41 47	0.0580	II	207	190‡
3C 388	1842+45	18 44 02.4	+45 33 30	0.0910	II	62	50*
3C 390.3	1845+79	18 42 09.0	+79 46 17	0.0560	II	350	350
3C 402	1940+50	19 41 46.0	+50 35 45	0.0250	II	45	36*
NGC 7052	2116+26	21 18 33.1	+26 26 49	0.0156	I	47	38*
3C 445	2221–02	22 23 49.6	–02 06 12	0.0570	II	86	69*
3C 449	2229+39	22 31 20.5	+39 21 30	0.0181	I	37	30*
3C 452†	2243+39	22 45 48.8	+39 41 15	0.0810	II	150	120
3C 465	2336+26	23 38 29.4	+27 01 53	0.0322	I	270	230

Col. 1 : Radio galaxy name, $\dagger$ objects with upper limits to optical nuclear emission in the *HST* data; Col. 6 : Fanaroff-Riley type; Col. 7 : Radio core flux densities at 5 GHz on arcsecond scales using either the Very Large Array (VLA) or the WSRT; Col. 8 : Total flux densities at 5 GHz on VLBI scales, $\star$ indicate values derived assuming that 80% of arcsec-scale radio core flux density is present on mas-scales, $\ddagger$ measured mas-scale flux density at 8.4 GHz, $\oplus$ measured mas-scale flux density at 1.6 GHz.

recording tape takes $\approx$ 40 mins) for each of the target sources, resulting in 8.5 hrs of observing for 3C 66B and approximately 5.5 hrs for 3C 78, 3C 264 and 3C 270. The data were recorded in two intermediate frequencies (IFs) of 8 MHz bandwidth using 1-bit sampling. Both right- and left-hand polarizations were recorded simultaneously in IF pairs, giving a total observing bandwidth of 32 MHz.

These were interspersed with shorter scans of the calibrators 3C 84, 1156+295, 2007+777 and 1308+326. There were single scans of 10 mins duration each for the two fringe finders – 2007+777 and 1308+326. 3C 84 was used as the D-term calibrator – accordingly, there were 6 scans of 5 min duration and 1 scan of 10 min duration scheduled so as to ensure a large range of parallactic angles, as well as good snapshot u–v coverage. 1156+295 served as the EVPA calibrator – to obtain good snapshot u–v coverage, we scheduled 5 scans of 5 min duration spanning the entire time the source was visible to most or all of the array. 13 antennas recorded both right and left circular polarizations (RCP and LCP), while 2 antennas *viz.*, Onsala and Yebes received only RCP.

During the observing run, the skies were mostly clear and the weather dry at most of the sites. Only Yebes had heavily clouded skies for the most part and North Liberty was affected by precipitation due to snow-fall for a few hours towards the end of the run. The EVN and global VLBI observations were correlated at the EVN MkIV Data Processor at the Joint Institute for VLBI in Europe (JIVE).

3.4   Data reduction

The calibration and imaging of the data were done using the AIPS package. The *a priori* amplitude calibration was performed with the tasks ANTAB and APCAL using the system temperatures and the gains for the antennas. The *a priori* phase calibration was done 'manually' (*i.e.*, the pulse cal tones were not used) and the phase, delay and phase rate solutions were derived using the AIPS task FRING. The cross polarization delays were calibrated with the procedure VLBACPOL. Los Alamos (LA) was used as the reference antenna for this experiment. The details of the calibration are described in Chapter 2.

After imaging 3C 84, the task LPCAL was used to find a solution for the antenna $D-terms$ assuming the source to be unpolarized (as prior observations have shown). The instrumental polarizations for the VLBA, Effelsberg and Yebes were all of the order of 2% or less, while those for Onsala and Medicina were 6–7%. The instrumental polarization for the WSRT was very high ($\sim$ 20%); trial and error showed that it was

Table 3.2: Details of the VLBP observing program for FRIs.

Program code	GK022
Observing date	1–2 March 2002
Targets	3C 66B, 3C 78, 3C 264, 3C 270
Total time per target (hrs)	8.5, 5.5, 5.5, 5.5, respectively
Fringe finders	2007+777, 1308+326 (10 min each)
D-term calibrator	3C 84 (40 min)
EVPA calibrator	1156+295 (25 min)
Stations*	**EVN :** EB, WB, ON, MC, YB
	VLBA : SC, HN, NL, FD, LA, PT, KP, OV, BR, MK
Frequency (MHz)	8407.49
Number of IFs	2
Polarizations per IF	RR, LL, RL, LR
Bandwidth per IF (MHz)	8
Total Bandwidth (MHz)	32
Frequency points per IF/polarization	16
Integration time per visibility (sec)	4
Correlator	EVN MkIV Data Processor at JIVE
Correlated in	December, 2002

* Details of the antennas are given in Table 3.3.

Table 3.3: Characteristics of the telescopes used in the global VLBI array.

Antenna codes	Antennas	Diameter (m)	Polarization	Location
EB	Effelsberg	100	RCP, LCP	Germany
WB	WSRT*	$\sqrt{12} \times 25$	RCP, LCP	The Netherlands
ON	Onsala	20	RCP	Sweden
MC	Medicina	32	RCP, LCP	Italy
YB	Yebes	14	RCP	Spain
SC	St Croix	25	RCP, LCP	Virgin Islands, USA
HN	Hancock	25	RCP, LCP	New Hampshire, USA
NL	North Liberty	25	RCP, LCP	Iowa, USA
FD	Fort Davis	25	RCP, LCP	Texas, USA
LA	Los Alamos	25	RCP, LCP	New Mexico, USA
PT	Pie Town	25	RCP, LCP	New Mexico, USA
KP	Kitt Peak	25	RCP, LCP	Arizona, USA
OV	Owens Valley	25	RCP, LCP	California, USA
BR	Brewster	25	RCP, LCP	Washington, USA
MK	Mauna Kea	25	RCP, LCP	Hawaii, USA

* Twelve antennas of the WSRT were used as a phased-array.

not possible to adequately calibrate and remove the WSRT $D-term$, and so we did not use any of the WSRT polarization (RL and LR) data.

Absolute calibration of the polarization position angle was performed using observations of the compact, highly polarized source 1156+295 during the VLBI observations and integrated measurements of the polarization of this source provided by 8 GHz VLA observations of 8th March, 2002 which were taken from the VLA/VLBA polarization calibration database, [1] closest in time to our observations of 1st March, 2002. The adopted convention for the position angle (PA) is such that North is $0°$ and the angle increases to $+90°$ from North through East. The rationale behind using the integrated polarization measurements for EVPA calibration is described in Chapter 2.

The AIPS tasks IMAGR and CALIB were used to make the total intensity (I) maps. Many rounds of self-calibration were performed, down to timescales of 30 sec in phase and 2 min in amplitude, till the source structure stopped changing significantly. The robustness parameter in IMAGR was chosen as 0 – a weighting intermediate between purely natural and purely uniform (see Chapter 2 for a description). Since there were only RR and LR correlations for all baselines to On and Yb (as On and Yb observed only RCP) the polarization $u-v$ coverage was not symmetric, the polarization (P) beam was complex – so the Fourier transform and CLEAN of the P data has to take this into account. Therefore, the procedure CXPOLN and the task CXCLN were used for making the polarization maps of the sources.

However, in some cases, the polarization images produced including the On and Yb polarization had appreciably higher noise levels than those obtained using only the VLBA, Eb and Mc, and we accordingly adopted the latter image as our final polarization image. We used a large empty region covering typically > 200 beam areas to obtain the I image rms noise and ~ 100 beam areas for P image rms noise.

3.5   Results

We detect polarization from the parsec-scale cores and/or jets of all the FRI radio galaxies. The fractional polarization in the radio cores ranges from 0.4% to 1.1% while the fractional polarization in the jet components varies from being $\sim 0.7\%$ in the inner jets to 5–20% further from the core and even as large as $\sim 60\%$ in the jet of 3C 264 $\sim$ 3 mas away from the core. The rms noise in the I maps is typically $\sim 100~\mu$Jy beam^{-1}, while rms noise ranges from $\sim 60-100~\mu$Jy beam^{-1} in the P maps. The total intensity and polarization maps are shown in Figures 3.2 through 3.13 and are described in detail

---

[1]http://www.vla.nrao.edu/astro/calib/polar by Steve Myers & Greg Taylor at NRAO

in § 3.6. Tables 3.5 and 3.6 list many observed and inferred quantities of the radio galaxies.

We note that three FRI radio galaxies *viz.*, Centaurus A, Hydra A and 3C 270 have been observed for parsec-scale polarization by Middelberg *et al.* (2003) using the VLBA at 15 GHz. However, they have failed to detect polarization in them. Zavala & Taylor (2002) have observed the FRI radio galaxy M 87 at 8, 12, and 15 GHz. They find that M 87 has less than 0.5% polarization in its central region. Linear polarization of a few tens of percent has been detected in some locations along the edges of the jet in M 87, observed with the VLBA at 5 and 8 GHz, by Junor *et al.* (2001).

We have derived an upper limit to the angle of jet axis to line-of-sight, θ_{max}, assuming $\beta \to 1$, of the FRI sources in the sky by using the jet-to-counter-jet ratio R_j (described in Chapter 1). A detailed description of the individual radio galaxies is given below and the derived θ_{max} for the radio galaxies are listed in table 3.5.

3.6 Description of individual radio galaxies

3.6.1 3C 66B

The radio galaxy 3C 66B is one of the nearest bright radio sources in the northern sky (Laing *et al.*, 1983) at a redshift of z = 0.0215 (Matthews *et al.*, 1964). It is hosted by the elliptical galaxy UGC 1841 (V = 12.63), which lies in a small group on the edge of the cluster Abell 347, part of the Perseus-Pisces supercluster.

Kiloparsec-scale observations

At radio wavelengths, 3C 66B's bright jet was one of the first to be discovered (Northover, 1973). 3C 66B has a complicated radio morphology on kiloparsec-scales (van Breugel & Jagers, 1982), which could be a result of tidal interaction with the nearby companion galaxy (van Breugel, 1982). Figure 3.2 from Leahy *et al.* (1986) shows the arcsec-scale jet of 3C 66B. van Breugel (1982) observed 3C 66B with the Westerbork synthesis radio telescope at λ 6, 21 and 49 cm and found the depolarization in the beginning of the jet to be small (depolarization is quantified by the ratio of polarized emission at a longer wavelength to that at a shorter wavelength; see Burn (1966)). Further, they found that near the base of the jet, the *B*-field flips from longitudinal to transverse and stayed transverse all the way to the end of the widening jet at $\sim 2.'5$ from the core but at the edges it is parallel in some places (RA = $02^h20^m09^s$). The spectral index is very flat

($\alpha_{21}^{6} \approx 0.4$) along the jet. van Breugel also find a gradient of Faraday depths along the jet. Further, the width of shear layer is inferred to be more than $\approx 15\%$ of the jet radius and its volume more than $\approx 30\%$ of the jet volume. Butcher *et al.* (1980) observed faint H_α emission near the nucleus which indicates the presence of inhomogeneous interstellar medium. 3C 66B lies in a direction where the Galactic foreground rotation measure is large (Simard-Normandin & Kronberg, 1980).

An optical counterpart to the jet was discovered by Butcher *et al.* (1980) and identified from its polarization properties as synchrotron radiation (Fraix-Burnet *et al.*, 1989). The optical jet has since been observed at a number of wavelengths with the *Hubble Space Telescope* Faint Object Camera (FOC) (Macchetto *et al.*, 1991; Sparks *et al.*, 1994). The radio and optical structures are very similar *across* the jet, and *along* the jet between the knots, as well as along the jet in the knots (Jackson *et al.*, 1993). Tansley *et al.* (2000) have detected a mid-infrared jet using the Infrared Space Observatory (ISO), the properties of which are consistent with those found at other wavebands. Using an 'inner jet' and an 'outer sheath' model, they have derived $\beta_{inner} \sim 0.7$ and $\beta_{sheath} \sim 0.2$ (using $\alpha_{inner} = 0.62$ and $\alpha_{sheath} = 0.88$ and source orientation to be $\theta = 45°$). An X-ray jet has been discovered by the *Chandra* observatory in 3C 66B (Hardcastle *et al.*, 2001). VLA core polarization at 5 GHz is 0.5 ± 0.01 % (Hardcastle *et al.*, 1996). These authors also report evidence of radio nuclear flux density variability. Table 3.4 lists some of the properties of this radio galaxy.

Other VLBI observations

Giovannini *et al.* (2001) report on global VLBI observations at 5 GHz which show that the high jet to counter-jet ratio persists to sub-parsec scales. 3C 66B has a well-defined core-jet structure on VLBI scales (see Fig. 3.2). The counter-jet, if present, is below the noise limit for most of the length of the pc-scale jet, although they do detect a counter-jet component very close to the VLBI core, perhaps implying jet velocity structure or variations in velocity along the jet. The jet-to-counter-jet ratio at 1.52 mas from the core is ~ 10, which corresponds to $\beta \cos \theta \sim 0.43$. At a larger distance (5 mas) the jet-to-counter-jet ratio increases up to $R_j > 100$. Taking into account the core prominence, they derive a jet orientation $\theta \sim 45°$ and a jet velocity $\beta \sim 0.6$ at 1.5 mas from the core and $\beta \sim 0.99$ at 4–5 mas from the core. They suggest that the source lies at about 45° to the line of sight, consistent with earlier inferences from the kpc-scale jet asymmetries.

Our VLBP observations of 3C 66B

The total intensity I and linear polarization P contour maps with polarization electric vectors χ superimposed are shown in Fig. 3.4. The peak and rms values of the maps are tabulated in Table 3.5 while the fractional polarization of the various components and B-field configurations are listed in Table 3.6. Using the rms noise level of the image as an upper limit to the counter-jet surface brightness, we obtain a lower limit on the jet-to-counter-jet brightness ratio of ~ 23 at a distance of 2.5 mas from the core. For β approaching 1 ($\beta \rightarrow 1$), we get the maximum θ_{max} to be $\sim 61°$ for 3C 66B. However, we find from the apparent motion of a knot in the jet of 3C 66B, that it is subluminal. Using β_{app} and R_j, we arrive at $\beta \sim 0.6$, resulting in $\theta \sim 40°$. This value is close to the value of θ ($\sim 45°$) derived by Giovannini *et al.* (2001). At $r < 1$ mas from the core, the χ-vectors are longitudinal to the local jet. Assuming optically thin emission, the B-field is transverse to the jet direction. For the core, the χ-vectors are transverse to the jet direction. If the core polarization is predominantly from optically thick regions, the inferred B-field is transverse in the core.

3.6.2   3C 78

The radio source 3C 78 is identified with the galaxy NGC 1218 (Maltby *et al.*, 1963), an SOa galaxy with an apparent magnitude V = 14.0 (Rusk & Seaquist, 1985) at a redshift z = 0.0289 (Schmidt, 1965).

Kiloparsec-scale observations

VLA observations at λ 6 cm have shown that the radio emission associated with the nucleus is extended for a few arcsec in PA $\sim 40°$. An optical synchrotron jet was detected in 3C 78 by Sparks *et al.* (1995). There is remarkable coincidence between radio and optical jet morphology. The optical position angle is $\simeq 55°$, indistinguishable from the radio position angle. The radio jet (Jones *et al.*, 1981; Unger *et al.*, 1984; Saikia *et al.*, 1986) continues in the same position angle even closer to the nucleus, down to VLBI scales where elongation in PA 55° is also seen. Saikia *et al.* (1986) find that the VLA core is $\approx 1.5\%$ polarized at λ 2 cm.

Other VLBI observations

VLBI observations at 5 GHz show a core-jet structure with the jet elongated in PA $\sim 50°$ (Jones, 1984). Variability has been observed in the VLBI core (Unger *et al.*,

1984; Saikia *et al.*, 1986).

Our VLBP observations of 3C 78

The total intensity I and linear polarization P contour maps with polarization electric vectors χ superimposed are shown in Fig. 3.7. This source shows a very rich polarization structure and high fractional polarization in the jet. The peak and rms values of the maps are tabulated in Table 3.5 while the fractional polarization of the various components and B-field configurations are listed in Table 3.6. At $r < 1$ mas from the core, the χ-vectors are longitudinal to the inner jet direction. Assuming that the emission is optically thin, we infer the B-field to be transverse to the inner jet.

3.6.3 3C 264

3C 264 is identified with the bright galaxy NGC 3862 in the Abell cluster 1367, having an apparent magnitude $m_v = 13.67$ at a redshift of z = 0.0206. The total radio power at 408 MHz is 24.85 WHz^{-1}.

Kiloparsec-scale observations

The radio structure of 3C 264 presents a head-tail morphology (Gavazzi *et al.*, 1981), with a prominent core and a wiggled jet extending toward the northeast. NGC 3862 contains a compact ($\sim 2''$) and possibly variable X-ray source embedded in the diffuse X-ray emission from the intracluster medium in a position consistent with that of the central 5 GHz radio source component (Elvis *et al.*, 1981). Baum *et al.* (1988) found an elongated region of line-emitting gas with its major axis oriented roughly perpendicular to the radio source ejection axis. The optical counterpart of the radio jet, with a length of 0.$''$65 and PA 280°, was discovered serendipitously with the *Hubble Space Telescope* (Crane *et al.*, 1993). Gavazzi *et al.* find some evidence of a counter-jet extending southwest from the core. The jet and counter-jet are embedded in a very extended and diffuse emission. Lara *et al.* (1997) obtained polarimetric data on 3C 264 with the VLA – the mean fractional polarization in the core was 3.5% and 5.8% in the northeast region (see Figure 3.7). The magnetic field appears to be parallel to the jet axis in the proximity of the core, becoming perpendicular at an angular distance of $\sim 3''$.

Quillen *et al.* (2003) have presented submillimeter continuum observations at 870μm of the core of 3C 264 and find that submillimeter emission is likely to be synchrotron emission and not thermal emission from dust. 3C 264 has a high X-ray to submillimeter

luminosity ratio. It is a candidate high or intermediate energy peaked BL Lac type object (Laurent-Muehleisen *et al.*, 1993,these BL Lacs are discussed further in Chapter 5).

Other VLBI observations

VLBI observations of 3C 264 were done at 5 GHz by Lara *et al.* (1997). Figure 3.8 shows a mas-scale structure that consists of a one-sided core-jet extending up to 20 mas from the core and directed in an average PA of $\sim 27°$.

Our VLBP observations of 3C 264

The total intensity I and linear polarization P contour maps with polarization electric vectors χ superimposed are shown in Fig. 3.10. This source shows a rich polarization structure with high fractional polarization observed in the jet components. This implies that not much depolarization has taken place. The peak and rms values of the maps are tabulated in Table 3.5 while the fractional polarization of the various components and B-field configurations are listed in Table 3.6. A region with χ vectors roughly transverse to the jet is visible in the innermost jet; since this region is probably optically thin, this implies a longitudinal B-field. Further along the jet, at $r \simeq 1 - 2$ mas from the core, there is a region of somewhat oblique polarization, not very close to being either aligned with or transverse to the jet. At a distance of 5–6 mas, the polarization moves to the edge of the jet and the inferred B-field becomes longitudinal, suggesting interaction of the jet with the interstellar medium, which stretches the field lines. If the core polarization is dominated by the contributions of optically thick regions, the inferred B-field is transverse to the jet direction.

3.6.4   3C 270

The nearby FRI radio galaxy 3C 270 (NGC 4261, z = 0.0074, V = 11.7 (Rusk & Seaquist, 1985)) is the main galaxy in a group of 33 galaxies in the Virgo West cloud (Nolthenius, 1993).

Kiloparsec-scale observations

NGC 4261 has a central dust disk (diameter 240 pc) discovered by Jaffe *et al.* (1993). Because of the detection of a gap in emission just east of the core component before the appearance of the counter-jet, it is a good candidate for the detection of free-free

absorption by ionized gas in an inner accretion disk (Jones & Wehrle, 1997). The galaxy is known to contain a central black hole with a mass of $5 \times 10^8 M_\odot$ as inferred from the Keplerian motion of gas studied at a resolution of 0.″1 with the HST (Ferrarese *et al.*, 1996). It also has a large-scale symmetric radio structure which implies that the radio axis is close to the plane of the sky (Birkinshaw & Davies, 1985). VLBA observations of this galaxy have revealed a parsec-scale radio jet and counter-jet aligned with the kiloparsec-scale jet (Jones & Wehrle, 1997). It is believed that the west-pointing jet is oriented slightly toward us (so the east-pointing jet is the counter-jet) based on the orientation of the dust disk imaged by HST and the fact that the west-pointing kiloparsec-scale jet is slightly brighter over most of its length in the VLA images (Birkinshaw & Davies, 1985; de Koff *et al.*, 2000). The opening angle of the jets is less than 20° during the first 0.2 pc and less than 5° during the first 0.8 pc.

Other VLBI observations

3C 270 was observed with VLBI at 8.4 GHz by Jones & Wehrle (1997). They found evidence for a narrow gap in radio brightness at the base of the parsec-scale counter-jet, just east of the brightest peak, which they identified as the core based on its inverted spectrum between 1.6 and 8.4 GHz. They also tentatively identified this gap as the signature of free-free absorption by a nearly edge-on inner disk with a width much less than 0.1 pc and an average electron density of $10^3 - 10^8$ cm^3 over the inner 0.1 pc. VLBA observations were made of 3C 270 at 1.6 GHz by Xu *et al.* (2000) but with a higher resolution compared to Jones & Wehrle (1997). This image has a peak surface brightness of 67.4 mJy beam^{-1}.

Our VLBP observations of 3C 270

The total intensity I and linear polarization P contour maps with polarization electric vectors χ superimposed are shown in Fig. 3.13. The peak and rms values of the maps are tabulated in Table 3.5 while the fractional polarization of the various components and B-field configurations are listed in Table 3.6. For the core, the polarization vectors are oblique to the jet direction. This suggests that Faraday rotation is occurring for the polarized emission which would be expected for this plane-of-sky object if there is thermal plasma associated with the accretion disk or a larger disk, which is causing free-free absorption. Polarization is not detected in the jet for this source.

Although the magneto-ionic medium probably associated with the disk could depolarize the counter-jet more than the jet if the jet is approaching us, with our observations we are unable to ascertain this, because the predicted polarized flux density in the

counter-jet falls below our detection limit.

3.7 Discussion

Polarization is detected on parsec-scales in the core and/or jets of four FRI radio galaxies. We had applied mainly two selection criteria for choosing the FRI radio galaxies for the VLBP study. First, we looked for sources which had detectable arcsec-scale polarization. Second, provided the first criterion was satisfied, we chose sources with high flux density in their pc-scale jets. The rationale behind concentrating on the jets was that we expected the jets to not be surrounded by much depolarizing material.

In two out of four sources, the core showed the highest polarization while for the other two, it was a knot in the jet. This is perhaps pointing to the fact that FRIs have little depolarizing material close to the base of the radio jets. This hypothesis is supported by recent IR observations of the FRI radio galaxy M 87, where Perlman *et al.* (2001) fail to detect a dusty torus. As we will see in Chapter 6, this is also our conclusion based on the *HST* nuclei study. If we assume that the 'shock-in-jet' model of Wardle (1998) is correct for the BL Lac jets and orientation does not influence the *B*-field orientation much and the RM correction to the observed χ vectors in FRIs is small ($\leq 10°$), then our finding of BL Lac-like *B*-field geometry in three out of four FRIs is consistent with the predictions of the Unified Scheme.

Interestingly, we find the hint of a 'sheath-layer' with a longitudinal *B*-field in the southern edge of the jet (at ~ 3 mas from core) of the radio galaxy 3C 264. As we will see in Chapter 5, some HBLs also show such a 'sheath-layer'. This could be a consequence of the shearing of the jet due to its interaction with the galactic medium (e.g., Bridle & Perley, 1984; Laing *et al.*, 1999). Such a 'sheath' or 'shear' layer has been observed in some radio-loud AGNs, for e.g., the quasar 1055+088 (Attridge *et al.*, 1999), the BL Lacs 0745+241 (Pushkarev & Gabuzda, 2001) and 0820+225 (Gabuzda *et al.*, 2001) .

Two of the four FRIs *viz.*, 3C 66B and 3C 270 did not show polarization when only the VLBA data was used. Therefore, global VLBP with sensitive large-collecting area telescopes like Effelsberg, are needed for studying polarization in these relatively faint radio galaxies.

3.7.1   Magnetic field geometry

The 'spine-shear' structure in a jet consists of a fast moving predominantly transverse B-field spine in the centre and a slower moving predominantly longitudinal B-field outer shear layer (Laing, 1980). If such a geometry holds for all AGN jets, then due to the Doppler boosting and dimming effects which depend on the Lorentz factors and orientation of the jets with respect to the observer, different layers in the jets dominate and to differing extents. Based on these considerations, we attempt to predict the B-field configurations in AGNs at different orientations.

Following Laing's 'spine-sheath' model for the case of BL Lac objects, which lie with their jets aligned close to our line of sight (θ probably$< 30°$), the faster moving spine which in general has a smaller opening angle due to its faster velocity and a predominantly $B_\perp$ field would dominate, resulting in these objects exhibiting a $B_\perp$ configuration, consistent with the observations.

For the radio galaxies, their orientation is relatively close to the plane of the sky ($\theta > 30°$). The spine with its smaller opening angle, would then not be observed unless its Lorentz factor becomes low, like far from the core. Such a B-field geometry is observed in 3C 78 at around 6 mas. For $\theta \sim 40 - 50°$, the $B_\parallel$ 'sheath' would dominate in radio galaxies, except close to the core where the higher Lorentz factor of the 'spine' would make it more prominent than the 'sheath' layer. It is also possible that the 'sheath' has not yet formed completely, close to the core (for e.g., 1055+018 Attridge *et al.*, 1999). Therefore, the $B_\perp$ would be dominant near the core. This B-field configuration is observed in 3C 66B, 3C 78 and 3C 264.

3.7.2   Proper motion

Since the four radio galaxies have been observed with VLBI earlier, we have used these similar resolution images (for e.g., Fig. 3.2) from the literature, to attempt to infer any proper motions in their jets. This has been done at present by simply measuring the distances of jet components from the cores in the radio maps, using a ruler. For the FRI 3C 66B, a knot in the jet observed at ~ 3 mas from the core in the VLBI map of epoch 1993.67 (Giovannini *et al.*, 2001) seems to have moved to a distance of ~ 4.5 mas by epoch 2002.16 (our observations). If the knot has been correctly identified, this implies that the knot has moved ~ 0.2 mas per year, which translates to a subluminal velocity of $0.22c$, 'c' being the speed of light. It was not possible to identify jet components in the maps of 3C 78 and 3C 264. However, it seems, by a comparison of the VLBI maps of 3C 270, that this FRI shows the lowest relative proper motion. This is consistent with its 'plane-of-sky' orientation.

3.8 Conclusions

1. We have constructed a sample to meaningfully compare the nuclear properties of FRI and FRII radio galaxies.

2. We detect parsec-scale polarization in all four radio galaxies observed as part of a pilot study.

3. Comparison with VLBI maps of the radio galaxy 3C 66B from the literature suggest that the motion of jet components is subluminal.

4. *B*-field geometry in FRIs is similar to that observed in BL Lac objects in three out of four sources. As Gabuzda *et al.* (1994) postulate, the BL Lac jets have lower velocities and weaker longitudinal magnetic fields which allow shocks to form easily, gively rise to a predominantly transverse *B*-field configuration. Alternatively as Gabuzda *et al.* (2003) suggest, the toroidal component of the magnetic field may dominate in BL Lac objects. If so, then the *B*-field geometry in FRIs is consistent with the predictions of the radio-loud Unified Scheme.

5. The radio galaxies with relatively high inferred angles to line of sight *viz.*, 3C 270, show little polarized structure in the jets. The sources with smaller inferred angles to line-of-sight *viz.*, 3C 78 and 3C 264, show a lot of polarization structure in their jets. This could be a consequence of greater beaming in their jets compared to the relatively plane-of-sky objects. 3C 66B does not show much polarization in its jet even though its inferred θ is small. We note however that 3C 66B lies in the region of high Galactic RM (Simard-Normandin & Kronberg, 1980).

6. Extensive parsec-scale radio structure has been detected for the first time in the radio galaxy 3C 78.

7. The detection of polarization in all the FRI radio galaxies observed points to the possible absence of circumnuclear ionised matter, possibly in the form of a dusty obscuring torus, in FRIs, which could depolarize the synchrotron emission.

8. Detection of polarization in the core of 3C 270, which is suggested to have free-free absorption in a nuclear gas disk, implies that the nuclear disk is probably thin and fails to depolarise the emission from the base of the radio jet, significantly. This has also been predicted by Jones & Wehrle (1997).

9. 3C 264 shows evidence of a 'sheath-layer' with longitudinal *B*-field consistent with the 'spine-shear' geometry seen in radio galaxies on kiloparsec-scales.

10. 3C 270 shows the lowest jet-to-counter-jet ratio and the highest inferred angle to line-of-sight θ. Its lowest relative proper motion is consistent with its plane-of-sky orientation, where Doppler beaming effects are the least.

Table 3.4: Radio galaxies used in the pilot study.

Source name	Alternate name	IAU name	RA (J2000.0)	DEC (J2000.0)	Redshift	S_t (8 GHz)	D	Scale^a	Integrated RM	IPA
			h m s	d m s	z	Jy	(Mpc)	(pc/mas)	rad m^{-2}	(deg)
3C 66B	UGC 1841	0220+427	02 23 11.4	+42 59 31.4	0.0212	3.72[1]	89.1	0.42	-67 ± 3	76 ± 6
3C 78	NGC 1218	0305+039	03 08 26.2	+04 06 39.0	0.0286	2.86[2]	120.1	0.57	$+14 \pm 2$	85 ± 3
3C 264	NGC 3862	1142+198	11 45 05.0	+19 36 23.0	0.0217	1.54[2]	91.2	0.43	$+16 \pm 8$	129 ± 2
3C 270	NGC 4261	1216+061	12 19 23.2	+05 49 31.0	0.0074	6.23[2]	31.2	0.15	$+12 \pm 1$	93 ± 1

Cols. 1 through 6 list the radio galaxies, their alternate names and IAU names, the RA and DEC in J2000 co-ordinates and the redshifts from the NED, respectively; Col. 7 : The total flux density at 8 GHz in Jy – superscripts '1' and '2' are the references for S_t, 1 = Kuehr *et al.* (1981), 2 = Stull (1971); Col. 8 : Proper distance to the source; Col. 9 : Projected linear scale of source corresponding to the angular scale of 1 mas; Col. 10 : Integrated rotation measure in rad m^{-2} from Simard-Normandin *et al.* (1981); Col. 11 : Instrinsic or "zero λ", integrated position angle (IPA) in degrees.
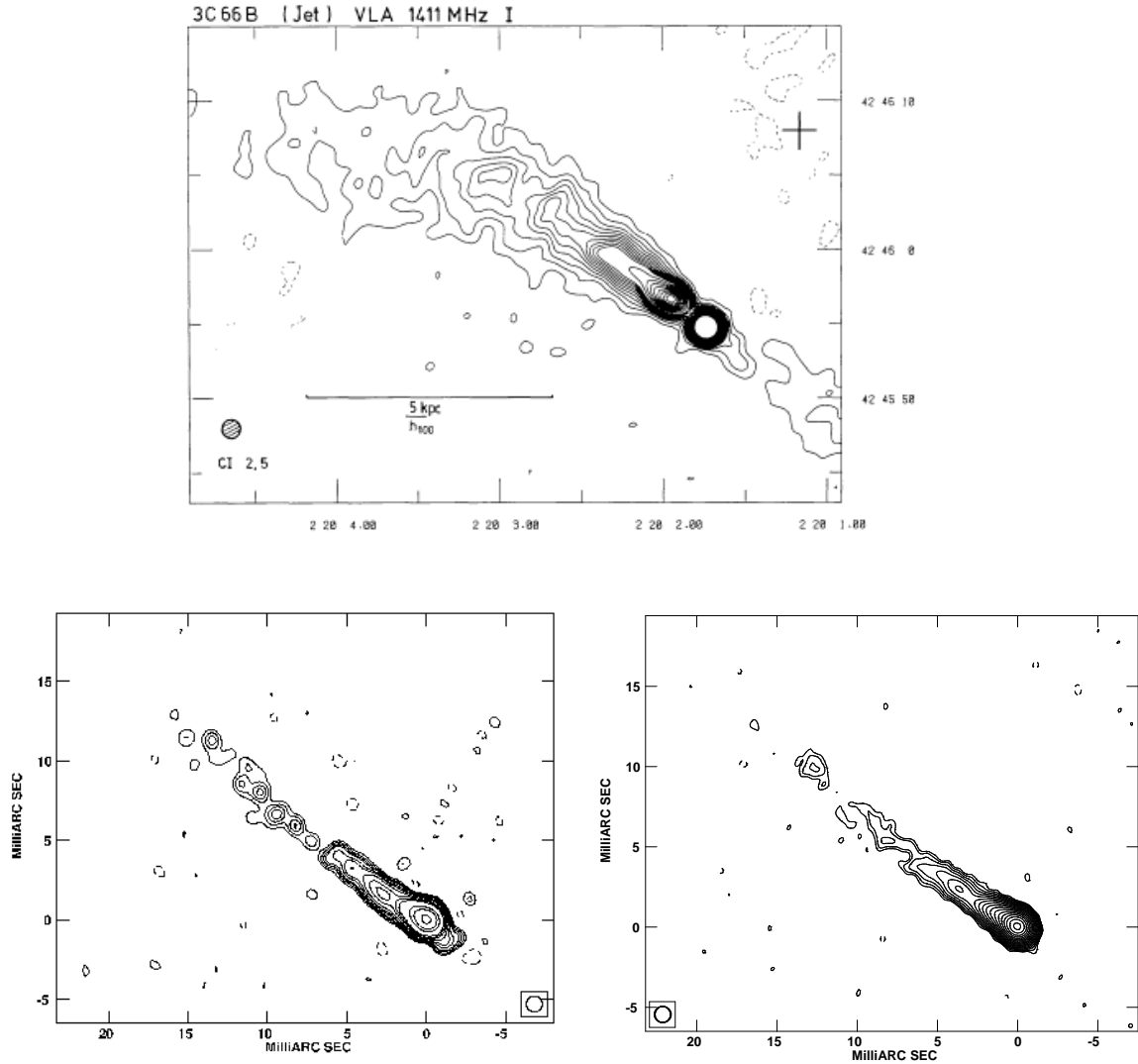
Figure 3.2: *Top.* VLA image (the x,y axes being the Right Ascension and Declination, respectively) of the jet in 3C 66B observed at 1.4 GHz by Leahy *et al.* (1986). *Bottom left.* Total intensity VLBI image of 3C 66B at 5 GHz observed by Giovannini *et al.* (2001) in epoch 1993.66. Restoring beam = 1×1 mas; contours are –0.4, 0.4, 0.6, 0.8, 1, 1.5, 2, 3, 5, 7, 10, 30, 50, and 100 mJy beam^{-1}. *Bottom right.* Our total intensity VLBI image in epoch 2002.16 at 8 GHz with the same beam and region of sky as the image of Giovannini *et al.*. Peak surface brightness = 134.5 mJy beam^{-1}. Contours are in percentage of peak and increase in steps of $\times \sqrt{2}$, lowest contour = 0.245% of peak.
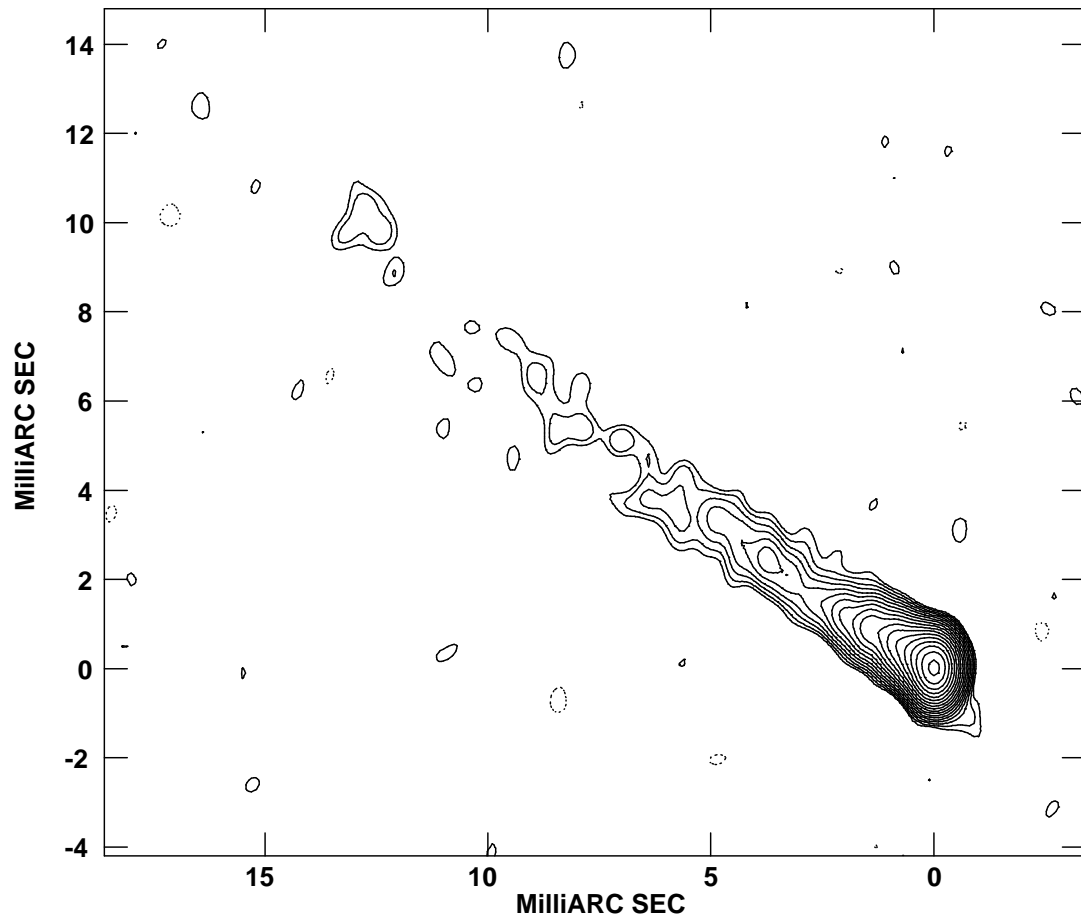
Figure 3.3: Our total intensity image of the FRI radio galaxy 3C 66B. The contours are –0.25, 0.25, 0.35, 0.5, 0.7, 1, 1.4, 2, 2.8, 4, 5.6, 8, 11.25, 16, 22.5, 32, 45, 64, 90% of the peak surface brightness of 118.2 mJy beam^{-1}.
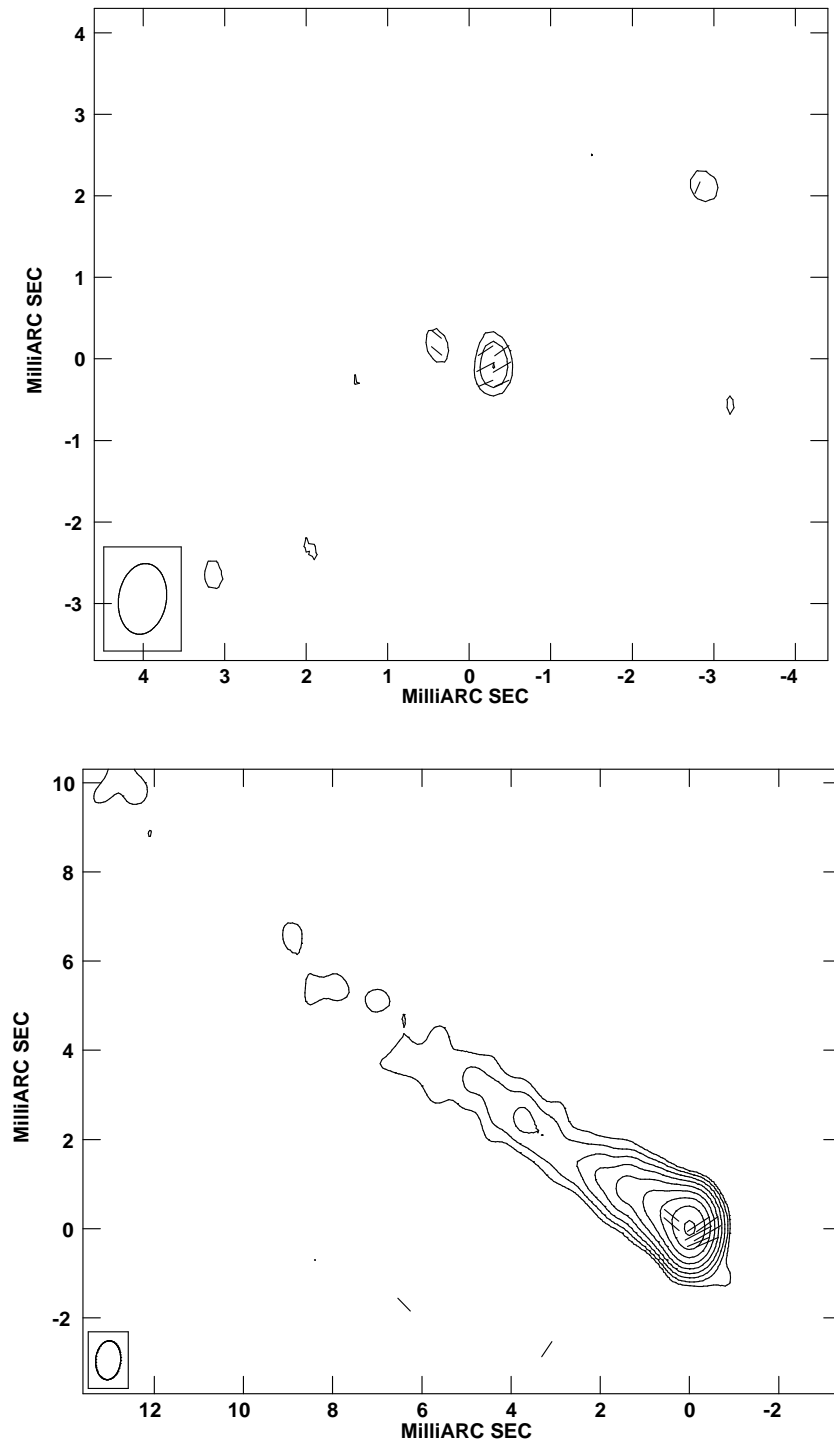
Figure 3.4: *Top.* Polarization contours with polarization electric vectors (χ) superimposed for 3C 66B. Contours are 50, 70, 99% of peak. Peak surface brightness = 0.685 mJy beam^{-1}. χ vectors : 1 mas = 2.5 mJy beam^{-1}. *Bottom.* Total intensity map with χ vectors superimposed. Peak surface brightness = 118.2 mJy beam^{-1}. Contours are in percentage of the peak surface brightness and increase in steps of $\times$ 2, lowest contour = –0.35% of peak.
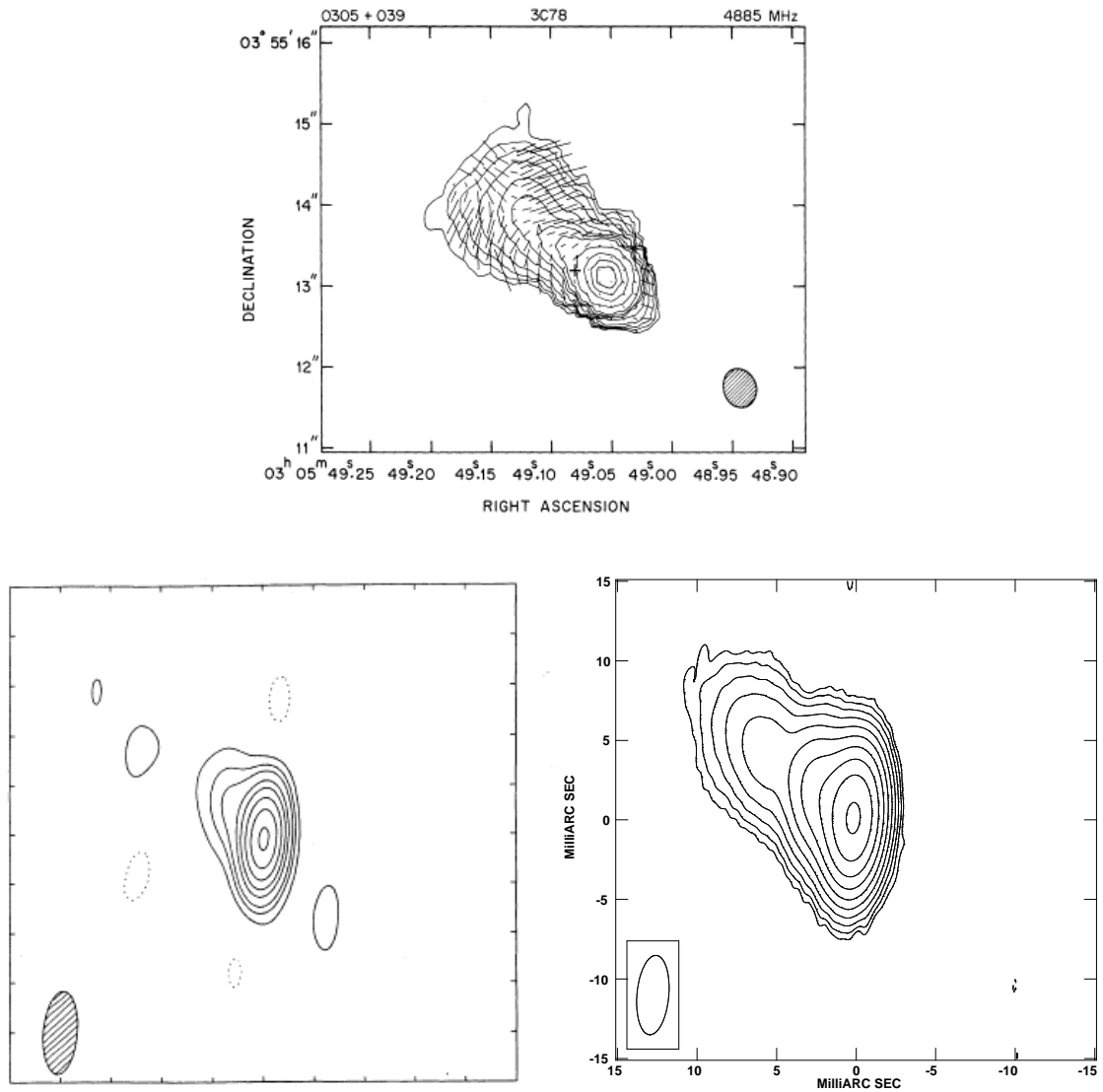
Figure 3.5: *Top.* VLA image of the jet in 3C 78 observed at 5 GHz by Saikia *et al.* (1986) with χ vectors superimposed. Peak surface brightness = 628 mJy beam^{-1}. Polarization : 1 arcsec = 55% polarization. *Bottom left.* Total intensity VLBI image of 3C 78 at 5 GHz observed by Jones (1984) in epoch 1980.75. Restoring beam = 5×2 mas in PA = –5°. The tick marks along the borders are 3 mas apart. Peak surface brightness = 400 mJy beam^{-1}. *Bottom right.* Our total intensity VLBI image in epoch 2002.16 at 8 GHz with the same beam and region of sky as the image of Jones. Peak surface brightness = 420 mJy beam^{-1}. Contours are in percentage of peak and increase in steps of × 2, lowest contour = –0.175% of peak which is 2 contours lower than the Jones image.
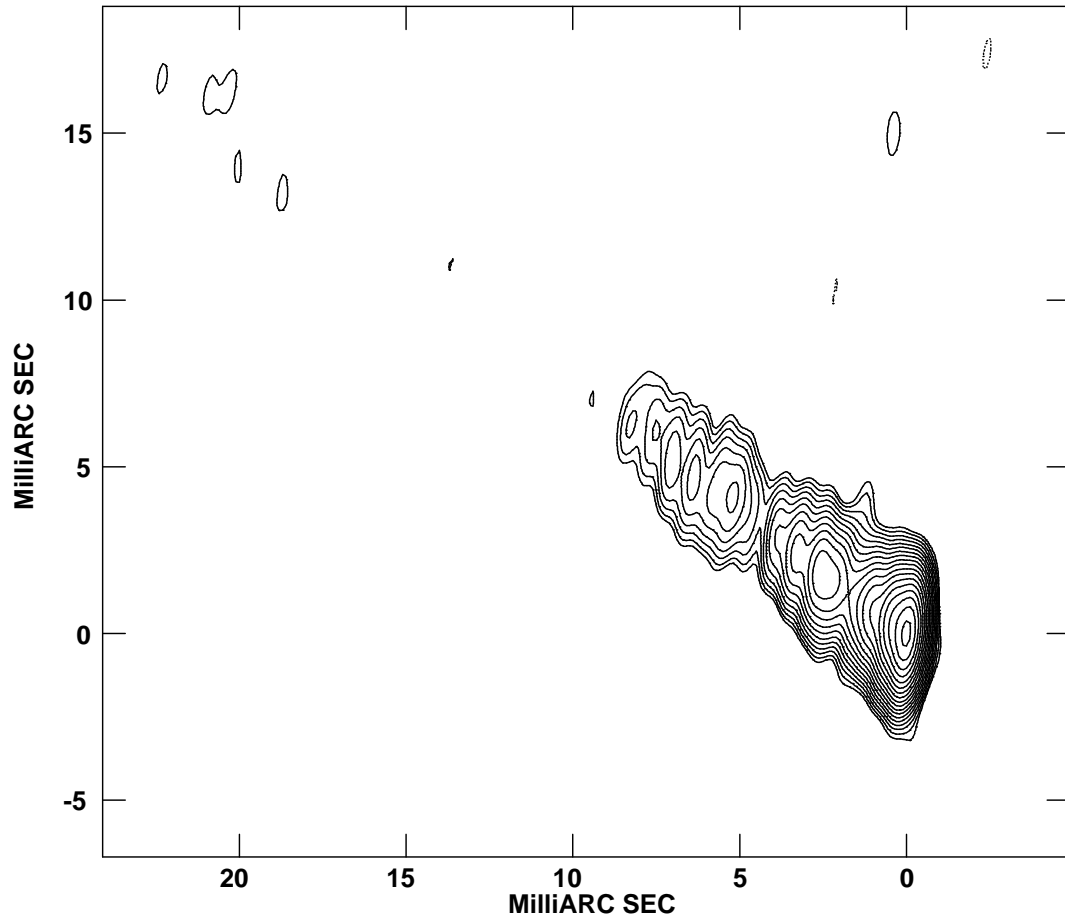
Figure 3.6: Our total intensity map of the FRI radio galaxy 3C 78. The contours are –0.25, 0.25, 0.35, 0.5, 0.7, 1, 1.4, 2, 2.8, 4, 5.6, 8, 11.25, 16, 22.5, 32, 45, 64, 90% of the peak surface brightness of 285.9 mJy beam^{-1}.
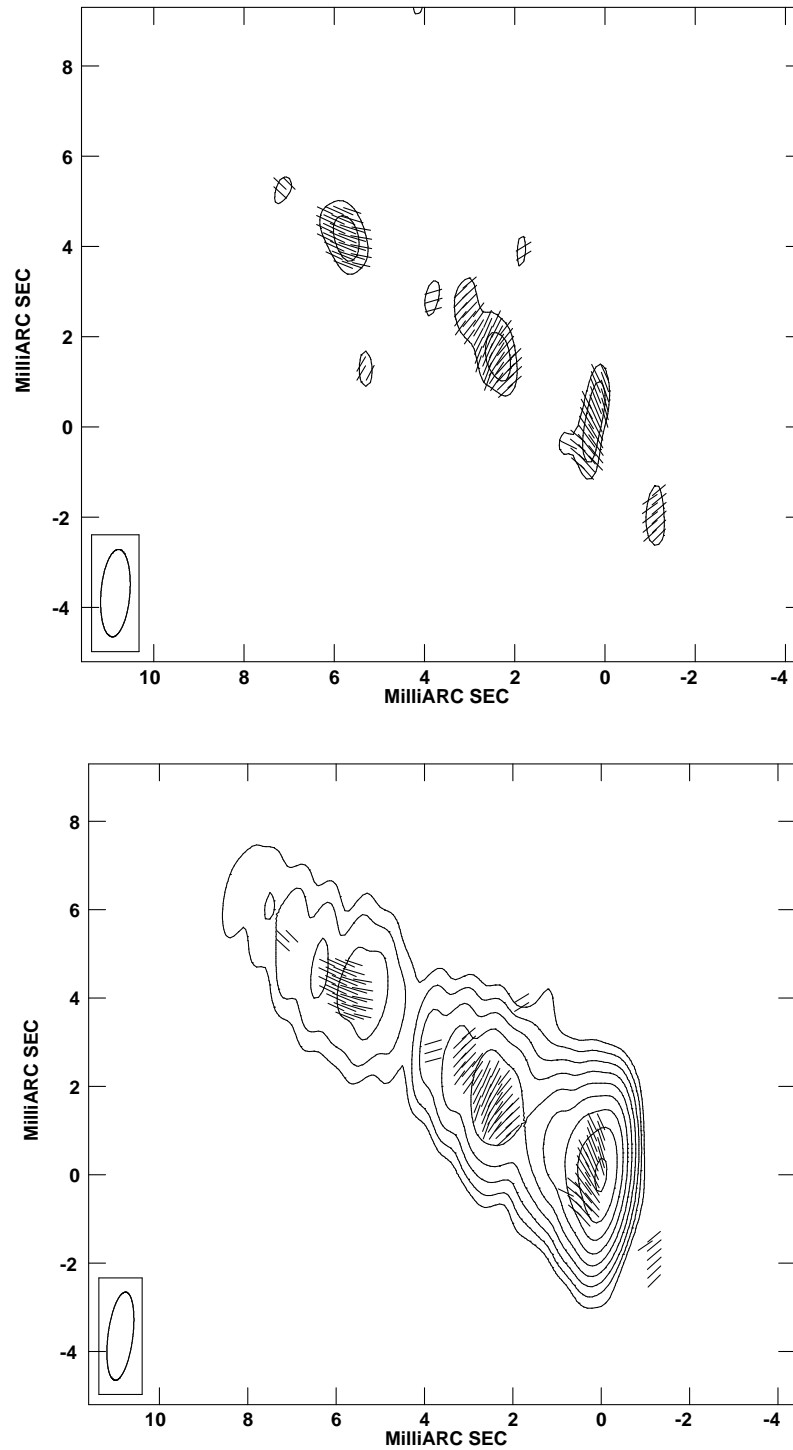
Figure 3.7: *Top.* Polarization contours with polarization electric vectors (χ) superimposed for 3C 78. Contours are 53 and 76% of the peak surface brightness of 1.36 mJy beam^{-1}. χ vectors : 1 mas = 2.0 mJy beam^{-1}. *Bottom.* Total intensity map with χ vectors superimposed. Peak surface brightness = 285.9 mJy beam^{-1}. Contours are in percentage of the peak and increase in steps of $\times$ 2, lowest contour = –0.35% of peak.
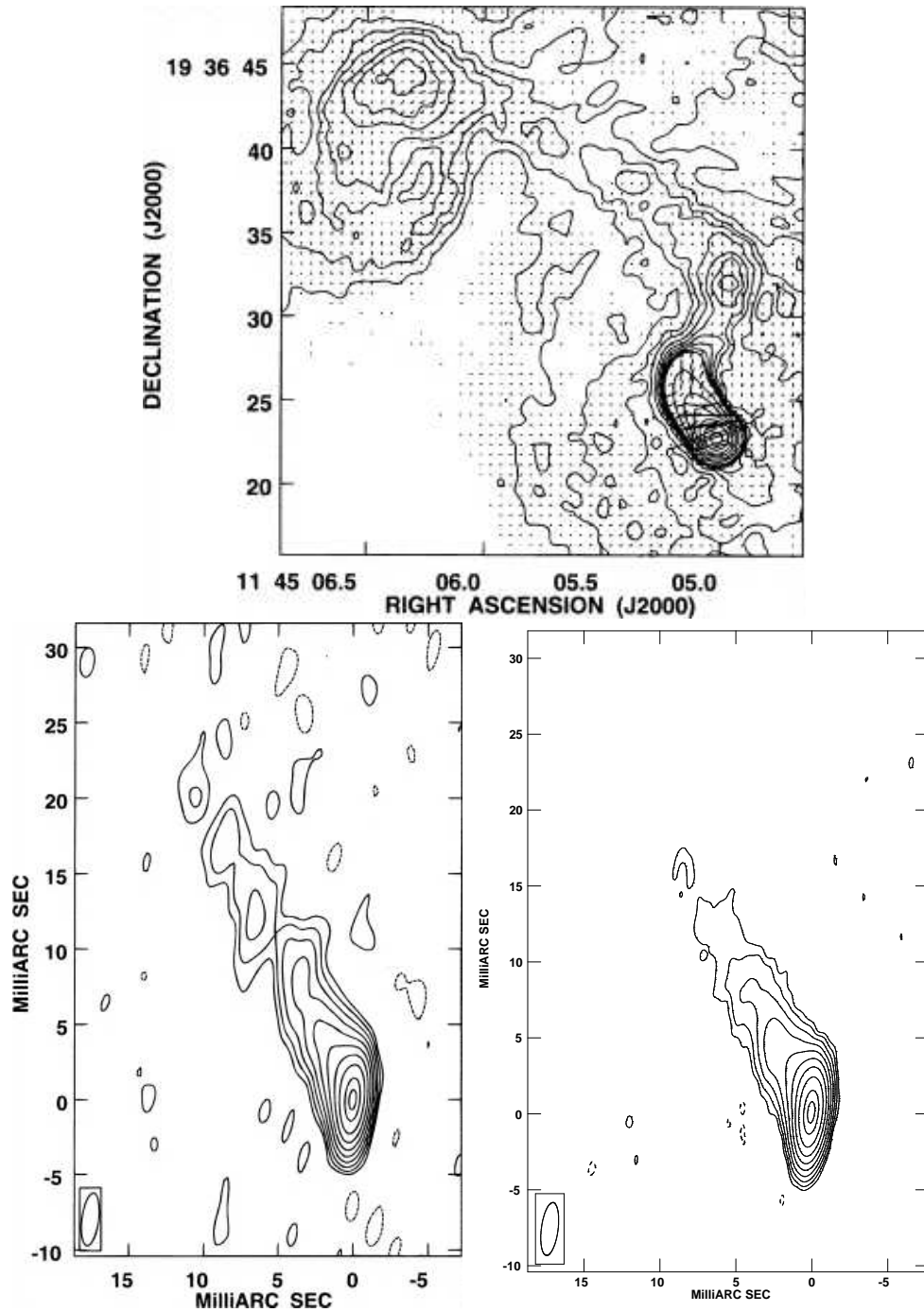
Figure 3.8: *Top.* VLA image of the jet in 3C 264 observed at 5 GHz by Lara *et al.* (1997) with χ vectors superimposed. Peak surface brightness = 263 mJy beam^{-1}. Polarization : 1 arcsec = 1.33 mJy beam^{-1}. *Bottom left.* Total intensity VLBI image of 3C 264 at 5 GHz observed by Lara *et al.* (1997) in epoch 1993.15. Restoring beam = 3.5×1.11 mas in PA = –7°.3. Peak surface brightness = 121 mJy beam^{-1}. *Bottom right.* Our total intensity VLBI image in epoch 2002.16 at 8 GHz with the same beam and region of sky as the image of Lara *et al.*. Peak surface brightness = 158.2 mJy beam^{-1}. The contours in both the *Bottom left* and *Bottom right* images are –0.25, 0.25, 0.5, 1, 2, 4, 8, 16, 32, 64, and 90% of the peak.
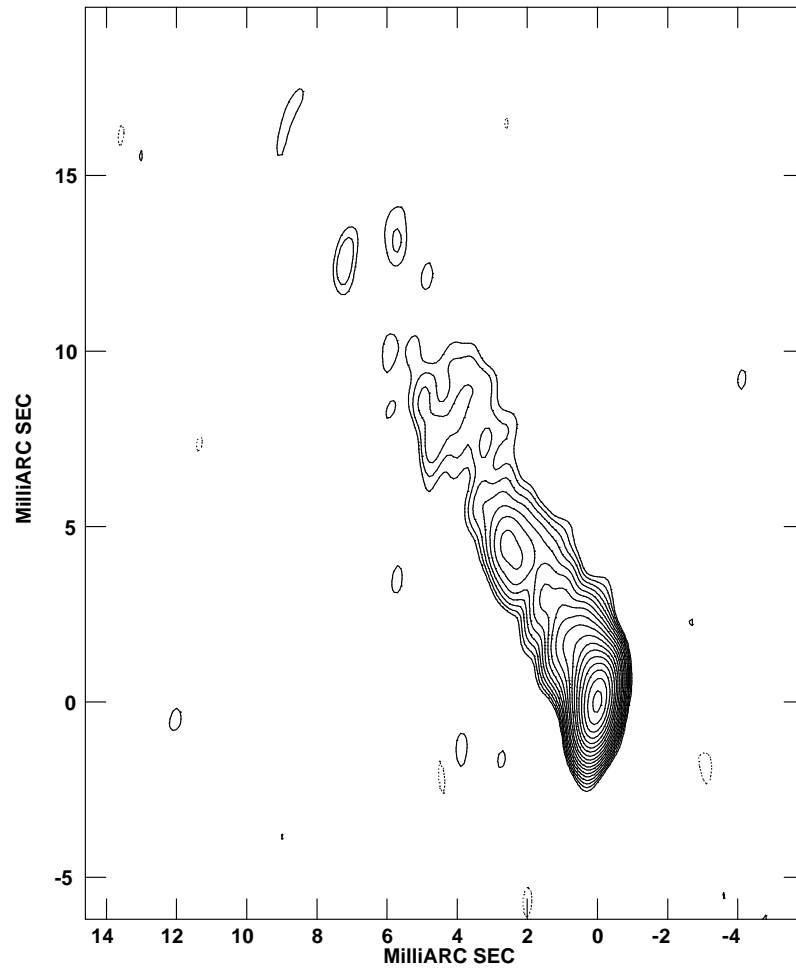
Figure 3.9: Our total intensity map of the FRI radio galaxy 3C 264. The contours are –0.25, 0.25, 0.35, 0.5, 0.7, 1, 1.4, 2, 2.8, 4, 5.6, 8, 11.25, 16, 22.5, 32, 45, 64, 90% of the peak surface brightness of 136.3 mJy beam^{-1}.
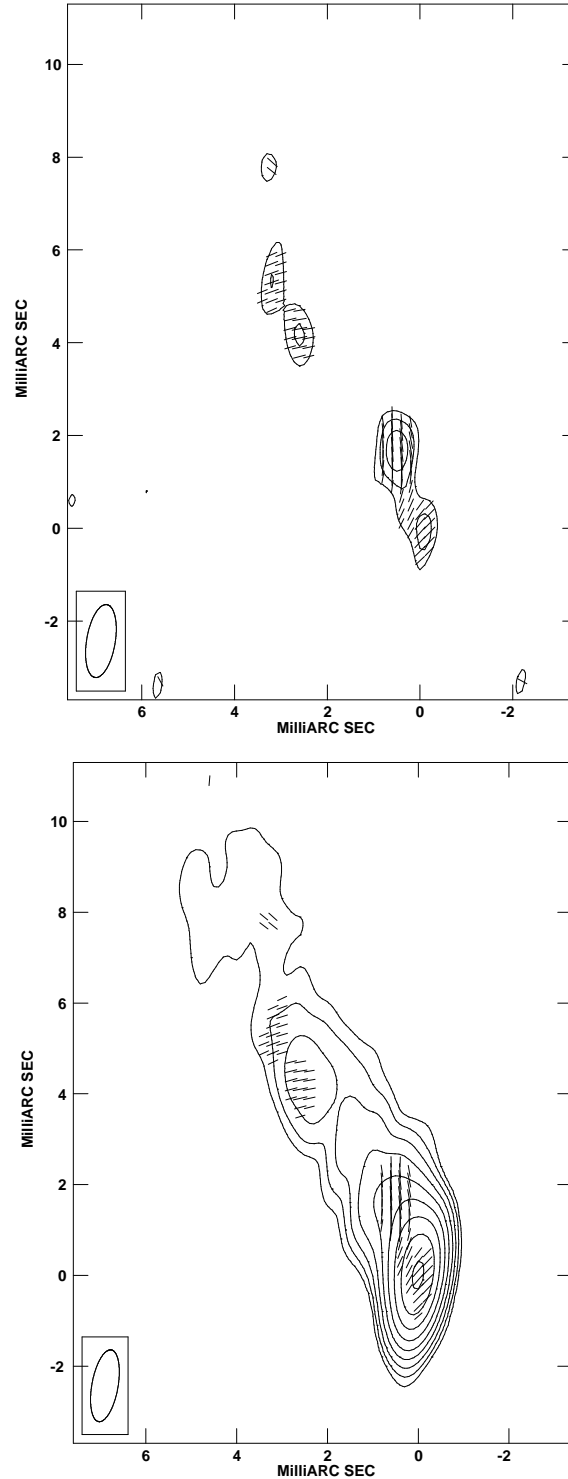
Figure 3.10: *Top.* Polarization contours with polarization electric vectors (χ) superimposed for 3C 264. Contours are 40, 57 and 80% of the peak surface brightness of 1.08 mJy beam^{-1}. χ vectors : 1 mas = 2.0 mJy beam^{-1}. *Bottom.* Total intensity map with χ vectors superimposed. Peak surface brightness = 136.3 mJy beam^{-1}. Contours are in percentage of the peak and increase in steps of $\times$ 2, lowest contour = –0.35% of peak.
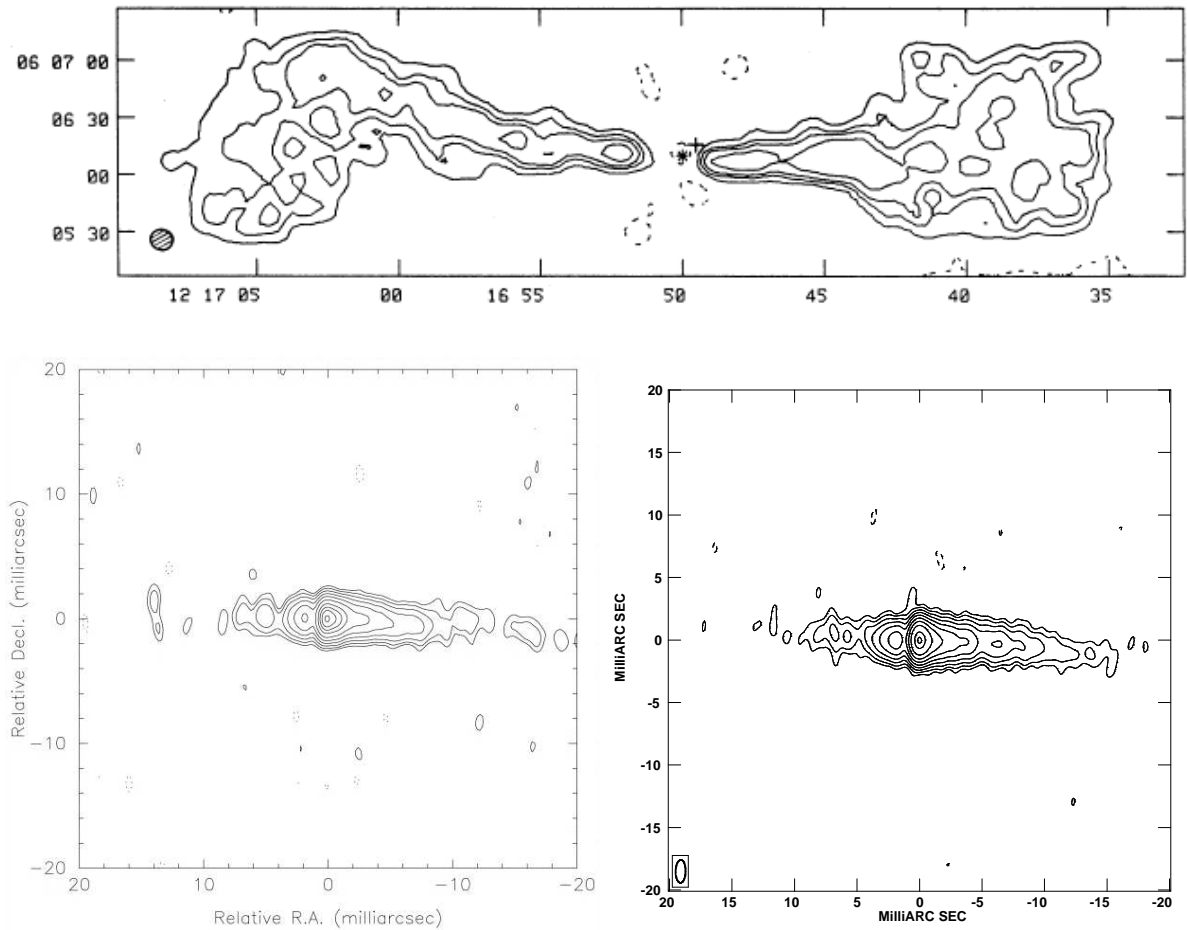
Figure 3.11: *Top.* VLA image of 3C 270 observed at 5 GHz by Birkinshaw & Davies (1985). The asterisk marks the location of a point source of 315 ± 5 mJy that has been subtracted from this map. *Bottom left.* Total intensity VLBA image of 3C 270 at 8.4 GHz observed by Jones & Wehrle (1997) in epoch 1995.25. Restoring beam $= 1.84 \times 0.80$ mas in PA $= -1.1°$. Peak surface brightness $= 101$ mJy beam^{-1}. *Bottom right.* Our total intensity VLBI image at 8 GHz with the same beam and region of sky as the image of Jones & Wehrle. Peak surface brightness $= 172.7$ mJy beam^{-1}. Contours are -0.25, 0.25, 0.5, 1, 2, 4, 8, 16, 32, 70,and 95% of the peak surface brightness, one contour lower than the Jones & Wehrle image.
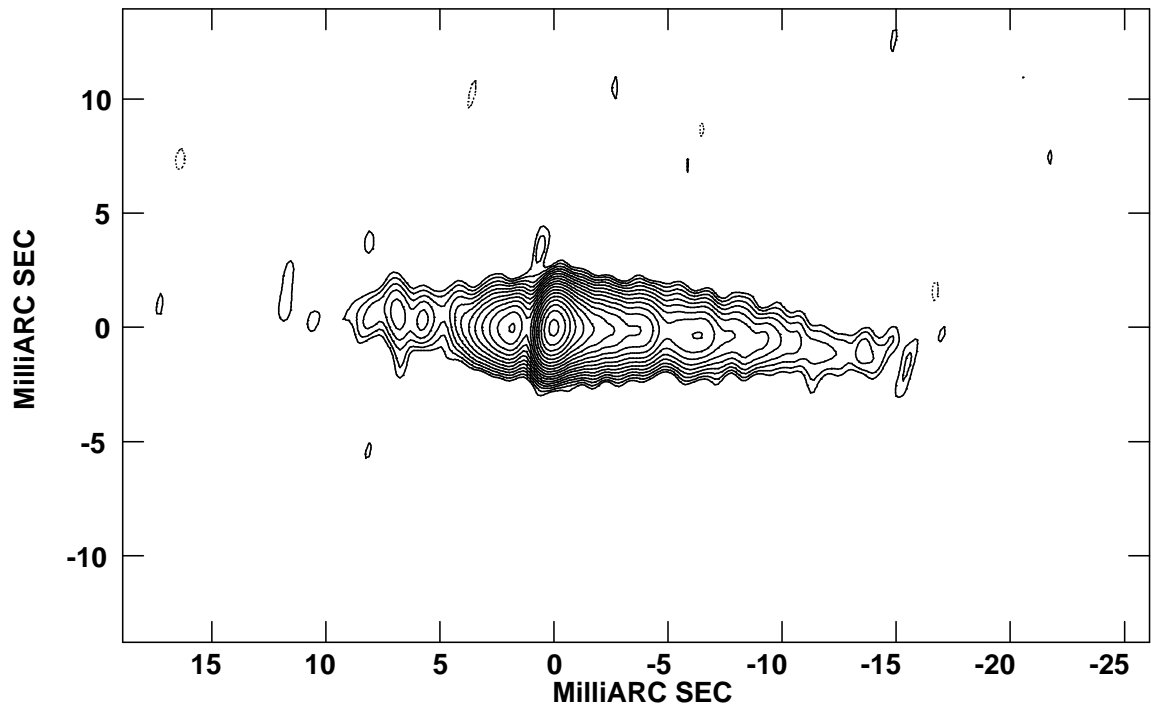
Figure 3.12: Our total intensity map of the FRI radio galaxy 3C 270. The contours are –0.25, 0.25, 0.35, 0.5, 0.7, 1, 1.4, 2, 2.8, 4, 5.6, 8, 11.25, 16, 22.5, 32, 45, 64, 90% of the peak surface brightness of 165.3 mJy beam^{-1}.
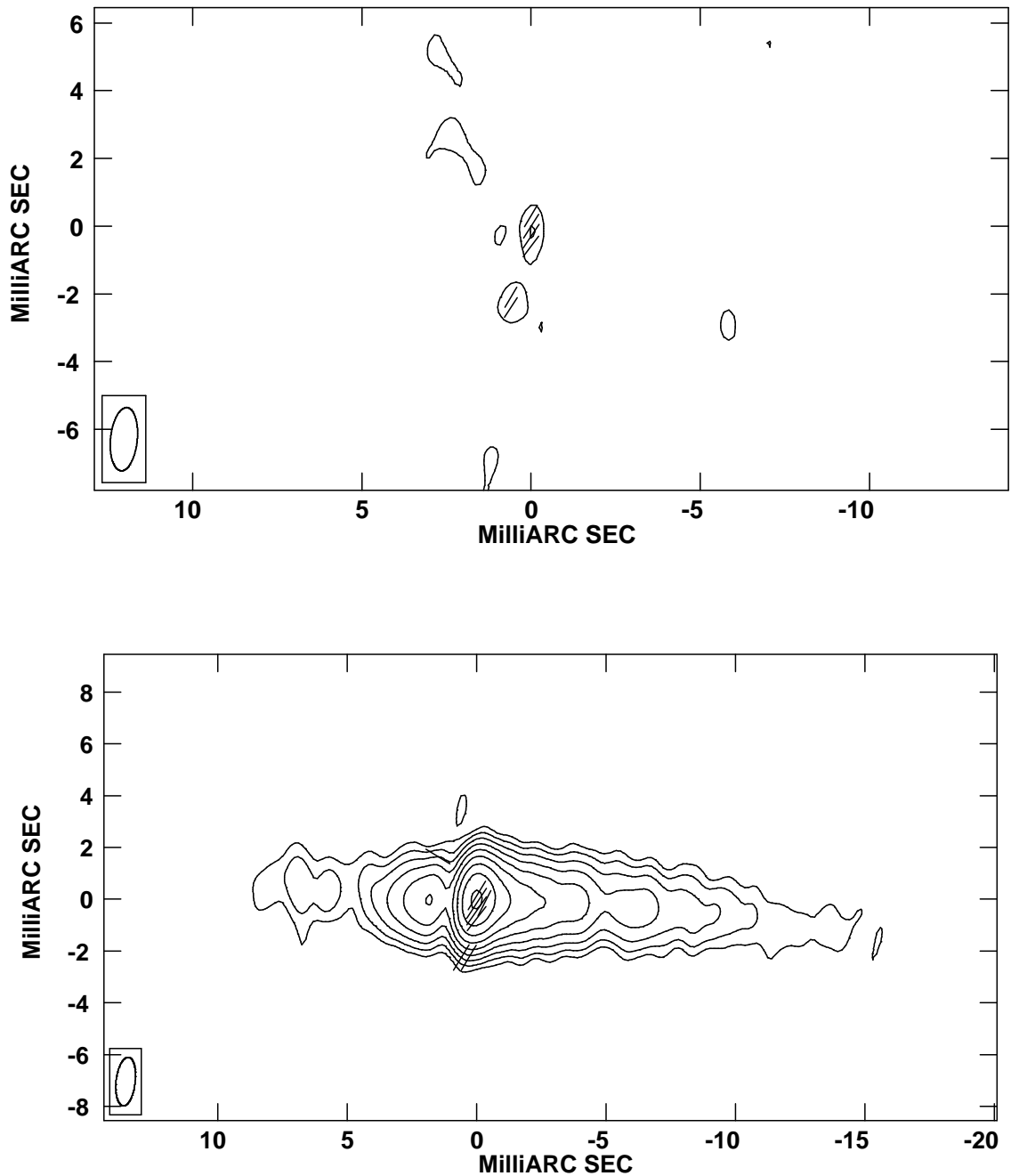
Figure 3.13: *Top*. Polarization contours with polarization electric vectors (χ) superimposed for 3C 270. Contours are 68 and 98% of the peak surface brightness of 0.7 mJy beam^{-1}. χ vectors : 1 mas = 0.8 mJy beam^{-1}. *Bottom*. Total intensity map with χ vectors superimposed. Peak surface brightness = 165.3 mJy beam^{-1}. Contours are in percentage of the peak and increase in steps of $\times$ 2, lowest contour = –0.35% of peak.

Table 3.5: Results from the VLBP observations of FRIs.

Radio galaxy	I_{peak} mJy beam^{-1}	P_{peak} mJy beam^{-1}	I_{rms} μJy beam^{-1}	P_{rms} μJy beam^{-1}	R$_j$	r mas	θ_{max} deg
3C 66B	118.2	0.68	101	56	23	2.5	40*
3C 78	286.0	1.36	171	104	134	2.5	48
3C 264	136.3	1.09	106	76	51	2.5	55
3C 270	165.3	0.70	124	78	2	2.6	84

Col. 1 : Radio galaxy name; Col. 2 : Total intensity peak surface brightness; Col. 3 : Polarized intensity peak surface brightness; Col. 4 : rms in I map in μJy beam^{-1} – this was calculated from large empty regions in the map covering typically >200 beam areas; Col. 5 : rms in P map in μJy beam^{-1} – this was calculated from empty regions in the P map covering typically $\sim$100 beam areas; Col. 6 : Jet-to-counter-jet brightness ratio; Col. 7 : Distance from the core in milliarcseconds at which the jet-to-counter-jet ratio was estimated; Col. 8 : Maximum inferred angle to line of sight – it is calculated from R$_j$ for $\beta \rightarrow 1$. * Used R$_j$ and the apparent velocity (β_{app}) measurement to derive this.

Table 3.6: *B*-field configurations of pc-scale components inferred from the VLBP observations of FRIs.

Source	F_{VLBI}^{VLA}	Component	Dist. from core	Frac. pol.	B-field
	%		mas	%	
3C 66B	65	C	0	1.1	$\perp$ (?)
		1	0.4	0.8	$\perp$
3C 78	30	C	0	...	...
		1	0.2	0.6	$\perp$
		2	2.4	4.6	$\parallel$
		3	3.0	7.8	$\parallel$
		4	5.6	25.1	$\perp$
3C 264	68	C	0	0.6	$\perp$ (?)
		1	0.2	0.7	$\parallel$
		2	0.6	9.3	$\perp$ (?)
		3	2.6	21.9	$\parallel$
		4	3.2	63.4	$\parallel$
3C 270	54	C	0	0.4	$\perp$ (?)

Col. 1 : Radio galaxy name; Col. 2 : Fraction of VLA core flux density found on VLBI scales; Col. 3 : Components in the map where polarization is observed – 'C' stands for the core while 1, 2, 3 etc. are the polarized components in the jet; Col. 4 : Distance of the corresponding component from the core along the x-axis in milliarsec; Col. 5 : Fractional polarization of the corresponding component; Col. 6 : inferred *B*-field geometry w.r.t. to the local jet direction assuming that 'core' emission is optically thick while jet emission is optically thin – '?' means the geometry is unclear due to lack of knowledge of local jet direction and/or optical thickness of the component.

Chapter 4

The pc-scale magnetic field geometry of FRII radio galaxies and the case of 3C 111

4.1   Introduction

In this chapter, we extend our investigation of the parsec-scale radio structures and magnetic fields to FRII radio galaxies in order to search for clues to explain the Fanaroff-Riley dichotomy and to test its validity. In Chapter 2, we had asked the question – "Do the FR radio galaxies display a dichotomy in magnetic field orientations, which is seen in their beamed counterparts *viz.*, radio-loud quasars and BL Lacs objects ?" We know that the B-field geometry in parsec-scale jets of quasars is predominantly parallel to the jet direction while in a majority of the BL Lac objects, the B-fields are transverse. Within the framework of the Unified Scheme, the FRII radio galaxies must show similar characteristics in the magnetic-field geometry as observed in quasars. In this chapter, we first review nuclear magnetic fields in FRII radio galaxies, and then describe our observations of the parsec-scale magnetic field geometry in the nearest classical FRII radio galaxy, 3C 111, at 8 and 43 GHz. The observations were made at six different epochs, thus allowing us to do an in-depth analysis of the propagation of the parsec-scale radio jet, the propagation of shocks and the variation in optical depth effects along the body of the synchrotron jet.

4.2 The parsec-scale magnetic field geometry of FRII radio galaxies

We discussed in Chapter 1 that the cores and inner jets of quasars are probably viewed through ionized gas associated with the nuclear region (e.g., Taylor, 2000). According to the Unified scheme linking quasars to FRII radio galaxies, one then expects that the jet components of FRII radio galaxies within 100 parsec of the cores will be viewed through a deep Faraday screen. This would explain the low fractional polarization of FRII radio galaxy cores (e.g., Rudnick *et al.*, 1986; Rusk, 1988). For the reasons of technical feasibility, parsec-scale polarimetric studies of FRII radio galaxies have focused on the well-known sources with strong cores.

A number of broad-line radio galaxies, which are intermediate in orientation between core-dominated quasars and the plane-of-sky FRII radio galaxies, have thus been observed with VLBP. These are 3C 120 and 3C 111 (Zavala & Taylor, 2002), 3C 166, 3C 236 and 3C 390.3 (Taylor *et al.*, 2001), and Cygnus A (Middelberg *et al.*, 2003). More recently Pollack *et al.* (2003) have observed with VLBP around 30 radio galaxies – only four FRIIs out of the 30 radio galaxies however *viz.*, 0600+442, 0847+379, 1010+350, 1223+395, show polarization. Of all the sources listed above, in only 3C 166, 3C 120 and 1010+350, some polarized emission has been detected in the cores while in 3C 111, Cygnus A, 0600+442, 0847+379 and 1223+395, polarized emission is detected in the jets (in two cases, only at the edges of the jet).

The BLRG 3C 166 was observed with the VLBA at 5 GHz (Taylor *et al.*, 2001). On parsec-scales, its core is very weakly polarized (0.2%), but the polarization increases quickly in the inner jet (2%) and reaches 12% at 8.5 mas out from the core. The EVPA is well ordered and transverse to the jet direction (Taylor *et al.*, 2001). After correcting for the RM which is derived for the jet ($+32 \pm 30$ rad m^{-2}) the projected magnetic field direction beyond 10 pc from the core is very nearly parallel to the jet direction, similar to that seen in quasars. In the inner jet, just north of the core, however, substantial RMs of –1500 rad m^{-2} are observed, which translate to RM of $-1500 \times (1+z)^2 = -2300$ rad m^{-2} in the rest-frame of the source. After correcting for this RM, the projected magnetic field in the inner jet is nearly perpendicular to the axis of the jet. A similar transition from a perpendicular to a parallel magnetic field configuration, with similar RM in the inner jet, has been observed in the nucleus of the lobe-dominated quasar 3C 245 (Hough *et al.*, 1998).

3C 111 lacks polarized emission from the core but shows a detectable RM within a projected distance of 5 pc from the core (Zavala & Taylor, 2002). The RMs in 3C 111

display a gradient which changes from –200 to –700 rad m^{-2} towards the core. 3C 111 has less than 0.5% polarization in its central region.

Of the four FRII radio galaxies with detected polarization in the 5 GHz observations of Pollack *et al.* (2003 ; two other "galaxies" in their sample are a GigaHertz peaked spectrum source and the BL Lac 3C 371), only one source has polarized emission in the core *viz.*, 1010+350. The χ vectors are transverse in the core and also in the jet. If the core polarization is dominated by the contributions of optically thick regions, and the jet polarization by optically thin regions, the inferred B-field changes from transverse in the core to longitudinal in the jet. 0600+442 shows polarization aligned with the edge of the jet, 0847+379 shows oblique polarization in its jet while 1223+395 shows purely transverse χ vectors in its jet, implying a longitudinal B-field.

Coming to the observing frequency, 3C 120 and 3C 111 have been observed at 8, 12 and 15 GHz with the VLBA while Cygnus A was observed at 15 GHz with the VLBA. The radio galaxies 0600+442, 0847+379, 1010+350, 1223+395 were observed at 5 GHz with the VLBA. None of these FRII radio galaxies have been observed with a global VLBI array. Therefore, beam depolarization due to varying B-field orientations on scales smaller than the beam, cannot be ruled out for the FRIIs which fail to show polarized emission, especially in their parsec-scale cores where new emergent components cannot be resolved from the cores.

4.3   The broad-line radio galaxy 3C 111

The broad-line radio galaxy 3C 111 is the nearest ($z = 0.0485$, Sargent (1977)) classical FRII radio galaxy with a strong compact core at centimeter/millimeter wavelengths (Wills, 1975). The bright central component coincides with an 18th-magnitude nuclear dominant 'N-galaxy' (Longair & Gunn, 1975). Radio observations on arcsec-scales show a highly collimated jet leading from the core to the northeastern lobe at a position angle of 63° (Linfield & Perley, 1984). The total flux density at 5 GHz is around 5 Jy (Aller *et al.*, 1985), one-third of which is contained in the central component. The arcsec-scale radio core is strongly variable on a time scale of a few months (Wills, 1975). 3C 111 was detected as an X-ray source by *HEAO-1* (Marshall *et al.*, 1978).

The first VLBI observations of 3C 111 were made at λ 2.8 cm in 1976 by Pauliny-Toth *et al.* (1976) just after a large outburst occurred (e.g., O'Dea *et al.*, 1985) in which the 90 GHz flux density increased by a factor of 5. On parsec-scales, the jet is much more prominent and is one-sided towards the northeast, roughly aligned with the kpc-scale jet (Linfield, 1981). 3C 111 is well known for showing strong structural variability (eg.,

Goetz *et al.*, 1987; Preuss *et al.*, 1988, 1990). Table 4.3 lists the properties of 3C 111.
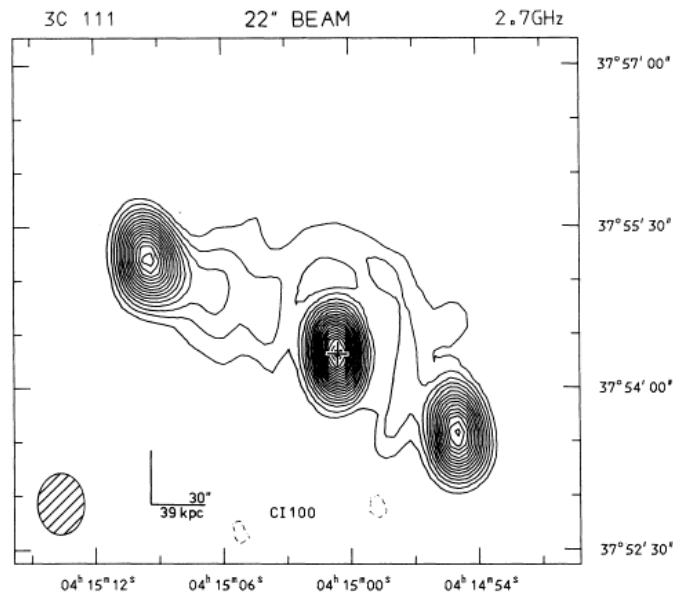
Figure 4.1: Image of 3C 111 at 2.7 GHz observed with the Cambridge 5 km telescope by Laing (1981). The contour interval is 100 mJy beam^{-1}. The cross marks the position of the optical host galaxy.

4.4 The VLBP observations

Following a large millimeter-outburst in January 1996 (Alef *et al.*, 1998), the source was observed with the NRAO Very Long Baseline Array and the Effelsberg antenna in dual-polarization mode at 8.4 GHz and 43 GHz, in July and September of 1996 and subsequently at 43 GHz on June and November of 1997 and finally in May and September of 1998. Table 4.4 gives the details of the observations.

4.5 Data reduction and analysis

The calibration and imaging of the data was done using the AIPS package. We found a joint solution for the instrumental polarization of all antennas and for the calibrator source polarization using the task LPCAL. To compute the instrumental polarization corrections with LPCAL, we used the bright source 3C 84, assuming it was unpolarized. The resulting instrumental polarizations for the VLBA and Effelsberg were < 1%. The EVPA was calibrated using the EVPA calibration results from other experiments within
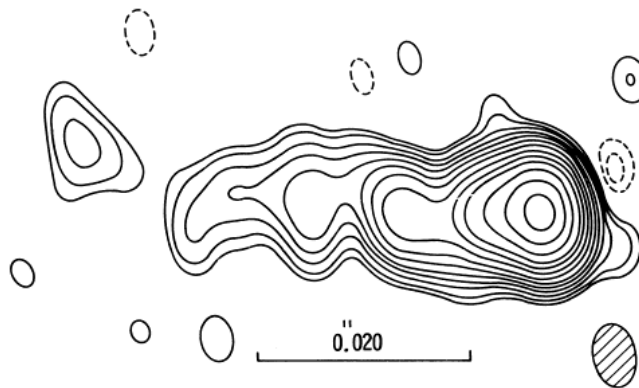
Figure 4.2: VLBI map of 3C 111 at 1.7 GHz, rotated by $+28°$ in PA taken from Linfield (1987). The restoring beam is 6.0×4.0 mas. The peak intensity is 268 mJy beam^{-1}.

three to six months of the 3C 111 observations which were calibrated using the same reference antenna (Los Alamos) (Gabuzda, private communication). The tasks IMAGR (for the Fourier transform and CLEAN) and CALIB (for self-calibration) were used to make the total intensity (I) maps. Polarization (P) maps were made using the tasks IMAGR and COMB.

4.6 Results of the multi-frequency, multi-epoch observations

The VLBP images of 3C 111 are presented in Figures 4.3 through 4.5. These images clearly show the parsec-scale radio jet pointing towards the north-east, similar to the kiloparsec radio jet. We present below a detailed discussion of the images – the changing radio structure, the flux densities of components, the magnetic field orientations and our inferences on the evolution of the source structure and optical depth effects.

4.6.1 Three epochs of simultaneous 8 & 43 GHz observations : comparison of B-field geometry and optical depth inferences

Epoch 1996.52

On comparing the 8 and 43 GHz images from epoch 1996.52, we find that there is a large offset between the polarization (P) electric vectors χ for a knot at $r \simeq 0.5$ mas

from the core. At 43 GHz, $\chi \simeq -20°$ while at 8 GHz, $\chi \simeq 90°$. This indicates that the Faraday and/or optical depth effects may be playing a significant role here. However, since the χ vectors in the core region for this epoch had nearly the same orientations at the two frequencies, the Faraday and optical depths appear to be less important near the core.

Epoch 1996.72

The 43 GHz image of 3C 111 in the epoch 1996.72 is shown in Figures 4.3c and 4.3d. The bright feature at $r \simeq 0.75$ mas shows χ vectors which appear to be oblique to the jet direction. However, the possibility that this is due to the inexact knowledge about the direction of the jet flow, cannot be ruled out. The peak surface brightness decreased from 2.0 Jy beam^{-1} to 1.3 Jy beam^{-1} between 1996.52 and 1996.72.

Epoch 1997.45

Figure 4.3e shows the 43 GHz image for the observations in 1997.45. This image shows a rich polarization structure. The peak flux density decreased from around 1.3 Jy beam^{-1} in 1996.72 to 0.8 Jy beam^{-1}. Polarization was detected in the inner jet, to the north of the core, where the χ vectors are transverse to the jet direction. Assuming this region is optically thin and Faraday effects are not important (which is likely to be the case at 43 GHz), the inferred magnetic field is longitudinal at the edge.

A bright knot between $r \simeq 0.5 - 1.0$ mas from the core shows different behaviour for the χ vectors on the northern and southern sides of this feature : χ is $\simeq 90°$ at the southern edge, bearing no obvious relation to the flow direction, and χ is roughly transverse to the jet direction at the northern edge.

Polarization with $\chi \simeq 90°$ was also seen in the $r \simeq 0.5$ mas knot in the 1996.52 image (Figure 4.3a), suggesting that these correspond to the same bright feature. The polarization at the northern edge of the jet supports the idea that the jet flow direction is to the northhest; in this light, the knot at $r \simeq 0.75$ mas, in the 43 GHz image of epoch 1996.72, has χ vectors which are indeed oblique to the jet direction.

At $r \simeq 1.2$ mas there is another extended polarized knot of emission with a complex polarization structure in the 43 GHz image of this epoch. Regions with nearly the same χ vectors as in the $r \simeq 0.75$ mas knot are present. There is also an additional region with χ vectors nearly aligned with the jet direction further to the north. The origin of this structure is not clear, though it may be due to a combination of bending of the jet (possibly giving rise to shocks) and interaction with the surrounding medium.

Core polarization

Figure 4.3f shows the 8 GHz image for the 1997.45 epoch. The core region in this image looks very similar to the core region in the 1996.52 image. The peak flux density remained around 2.5 Jy beam^{-1} (it was 2.4 Jy beam^{-1} in 1996.72 and 2.2 Jy beam^{-1} in 1996.72). The χ vectors in the core region are aligned with the inner jet, as was seen in 1996.52 and 1996.72. There is a region of roughly transverse χ vectors between $r \simeq 1.0 - 2.0$ mas, similar to the 1996.52 epoch.

Inner jet polarization

The polarization at the northern edge of the inner 8 GHz jet at 1997.45 has a similar orientation to the northern edge of the $r \simeq 0.75$ knot in the 43 GHz image, suggesting Faraday and optical depth effects are small in this region. The 8-GHz map does not have sufficient resolution for us to know whether the core region corresponds to the near-core region in the 43 GHz image; if it does, the χ vectors at 8 and 43 GHz differ by nearly 90°, suggestive that this region may be optically thin at 43 GHz but optically thick at 8 GHz.

In view of the rapidly changing outer jet structure, the magnetic field configuration seems to be more stable in the inner-jet/core region (at least over the time-period of a year). A knot at $r \simeq 3.5$ mas shows aligned χ vectors, implying a transverse B-field region. If this bright feature corresponds to the $r \simeq 2.5$ mas feature seen in the September, 1996 image, its χ has changed from 0° to about 60°.

4.6.2   Three epochs of 43 GHz observations : evolution in jet structure and B-field geometry

Epoch 1997.45

The 43 GHz image of 3C 111 in this epoch (see Figure 4.4, *top*) was discussed in the last section.

Epoch 1997.78

The Figure 4.4 (*bottom*) shows the 43 GHz image in epoch 1997.78. The overall polarization structure is similar to that observed in 1997.45. The region of extended emission with complex polarization structure has moved to the north-east by about 1 mas, and

the shape of the contours in this region suggest that the jet indeed bends toward the south and then back toward the north-east.

In this case, the χ vectors along the central region of the jet appear to be transverse to the flow direction, indicating a longitudinal B-field if the region is optically thin and Faraday effects are not significant. The origin of the polarization with $\chi \simeq 90°$ at the southern edge of this feature remains unclear; again, the polarization in this region is presumably due to a combination of shocks associated with the bending and interaction between the jet and the surrounding medium.

Epoch 1998.37

The polarization structure seen in the 43 GHz image for this epoch (Figure 4.4, *top*) is appreciably simpler. The polarization in the innermost jet remains transverse and concentrated toward the northern edge of the jet, as in 1997.45 and 1997.78. This probably indicates a longitudinal B-field. The knot at $r \simeq 0.75$ mas in 1997.78 has moved outward, with χ remaining near $90°$.

The region where the jet seemed to bend and flare has also moved outward to $r \simeq 2.0 - 3.0$ mas from the core, and the polarization structure now implies primarily a longitudinal B-field nearly throughout this expanding structure. There is only a hint of polarization with $\chi \simeq 90°$ at the very southern edge. This extended region is clearly offset from the direction of the inner jet, consistent with the idea that the jet did indeed bend toward the south and then back toward the northeast. The polarization structure of this feature seems to have been complex during the bending, then became simpler after the jet flow had passed the region of bending and the flow stabilized.

Epoch 1998.69

In the last epoch of observations (Figure 4.5, *bottom*), the dominant polarization near the core is partially transverse to the jet and partially oblique, $\chi \simeq 0$. The polarization in the outer jet overall remains transverse (B longitudinal), though there is now a region of oblique (horizontal) χ vectors at the northern edge of the polarized region. This extended outer region has moved to $r \simeq 2.5 - 3.5$ mas from the core.

4.7   Results

The total intensity images of 3C 111 with polarization vectors superimposed are shown in Figures 4.3 to 4.5. We show all the six 43-GHz and the three 8-GHz images convolved

with the same beams, corresponding roughly to the beam sizes obtained for uniform weighting: 0.20×0.15 mas in $PA = -20°$ for the 43-GHz maps and 1.15×0.70 mas in $PA = -20°$ for the 8-GHz maps. We attempted to derive the spectral index and rotation measures from the images of 3C 111. However, we found that for the 8 and 43 GHz images, the peaks in surface brightness did not coincide, making it impossible to 'latch' onto a common feature in the two images.

4.7.1 Superluminal motion

We examined the proper motion of the bright knot of radio emission in the jet, closest to the core and observed at 43 GHz at four epochs (seen at a distance $r \simeq 0.30$ mas from the core in Figure 4.3a). We considered only this one knot as it was difficult to identify other knots of emission without doing a detailed model-fitting analysis. Figure 4.6 shows the separation of this knot with respect to the epoch of observation. The slope gives an average speed of $v \simeq 1.6c$, which is mildly superluminal. Goetz *et al.* (1987) have found from 5 GHz multi-epoch observations made in 1985 and 1987 that knots in the parsec-scale jet of 3C111 show 'superluminal behaviour' and have characteristic speeds of $> 3c$.

4.8 Conclusions

From our investigation of multi-frequency, multi-epoch observations of the Broad Line Radio galaxy 3C 111, five months after a large millimeter outburst, we find that :

1. The parsec-scale radio structure and the corresponding magnetic field is rapidly evolving.

2. Assuming that the radio emission is optically thin, the inferred B-field is perpendicular to the observed orientation of the χ vectors. The 43 GHz observations provide evidence for a region of substantial bending 1–2 mas from the core. The B-field structure is complex in the region of bending, presumably due to a combination of bending (possibly giving rise to shocks) and interaction of the jet with its surrounding medium, but becomes much more uniform and longitudinal beyond this region.

3. The comparison of 43 and 8 GHz images at three epochs separated by a few months shows that Faraday and/or optical depth effects were important at $r \simeq 0.5$ mas from the core in July 1996, but appear to be less important near the inner-jet/core

regions. It is possible that the near-core region in the June 1997 43 GHz image which was presumably optically thin and had a longitudinal B-field, coincides with the core in the 8 GHz image which was presumably optically thick and exhibited a similar B-field orientation, but further analysis is required to confirm this.

4. The 43 GHz images point to the dominant B-field being longitudinal in the inner and outermost jet.

5. Assuming that the 43 GHz emission is optically thin, the B-field is primarily longitudinal in both the innermost and outermost parts of the jet. In the region of substantial bending at 1–2 mas from the core, however, the B-field structure is complex, presumably due to a combination of bending (possibly giving rise to shocks) and interaction of the jet with its surrounding medium.

6. The jet motion is mildly superluminal. A preliminary analysis suggests speeds of $v \simeq 1.6c$, but this must be verified by more detailed modeling of the jet structure at 43 GHz.

7. Our tentative interpretation from the comparison of the multi-epoch, dual frequency images is that, for e.g., in July 1996, the Faraday and/or optical depth effects were dominant at $r \simeq 0.5$ mas from the core but appear to be less important near the inner-jet/core regions, and in November 1997, the core is optically thick at 8 GHz but optically thin at 43 GHz. Thus, the Faraday and optical depth effects are seen to evolve along the jet.

Table 4.1: Properties of 3C 111.

IAU name	RA J2000.0	DEC J2000.0	Redshift	S_t (5 GHz)	S_c (5 GHz)	D	Scale^a	Integrated RM	IPA
	h m s	d m s	z	Jy	mJy	Mpc	pc/mas	rad m^{-2}	deg
0415+739	02 23 11.4	+42 59 31.4	0.0485	5.0	212.6	212.6	0.937	-19 ± 2	140 ± 4

Cols. 1, 2, 3, 4 list the IAU name, the Right Ascension, Declination and redshift of 3C 111; Col. 5 : Total flux density at 5 GHz observed on arcsec-scales; Col. 6 : Arcsec-scale core flux density at 5 GHz in mJy; Col. 7 : Proper distance to 3C 111, Col. 8 : Projected linear scale of source corresponding to the angular scale of 1 mas; Col. 9 : Integrated rotation measure in rad m^{-2} from Simard-Normandin *et al.* (1981); Col. 10 : Instrinsic or "zero λ", integrated position angle (IPA) in degrees.

Table 4.2: Details of the VLBP observations of 3C 111.

Program code	Observing date	Epoch year	Frequency MHz	Stations	D-term calibrator
BP031 (A)	8 July 1996	1996.52	8405.5	VLBA (9)	3C84
			43201.5	”	0420-014
BP031 (B)	19 Sept 1996	1996.72	8405.9	EB, VLBA	3C84
			43201.9	”	0420-014
BA027 (A)	12 June 1997	1997.45	8405.5	EB, VLBA	0300+470, 3C 279
			43201.5	”	0420-014
BA027 (B)	12 Nov 1997	1997.78	43201.7	EB, VLBA	0420-014, 3C 279
BA027 (C)	14 May 1998	1998.37	43201.7	EB, VLBA	0420-014, 3C 111
BA027 (D)	12 Sept 1998	1998.69	43201.5	EB, VLBA	0420-014

Notes : Col. 5 : All the experiments except BP031 (A) used Effelsberg (100m) and the ten (25m each) VLBA antennas. Only 9 VLBA antennas (minus St. Croix) were used for BP031 (A). Each experiment used 4 Intermediate Frequencies (IFs) with a Bandwidth of 8 MHz each. Col. 6 : 3C 454.3 was used as a fringe finder for all the experiments. The EVPA was calibrated using the EVPA calibration results from other experiments within three to six months of the 3C 111 observations which were calibrated using the same reference antenna (LA) (Gabuzda, private communication).
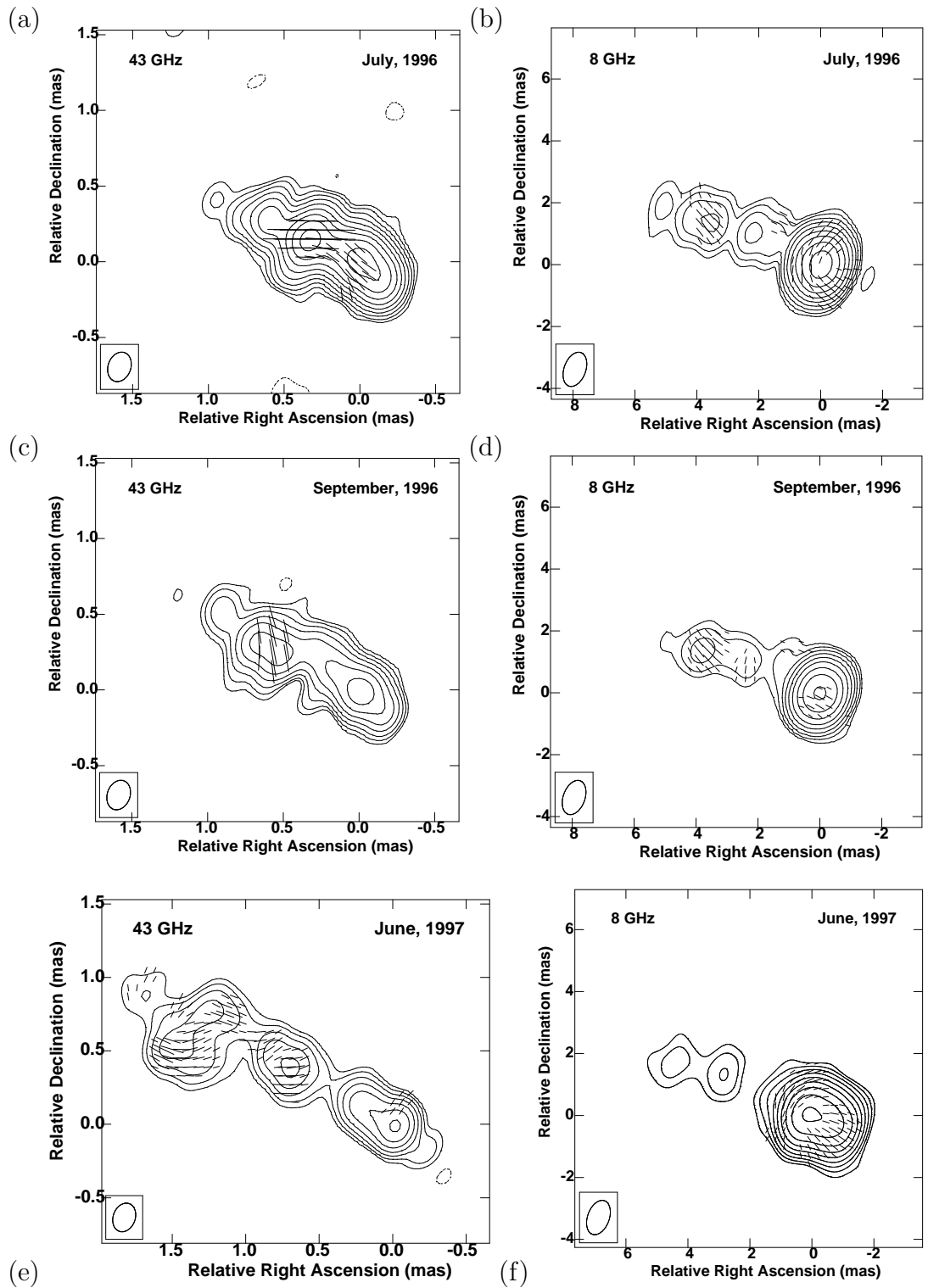
Figure 4.3: Total intensity maps of 3C 111 with χ vectors superimposed. The surface brightness peaks in Jy beam^{-1} and the bottom contours in % of the peak are (a) 2.12, ±0.25, (b) 2.16, ±0.25, (c) 1.26, ±1.0, (d) 2.36, ±0.35, (e) 0.74, ±1.4 and (f) 2.06, ±0.35; successive contours increase by a factor of 2. Restoring beams are 0.20×0.15 mas (43 GHz) and 1.15×0.70 mas (8 GHz) in $PA = -20°$.
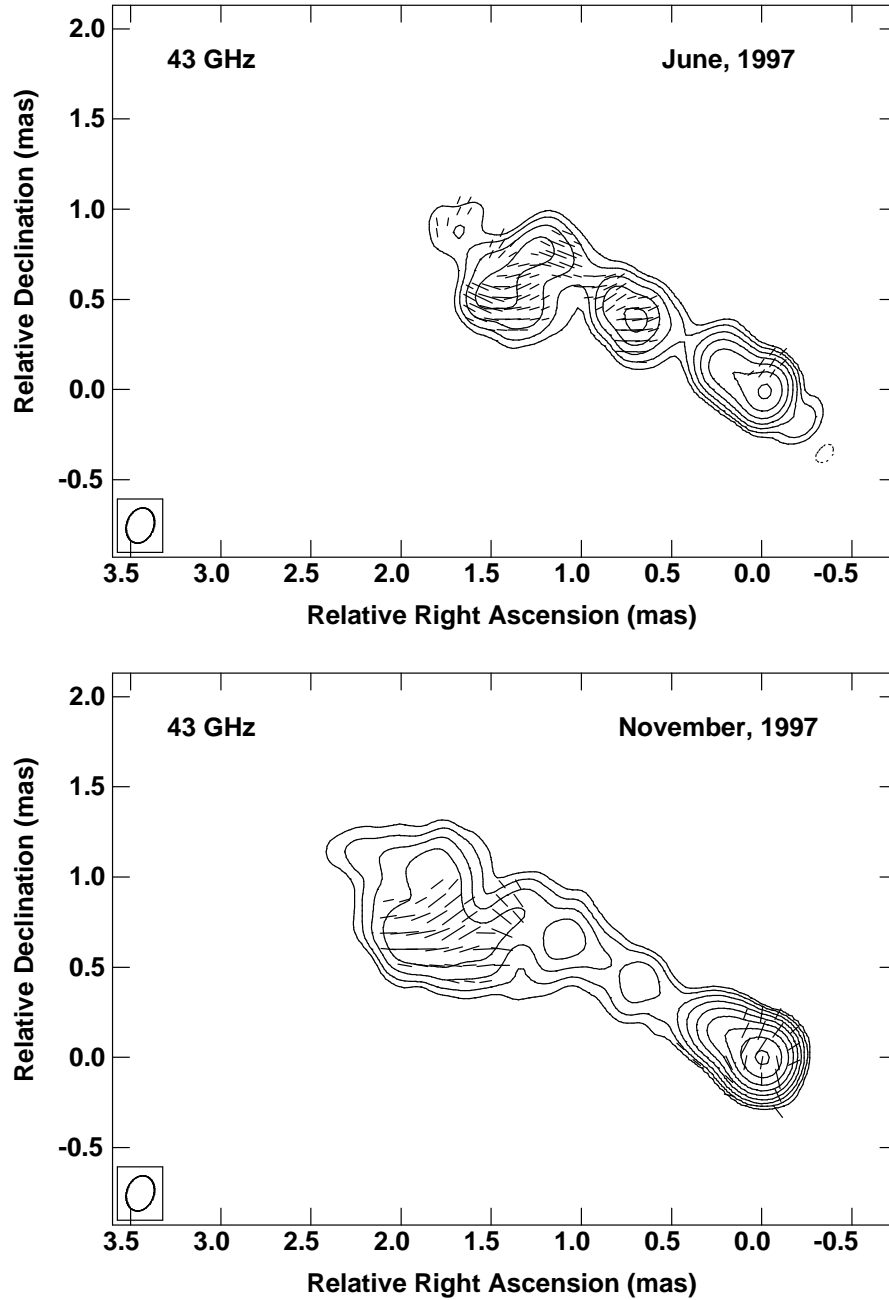
Figure 4.4: Total intensity maps of 3C 111 at 43 GHz with χ vectors superimposed. The surface brightness peaks in Jy beam^{-1} and the bottom contours in % of the peak are (Top) 0.74, ± 1.4 and ($Bottom$) 1.14, ± 0.35; successive contours increase by a factor of two. Restoring beam is 0.20×0.15 mas in $PA = -20°$.
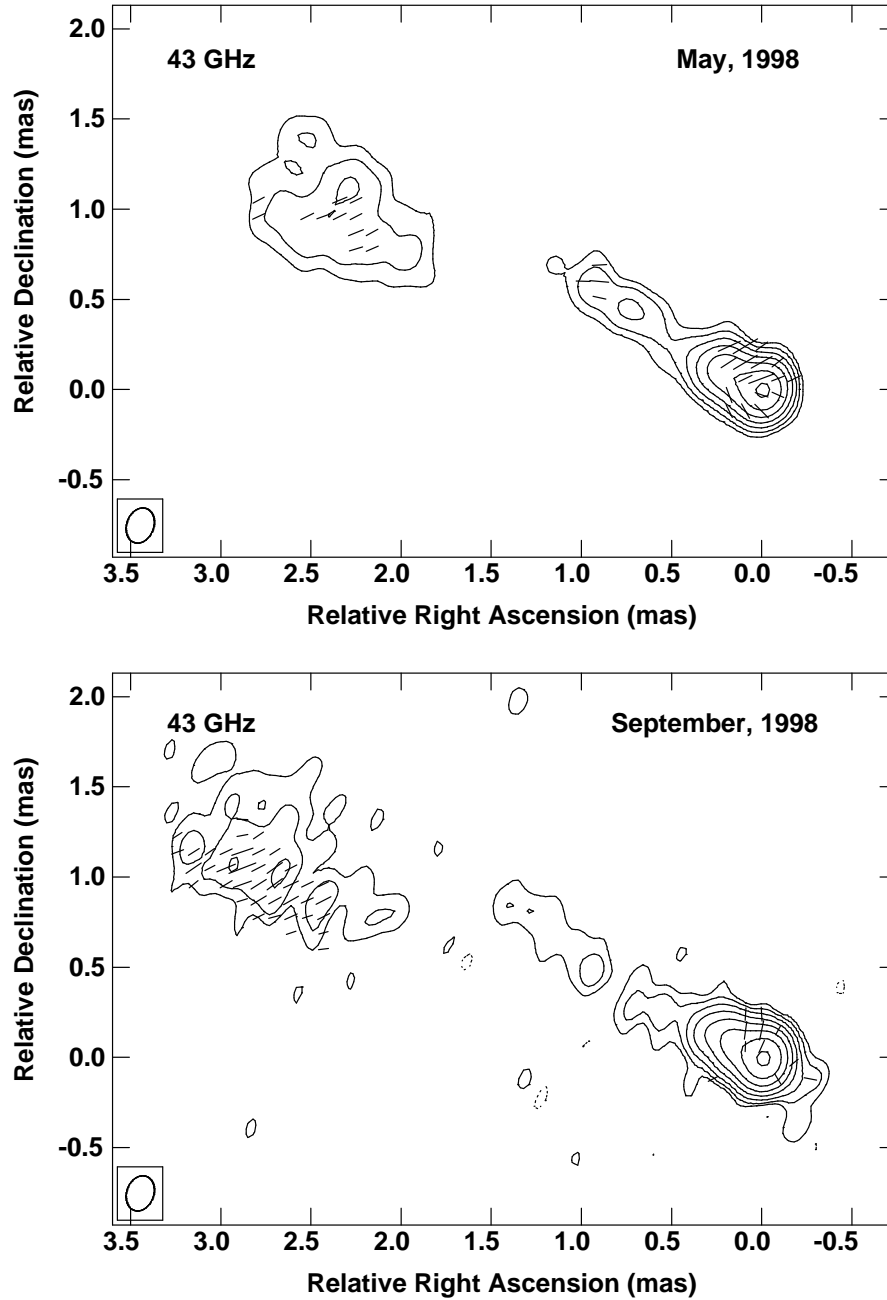
Figure 4.5: Total intensity maps of 3C 111 at 43 GHz with χ vectors superimposed. The surface brightness peaks in Jy beam^{-1} and the bottom contours in % of the peak are (*Top*) 0.51, ± 1.4 and (*Bottom*) 0.82, ± 0.7; successive contours increase by a factor of two. Restoring beam is 0.20×0.15 mas in $PA = -20°$.

Table 4.3: Results of the VLBP observations of 3C 111.

Program	Freq	Epoch	I_{peak}	I_{rms}	P_{peak}	P_{rms}
	GHz	year	Jy beam^{-1}	mJy beam^{-1}	mJy beam^{-1}	μJy beam^{-1}
BP031-B	8	1996.72	2.3	2.8	4.6	240
BA027-A	8	1997.45	2.5	1.5	7.5	220
BP031-B	43	1996.72	1.8	2.6	44.7	2100
BA027-A	43	1997.45	0.8	1.4	13.3	340
BA027-B	43	1997.78	1.1	0.9	7.0	320
BA027-C	43	1998.37	0.5	1.4	12.0	348
BA027-D	43	1998.69	0.9	1.6	7.0	330

Col. 1 : Program code; Col. 2 : Frequency of observation; Col. 3 : Epoch of observation; Col. 4 : Total intensity peak surface brightness; Col. 5 : rms in I map in mJy beam^{-1} – this was calculated from large empty regions in the I map covering typically >250 beam areas; Col. 6 : Polarized intensity peak surface brightness; Col. 7 : rms in P map in μJy beam^{-1} – this was calculated from large empty regions in the P map covering typically >250 beam areas.
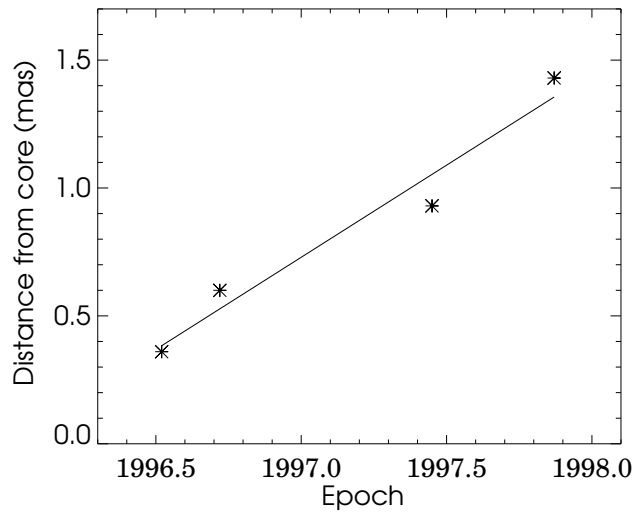
Figure 4.6: The separation of a knot in the jet from the core of 3C 111 at four different epochs. The slope of the line is $\sim$ 1.3 mas per year which implies a mildly superluminal motion of 1.6c for the knot.

Chapter 5

The pc-scale magnetic field geometry of BL Lacs and quasars

5.1   Introduction

In this chapter, we turn our attention to the pc-scale magnetic fields in the relatively new subclass of BL Lac objects, the HBLs. As a class, the BL Lac objects are characterized by a predominantly non-thermal, highly polarized continuum that is variable in total intensity and polarization at all observed wavelengths, and have weak or no optical line emission. Radio-loud quasars also exhibit these characteristics except for the presence of prominent broad and narrow emission lines in these objects. As discussed in Chapter 1, these extreme phenomena are understood as a consequence of relativistic beaming in their nuclei. According to the radio-loud Unified Scheme, the BL Lac objects and radio-loud quasars are the likely beamed counterparts of FRI and FRII radio galaxies, respectively.

Most of the BL Lac objects uptil recently had been discovered with radio searches (e.g., Ledden & Odell, 1985; Burbidge & Hewitt, 1987). However, space-based X-ray surveys have been highly efficient in discovering new BL Lac objects (e.g., Giommi *et al.*, 1989; Stocke *et al.*, 1989). It is disputed if one kind are commoner than the other (for e.g., Giommi & Padovani, 1994; Padovani & Giommi, 1995b) but probably more data are required to settle the dispute. An understanding of the properties of the poorly studied XBLs and relationship to RBLs is clearly desirable.

5.1.1   The two subclasses of BL Lacs : RBLs and XBLs

RBLs and XBLs show systematic differences. The RBLs are typically more core-dominated on arcsec-scales (Perlman & Stocke, 1993; Kollgaard *et al.*, 1996), they show higher average optical polarization and greater variability (Schwartz *et al.*, 1989; Jannuzi *et al.*, 1994) than XBLs. They also have more powerful radio lobes than the XBLs (Kollgaard *et al.*, 1992; Laurent-Muehleisen *et al.*, 1993).

Based on the nuclear trends, it appears that the RBLs are more "extreme" than XBLs. In the light of the fact that orientation is known to play a major role in the observed properties of AGNs, it has been suggested that RBLs are oriented at closer angles to the line of sight than XBLs, also referred to as the "different angle scenario" (Stocke *et al.*, 1985). This scenario is supported by population studies (e.g., Padovani & Urry, 1990; Urry *et al.*, 1991) and has been explained in the framework of an 'accelerating jet model' (Ghisellini & Maraschi, 1989), wherein the X-rays are radiated in the slower part of the jet and are therefore less beamed than the radio photons coming from the faster portion of the jet. The different-angle scenario predicts that XBLs should be more numerous than RBLs in a statistically complete sample.

The Spectral Energy Distributions of RBLs and XBLs

The fly in the ointment however is the systematic trend discovered in the spectral energy distributions (SEDs) of RBLs and XBLs (see Chapter 1). Based on the nuclear trends discussed above, the SEDs of XBLs were expected to be different from RBLs due to their inferred less extreme orientations, but the SEDs showed that the synchrotron emission in RBLs typically peaks in the near infrared (*i.e.*, they are low–energy peaked BL Lacs or LBLs), whereas the XBL synchrotron emission typically peaks in the soft X-ray regime (the high–energy peaked BL Lacs or HBLs). Padovani & Giommi (1995a) have suggested a division according to whether α_{rx} (between 5 GHz and 1 keV) is greater (LBL) than or less (HBL) than 0.75. Georganopoulos (2000) have used angle dependence to explain the different SEDs. Most, though not all, RBLs are LBLs and most, though not all, XBLs are HBLs. We will adopt this latter terminology, since it is more physical.

The discovery of the systematic differences in the SED peaks of the HBLs and LBLs gave rise to the alternative "different energy cutoff Scenario", wherein the X-ray emitting regions of HBLs have higher electron Lorentz factors or magnetic fields than LBLs (Sambruna *et al.*, 1996). This scenario can be explained with a luminosity sequence (Fossati *et al.*, 1997, 1998), in which HBLs outnumber LBLs.

The HBLs have less luminous nuclei and jets with lower kinetic powers (Celotti *et al.*, 1997) and it has been suggested that they dissipate most of their energy in synchrotron

radiation from highly relativistic electrons. The LBLs, which have systematically higher bolometric luminosities, are probably redder because the highest energy electrons cool quickly by Compton-scattering ambient UV and X-ray photons to gamma-ray energies, which can dominate the bolometric output (Ghisellini *et al.*, 1998).

Wang *et al.* (2002) find that HBLs have characteristically lower accretion rates ($\dot{m}$) than LBLs. $\dot{m}$ decreases along the sequence FSRQs (flat spectrum radio quasars) to LBLs to HBLs (Wang *et al.*, 2003). The low-power HBLs and some LBLs may have pure optically thin ADAFs (Wang *et al.*, 2003).

Despite the strong nuclear trends between LBLs and HBLs, Urry *et al.* (2000) find no differences between the host galaxies of LBLs and HBLs, either in luminosity or size. Further, stellar velocity dispersion studies (e.g., Woo *et al.*, 2004) have shown that there are no differences between the black hole masses of the two BL Lac subclasses. This strongly suggests that nuclear properties, which can strongly influence jet formation and propagation, do not have a dramatic effect on large-scale host galaxy properties (or vice versa).

5.1.2 Pc-scale B-field geometry and SEDs of LBLs, HBLs and quasars

As discussed in Chapters 2 and 3, polarization sensitive VLBI observations have shown systematic differences between BL Lacs, which are mostly LBLs, and core-dominated quasars (e.g., Gabuzda *et al.*, 1992; Cawthorne *et al.*, 1993; Gabuzda *et al.*, 2000). LBLs have moderately polarized cores ($m_c \sim 2 - 5\%$) with predominantly transverse B-fields in their jets, while quasars have weakly polarized cores ($m_c < 2\%$) and predominantly longitudinal B-fields.

The peaks of the SEDs of core-dominated quasars (CDQs), LBLs and HBLs form a sequence of increasing frequency. The CDQs are thought to be beamed FRII radio galaxies, while the BL Lac objects are thought to be beamed FRI radio galaxies. VLBI observations of RBLs (e.g., Gabuzda *et al.*, 1992) have found them to be typically compact, with a core and a small number of discrete jet components. Several have measured superluminal speeds, typically in the range of 2–4c (Mutel *et al.*, 1990). However only a few radio bright XBLs had been observed with VLBI (e.g., Kollgaard *et al.*, 1996).

We wished to explore the parsec-scale radio structures and magnetic field geometries in the HBLs, to see if this geometry reflected the sequence in the SED peaks. Our goal was to determine if LBLs and HBLs shared the same pc-scale polarization properties. If HBLs were instrinsically weaker than LBLs, this could imply weaker shocks and lower

fractional polarizations in HBLs, although if HBLs are oriented farther away from the line of sight, it is possible that the field orientation would systematically differ. If the latter is true, the jet components in HBLs may exhibit lower apparent speeds. However, a multi-velocity jet (e.g., Komissarov, 1990) will complicate the issue. We therefore undertook pc-scale polarimetric imaging of X-ray selected BL Lacs from the *HEAO-1* survey, the results of which are presented in this chapter.

We further investigate possible connections between the observed parsec-scale magnetic field structures and circular polarization measurements of AGNs in the literature on various spatial scales.

5.2   VLBP observations and data reduction

Polarization observations were made at 5 GHz with a global VLBI array in February 1993, and later in July 1995 and June 1998 using the Very Large Baseline Array. The sample consisted of 21 northern hemisphere BL Lacs detected in hard X-rays by the *HEAO-1* survey (Wood *et al.*, 1984) and six BL Lacs from the *ROSAT*-Green Bank (RGB) sample (Laurent-Muehleisen *et al.*, 1997). The RGB sample of BL Lacs has been generated from a cross-correlation of the *ROSAT* All-Sky Survey (RASS) and a reanalysis of the 1987 Green Bank (GB) 6 cm radio survey (Gregory *et al.*, 1996). The results for four XBLs from this sample have been presented in Kollgaard *et al.* (1996). The calibration, fringe fitting and imaging were done using the AIPS software with the polarization calibration following standard methods (Cotton, 1989). Los Alamos (LA) was used as the reference antenna for this experiment. The February 1993 observations (GK007) included the phased VLA. The primary flux and polarization calibrators for the VLA data were 3C 286 and 3C 48. The VLBI D-term calibrator was OQ 208, which was assumed to be unpolarized. The source whose VLA core and VLBI polarizations were compared to do the EVPA calibration was OJ 287, for which about 80% of the VLA polarized flux was on VLBI scales. Table 5.2 describes the details of the observations while table 5.2 lists the sample BL Lac objects.

5.3   Results and comparison with LBLs

The total intensity images of the *HEAO-1* BL Lacs with polarization electric vectors superimposed, are presented in Figures 5.1 to 5.12. The rms noise in the I maps is typically ~ 100 μJy beam^{-1}. Tables 5.2 and 5.3 list many observed and inferred quantities of the BL Lac objects. In Table 5.3, when the polarization electric vectors

are aligned to within 30° of the VLBI jet, they are denoted by ∥ and when they are close to 90° with respect to the local jet direction, they are denoted by ⊥.

5.3.1 Total intensity parsec-scale radio images

The VLBI images of the *HEAO-1* BL Lacs show a compact "core-jet" morphology. There are no differences in the VLBI structure of these BL Lacs and the RBLs belonging primarily to the 1-Jy sample of (Kuehr & Schmidt, 1990), observed by Gabuzda *et al.* (2000) and others.

5.3.2 Parsec-scale magnetic-field structure

Some of the HBLs that we have observed show evidence for a "spine-sheath" magnetic-field structure, with the inner region of the jet having transverse B-fields and the edges having longitudinal magnetic-field. This type of B-field structure could be a result of interaction of the jet with the surrounding medium. Particularly good examples are the HBLs 1230+253 (Figure 5.9) and 1727+502 (Figure 5.11, bottom image). This may point in the direction of a helical magnetic field threading the jets of these objects, which could have implications for mechanisms for the production of circular polarization in them.

Polarization in the radio cores

The fractional polarization in the core, m_c, is $\leq 1.5\%$ in a majority of the HBLs with only two HBLs having $m_c > 4\%$. On the other hand, the LBLs have $m_c \geq 3\%$ with one LBL 0929+502 having as much as 15% core polarization. This trend of higher fractional core polarization in LBLs compared to HBLs, is similar to what is observed in kpc-scale cores (e.g., Kollgaard *et al.*, 1996).

The B-field orientation in the parsec-scale cores of HBLs and LBLs, relative to the inner VLBI jet direction, does not show any obvious systematic difference. In both cases, there is a clear tendency for the core polarization electric vectors to lie either parallel or perpendicular to the jet direction (e.g., Gabuzda *et al.*, 2000). The physical origin of this bimodal behaviour is not entirely clear, though it may be due at least in part to optical depth effects (Gabuzda, 2003). We note that though the HBLs and LBLs considered here share the lower end of the redshift range, LBLs tend to be at relatively higher redshifts (see Laurent-Muehleisen *et al.*, 1999). This could result in the observations probing different spatial scales in the two BL Lac sub-classes.

Polarization in the radio jets

The fractional polarization in the inner jets (m_j, typically < 5 mas from the core) range from 1.7% in the HBL 1727+502 to 56.5% in the HBL Mrk 421. The Kolmogorov-Smirnov test on the distribution of m_j for the HBL and LBL subclasses indicates only a $< 0.01\%$ probability that the two are from the same parent population.

The jet B-field orientations of HBLs and LBLs however, does display systematic differences, as can be seen in Table 5.4. Among both types of BL Lacs there are sources in which the observed jet polarization angles lie parallel or perpendicular to the local jet direction. However, the polarization angles are perpendicular to the jet in the majority of HBLs, while they are aligned with the jet in the majority of LBLs. Assuming that the emission region is optically thin, which is expected in the jet, we infer that the magnetic-field is perpendicular to the observed polarization angle. Thus, the LBLs show predominantly *transverse* jet magnetic fields, while the HBLs show predominantly *longitudinal* jet fields. We note that from the integrated RM study, Simard-Normandin *et al.* (1981) conclude that the primary contributor to Faraday rotation is our Galaxy itself. The $\Delta\chi$ is expected to be $\sim 10-15°$, which will not alter drastically our inferences on the magnetic-field configurations in BL Lac objects.

Since the jets of CDQs exhibit predominantly *longitudinal* magnetic fields, we find that the systematics of the jet B field geometry in CDQs, LBLs and HBLs, which goes from longitudinal to transverse to longitudinal, does not reflect the sequence in the SED peaks.

We note that our results agree with the picture of LBLs being in the 'active' state (e.g., Lister, 2001) where new components/shocks are emerging from the core, increasing the polarization and resulting in transverse B-fields close to the core. HBLs on the other hand, are in a 'quiescent' phase, with lower polarization and longitudinal B fields. This picture is similar to that suggested for LPRQs and HPQs by Lister (2001). It is also possible that the jets in HBLs are lower power and slower than the jets in LBLs. This could result in weaker shocks in the HBL jets resulting in a primarily longitudinal B-field.

5.4 Notes on individual BL Lacs

5.4.1 0829+046

0829+046 or OJ 049 is a γ-ray loud blazar (> 100 MeV) (Dondi & Ghisellini, 1995). Using rapid optical variability observations, Xie *et al.* (2002) have estimated the mass

of the central black hole in this BL Lac to be $\sim 10^{7.4}$M$\odot$. This BL Lac was observed in all the three epochs of VLBP. It shows a rich polarization structure which does not seem to vary much in B-field geometry over a period of 5 years.

5.4.2   1011+496

This object is a candidate TeV BL Lac (Costamante & Ghisellini, 2002). Using the fundamental plane for ellipticals, Wu *et al.* (2002) have estimated the mass of the central black hole in this BL Lac to be $\sim 10^{8.3}$M$\odot$. At ~ 6 mas (along the X-axis) from the core, the χ vectors are aligned with the jet direction implying a transverse B-field in the outer jet, assuming optically thin emission.

5.4.3   1101+384

1104+382 or Mrk 421 is a well-known high-energy-peaked BL Lac. It was the first TeV γ-ray emitting blazar to be detected (Punch *et al.*, 1992). In the 0.5–10 keV band, this source is variable on time-scales ranging from 14 hours to several days and occasionally exhibits large (factor 10) X-ray outbursts which are characterized by a marked flattening of the spectrum (George *et al.*, 1988). The 1995.53 observations (see Figure 5.6) reveal a bend in the jet at ~ 14 mas (along the X-axis). Interestingly, a longitudinal B-field 'sheath' is seen on both sides of the jet, all along the bend.

5.4.4   1133+704

1133+704 or Mrk 180 is high-energy-peaked BL Lac. Mrk 180 is a giant elliptical galaxy; spectroscopy shows absorption lines at a redshift of z = 0.046 (Ulrich, 1978). X-ray emission was detected by the Einstien and *HEAO-1* observatories (Hutter & Mufson, 1980). It is a candidate TeV BL Lac (Costamante & Ghisellini, 2002). Using the fundamental plane for ellipticals, Wu *et al.* (2002) have estimated the mass of the central black hole in this BL Lac to be $\sim 10^{8.5}$M$\odot$.

5.4.5   1727+502

This object is a candidate TeV BL Lac (Costamante & Ghisellini, 2002). Using the fundamental plane for ellipticals, Wu *et al.* (2002) have estimated the mass of the central black hole in this BL Lac to be $\sim 10^{7.7}$M$\odot$. Our VLBP observations show that this

BL Lac is a good example for the 'spine-shear' jet structure, with a $B_\perp - B_\parallel$ field geometry in the inner jet, close to the core.

5.4.6   Jets in 1147+245, 1230+253, 1745+398

Our VLBP observations show that the LBL 1147+245 shows χ vectors which are aligned with the jet throughout its length, implying a transverse B-field throughout, in the optically thin jet. A longitudinal B-field 'sheath' is seen on the edge of the jet in 1230+253, where the jet seems to be bending. Also, a longitudinal B-field 'sheath' is present on the east side of the jet of 1745+398, at around 6 mas (along the Y-axis) from the core, where the VLBI jet bends towards the south-east.

5.5   Trends in circular polarization

Circular polarization is only a tiny fraction ($< 0.5\%$) of the integrated synchrotron emission from AGN jets (Weiler & de Pater, 1983, and references therein). Circular polarization in AGN jets may be produced either as a direct (intrinsic) component of synchrotron radiation or through the Faraday conversion process which converts linear polarization to circular polarization.

It has been argued that the sequence in the SED peaks of CDQs, LBLs and HBLs might reflect a sequence in magnetic field strength/Lorentz factors (Sambruna, 1994). Since the detectability of circular polarization may also be linked to the magnetic field strength and/or geometry and the low-end of the Lorentz factor distrubution (if the circular polarization is produced by Faraday conversion of linear polarization), we looked for evidence for a connection between the parsec-scale B-field geometry and previous detections of circular polarization.

To this end, we compiled all previous circular polarization measurements we could find in the literature (see Table 5.5). We found such measurements for a total of 73 quasars and 21 BL Lacs, in addition to 52 galaxies, made on various spatial scales. Of the 21 BL Lacs, 19 are LBLs and only 2 are HBLs. We divided the measurements into three groups on the basis of spatial scale: parsec-scale, kiloparsec-scale ATCA, and kiloparsec-scale single-dish (Table 5.5).

5.5.1   Results

The statistics are insufficient to discern differences between the circular-polarization detection rates for LBLs and HBLs, since only 2 HBLs were observed in the circular polarization experiments. There is some evidence from the VLBI measurements (Homan *et al.*, 2001) and single-dish measurements (Weiler & de Pater, 1983; Komesaroff *et al.*, 1984) that the circular-polarization detection rate may be higher for quasars than for BL Lacs. Could this be a consequence of the fact that most of the quasars observed have brighter compact nuclei than the BL Lacs ? This question can only be answered by having a greater number of sensitive circular polarization observations of the BL Lac objects.

Figure 5.13 shows the distribution of the total flux density on the *relevant* spatial scales for all the circular polarization observations. The observations are again divided into groups as in Table 5.5 (see above). In the case of the single-dish measurements of circular polarization (left-most panels in each row), the distributions are of the total flux density of the *compact* component, *i.e.,* from a VLBI measurement, as given in Weiler and de Pater, 1983. In the case of the ATCA and VLBI measurements (middle and right-most panels), the distributions are of the total intensity measured by ATCA and VLBI, respectively. It is especially clear in the VLBI circular polarization measurements (last column of histograms) that nearly all of the relatively few BL Lac objects for which circular polarization measurements are available fall at the low end of the flux density range for the observed quasars.

However, the situation is not clear, since (i) there is no obvious difference in the detection rates for CDQs and BL Lacs in the ATCA measurements (Rayner *et al.*, 2000), and (ii) the quasars in which circular polarization is detected in the ATCA and single-dish observations have flux densities that fall in the same range as those of BL Lac objects. Further, in the single-dish observations of radio galaxies, circular polarization is detected in compact components with much lower flux densities than the weakest components in BL Lacs in which circular polarization is detected.

If systematic differences in the circular-polarization detection rates (or other properties of the circular polarization) observed in CDQs, LBLs and HBLs could reliably be shown to be present or absent, this could lead to interesting clues to the origin of the circular polarization. Circular polarization observations of well-selected samples, for e.g., comparable HBLs and LBLs, are needed to search for relationships between magnetic-field geometry and other properties of the compact radio emission and the circular-polarization detection rate. Well-selected samples might necessitate observations of relatively faint sources, but this is not unrealistic as Figure 5.13 shows. If established, such relationships could potentially provide useful information about the

Lorentz factors and magnetic-field strengths in the jets of different subclasses of BL Lacs and quasars.

5.6 Conclusions

1. VLBP observations of LBLs and HBLs reveal differences in the core fractional polarizations, similar to the trend observed on arcsec-scales – the LBLs have higher core fractional polarizations compared to the HBLs.

2. The jet fractional polarizations do not differ systematically in LBLs and HBLs.

3. The ordered component of the B-fields in the parsec-scale jets of HBLs tend to be parallel to the local jet direction. This contrasts with the tendency for the B-fields in the parsec-scale jets of LBLs which are perpendicular to the local jet direction.

4. The systematics of the magnetic field geometry thus do not reflect the sequence in the SED peaks of CDQs, LBLs and HBLs.

5. The VLBI core polarization angles do not show any systematic differences between HBLs and LBLs. In both cases, there is a clear tendency for the core polarization electric vectors to lie either parallel or perpendicular to the jet direction (e.g., Gabuzda *et al.*, 2000).

6. Some of the observed HBLs show evidence for a "spine-sheath" magnetic-field structure, with transverse B-field in the inner region of the jet and longitudinal B-field at the edges. This may point in the direction of a helical magnetic field threading the jets of these objects, in turn having implications for mechanisms for the production of circular polarization in them.

7. Currently available circular polarization measurements in the literature suggest that quasars may be more likely to show detectable circular polarization than BL Lacs. However, the situation is not clear, since the largest difference in detection rates are found in the VLBI measurements, and the low detection rate for the BL Lac objects in this case may be due to the fact that the observed quasars have on average brighter VLBI cores than the BL Lacs.

8. Given the recent advances in circular polarization measurement techniques on both arcsecond (ATCA) and milliarcsecond (VLBI) scales, which have made detections possible in at least a minority of BL Lacs (and quasars) with relatively faint compact cores, it is beginning to become feasible to obtain circular polarization

measurements of well-defined samples on various scales. This would then enable *rigorous* tests of the predictions of various scenarios for the physical differences between different types of object.

Table 5.1: Details of the VLBP observing program of *HEAO-1* BL Lacs.

Program code	Observing date	Freq MHz	IFs	BW/IF MHz	Antennas	D-term calibrator	EVPA calibrator
GK007	23 Feb 1993	4979.99	2	8	BR, EB, GB, HN, MC, NL, OV, WB, Y	OQ 208	OJ 287
BK033	13 July 1995	4987.49	2	8	VLBA	3C 84	OJ 287
BK055	28 June 1998	4991.46	2	8	VLBA	0749+540	OJ 287

Col. 1 : The name of the program; Col. 2 : The date of observations; Col. 3 : Observing frequency; Col. 4 : Number of intermediate frequencies (IFs); Col. 5 : Bandwidth in MHz per IF; Col. 6 : The codes of antennas which participated in the observations – BR : Brewster (VLBA), EB : Effelsberg, GB : Green Bank, HN : Hancock (VLBA), MC : Medicina, NL : North Liberty (VLBA), OV : Owen's valley (VLBA), WB : Westerbork, Y : Phased VLA, VLBA includes all 10 antennas which are listed in the Observations section of Chapter 3; Col. 7 : D-term calibrator; Col. 8 : EVPA calibrator.

Table 5.2: Properties of the sample BL Lacs.

IAU name	Other name	Class	z	Scale mas/pc	Epoch of Observation
0414+009	...	HBL	0.2870	2.677	1, 2
0656+426	...	HBL$^\bullet$	0.0590	0.775	3
0706+592	1H0658+6	HBL$^\bullet$	0.1250	1.477	1, 2
0749+540	...	RGB	$\geq$0.20	2.110	3
0829+046	OJ 049	LBL$^\bullet$	0.1800	1.956	1, 2, 3
0929+502	...	LBL$^\bullet$	N.A.	...	3
1011+496	...	HBL$^\bullet$	0.2*	2.11	3
1101+384	Mrk 421	HBL	0.0300	0.414	2, 3
1133+704	Mrk 180	HBL	0.0450	0.605	3
1147+245	...	LBL	$\geq$0.20	2.110	2
1215+303	...	HBL$^\bullet$	0.2370	2.370	3
1219+301	...	LBL	0.00208	0.030	1
1230+253	...	HBL$^\bullet$	N.A.	...	3
1235+632	...	HBL	0.2970	2.732	1
1555+111	...	LBL$^\bullet$	0.3600	3.045	3
1727+502	I Zw 187	HBL	0.0554	0.732	2, 3
1743+195	...	HBL$^\bullet$	0.0840	1.059	3
1745+398	...	HBL$^\bullet$	0.2670	2.560	3
2201+044	...	LBL	0.0270	0.374	3

Col. 1 : IAU names of the BL Lac objects; Col. 2 : Other common names; Col. 3 : Classification of BL Lacs based on SED peaks and/or f_x/f_r ratio, $^\bullet$ denotes those BL Lacs which also belong to the RGB sample (Laurent-Muehleisen *et al.*, 1999); Col. 4 : Redshift taken from the NED except * which is from Laurent-Muehleisen *et al.* (1999), N.A. = Not available in NED or Laurent-Muehleisen *et al.* (1999); Col. 5 : Projected linear scale of source corresponding to the angular scale of 1 mas; Col. 6 : Epoch of observation – Epoch 1 : 1993.15, Epoch 2 : 1995.53, Epoch 3 : 1998.49.

Table 5.3: Results from the VLBP observations of *HEAO-1* BL Lacs.

IAU name	Epoch of Observation	I_{peak} mJy beam^{-1}	P_{peak} mJy beam^{-1}	m_c %	m_j %	χ_c	χ_j
0414+009	1993.15	27.2	...	...	...	...	...
	1995.53	38.6	...	...	...	...	...
0656+426	1998.49	136.6	0.7	...	2.3	...	$\perp$?
0706+592	1993.15	23.9	...	...	...	...	...
	1995.53	27.5	...	...	...	...	...
0749+540	1998.49	163.3	147.7	9.1	...	?	...
0829+046	1993.15	469.0	16.0	3.4	9.5	$\parallel$	$\perp$
	1995.53	699.3	20.4	2.9	5.7	$\parallel$	$\perp$
	1998.49	441.2	17.2	3.9	7.8	$\parallel$	$\perp$
0929+502	1998.49	433.3	64.0	14.9	...	$\perp$	...
1011+496	1998.49	93.8	4.0	4.3	6.2	$\perp$	$\perp$
1101+384	1995.53	326.0	4.0	1.2	56.5	M	$\parallel$
	1998.49	356.5	5.8	1.6	26.4	$\parallel$	?
1133+704	1998.49	98.0	3.0	1.4	34.9	$\perp$	$\perp$
1147+245	1995.53	479.4	16.6	3.5	3.5	$\perp$	$\parallel$
1215+303	1998.49	231.1	6.7	...	6.5	...	$\perp$
1219+301	1993.15	33.4	...	...	...	...	...
1230+253	1998.49	183.7	6.5	3.6	10.2	$\parallel$	$\parallel$
1235+632	1993.15	13.8	...	...	...	...	...
1555+111	1998.49	189.7	5.2	2.7	...	$\parallel$	?
1727+502	1995.53	77.2	1.5	1.9	5.5	...	$\perp$
	1998.49	64.2	1.5	...	1.7	...	$\parallel$?
1743+195	1998.49	84.3	1.1	1.3	10.9	$\perp$?	$\perp$?
1745+398	1998.49	49.3	0.8	1.6	...	M	...
2201+044	1998.49	162.3	0.6	...	1.8	...	$\parallel$

Col. 1 : IAU names of the BL Lac objects; Col. 2 : Epoch of observation; Col. 3 : Total intensity peak surface brightness; Col. 4 : Polarized intensity peak surface brightness; Col. 5 : Fractional polarization of the core component; Col. 6 : Fractional polarization of the inner jet; Col. 7 : Observed polarization electric (χ) vectors in the VLBI cores; Col. 8 : Observed polarization electric (χ) vectors in the inner VLBI jets. 'M' stands for 'misaligned' *i.e.*, in between $\perp$ and $\parallel$, '?' means that the local jet direction is not clear due to lack of resolution.
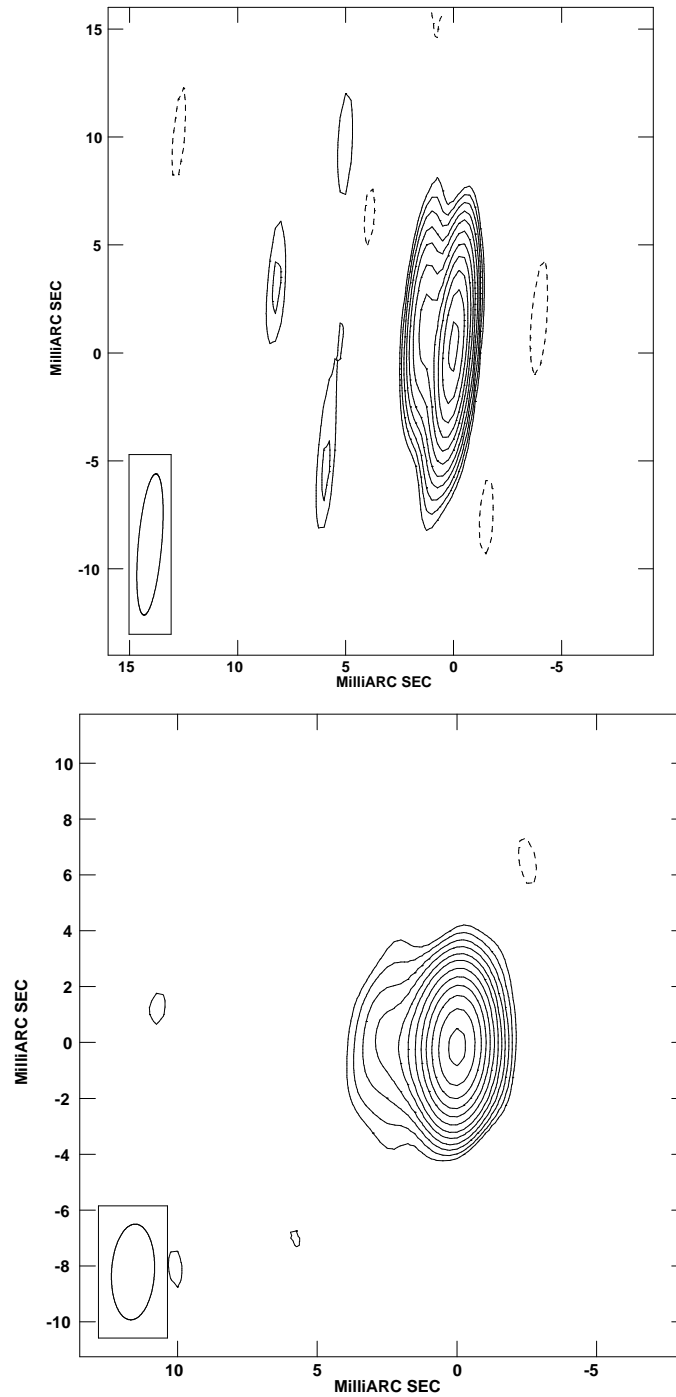
Figure 5.1: *Top.* Total intensity image of the HBL 0414+009 observed in 1993.15. No polarization was detected in this source. Contours are –2.8, 2.8, 5.6, 11.2, 22.5, 45 and 90% of the peak surface brightness of 27.2 mJy beam^{-1}. *Bottom.* Total intensity image of 0414+009 observed in 1995.53. No polarization was detected. Contours are –2, 2, 2.8, 4, 5.6, 8, 11, 16, 23, 32, 45, 64, 90% of the peak surface brightness of 38.6 mJy beam^{-1}.
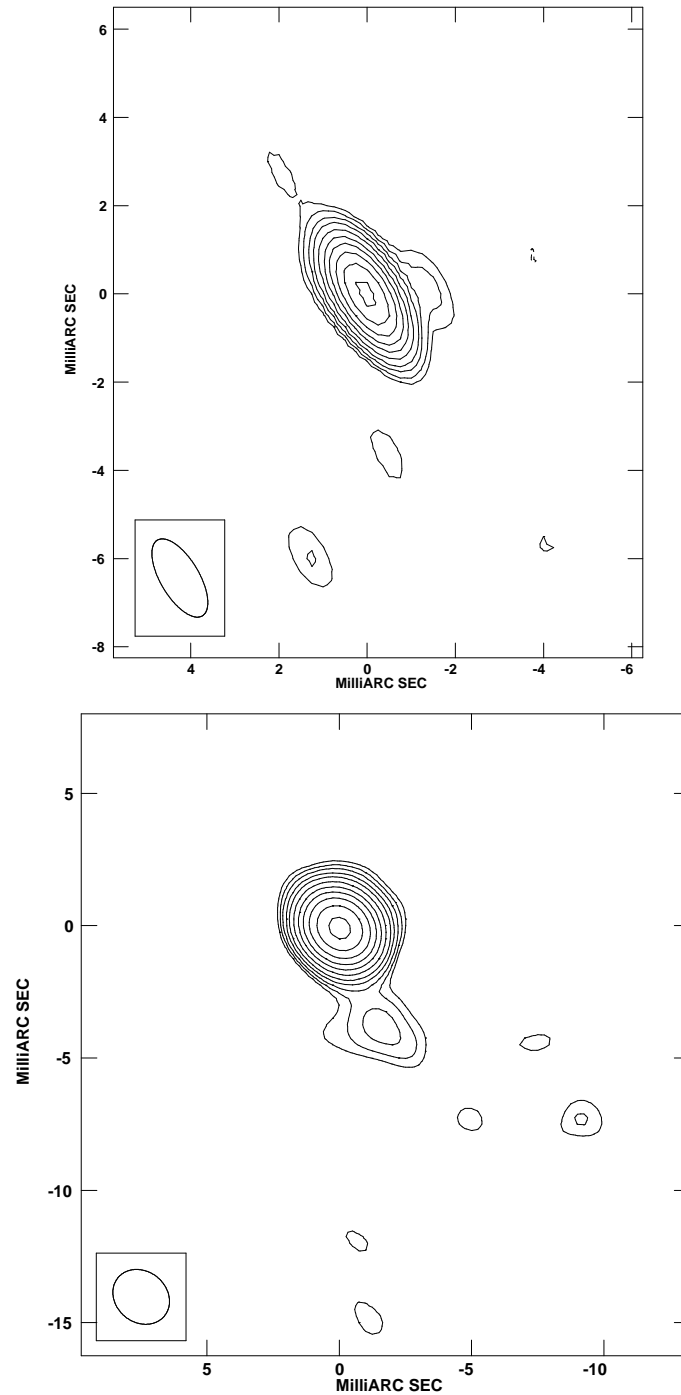
Figure 5.2: *Top.* Total intensity image of the HBL 0706+592 observed in 1993.15. No polarization was detected in this source. Contours are –4, 4, 5.6, 8, 11, 16, 23, 32, 45, 64, 90% of the peak surface brightness of 23.9 mJy beam^{-1}. *Bottom.* Total intensity image of 0706+592 observed in 1995.53. No polarization was detected. Contours are –2.8, 2.8, 4, 5.6, 8, 11, 16, 23, 32, 45, 64, 90% of the peak surface brightness of 27.5 mJy beam^{-1}.
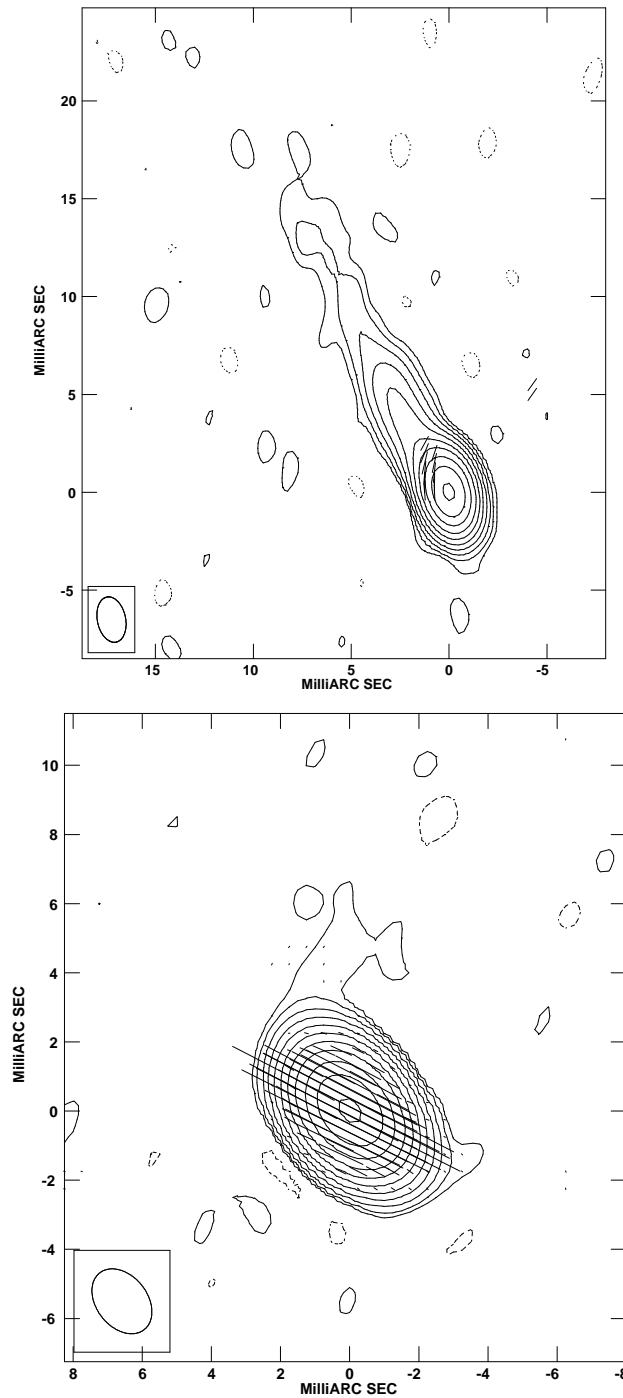
Figure 5.3: *Top.* Total intensity image of the HBL 0656+426 observed in epoch 1998.49 with χ vectors superimposed. Contours are –0.17, 0.17, 0.35, 0.70, 1.40, 2.80, 5.60, 11.20, 22.50, 45 and 90% of the peak surface brightness of 136.6 mJy beam^{-1}, χ vectors: 1 mas = 1 mJy beam^{-1}. *Bottom.* Total intensity image of 0749+540 observed in epoch 1998.49 with χ vectors superimposed. Contours are –0.09, 0.09 0.17, 0.35, 0.70, 1.40, 2.80, 5.60, 11.20, 22.50, 45 and 90% of the peak surface brightness of 163.3 mJy beam^{-1}, χ vectors: 1 mas = 20 mJy beam^{-1}.
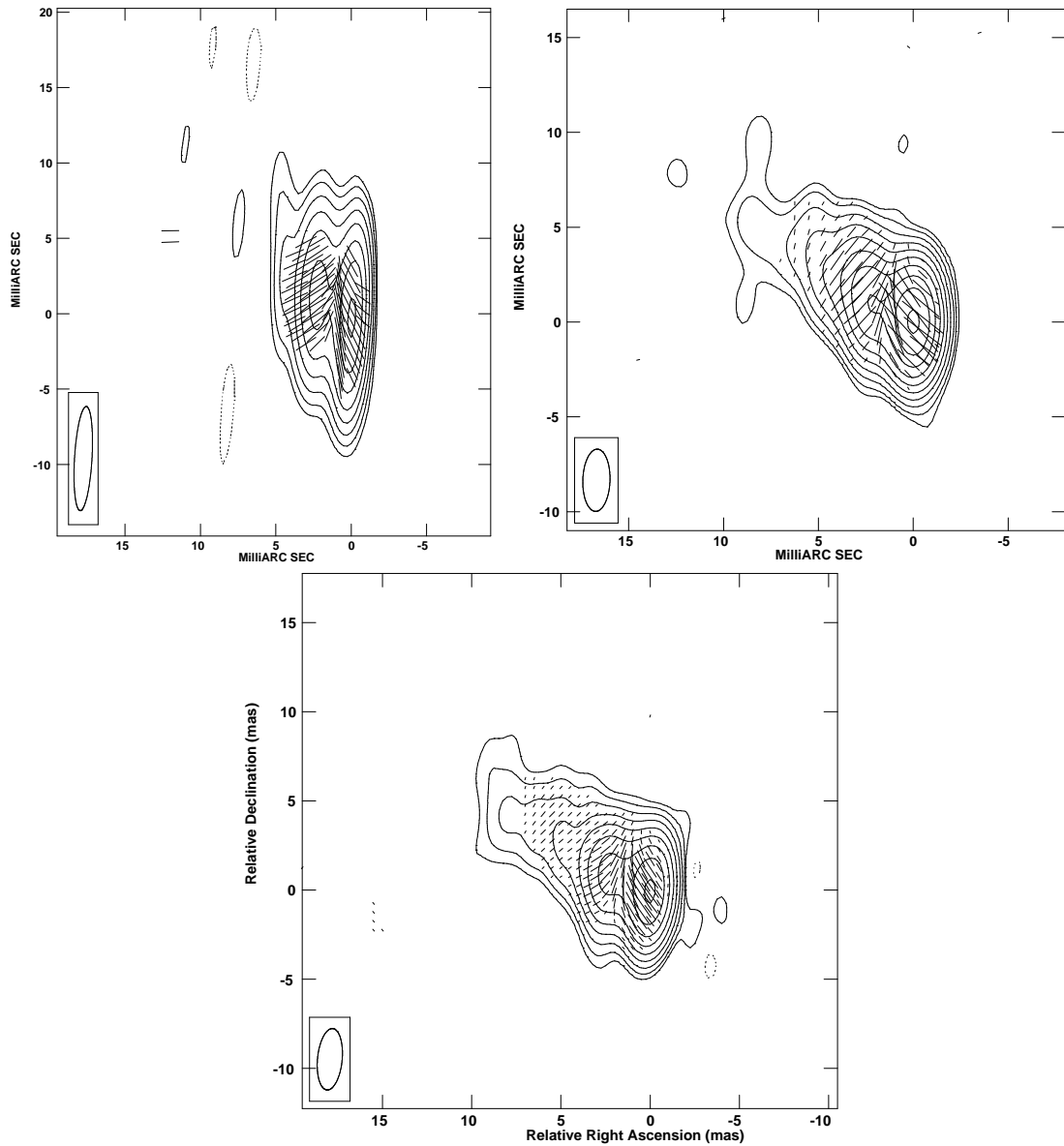
Figure 5.4: *Top left*. Total intensity image of the LBL 0829+046 observed in epoch 1993.15 with χ vectors superimposed. Contours are –0.70, 0.70, 1.40, 2.80, 5.60, 11.20, 22.50, 45 and 90 per cent of the peak brightness of 469 mJy beam^{-1}, χ vectors: 1 mas = 4 mJy beam^{-1}. *Top right*. Total intensity image of 0829+046 observed in epoch 1995.53 with χ vectors superimposed. Contours are –0.2, 0.2, 0.35, 0.70, 1.40, 2.80, 5.60, 11.20, 22.50, 45 and 90 per cent of the peak brightness of 699.3 mJy beam^{-1}, χ vectors: 1 mas = 5 mJy beam^{-1}. *Bottom*. Total intensity image of 0829+046 in epoch 1998.49 with χ vectors superimposed. Contours are –0.35, 0.35, 0.70, 1.40, 2.80, 5.60, 11.20, 22.50, 45 and 90% of the peak surface brightness of 441 mJy beam^{-1}, χ vectors: 1 mas = 8 mJy beam^{-1}.
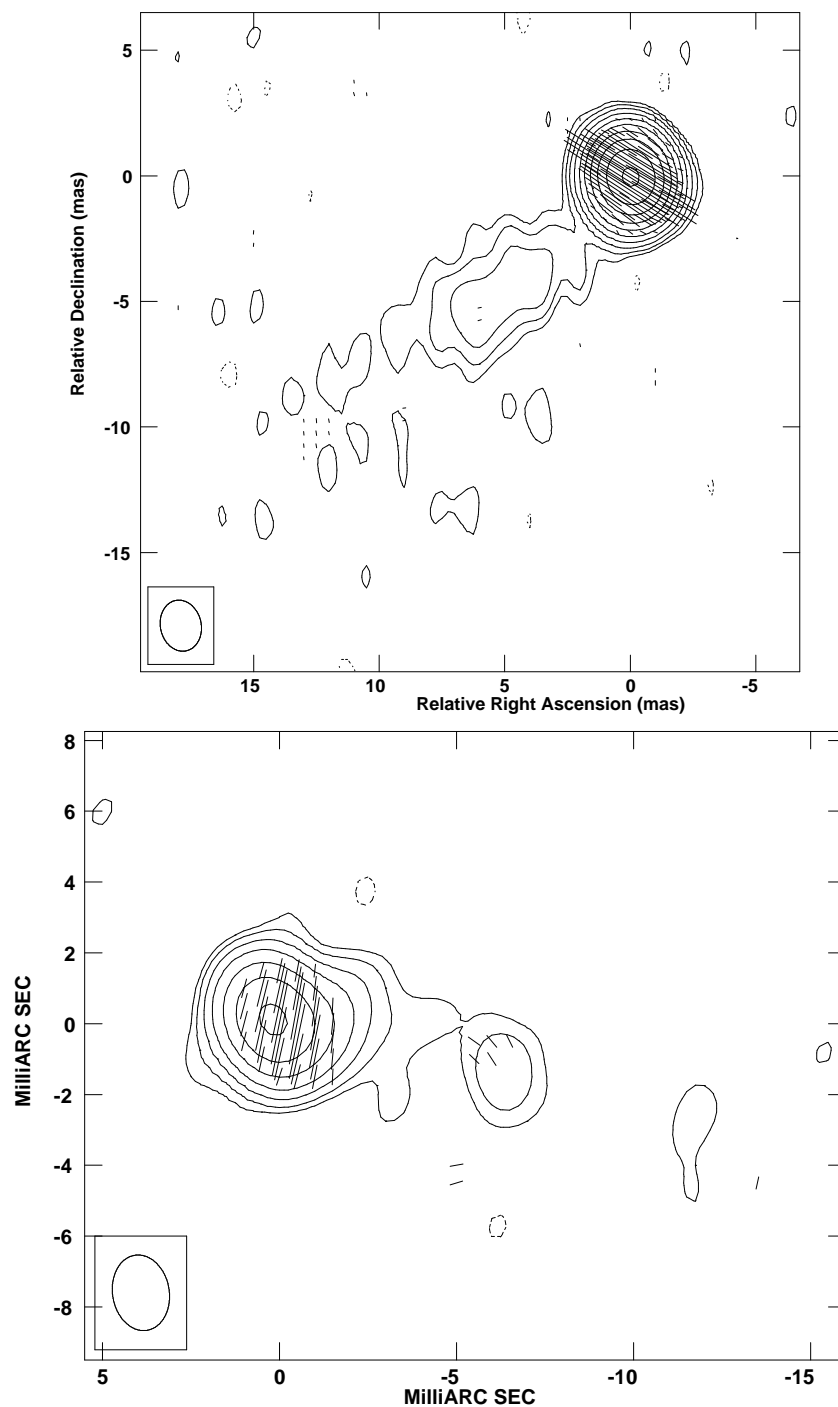
Figure 5.5: *Top.* Total intensity image of the LBL 0929+502 observed in 1998.49 with χ vectors superimposed. Contours are –0.17, 0.17, 0.35, 0.70, 1.40, 2.80, 5.60, 11.20, 22.50, 45 and 90% of the peak brightness of 433.3 mJy beam^{-1}, χ vectors: 1 mas = 10 mJy beam^{-1}. *Bottom.* Total intensity image of HBL 1011+496 observed in epoch 1998.49 with χ vectors superimposed. Contours are –1.4, 1.40, 2.80, 5.60, 11.20, 22.50, 45 and 90% of the peak brightness of 93.8 mJy beam^{-1}, χ vectors: 1 mas = 3 mJy beam^{-1}.
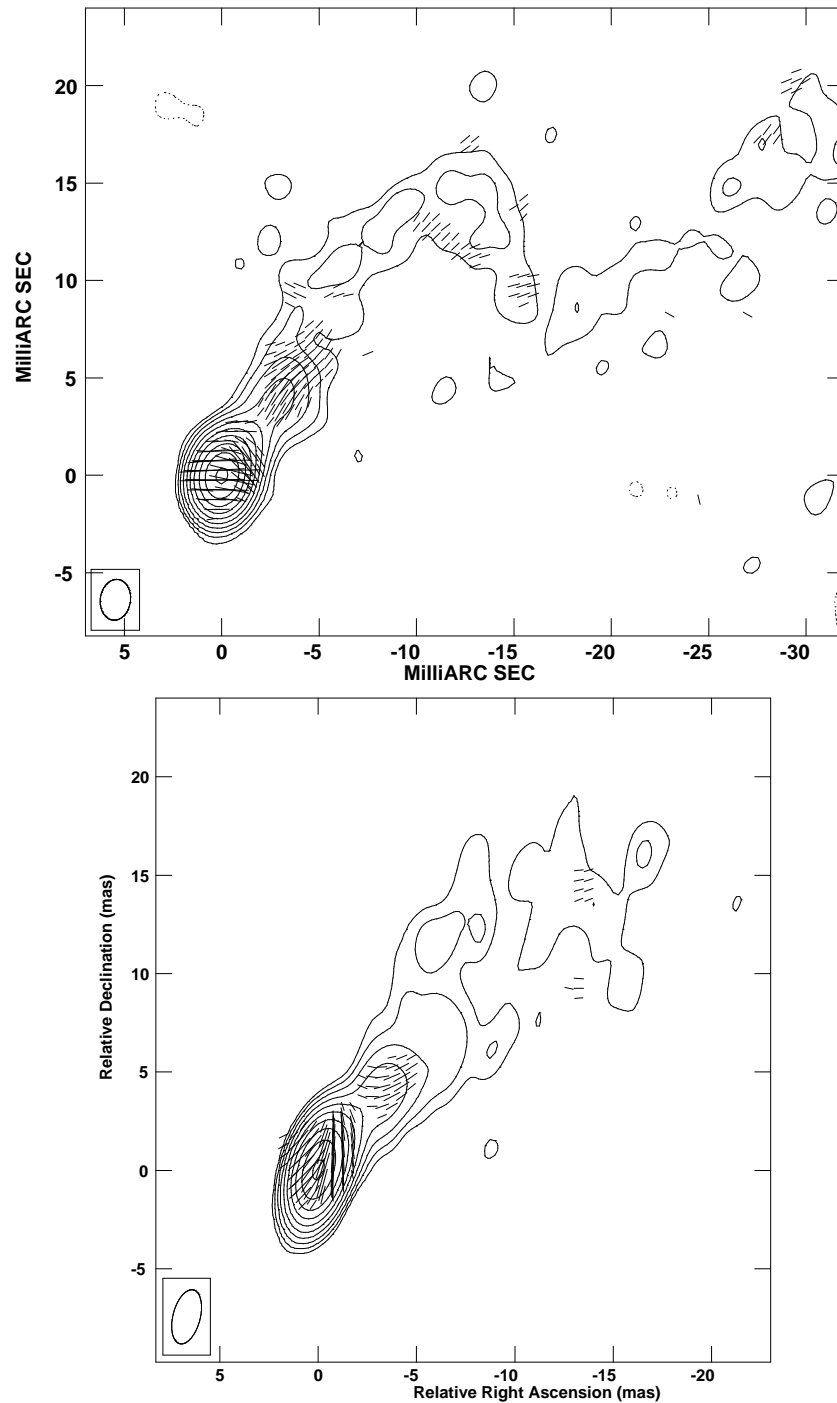
Figure 5.6: *Top.* Total intensity image of HBL 1101+384 in epoch 1995.53 with χ vectors superimposed. Contours are –0.17, 0.17, 0.35, 0.70, 1.40, 2.80, 5.70, 11.50, 22.50, 45 and 90% of the peak surface brightness of 326 mJy beam^{-1}, χ vectors: 1 mas = 0.9 mJy beam^{-1}. *Bottom.* Total intensity image of 1101+384 in epoch 1998.5 with χ vectors superimposed. Contours are –0.17, 0.17, 0.35, 0.70, 1.40, 2.80, 5.70, 11.50, 22.50, 45 and 90% of the peak surface brightness of 356.5 mJy beam^{-1}, χ vectors: 1 mas = 1.8 mJy beam^{-1}.
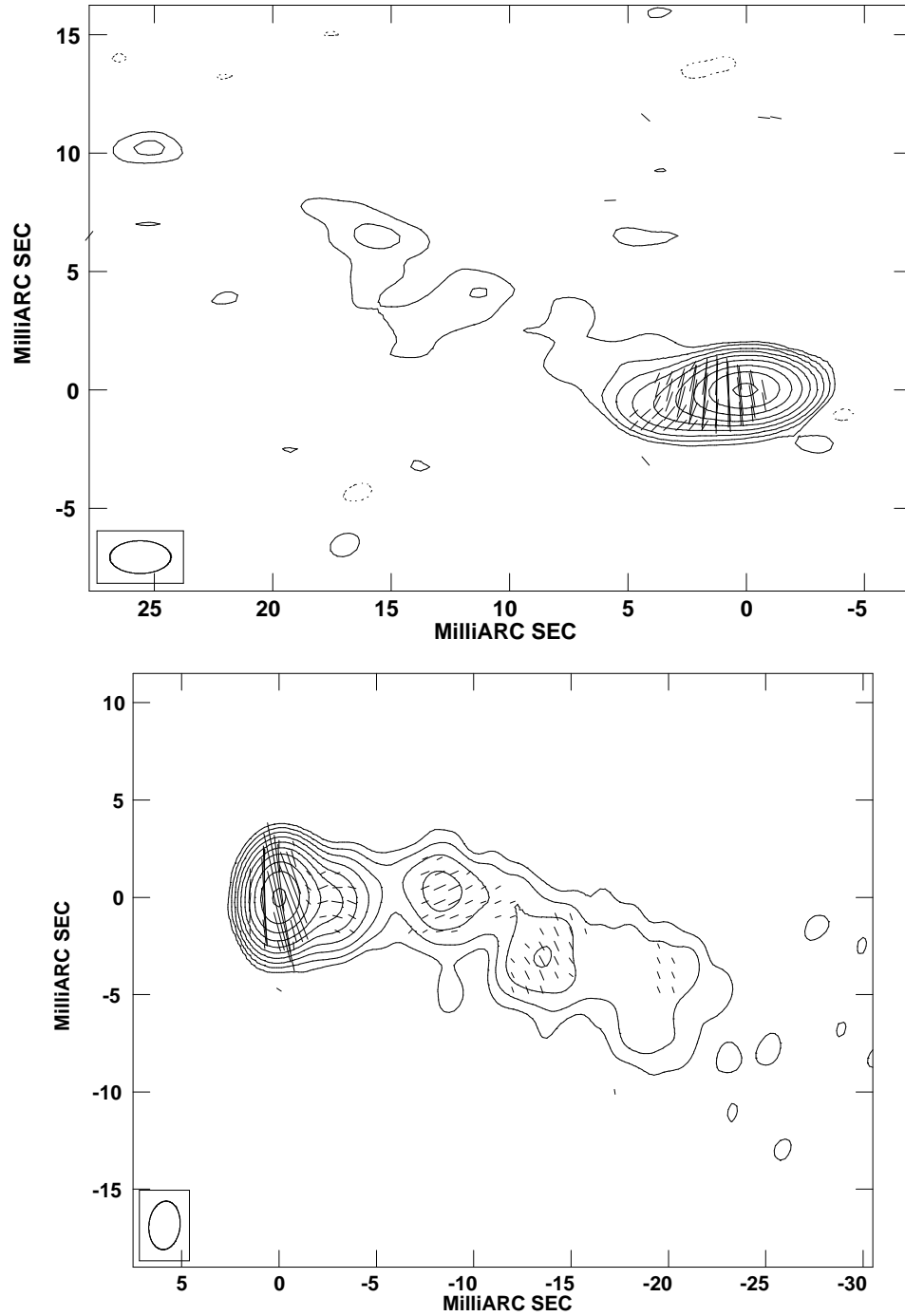
Figure 5.7: *Top.* Total intensity image of the HBL 1133+704 observed in epoch 1998.49 with χ vectors superimposed. Contours are –0.35, 0.35, 0.70, 1.40, 2.80, 5.70, 11.50, 22.50, 45 and 90% of the peak surface brightness of 98 mJy beam^{-1}, χ vectors: 1 mas = 1.7 mJy beam^{-1}. *Bottom.* Total intensity image of the LBL 1147+245 observed in 1995.53 with χ vectors superimposed. Contours are –0.17, 0.17, 0.35, 0.70, 1.40, 2.80, 5.6, 11, 23, 45 and 90% of the peak surface brightness of 479.4 mJy beam^{-1}, χ vectors: 1 mas = 2.5 mJy beam^{-1}.
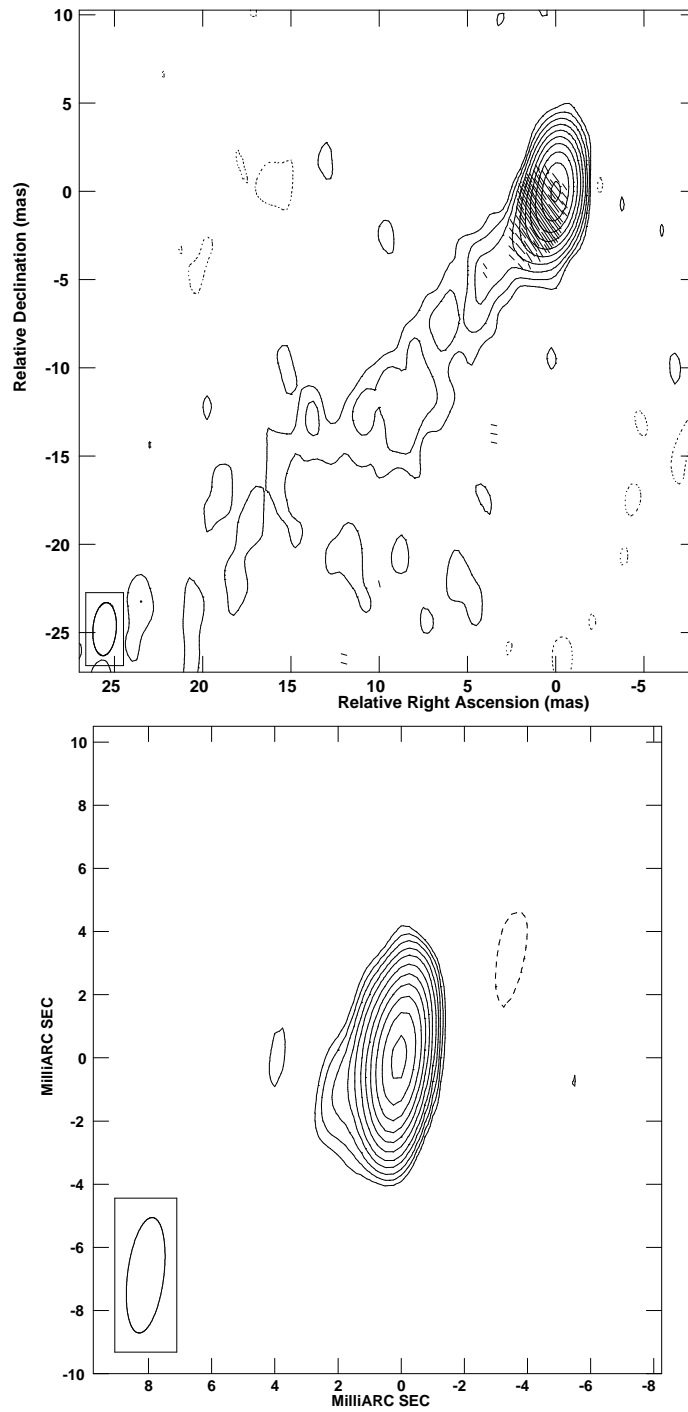
Figure 5.8: *Top*. Total intensity image of the HBL 1215+303 observed in epoch 1998.49 with χ vectors superimposed. Contours are –0.17, 0.17, 0.35, 0.70, 1.40, 2.80, 5.70, 11.50, 22.50, 45 and 90% of the peak surface brightness of 231 mJy beam^{-1}, χ vectors: 1 mas = 2 mJy beam^{-1}. *Bottom*. Total intensity image of the LBL 1219+301 observed in 1993.15. No polarization was detected in this source. Contours are –2.8, 2.8, 4.0, 5.6, 8, 11, 16, 23, 32, 45, 64 and 90% of the peak surface brightness of 33.4 mJy beam^{-1}.
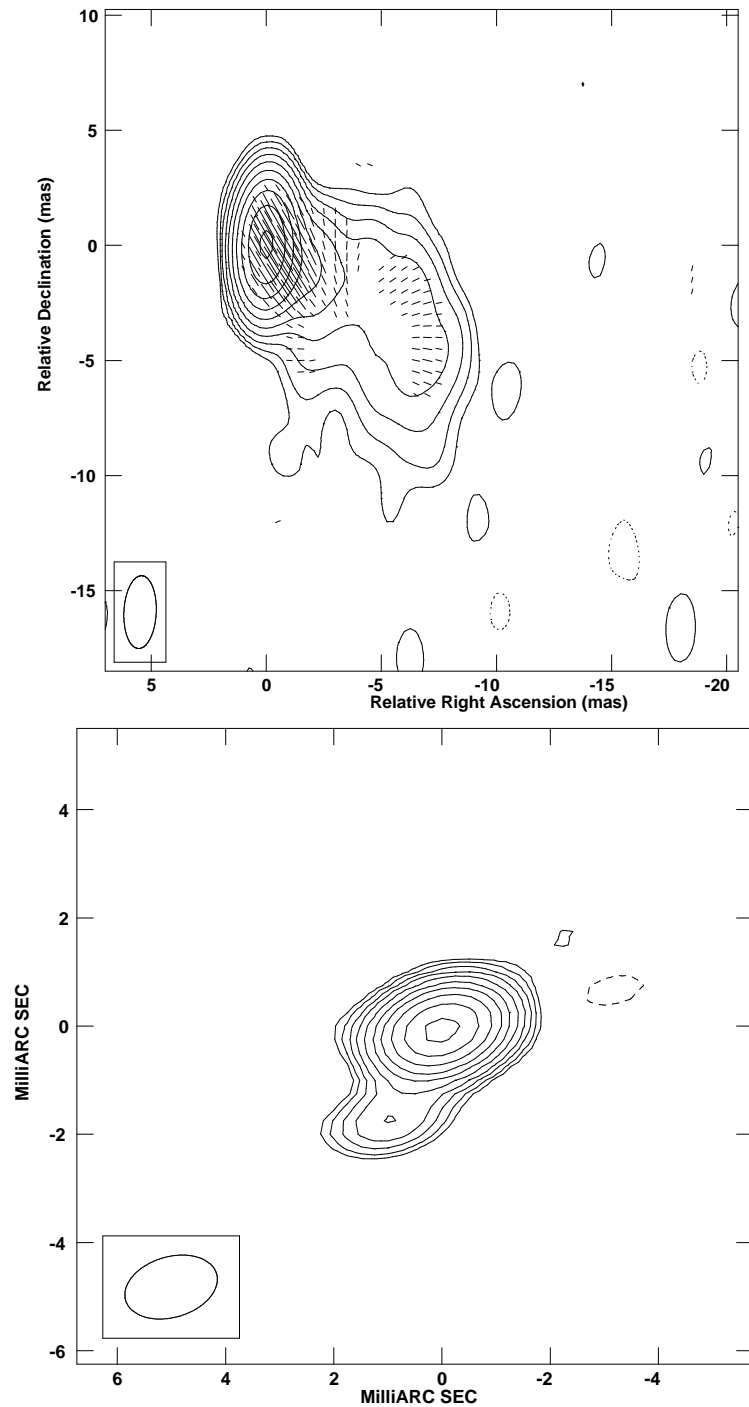
Figure 5.9: *Top.* Total intensity image of the HBL 1230+253 observed in 1998.49 with χ vectors superimposed. Contours are –0.17, 0.17, 0.35, 0.70, 1.40, 2.80, 5.60, 11.20, 22.50, 45 and 90% of the peak surface brightness of 183.7 mJy beam^{-1}, χ vectors: 1 mas = 2.5 mJy beam^{-1}. *Bottom.* Total intensity image of HBL 1235+632 observed in epoch 1993.15. No polarization was detected. Contours are –4, 4, 5.6, 8, 11, 16, 23, 32, 45, 64, 90% of the peak surface brightness of 13.8 mJy beam^{-1}.
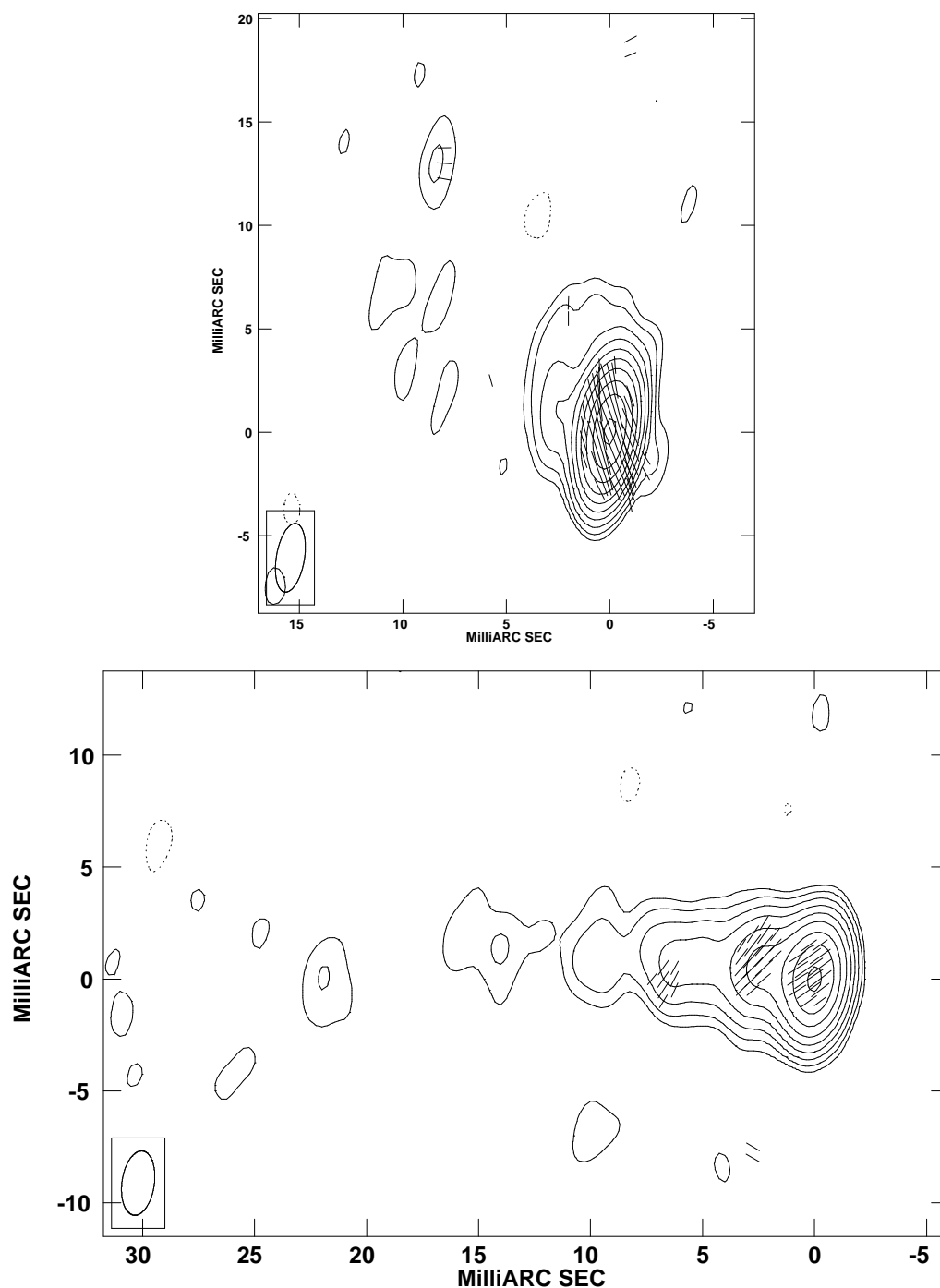
Figure 5.10: *Top.* Total intensity image of the LBL 1555+111 observed in 1998.49 with χ vectors superimposed. Contours are –0.19, 0.19, 0.35, 0.70, 1.40, 2.80, 5.60, 11, 23, 45 and 90% of the peak surface brightness of 189.7 mJy beam^{-1}, χ vectors: 1 mas = 1.5 mJy beam^{-1}. *Bottom.* Total intensity image of HBL 1743+195 observed in 1998.49 with χ vectors superimposed. Contours are –0.35, 0.35, 0.70, 1.40, 2.80, 5.60, 11.20, 22.50, 45 and 90% of the peak surface brightness of 84.3 mJy beam^{-1}, χ vectors: 1 mas = 1.3 mJy beam^{-1}.
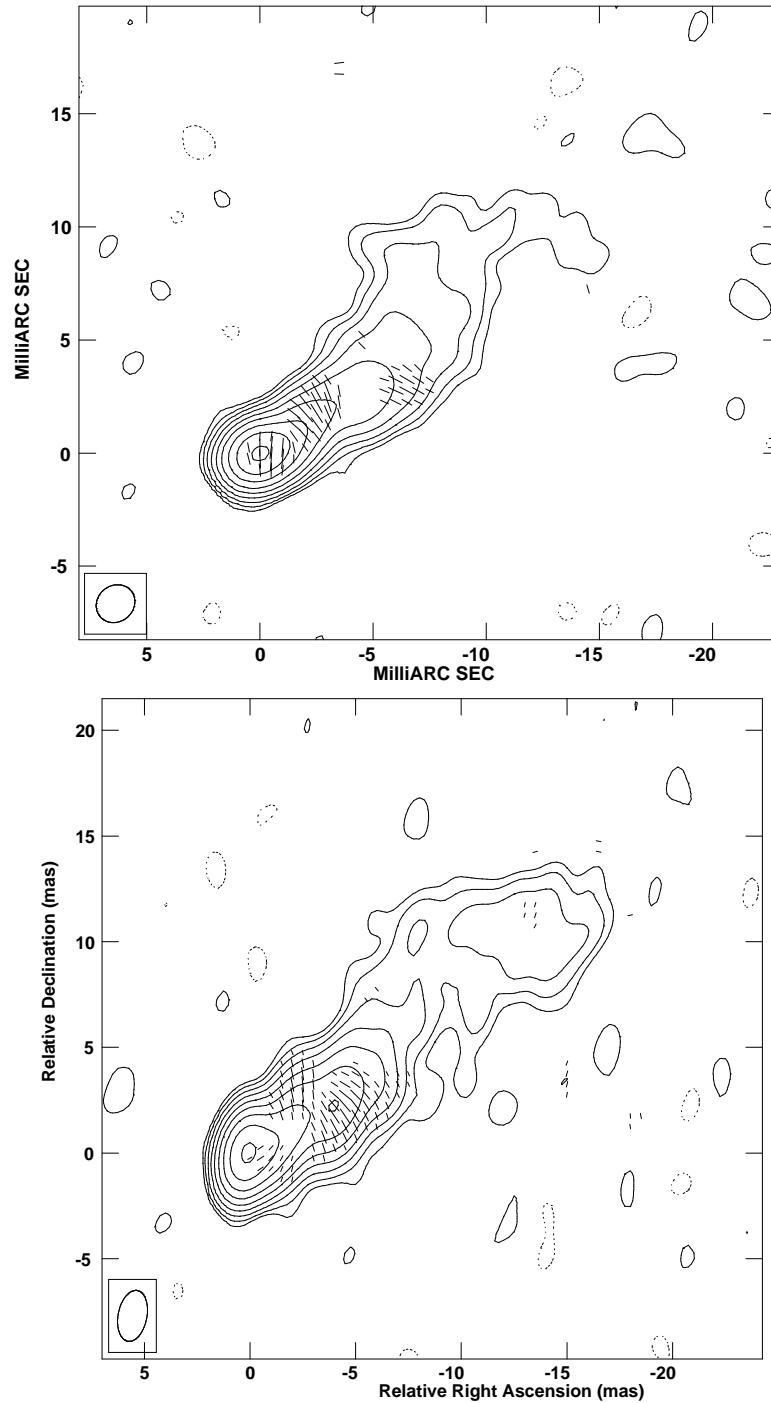
Figure 5.11: *Top.* Total intensity image of the HBL 1727+502 observed in 1995.53 with χ vectors superimposed. Contours are –0.35, 0.35, 0.70, 1.40, 2.80, 5.60, 11, 23, 45 and 90% of the peak surface brightness of 77.2 mJy beam^{-1}, χ vectors: 1 mas = 1 mJy beam^{-1}. *Bottom.* Total intensity image of the HBL 1727+502 observed in 1998.49 with χ vectors superimposed. Contours are –0.35, 0.35, 0.70, 1.40, 2.80, 5.60, 11.20, 22.50, 45 and 90% of the peak brightness of 64.2 mJy beam^{-1}, χ vectors: 1 mas = 1.8 mJy beam^{-1}.
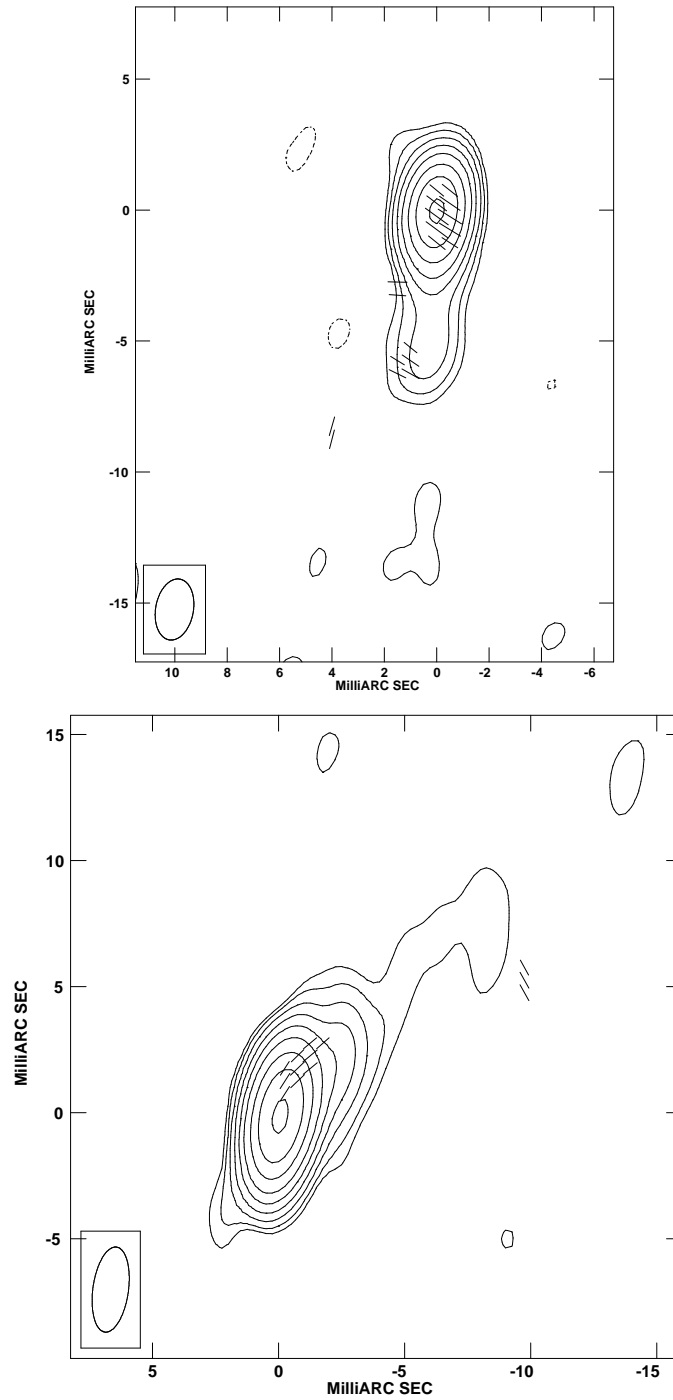
Figure 5.12: *Top.* Total intensity image of the HBL 1745+398 observed in 1998.49 with χ vectors superimposed. Contours are –0.70, 0.70, 1.40, 2.80, 5.60, 11, 23, 45 and 90% of the peak surface brightness of 49.3 mJy beam^{-1}, χ vectors: 1 mas = 0.9 mJy beam^{-1}. *Bottom.* Total intensity image of the LBL 2201+044 observed in 1998.49 with χ vectors superimposed. Contours are –0.4, 0.4, 0.70, 1.40, 2.80, 5.60, 11, 23, 45 and 90% of the peak surface brightness of 162.3 mJy beam^{-1}, χ vectors: 1 mas = 0.9 mJy beam^{-1}.

Table 5.4: Systematics of the B-field geometry in the two subclasses of BL Lacs.

B–field structure w.r.t. local VLBI jet	LBL	HBL
B is transverse to local jet	65 %	35 %
B is parallel to local jet	35 %	55 %
No obvious relation	...	10 %

The LBLs have been corrected for Faraday rotations. RM observations are needed for the HBLs. These data have been recently obtained by us, using the VLA.

Table 5.5: Circular polarization detection rates in Quasars and BL Lacs.

	Detection rate % (no. observed)		
	Single-dish (4, 5) (kpc-scale)	ATCA (3) (kpc-scale)	VLBI (1, 2) (pc-scale)
Quasars	46 % (52)	67 % (15)	23 % (35)
BL Lacs	27 % (11)	60 % (5)	0 % (12)

References : 1: Homan & Wardle (1999), 2: Homan *et al.* (2001), 3: Rayner *et al.* (2000), 4: Weiler & de Pater (1983), 5: Komesaroff *et al.* (1984)
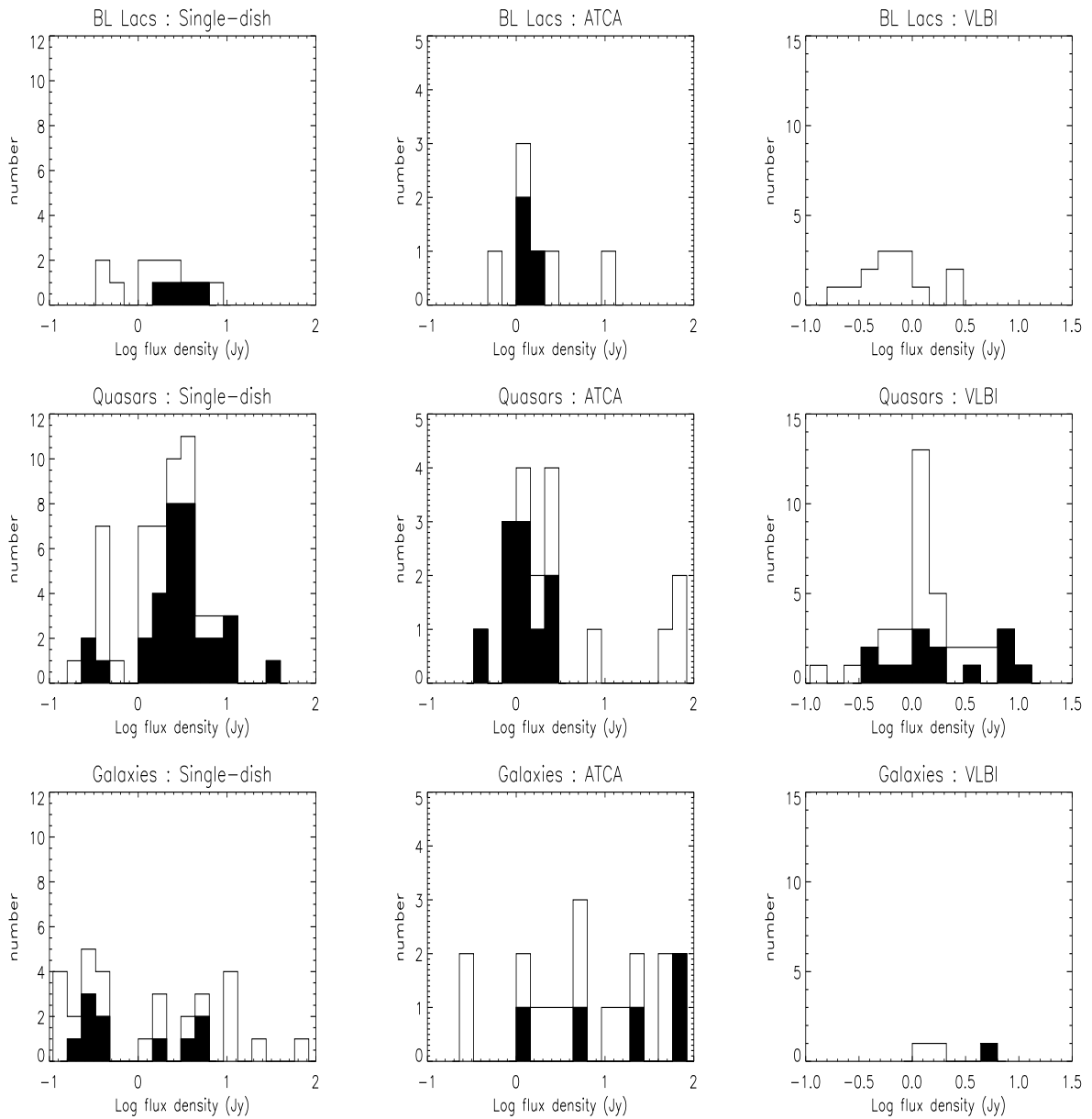
Figure 5.13: The histograms showing the number of observed and detected (shaded black) BL Lac objects, quasars and radio galaxies with respect to the total flux density, at three different spatial scales for circular polarization (see text for details), with resolution increasing from left to right panels in each row.

Chapter 6

Optical Nuclei of Radio-loud AGN and the Fanaroff-Riley Divide

6.1   Introduction

We investigate the nature of the point-like optical "cores" that have been found in the centres of the host galaxies of a majority of radio galaxies by the *Hubble Space Telescope*. We examine the evidence that these optical cores are relativistically beamed, and look for differences in the behaviour of the cores found in radio galaxies of the two Fanaroff-Riley types. We also attempt to relate this behaviour to the properties of the optical nuclei in their highly beamed counterparts (the BL Lac objects and radio-loud quasars) as hypothesized by the simple Unified Scheme.

The beamed synchrotron emission from the base of the jet or the 'core' may extend to visible wavelengths and there is strong evidence for it in BL Lacs and quasars (Impey & Tapia, 1990; Wills *et al.*, 1992). Recently, evidence for an optical synchrotron component in the relatively unbeamed radio galaxies has also surfaced, in the form of unresolved nuclear sources in the high resolution galaxy images with the *Hubble Space Telescope* (*HST*) (e.g., Chiaberge *et al.*, 1999, 2002; Verdoes Kleijn *et al.*, 2002). These authors argue on the basis of the strong connection with the radio core emission, anisotropy (Capetti & Celotti, 1999) and colour information that these optical cores are indeed optical synchrotron radiation.

We further test the idea that the unresolved nuclear optical emission from radio galaxies is beamed synchrotron emission from the base of the jet, using the radio core prominence parameter (R_c) as an indicator of the orientation of the AGN axis. We then

attempt to place these correlations in the broader framework of the Unified Scheme and test for consistencies. We come up with a model-fitting approach to investigate quantitatively the dependence of the optical emission on orientation and further test the predictions of the Unified Scheme in terms of the presence (or absence) of obscuring tori and the contribution of thermal accretion disks. We attempt to apply this to the available data and present the results. We further outline the caveats with our current sample and attempt to address them. A Hubble's constant of $H_0 = 75$ km s^{-1} Mpc^{-1} and deceleration parameter $q_0 = 0.5$ have been adopted.

6.2 The optical nuclei in FRI and FRII radio galaxies

Optical nuclei have been detected in a majority of 3CR, B2 and UGC FRI and FRII radio galaxies with the *WFPC2* on board the *HST*. They appear as unresolved sources with angular sizes $\sim 0.''1$ (the PSF of the *HST*). The results of studies based on this discovery have been presented by Chiaberge *et al.* (1999); Capetti & Celotti (1999); Hardcastle & Worrall (2000); Capetti *et al.* (2002); Chiaberge *et al.* (2002); Verdoes Kleijn *et al.* (2002).

For our study we chose an eclectic sample of FRI and FRII radio galaxies with either such a detected optical nucleus or with an upper limit to its optical flux density from the above-mentioned papers. Our set of FRI radio galaxies comprises of 25 3CR (Chiaberge *et al.*, 1999), 17 B2 (Capetti *et al.*, 2002) and 10 UGC FRIs (Verdoes Kleijn *et al.*, 2002) along with NGC 7052 and NGC 6251 from Capetti & Celotti (1999) and Hardcastle & Worrall (1999) respectively. Objects with ambiguous (*e.g.,* FRI/II) morphologies are excluded. So is 3C 386 whose optical "nucleus" is in fact a foreground star (Chiaberge *et al.*, 2002). We thus have 54 FRI radio galaxies spanning a redshift range of $0.0037 \leq z \leq 0.29$. The set of FRII radio galaxies includes 53 objects from the 3CR sample presented in Chiaberge *et al.* (2002) and 2 B2 FRIIs from Capetti *et al.* (2002). Among the 55 FRIIs considered, there are 42 narrow-line radio galaxies (NLRGs) and 13 broad-line radio galaxies (BLRGs). The FRII radio galaxies span a redshift range of $0.025 \leq z \leq 0.296$.

Tables 6.1 and 6.2 list the FRI and FRII radio galaxies respectively, along with their optical and radio data. Col. (1) lists the IAU name (B1950); Col. (2) Alternate name; Col. (3) Redshift (from the references for radio core data, except for UGC FRIs which are from NED); Col. (4) dust disk minor-to-major axis ratio (superscripts '*d*' and '*l*' stand for disks and lanes respectively) from Verdoes Kleijn *et al.* (1999) except 3C 83.1,

3C 296, 3C 449, 3C 465, 3C 326 and 3C 452 which are from de Koff *et al.* (2000); Col. (5) logarithm of extended radio luminosity at 1.4 GHz in W Hz^{-1}, calculated using the difference between total and core flux density; data at 5 GHz was converted to 1.4 GHz using $\alpha_{radio}^{ext} = 0.7$ for extended radio emission; Col. (6) 5 GHz radio core flux density in mJy; Col. (7) reference for the radio core (and total flux density if different); Col. (8): logarithm of radio core prominence standardized to an emitted wavelength of 6 cm; Col. (9): optical core luminosity in W Hz^{-1} estimated at an emitted wavelength of 5500 $\AA$; Col. (10): reference for optical core flux density/luminosity.

6.2.1 The correlations with radio core prominence for radio galaxies

The radio core prominence parameter R_c, which is the ratio of the core to extended radio flux density ($R_c \equiv S_{core}/S_{ext}$) is a known statistical indicator of orientation (Kapahi & Saikia, 1982; Orr & Browne, 1982) assuming that the core is the unresolved relativistically beamed nuclear jet and the lobes are unbeamed. R_c has indeed been shown to correlate with other orientation-dependent properties both in FRIIs (Kapahi & Saikia, 1982) and FRIs (Laing *et al.*, 1999). We use the parameter R_c to test if the luminosity of the optical nuclei is orientation-dependent. If the intrinsic optical synchrotron emission from the jet L_{jet}^{int}, is relativistically beamed by the Doppler factor δ where $\delta \equiv [\gamma(1 - \beta \cos\theta)]^{-1}$, β being the bulk velocity in units of the speed of light and θ is the angle between the radio axis and our line of sight, then the luminosity of the optical nuclei (L_o) should correlate with R_c.

The optical luminosities of the unresolved *HST* nuclei were *K*-corrected and calculated at an emitted wavelength of 5500 $\AA$, assuming an optical spectral index $\alpha_{opt} = 1$. The radio core prominence was calculated using observed radio core and total flux densities at 5 GHz and was further *K*-corrected to an emitted frequency of 5 GHz. For some sources flux densities were estimated from 1.4 GHz assuming $\alpha_{radio}^{ext} = 0.7$ and $\alpha_{radio}^{core} = 0$ for the extended and core radio emission, respectively. In Figure 6.1 we plot the luminosity of the optical nuclei versus the radio core prominence for the FRI and FRII radio galaxies.

We note that there are many upper limits to nuclear optical luminosities. We have analysed the statistical significance of the correlations with the aid of the Astronomical Survival Analysis (ASURV) package as implemented in IRAF, which takes into account data which are only upper/lower limits. logL_o turns out to be significantly correlated with logR_c for the FRI radio galaxies ($p = 0.0001$, generalized Spearman Rank test, see Table 6.5), arguing that the nuclear optical emission is orientation-dependent in the
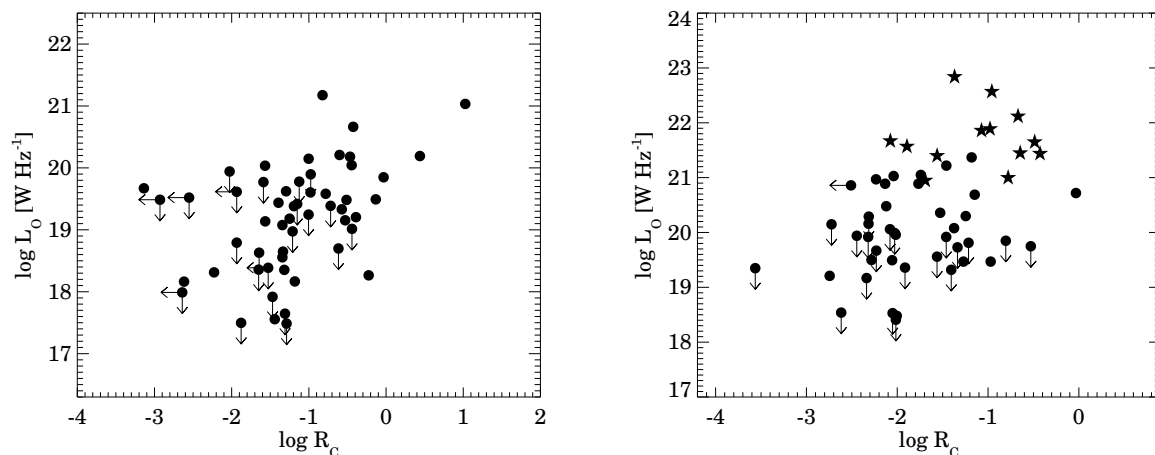
Figure 6.1: The luminosity of the optical nuclei L_o, plotted against the radio core prominence R_c, for the FRI (left) and FRII radio galaxies (right). • denote radio galaxies, ⋆ are BLRGs, ↓ and ← denote upper limits. Statistics for the fits are listed in Table 6.5.

same sense as the radio emission and may also originate in the relativistic jet and be likewise beamed.

For the FRII radio galaxies, the correlation is significant *only with the inclusion of the broad-line radio galaxies* (plotted as stars in the figure), while the narrow-line objects do not show a significant correlation by themselves ($p > 0.2$, generalized Spearman Rank test). The narrow-line FRII galaxies, show no correlation even with the more sensitive parametric Pearson's correlation test which however uses uncensored data ($p > 0.1$). This lack of correlation could be explained by the presence of a dusty obscuring torus that is hypothesized by the Unified Scheme, which could also result in many limits.

We note that the implication of the above result for the FRIs is consistent with what Verdoes Kleijn *et al.* (2002) suggest for their UGC FRI sample, *viz.*, that beaming also plays a role in the variance of optical luminosity of the nuclei L_o, in addition to the intrinsic variance in the nuclear jet L_{jet}^{int}, which presumably ionizes the line-emitting gas.

6.2.2 Optical Nuclei and the Narrow Emission-line Luminosity

Notwithstanding the strong correlation seen above for the FRI galaxies, there is still considerable scatter in the plot. In order to examine if variation in the intrinsic AGN power, and therefore the intrinsic L_o might be responsible for this, we plot L_o against the Hα+[NII] emission-line luminosity L_{line} from Zirbel & Baum (1995) for both the FRI and FRII radio galaxies, where L_{line} is assumed to come from the narrow-line region and is therefore a reasonable proxy for the intrinsic AGN power. We note here

that Verdoes Kleijn *et al.* (2002) found a correlation of L_o with *nuclear* L_{line} leading to the natural conclusion that the *nuclear* Hα , *i.e.,* on scales of $0.''1$ is ionized by the synchrotron emission from the optical nucleus. But the L_{line} that we use comes from scales of $\sim$ kpc.

We find that L_o correlates strongly with L_{line} for FRIs ($p = 0.013$) and FRIIs ($p = 0.0014$, Kendall's τ test). See Figure 6.2. The FRII correlation is strengthened further if the BLRGs are included ($p = 0.0002$). We note that a linear regression of logL_o on logR_c for FRI galaxies including censored data with survival statistics yields an r^2 of 0.60, whereas a multiple regression on independent variables logR_c and logL_{line} including censored data marginally improves the r^2 (0.63).

Multiple linear regression tests using STATISTICA and ASURV with independent variables z, L_{line}, R_c and dependent variable L_o show that redshift is not significant ($p = 0.269$ for FRIs and $p = 0.836$ for FRIIs – both NLRGs and BLRGs taken together) in the correlations. The multiple regression tests showed that for narrow-line FRIIs alone, where obscuration may be important, the correlation of L_o - L_{line} is not significant due to L_{line} ($p = 0.104$) but due to redshift ($p = 0.069$).

We note that Zirbel & Baum (1995) have found a L_{line} – radio core luminosity correlation, and the slope is 0.67 for FRIIs and 0.4 for FRIs. Interestingly, we find the slopes of the L_{line} – L_o correlation are similar : 0.67 for FRIIs and 0.56 for FRIs. Zirbel & Baum (1995) point out that for the same radio core power, FRIIs produce 10–50 times more emission line luminosity. Emission line luminosity also correlates with total radio power (Zirbel & Baum, 1995), further justifying our assumption of L_{line} being an indicator of AGN power.

Photoionization from the AGN may be dominant for the "nuclear" pc-scale emission lines as also suggested by Verdoes Kleijn *et al.* (2002) in their paper. However it is not clear if photoionization from the central source dominates also for emission lines on kpc-scales, especially for the low-luminosity FRIs. (Zirbel & Baum, 1995) suggest that the line emission in FRIs is likely to be energized by processes associated with the host galaxy itself (e.g., from old stars, Binette *et al.*, 1994).

6.2.3   Kpc-scale dust disks in FRI radio galaxies

While the evidence for an obscuring torus in FRIs is thus far meager, much larger dust disks and lanes of sizes varying from a few 100 pc to a few kpc have been discovered in many FRI radio galaxies (e.g., Verdoes Kleijn *et al.*, 1999; de Koff *et al.*, 2000). It has been suggested by Verdoes Kleijn *et al.* (1999); Capetti & Celotti (1999) and de Koff *et al.* (2000) that the kpc-scale radio jet tends to align with the axis of this disk. We
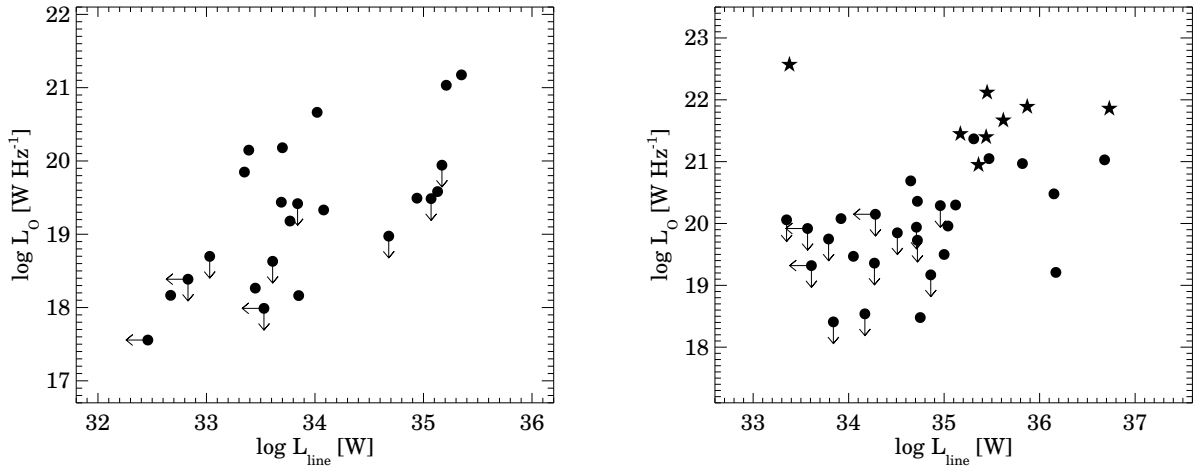
Figure 6.2: Optical core luminosity L_o vs. line luminosity L_{line} for the FRI (left) and FRII galaxies (right). $\star$ are the BLRGs, $\downarrow$ and $\leftarrow$ denote upper limits. Table 6.5 lists the statistics of the correlations.

investigate this question here for the subset of objects where data on this disk, as well as L_o and R_c are available. The results of the statistical tests are given in Table 6.5. We find different relations of the minor-to-major-axis ratio, b/a of the extended dust disk with nuclear optical luminosity and radio core prominence for the samples presented in the above papers. b/a of the extended dust disk correlates significantly both with the nuclear optical luminosity and radio core prominence for the de Koff *et al.* FRI galaxies. b/a correlates significantly with L_o for the Verdoes Kleijn *et al.* FRI sources only when both disks and lanes are considered together. However they show no correlation with radio core prominence. When all the objects are taken together and both dust disks and lanes are considered, b/a correlates with nuclear optical luminosity but not with radio core prominence (see Figure 6.3).

It thus appears that the axes of the extended dust disks do not tend to be aligned with the orientation of the AGN, but that these disks could be causing some extinction of the flux density of the optical nuclei in FRI radio galaxies. This extinction would of course contribute to the variation in L_o in the L_o–L_{line} correlation and to the scatter in the L_o–R_c correlation. Multiple linear regression of L_o on the independent variables R_c, L_{line} and b/a (ignoring limits) marginally improves the r^2 to 0.64.

Table 6.1: The FRI radio galaxies.

IAU name	Alternate name	Redshift z	b/a	$\log L_{ext}$ W Hz^{-1}	S_c(5 GHz) mJy	ref.	$\log R_c$	$\log L_o$ W Hz^{-1}	ref.
0036+030	NGC 193	0.0144	0.18^l	22.60	40.0	6,15	−1.31	18.35	5
0053+261	3C 28	0.1952	...	25.42	<0.2	1,3	<−2.92	<19.48	1
0055−016	3C 29	0.0448	...	25.29	93.0	1,3	−1.39	19.43	1
0055+265	4C 26.03	0.0472	...	24.61	9.0	2	−1.93	<18.54	2
0055+300	NGC 315	0.0167	0.23^d	24.01	617.6	2	−0.39	19.19	5
0104+321	3C 31	0.0169	0.77^d	24.40	92.0	1,3	−1.34	19.08	5
0120+329	NGC 507	0.0164	...	22.29	1.5	2	−1.30	<17.64	2
0123−016	3C 40	0.0180	0.91^d	22.17	67.8	10	−1.64	<18.63	5
0153+053	NGC 741	0.0185	...	22.75	6.0	11	−1.65	<18.35	5
0220+427	3C 66B	0.0215	0.98^d	24.86	182.0	1,3	−1.29	19.62	5
0305+039	3C 78	0.0288	...	24.96	964.0	1,3	−0.42	20.66	1
0318+415	3C 83.1	0.0251	0.09^d	24.98	21.0	1,3	−2.22	18.31	1
0316+413	3C 84	0.0176	...	24.73	42370.0	1,3	1.02	21.03	1
0331−013	3C 89	0.1386	...	25.80	49.0	1,3	−1.21	<18.97	1
0705+486	NGC 2329	0.0193	0.68^d	23.02	69.0	11	−0.44	20.04	5
0755+379	3C 189	0.0413	...	24.43	228.8	2	−0.46	20.18	2
0924+301	...	0.0266	...	23.52	0.4	2	<−2.64	<17.98	2
0928+678	NGC 2892	0.0225	...	22.82	30.0	12	−0.52	19.15	5
1142+198	3C 264	0.0206	0.99^d	24.57	200.0	1,3	−1.00	20.15	5
1205+255	UGC 7115	0.0226	...	22.58	44.0	11	−0.51	19.48	5
1216+061	3C 270	0.0074	0.46^d	24.31	308.0	1,3	−1.44	17.56	5
1220+587	NGC 4335	0.0154	0.41^d	22.64	15.0	6	−0.44	<19.01	5
1222+131	3C 272.1	0.0037	0.15^l	23.22	180.0	1,3	−1.18	18.17	5
1228+126	3C 274	0.0037	...	24.63	4000.0	1,3	−1.24	19.18	5
1257+282	NGC 4874	0.0239	...	23.07	1.2	2	−1.87	<17.49	2
1322+366	NGC 5141	0.0173	0.25^l	23.63	78.7	10	−0.61	<18.69	5
1336+391	3C 288	0.2460	...	26.42	30.0	1,3	−1.56	20.03	1
1346+268	4C 26.42	0.0633	...	24.52	59.3	2	−0.78	19.58	2
1407+177	NGC 5490	0.0162	0.35^l	23.24	37.8	10	−1.28	<17.48	5
1414+110	3C 296	0.0237	0.29^d	24.61	77.0	1,3	−1.33	18.64	1
1422+268	...	0.0370	...	23.99	21.1	2	−1.15	<19.41	2
1430+251	4C 25.46	0.0813	...	24.20	1.2	2	<−1.93	<19.61	2
1450+281	...	0.1265	...	24.48	6.7	2	−1.12	<19.77	2

Table 6.1: (continued)

IAU name	Alternate name	Redshift z	b/a	$\log L_{ext}$ W Hz^{-1}	S_c(5 GHz) mJy	ref.	$\log R_c$	$\log L_o$ W Hz^{-1}	ref.
1502+261	3C 310	0.0540	...	25.19	80.0	1,3	−1.19	19.38	1
1510+709	3C 314.1	0.1197	...	25.33	<1.0	1,3	<−2.55	<19.52	1
1514+072	3C 317	0.0342	...	24.43	391.0	1,3	−0.13	19.49	1
1521+288	4C 28.39	0.0825	...	24.53	55.8	2	−0.60	20.20	2
1527+308	...	0.1143	...	24.03	4.0	2	−0.97	<19.89	2
1553+245	...	0.0426	...	23.43	57.9	2	−0.03	19.84	2
1610+296	NGC 6086	0.0313	...	22.92	1.1	2	<−1.52	<18.38	2
1613+275	...	0.0647	...	24.01	10.6	2	−1.00	<19.24	2
1626+396	3C 338	0.0303	...	24.19	105.0	1,3	−0.57	19.33	1
1637+826	NGC 6251	0.024	...	23.82	720.0	13,4	0.44	20.19	7
1641+173	3C 346	0.1620	...	26.20	220.0	1,3	−0.82	21.17	1
1648+050	3C 348	0.1540	...	27.12	10.0	1,3	−3.13	19.67	1
1827+323	...	0.0659	...	24.04	20.8	2	−0.71	<19.38	2
2045+068	3C 424	0.1270	...	25.67	18.0	1,3	−1.58	<19.77	1
2116+262	NGC 7052	0.0164	0.30[d]	22.97	47.0	9,14	−0.22	18.26	8
2153+377	3C 438	0.2900	...	26.77	17.0	1,3	−2.02	<19.94	1
2212+135	3C 442	0.0262	...	24.39	2.0	1,3	−2.61	18.16	1
2229+391	3C 449	0.0181	0.50[d]	24.29	37.0	1,3	−1.56	19.13	1
2236+350	UGC 12127	0.0277	...	23.46	7.1	2	−1.34	18.55	2
2318+079	NGC 7626	0.0113	0.17[l]	22.39	15.6	10	−1.47	<17.91	5
2335+267	3C 465	0.0301	0.69[l]	25.00	270.0	1,3	−0.97	19.60	1

Superscripts 'd' and 'l' for b/a stand for extended dust disks and lanes, respectively. References: (1) : Chiaberge *et al.* (1999) (F702W filter); For the 7 sources which were common between the 3CR, B2 and the UGC samples we used the F555W flux densities from Verdoes Kleijn *et al.* (2002); (2) : Capetti *et al.* (2002) (1.4 GHz, F814W filter); (3) : Kuehr *et al.* (1979) (5 GHz); (4) : Kuehr *et al.* (1981) (5 GHz); (5) : Verdoes Kleijn *et al.* (2002) (F555W filter); (6) : Xu *et al.* (2000) (1.4 GHz); (7) : Hardcastle & Worrall (1999) (F702W filter); (8) : (Capetti & Celotti, 1999) (F814W filter); (9) : Giovannini *et al.* (1988) (5 GHz); (10) : Bridle & Perley (1984) (core at 5 GHz, total flux density at 1.4 GHz); (11) : Laurent-Muehleisen *et al.* (1997) (5 GHz); (12) : Jenkins (1982) (5 GHz); (13) : Waggett *et al.* (1977) (2.7 GHz); (14) : Gregory & Condon (1991) (5 GHz); (15) : Becker *et al.* (1991) (5 GHz).

Table 6.2: The FRII radio galaxies.

IAU name	Alternate name	Redshift z	b/a	$\log L_{ext}$ W Hz^{-1}	S_c(5 GHz) mJy	ref.	$\log R_c$	$\log L_o$ W Hz^{-1}	ref.
0034-014	3C 15	0.073	...	25.46	372.8	1,3	−0.52	<19.74	1
0035-024	3C 17*	0.220	...	26.63	727.9	1,3	−0.48	21.64	1
0038+097	3C 18	0.188	...	26.41	118.2	1,3	−1.18	21.36	1
0106+729	3C 33.1*	0.181	...	26.11	19.7	1,3	−1.69	20.94	1
0109+492	3C 35	0.067	...	25.06	23.7	1,3	−1.40	<19.31	1
0218-021	3C 63	0.175	...	26.10	18.3	1,3	−1.74	21.04	1
0307+169	3C 79	0.256	...	26.62	14.7	1,3	−2.03	21.02	1
0325+023	3C 88	0.030	...	24.86	197.2	1,3	−0.97	19.46	1
0356+102	3C 98	0.030	...	25.25	11.1	1,3	−2.61	<18.53	1
0415+379	3C 111*	0.049	...	25.86	1155.3	1,4	−0.77	20.99	1
0433+295	3C 123	0.218	...	27.55	85.0	1,3	−2.33	<19.16	1
0453+227	3C 132	0.214	...	26.35	33.5	1,3	−1.56	<19.55	1
0459+252	3C 133	0.277	...	26.85	170.8	1,3	−1.14	20.68	1
0511+008	3C 135	0.127	...	25.88	5.5	1,3	−2.31	20.15	1
0605+480	3C 153	0.277	...	26.68	0.4	1,3	−3.56	<19.34	1
0640+233	3C 165	0.296	...	26.48	8.7	1,3	−2.01	19.95	1
0642+214	3C 166	0.245	...	26.15	553.6	1,3	−0.03	20.71	1
0651+542	3C 171	0.238	...	26.49	2.5	1,3	−2.74	19.20	1
0734+805	3C 184.1	0.118	...	25.87	7.5	1,3	−2.23	20.96	1
0802+243	3C 192	0.060	...	25.56	8.5	1,3	−2.44	<19.94	1
0818+472	3C 197.1	0.131	...	25.82	6.8	1,3	−2.13	20.88	1
0819+061	3C 198	0.082	...	25.14	<1.5	5,4	<−2.50	20.85	1
0917+458	3C 219*	0.174	...	26.49	68.7	1,3	−1.56	21.39	1
0936+361	3C 223	0.137	...	26.04	11.7	1,3	−2.07	<20.05	1
0938+399	3C 223.1	0.108	...	25.65	8.7	1,3	−2.02	<19.98	1
0945+076	3C 227*	0.086	...	25.94	23.5	1,3	−2.07	21.66	1
0958+290	3C 234*	0.185	...	26.34	133.6	1,3	−1.07	21.85	1
1003+351	3C 236	0.099	...	25.70	191.5	1,3	−0.80	<19.84	1
1205+341	...	0.0788	...	24.46	12.5	2	−1.21	<19.81	2
1251+278	3C 277.3	0.0857	...	25.37	12.4	2	−2.05	19.49	2
1319+428	3C 285	0.079	...	25.32	7.8	1,3	−2.00	18.47	1
1330+022	3C 287.1*	0.216	...	26.34	443.8	1,3	−0.42	21.43	1
1420+198	3C 300	0.270	...	26.58	10.1	1,3	−2.12	20.47	1

Table 6.2: (continued)

IAU name	Alternate name	Redshift z	b/a	$\log L_{ext}$ W Hz^{-1}	S_c(5 GHz) mJy	ref.	$\log R_c$	$\log L_o$ W Hz^{-1}	ref.
1441+522	3C 303*	0.141	...	25.83	187.6	1,3	−0.64	21.44	1
1519+078	3C 318.1	0.046	...	24.49	3.0	6,3	−2.05	<18.52	1
1522+546	3C 319	0.192	...	26.04	1.4	1,3	−2.72	<20.14	1
1545+210	3C 323.1*	0.264	...	26.44	43.8	1,3	−1.36	22.83	1
1549+202	3C 326	0.089	0.24^d	25.19	15.9	1,3	−1.46	<19.91	1
1559+021	3C 327	0.104	...	26.18	40.8	1,3	−1.91	<19.35	1
1615+325	3C 332*	0.152	...	25.93	11.5	1,3	−1.89	21.56	1
1658+471	3C 349	0.205	...	26.33	21.9	1,3	−1.76	20.88	1
1717-009	3C 353	0.030	...	25.94	216.2	1,3	−2.01	<18.40	1
1726+318	3C 357	0.167	...	26.10	6.5	1,3	−2.23	<19.66	1
1825+743	3C 379.1	0.256	...	26.32	3.9	7,3	−2.32	<19.91	1
1832+474	3C 381	0.161	...	26.18	6.9	1,3	−2.31	<20.28	1
1833+326	3C 382*	0.058	...	25.47	228.1	1,4	−0.95	22.56	1
1842+455	3C 388	0.091	...	25.80	76.5	1,3	−1.37	20.07	1
1845+797	3C 390.3*	0.056	...	25.74	434.7	1,3	−0.97	21.88	1
1939+605	3C 401	0.201	...	26.41	47.5	1,3	−1.52	20.35	1
1940+505	3C 402	0.025	...	24.39	48.1	1,3	−1.27	19.46	1
1949+023	3C 403	0.059	...	25.54	12.1	1,3	−2.28	19.49	1
2221-023	3C 445*	0.057	...	25.40	382.8	1,3	−0.66	22.11	1
2243+394	3C 452	0.081	0.27^l	25.96	152.3	1,3	−1.33	<19.72	1
2309+090	3C 456	0.233	...	26.24	27.8	1,3	−1.45	21.21	1
2318+235	3C 460	0.268	...	26.02	21.4	1,4	−1.24	20.29	1

Superscripts 'd' and 'l' for b/a stand for extended dust disks and lanes, respectively. There are only two FRIIs for which b/a for extended dust features are available (de Koff *et al.*, 2000). We do not include the FRIIs in our analysis of the extended dusty disks. Sources with a star are BLRGs. References : (1) : Chiaberge *et al.* (2002) (5 GHz, F702W filter, except 3C 192 observed with F555W); (2) : Capetti *et al.* (2002) (1.4 GHz); (3) : Kuehr *et al.* (1979) (5 GHz); (4) : Veron-Cetty & Veron (1998) (5 GHz); (5) : Fomalont & Bridle (1978) (5 GHz); (6) : Slee *et al.* (1989) (1.5 GHz); (7) : Spangler & Sakurai (1985) (1.4 GHz).
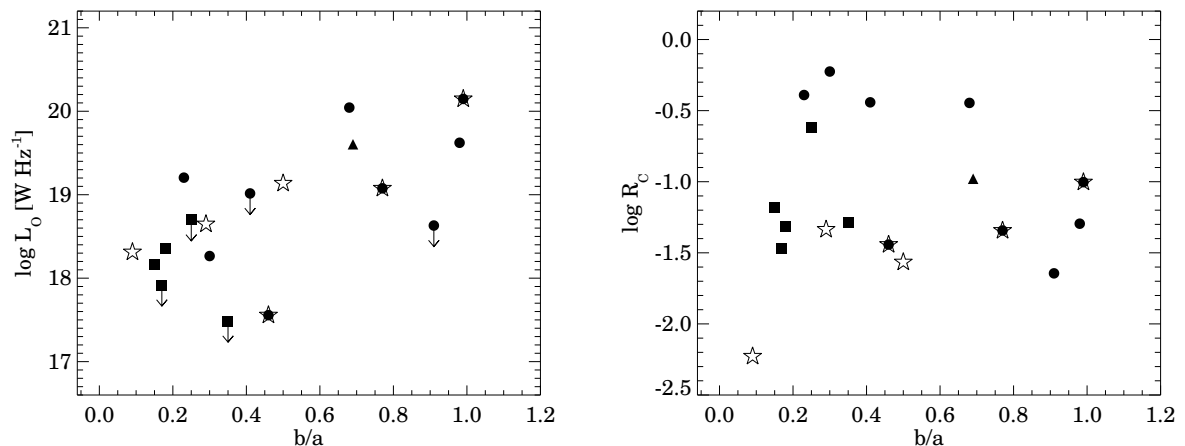
Figure 6.3: Nuclear optical luminosity L_o (left) and radio core prominence R_c (right) plotted against b/a for the FRI radio galaxies. The ● and filled square denote the dust disks and lanes respectively, from Verdoes Kleijn *et al.* (1999) while the open star and filled triangle denote the dust disks and lanes from de Koff *et al.* (2000), ↓ denote upper limits. The sources common to both the papers are shown by an open star superimposed by a ●. Table 6.5 lists the statistics for the correlations.

6.3 Comparison with the optical nuclei of the beamed objects and the Unified Scheme

In the simple Unified Scheme, the beamed counterparts of the FRI and FRII radio galaxies are the BL Lac objects and the radio-loud quasars respectively. In § 6.2.1 we find the optical emission from galaxy cores to be orientation-dependent. Given that optical emission from BL Lacs and quasars is also beamed (e.g., Kapahi & Shastri, 1987; Baker *et al.*, 1994), we attempt to relate the galaxy behaviour to that of BL Lacs and quasars in the framework of the Unified Scheme. We use this framework to extend the correlations of nuclear optical luminosity with radio core prominence to higher values of radio core prominence. We consider the FRI radio galaxies and BL Lacs together and henceforth refer to them as the "FRI population", and similarly consider the FRII radio galaxies and radio-loud quasars together and henceforth refer to them as the "FRII population". In order to investigate quantitatively the dependence of the optical emission on orientation, we come up with a model-fitting approach, described below.

6.3.1 The data

We have considered BL Lac objects which are both X-ray selected (belonging to *EMSS* and *HEAO-1* samples) and radio-selected, from Perlman & Stocke (1993); Vermeulen & Cohen (1994) and Laurent-Muehleisen *et al.* (1993). We have thus attempted to include both the high R_c (Vermeulen & Cohen, 1994) and intermediate R_c (Laurent-Muehleisen *et al.*, 1993) BL Lacs. The BL Lacs that showed FRII radio morphology in the form of terminal hotspots *viz.*, 1308+326, 1823+568, 2007+777 (Kollgaard *et al.*, 1992), 1749+701 (O'Dea *et al.*, 1988) and 1803+784 (Cassaro *et al.*, 1999); that were gravitational microlensing candidates, *viz.*, 1413+135 (this object also has other peculiarities like a spiral host galaxy; Perlman & Stocke, 1993) and that had uncertain redshifts *viz.*, 0716+714, were excluded from our set of BL Lacs. Our final BL Lac sample has 44 objects spanning a redshift range of $0.028 \leq z \leq 0.997$. For the beamed counterparts of FRII radio galaxies, we considered 34 high R_c radio-loud quasars from Vermeulen & Cohen (1994) spanning the redshift range of $0.158 \leq z \leq 2.367$.

We have taken the total optical luminosity of BL Lacs and quasars (as derived from their available *V*-band magnitudes) as the optical core luminosity, *assuming that the core overwhelms the host galaxy emission*. As the BL Lacs are known to be strongly variable, we took radio and optical measurements from the literature that were as closely spaced in time as was available. Several *V*-magnitudes come from optical monitoring campaigns of Pica *et al.* (1988); Webb *et al.* (1988) and Falomo *et al.* (1994). Quasars also can be Optically Violent Variables (OVVs) but OVVs constitute less than 25% of the quasars used in our analysis. The data are tabulated in Tables 6.3 and 6.4. Col. (1) lists the IAU name (B1950); Col. (2) Alternate name; Col. (3) Redshift (from the references for radio core data, except 1402+042, 0333+321, 0835+580 and 0836+710 which are from Veron-Cetty & Veron (1998)); Col. (4) *V*-band magnitude; Col. (5) reference for m_v; Col. (6) logarithm of extended radio luminosity at 1.4 GHz in W Hz^{-1} – taken from the reference for radio core flux density for BL Lacs and calculated using core flux density and radio core prominence for quasars and the BL Lacs 0454+844 and 0735+178; data at 5 GHz converted to 1.4 GHz using $\alpha_{radio}^{ext} = 0.7$ for extended radio emission; Col. (7) 5 GHz radio core flux density in mJy; Col. (8) reference for the radio core and total flux density (for quasars it is the reference for the radio core flux density and logR_c); Col. (9): logarithm of radio core prominence standardized to an emitted wavelength of 6 cm; Col. (10): optical core luminosity in W Hz^{-1} estimated at an emitted wavelength of 5500 $\mathring{A}$. The plots of nuclear optical luminosity against radio core prominence parameter are shown in Figure 6.4.

Table 6.3: The BL Lac objects.

IAU name	Alternate name	Redshift z	m_v	ref.	$\log L_{ext}$ W Hz^{-1}	S_c(5 GHz) mJy	ref.	$\log R_c$	$\log L_o$ W Hz^{-1}
0158+003	...	0.299	17.96	1	24.36	8.38	2	0.60	22.61
0219-164	...	0.698	17.0	9	25.50	358.0	5	0.84	23.78
0219+428	3C 66A	0.444	15.08	6	27.32	814.0	2^a	0.14	24.13
0257+344	...	0.247	18.53	1	23.22	11.78	2	1.69	22.21
0317+185	...	0.190	18.12	1	23.50	9.85	2	1.08	22.13
0323+022	...	0.147	16.98	6	23.20	55.0	5	1.21	22.36
0414+009	...	0.287	17.11	6	24.50	67.0	5	0.54	22.91
0454+844	...	1.34*	17.3	9	24.21	1400.0	4	>3.37†	24.29
0521-365	...	0.055	14.62	9	26.12	3124.0	2^a	−0.14	22.43
0548-322	...	0.069	16.05	8	24.67	80.0	2^a	−0.08	22.06
0607+711	...	0.267	19.60	1	24.79	14.08	2	0.29	21.85
0706+592	...	0.124	18.40	9	24.20	65.0	5	0.17	21.64
0735+178	...	>0.424	15.40	9	23.82	1990.0	4	>3.2	23.96
0737+746	...	0.315	16.89	1	23.85	24.47	2	1.64	23.09
0851+202	OJ287	0.306	13.81	7	24.21	2217.0	2^a	3.23	24.29
1101-232	...	0.186	17.01	8	24.40	49.0	5	0.41	22.56
1101+384	Mrk421	0.030	13.22	6	23.85	520.0	2^a	0.81	22.46
1133+704	Mrk180	0.044	14.49	9	24.31	131.0	2^a	0.09	22.29
1218+304	...	0.130	15.80	6	22.79	62.0	5	>1.34	22.72
1219+285	ON 231	0.102	15.40	7	23.07	2058.0	2^a	3.25	22.67
1221+248	...	0.218	17.65	1	23.64	27.85	2	1.53	22.45
1229+645	...	0.164	16.89	1	23.73	42.49	2	1.34	22.49
1235+632	...	0.297	18.59	1	24.00	13.0	5	>0.32	22.35
1400+162	...	0.244	16.74	9	26.27	233.0	2^a	−0.07	22.91
1402+042	...	0.344	16.88	8	24.40	21.43	2	0.53	23.17
1407+599	...	0.495	19.67	1	25.76	14.12	2	0.08	22.39
1418+546	...	0.152	15.39	6	24.31	1058.0	2^a	2.09	23.03
1426+427	...	0.130	16.40	9	23.50	31.0	5	>1.04	22.48
1443+638	...	0.299	19.65	1	24.63	8.36	2	0.33	21.93
1458+228	...	0.235	16.79	1	23.98	29.0	2	1.28	22.86
1514-241	AP Lib	0.049	14.97	7	23.61	2562.0	2^a	2.18	22.19
1534+018	...	0.312	18.70	1	25.28	28.84	2	0.26	22.35
1538+149	4C 14.60	0.605	17.89	6	26.94	1337.0	2^a	1.17	23.29
1552+203	...	0.222	17.70	1	24.65	33.09	2	0.61	22.44

Table 6.3: (continued)

IAU name	Alternate name	Redshift z	m_v	ref.	$\log L_{ext}$ W Hz^{-1}	S_c(5 GHz) mJy	ref.	$\log R_c$	$\log L_o$ W Hz^{-1}
1652+398	Mrk501	0.034	14.08	6	23.52	1376.0	2^a	1.66	22.23
1727+502	...	0.055	16.12	6	23.83	175.0	2^a	0.89	21.83
1749+096	...	0.320	17.32	6	23.89	744.0	2^a	>3.11	22.93
1807+698	3C 371	0.050	14.57	7	25.04	1350.0	2^a	0.48	22.37
2143+070	...	0.237	18.04	1	24.99	44.63	2	0.46	22.37
2155-304	...	0.117	13.31	6	25.18	252.00	2^a	0.37	23.62
2200+420	BL Lac	0.069	15.42	7	23.93	3310.00	2^a	2.26	22.31
2201+044	...	0.028	15.47	8	23.70	316.00	5	0.25	21.50
2254+074	...	0.190	16.29	6	24.51	454.00	2^a	1.73	22.87
2356-309	...	0.165	17.18	8	23.50	42.00	5	0.90	22.38

Redshift with a star is from Rector & Stocke (2001) – $\log R_c$ [†] was thus calculated for this new z using the $\log R_c$ quoted in Vermeulen & Cohen (1994). References : (1) : Morris *et al.* (1991); (2) : Perlman & Stocke (1993) (*EMSS* XBLs except 2^a which are RBLs, 1.4 GHz); (4) : $\log R_c$ from Vermeulen & Cohen (1994); (5) : Laurent-Muehleisen *et al.* (1993) (*HEAO-1* XBLs, 1.5 GHz); (6) : Pica *et al.* (1988); (7) : Webb *et al.* (1988); (8) : Falomo *et al.* (1994); (9) : Padovani & Giommi (1995a).

Table 6.4: The Radio-loud quasars.

IAU name	Alternate name	Redshift z	m_v	ref.	$\log L_{ext}$ W Hz^{-1}	S_c(5 GHz) mJy	ref.	$\log R_c$	$\log L_o$ W Hz^{-1}
0016+731	...	1.781	19.00	4	27.37	>1500.0	1	>0.7	23.88
0106+013	...	2.107	18.39	4	27.65	3470.0	1	0.9	24.29
0153+744	...	2.338	16.00	4	26.26	1510.0	1	>2.0	25.35
0212+735	...	2.367	20.00	4	25.03	2200.0	1	>3.4	23.76
0234+285	...	1.207	18.50	4	25.68	1440.0	1	2.1	23.71
0333+321	NRAO140	1.259	17.50	4	26.44	2460.0	1	1.6	24.15
0458-020	...	2.286	19.50	4	27.17	1600.0	1	1.1	23.93
0615+820	...	0.710	17.50	4	26.38	>900.0	1	>0.8	23.60
0711+356	...	1.620	19.00	4	25.96	1500.0	1	>2.1	23.79
0723+679	3C 179	0.846	18.00	4	27.54	320.0	1	−0.68	23.57
0835+580	3C 205	1.536	17.62	4	27.89	23.0	1	−1.74	24.29
0836+710	...	2.180	16.50	4	27.04	2550.0	1	1.4	25.08
0839+616	...	0.862	17.85	4	26.84	34.0	1	−0.94	23.64
0850+581	...	1.322	18.00	4	27.45	1090.0	1	0.27	23.99
0906+430	3C 216	0.670	18.10	4	27.21	1060.0	1	−0.01	23.30
0923+392	4C 39.25	0.698	17.86	4	26.77	7320.0	1	1.3	23.44
1039+811	...	1.260	16.50	4	26.20	1120.0	1	1.5	24.55
1040+123	3C 245	1.028	17.29	4	27.44	860.0	1	0.0	24.04
1150+812	...	1.250	18.50	4	26.50	1140.0	1	1.2	23.74
1156+295	...	0.729	14.41	4	26.32	810.0	1	0.83	24.86
1222+216	4C 21.35	0.435	17.50	4	26.47	420.0	1	−0.01	23.14
1226+023	3C 273	0.158	12.85	4	26.70	39000.0	1	0.9	24.08
1253-055	3C 279	0.538	17.75	4	27.07	14500.0	1	1.1	23.24
1458+718	3C 309.1	0.905	16.78	4	27.63	2680.0	1	0.2	24.12
1641+399	3C 345	0.594	15.96	4	26.33	5520.0	1	1.5	24.05
1642+690	...	0.751	20.50	4	26.67	1260.0	1	0.7	22.45
1721+343	4C 34.47	0.206	15.46	4	25.95	470.0	1	−0.05	23.27
1828+487	3C 380	0.691	16.81	4	27.32	6590.0	1	0.7	23.85
1830+285	4C 28.45	0.594	17.16	4	27.02	450.0	1	−0.28	23.57
1901+319	3C 395	0.635	17.50	4	26.81	1480.0	1	0.5	23.49
1928+738	...	0.302	16.06	4	25.75	3210.0	1	1.3	23.38
1951+498	...	0.466	17.50	4	26.09	91.0	1	−0.24	23.20
2223-052	3C 446	1.404	18.39	4	28.24	2310.0	1	−0.15	23.90
2251+158	3C 454.3	0.859	16.10	4	27.05	9690.0	1	1.3	24.34

References : (1) : $\log R_c$ from Vermeulen & Cohen (1994); (4) : Veron-Cetty & Veron (1998).

6.3.2 Caveats

While interpreting the $L_o - R_c$ plots, it is important to keep the following caveats in mind.

1. The objects constitute an *eclectic* sample, with no rigorous selection criteria applied.

2. The beamed and unbeamed objects are not matched in redshift, nor in extended radio luminosity. We discuss the significance of this in the following section and try to come up with a 'matched' sample.

3. The L_o values for the BL Lacs and quasars are derived from their total magnitudes, and include the host galaxy contribution. Particularly in the intermediate R_c regime for BL Lacs, the host galaxies could contribute significantly to the assumed nuclear optical luminosity.

We address some of these issues in the subsequent sections.

6.3.3 Correlations with radio core prominence for the two populations

For both the FR populations, the correlation *does* extend to higher radio core prominence, broadly consistent with the predictions of the Unified Scheme and again reinforcing the idea that the nuclear optical flux density is orientation-dependent in the same way as the core radio emission and it may thus constitute the optical counterpart of the relativistically beamed radio synchrotron jet. The generalized Spearman's Rank correlation test (which uses survival analysis) indicates that both the FRI and FRII populations show a significant correlation ($p < 0.0001$) of nuclear optical luminosity with radio core prominence (see Table 6.5).

For the FRII population, we showed in § 6.2.1 that the narrow-line FRIIs do not show any correlation by themselves. However, a significant correlation ($p < 0.0001$, generalized Spearman Rank test) exists for the broad-line objects *i.e.,* the broad-line radio galaxies and quasars. These two observations taken together are consistent with there being obscuration effects by a torus in the FRIIs. Also, though more FRIs show detected optical cores as compared to FRIIs, optical cores have been detected in *all* the BLRGs observed (where the US predicts no obscuration by the torus), again consistent with this idea.

The BL Lacs by themselves also show a significant correlation of L_o with R_c, but the plot is flatter than what is expected from beaming alone. This could be due to the fact that their L_o values include the contribution from the host galaxy, particularly since this contamination is likely to be more severe at intermediate values of R_c. Although
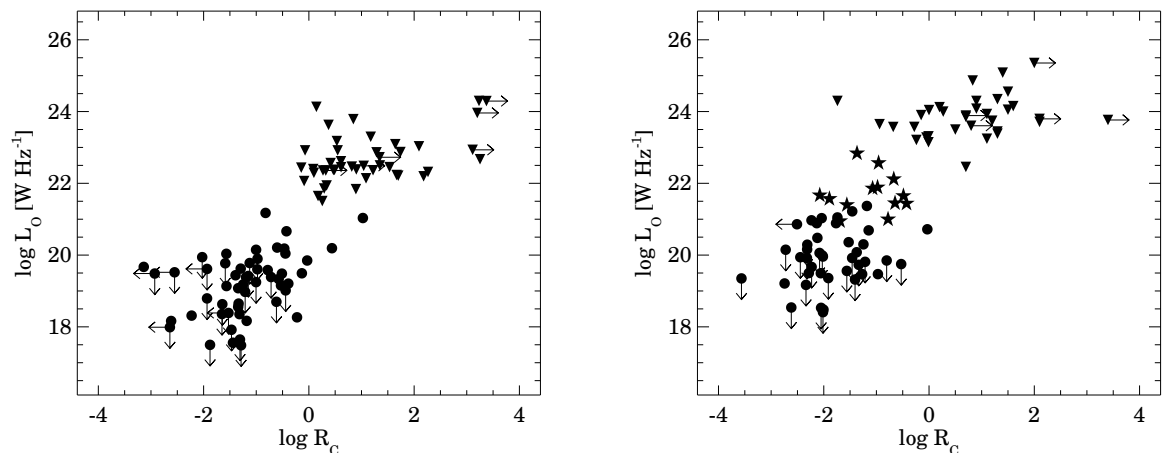
Figure 6.4: Nuclear optical luminosity L_o versus radio core prominence R_c for the FRI population (left) : • denote radio galaxies, filled triangles denote BL Lac objects. L_o vs. R_c for the FRII population (right) : • denote radio galaxies, filled triangles are radio-loud quasars and ⋆ are BLRGs. ↓ and ← denote upper limits, → denote lower limits. Statistics for the fits are listed in Table 6.5.

for many BL Lac objects where host galaxies have been imaged, the difference between the nuclear and the total optical luminosity (L_o) is less than the 50% errors assumed in L_o (for e.g., Jannuzi *et al.*, 1997), for some sources this difference can as high as a magnitude (e.g., Kotilainen *et al.*, 1998). In principle, the flattening could also be due to the presence of a luminous accretion disk, in which case the BL Lacs cannot be considered to be consistent with the unbeamed FRI radio galaxies. The use of nuclear luminosities uncontaminated by host galaxy emission for *all* the objects would clarify the issue.

A two-dimensional Kolmogorov-Smirnov test shows that the FRI and FRII populations are different at the $p < 0.0001$ level. For each of the populations, a multiple linear regression test using the statistics packages STATISTICA and ASURV (the 'Buckley James' algorithm) with radio core prominence, redshift and extended radio luminosity (L_{ext}) as independent variables for the nuclear optical luminosity, shows that the correlation coefficient for the L_o – R_c correlation is the most significant ($p < 0.0001$). Extended radio luminosity is the next most significant contributor. Since the extended radio luminosity can reasonably be assumed to be an indicator of intrinsic AGN power, this implies that variation in intrinsic nuclear power contributes significantly to the scatter in the L_o – R_c correlation. As expected, the nuclear optical luminosity is correlated with redshift, both because luminosity is expected to correlate with redshift, and because of the absence of high redshift radio galaxies in the samples.

6.3.4 Matched subsamples of FRI and FRII objects

Ideally, all the objects in each population ought to be intrinsically similar in the framework of the Unified Scheme, which means that they should all be of similar intrinsic power, from the same volume of space, and with a narrow distribution of other orientation-independent parameters. As a next best step, we attempt here to derive a 'matched' sample for the two FR populations, keeping in mind the multiple linear regression results for the whole sample discussed in the previous section.

For the FRI matched subsample, we restrict the redshifts to $z < 0.3$ and extended radio luminosity at 1.4 GHz to be $23.5 \leq \log L_{ext} \leq 25$ W Hz^{-1}. For the FRII matched subsample, the redshifts are constrained to $z < 1.3$, while the extended radio luminosity is $26.2 \leq \log L_{ext} \leq 27.6$ W Hz^{-1}. Figure 6.5 shows the $L_o - R_c$ correlations for these subsamples while the correlation and regression parameters are listed in Table 6.5. We find that the scatter seen in Figure 6.4 is considerably reduced in Figure 6.5 and the correlations improve significantly compared to the unrestricted samples. Multiple linear regression tests on the restricted samples with the independent variables, R_c, z, L_{ext} show that the $L_o - R_c$ is still the strongest correlation ($p < 0.0001$) while the contribution of L_{ext} is no longer significant.
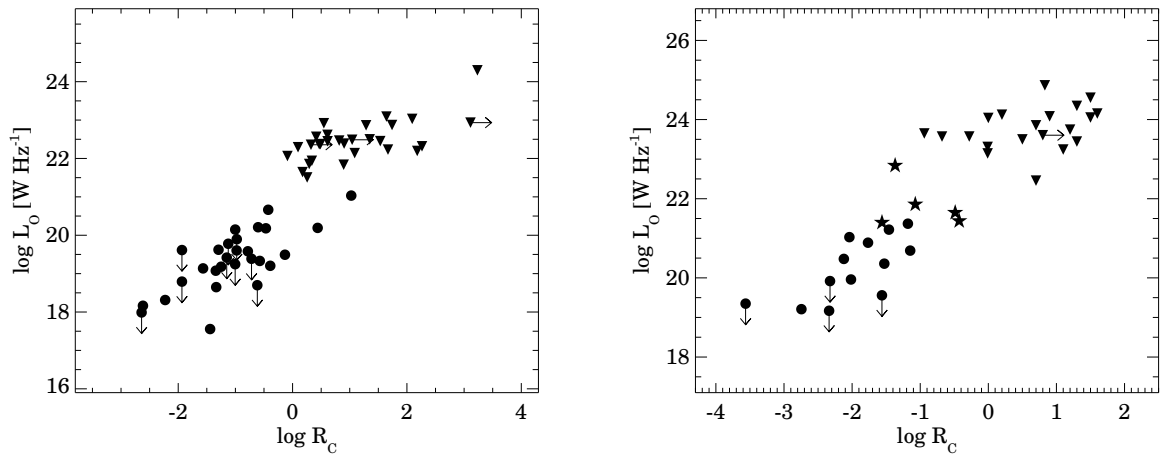
Figure 6.5: Nuclear optical luminosity L_o versus radio core prominence R_c for the matched subsample of FRI galaxies and BL Lac objects (left) and FRII galaxies and quasars (right). $\bullet$ denote radio galaxies, filled triangles denote BL Lac objects (left) and quasars (right), $\star$ are BLRGs, $\downarrow$ denote upper limits while $\rightarrow$ denote lower limits. Statistics for the fits are listed in Table 6.5.

6.3.5 Model-fitting the $L_o - R_c$ data

If bulk relativistic motion with a single Lorentz factor (γ) value applicable to the whole population were alone responsible for the variation in the nuclear optical luminosity, then the logarithmic plot of L_o against R_c would be linear. Any additional factors such as orientation effects due to a torus or thin thermal disk will cause this relationship to deviate from linearity. We attempt to fit some simple models to the data along these lines.

The model equations and the bulk Lorentz factor

We assume that the nuclear optical luminosity L_o is, in the most general case, due to the sum of synchrotron emission from the base of a relativistic jet, and thermal emission from a thin accretion disk, modified by the presence of an optically thick torus. We do not include the possibility of variation in the *intrinsic* nuclear power as discussed in § 6.3.3, nor the possibility of extinction of the optical nucleus by an extended kpc-scale dusty disk which was discussed in § 6.2.3. Our models also do not take into account any intrinsic spread in the Lorentz factors, nor the possibility that the relevant Lorentz factor for the highly beamed and mildly beamed subclasses may be systematically different due to a "spine-sheath" type structure of the jet (e.g., Hardcastle *et al.*, 1996; Laing *et al.*, 1999). However, as the multiple linear regression tests discussed in § 6.3.3 suggest, orientation appears to play the most dominant role in the variation of L_o. We write,

$$L_o = \left(\delta^p \, L_{jet}^{int} + L_{disk} \, cos \, \theta \right) \times 10^{-A_V/2.5} \tag{6.1}$$

L_{jet}^{int} is the intrinsic synchrotron luminosity from the base of the jet which is relativistically beamed by the factor δ^p, where δ is the Doppler factor and for a jet spectral index of α, the jet structure parameter p is given by $2+\alpha$ or $3+\alpha$ depending on whether the jet is continuous or blobby (e.g., Urry & Padovani, 1995). L_{disk} is the luminosity of a thin optically thick accretion disk, whose apparent luminosity is orientation-dependent due to projection (the $cos \, \theta$ term). A_V is the extinction resulting from the torus in the V band. For a half-opening angle of the torus θ_c, we have,

$$A_V = A_{V_0} \left(1 - \frac{cos \, \theta}{cos \, \theta_c} \right) \qquad \text{for} \quad \theta \geq \theta_c \tag{6.2}$$

$$A_V = 0 \qquad \text{for} \quad \theta < \theta_c$$

(Simpson, 1996)

Thus for $\theta = 90°, A_V = A_{V_0}$. For the Lorentz factor of bulk relativistic motion of the nuclear jet we have,

$$\gamma = \left(\frac{1}{2^{p-1}} \frac{R_c^{max}}{R_c^{min}} \right)^{\frac{1}{2p}}, \tag{6.3}$$

$$R_c^{int} = \frac{\gamma^p R_c^{min}}{2} \tag{6.4}$$

where R_c^{min} and R_c^{max} are the minimum and maximum values of R_c, *i.e.,* the values of R_c at edge-on ($\theta \sim 90°$) and pole-on ($\theta \sim 0°$) inclinations of the AGN respectively, and R_c^{int} is the intrinsic flux density ratio of the core and extended radio emission. We now obtain the orientation to the line of sight, θ, in terms of the core prominence, R_c. We use the relativistic beaming formulae which take into account contributions from both the approaching and receding jet (*e.g.,* Appendix C, Urry & Padovani (1995)).

$$R_c = R_c^{int} \left[\frac{1}{[\gamma(1 - \beta cos\theta)]^p} + \frac{1}{[\gamma(1 + \beta cos\theta)]^p} \right] \tag{6.5}$$

We assume a value of 3 for the jet structure factor p. We note that Urry & Padovani (1995) infer a p value of ≈ 3 based on the observations of superluminal motion within our own galaxy by Mirabel & Rodriguez (1994). We get,

$$\beta cos\theta = \sqrt{1 - \frac{(2b)^{2/3}}{\sqrt{R_c}(-2\sqrt{R_c} + \sqrt{2b + 4R_c})^{1/3}} + \frac{(2b)^{1/3}(-2\sqrt{R_c} + \sqrt{2b + 4R_c})^{1/3}}{\sqrt{R_c}}} \tag{6.6}$$

where $b = \dfrac{R_c^{int}}{\gamma^p}$.

As an approximation we assume that a single γ value is applicable to each population, and that all orientations are represented in each population, and therefore that the minimum and maximum values of R_c in each population, correspond to orientations perpendicular and parallel to our line of sight respectively. The formula using the R_c^{min} and R_c^{max} (Eq. 6.3) resulted in the lower limit to the maximum Lorentz factor $\gamma_{max} \approx 9.7$ for the FRI population. For the FRII population we get a value of $\gamma_{max} \geq 11.5$, obtained using a quasar with a upper limit to its extended radio emisson, and therefore the actual lower limit to γ_{max} could be higher. These values broadly agree with those obtained by Urry & Padovani (1995) : $\gamma_{max} \geq 9$ for the FRI population and ≥ 13 for the FRII population assuming $p = 3$. However, based on the correlation of optical and radio core emission with the isotropic Hα+[NII] emission Verdoes Kleijn *et al.* (2002) have obtained a constraint on the value of γ of ≤ 2 (assuming $p = 3$), albeit for FRI radio galaxies *alone.*

The models and the fitting procedure

We considered several simple models to compare the behaviour of the optical nuclei in the FRI and FRII populations. For the 'Jet-only' model, the entire nuclear optical luminosity is ascribed to synchrotron emission from a jet which is relativistically beamed. For the 'Jet+Disk' model, the nuclear optical luminosity is modelled as a combination of a beamed synchrotron jet and a thin optically thick disk. For the 'Jet+Disk+Torus' model, Eq. 6.1 is used *in toto*. In the 'Jet+Torus' model the entire nuclear optical luminosity is due to the beamed jet, modified by an obscuring torus.

Using the γ values derived as in Eq. 6.3 from the minimum and maximum values of R_c in our data set for each of the FRI and FRII populations and Eqs. 6.1 and 6.5 for L_o and R_c, we did a non-linear least squares fit to the data for both the FR populations separately. We used the Levenberg-Marquardt (LM) algorithm as implemented in the IDL package (the LMFIT routine). This routine gives the best-fit values of the free parameters, their standard deviations and the χ^2 goodness-of-fit. For the model-fitting we assumed the errors in the nuclear optical luminosity to be 50% (*e.g.*, Verdoes Kleijn *et al.* (2002)).

In order to quantify the goodness-of-fit of a particular model, we used the Akaike's information criterion (AIC). The AIC (Akaike, 1974) is a likelihood criterion with an added penalty term corresponding to the complexity of the model, and measures the trade-off between model complexity/parsimony and goodness-of-fit. This criterion is used to compare different model-fits and is defined as :

$$AIC = -2ln(L) + 2k \tag{6.7}$$

(Burnham & Anderson, 2002) where, ln(L) is the log likelihood function and is given by

$$ln(L) = -(n/2)[ln(2\pi) + ln(SEE/n) + 1] \tag{6.8}$$

where 'n' is the number of data-points, 'SEE' is the Standard error of estimate and 'k' is the number of parameters to be fit. Smaller AIC values indicate a better fit. We note that the goodness-of-fit criterion AIC, behaves in an inverse fashion to the χ^2 probability Q (Press *et al.*, 1992).

For the 'Jet-only' model, L_{jet}^{int} is the only free parameter and the LM algorithm yields its best fit value. For the 'Jet+Disk' model, both L_{jet}^{int} and L_{disk} are free parameters. The output of the algorithm turned out to be independent of the input seed values of these free parameters. The 'Jet+Disk+Torus' and the 'Jet+Torus' models have two additional parameters of the torus, *viz.*,, A_{V_0} and θ_c. However, apart from the quality of the data, the fact that there are more than one "local minimum" for θ_c did not allow a robust estimation of all the parameters simultaneously. (The estimated values for

θ_c strongly depended on the input seed value). We therefore adopted the procedure of manually varying the extinction A_{V_0} and torus half-opening angle θ_c and using the resulting AIC for each pair of (fixed) A_{V_0} and θ_c to infer the best fit.

Considering first the most general 'Jet+Disk+Torus' model to the fit the data, we chose a range of values for the torus parameters, A_{V_0} and θ_c, and estimated the best fit L_{jet}^{int} and L_{disk} using the LM algorithm. Results are tabulated in Table 6.6 for representative values, $A_{V_0} = 3$ and $\theta_c = 45°$ (e.g., Barthel, 1989). The resulting value of L_{disk} turned out to be insignificant in each case (see Table 6.6). We therefore further considered only the 'Jet+Torus' model which seemed more applicable to the data. For a given value of A_{V_0} we varied the θ_c from 0° through 90° and tabulated the resultant AIC. In Figure 6.7 we plot the AIC against the torus half-opening angle for different fixed values of A_{V_0}.

As a next step, we fixed the torus half-opening angle θ_c to the value which had resulted in the minimum AIC (Figure 6.7) – which is approximately the same for different values of A_{V_0} for each FR population, and let the A_{V_0} be the free parameter to be best-fitted by the LM algorithm. We found that the resultant A_{V_0} for the FRII objects was independent of the seed value whereas it depended on the initial value for the FRI objects. In this manner we estimated the "Best fit" 'Jet+Torus' model with values of A_{V_0} and θ_c which gave the least AIC. Table 6.6 lists the fitted parameters of the "Best fit" model for both the FR populations and Figure 6.6 shows the best fit curves to each of the FR populations.

The results

The results of the model-fitting are given in Table 6.6. For the FRI population, the 'Jet-only' model is better than all the others. The 'Jet+Disk' model in fact yields a value for L_{disk} which is comparable to its standard deviation σ obtained from the fitting. Further, the 'Jet+Torus' model is best fit by parameters $A_{V_0} \approx 0.1$ and $\theta_c \approx 90°$ which are equivalent to there being no torus.

For the FRII population as a whole, the results are less clear. Formally, the 'Jet-only' model has the least AIC, but the other models also yield comparable values. However, the L_{disk} that is obtained for 'Jet+Disk' and 'Jet+Disk+Torus' is unphysical. When only the broad-line objects among the FRIIs, *viz.*, the BLRGs and quasars are considered, the 'Jet+Disk' model was a better fit than the 'Jet-only' model (Table 6.6). This is consistent with the fact that the 'big blue bump' (attributed to the accretion disk) is observed in all these objects, and, in the framework of the Unified Scheme, the torus does not obscure the central regions in them. For the whole population, a larger number

of data points in the regime where the disk is expected to be relatively most prominent, *viz.*, the intermediate R_c region, are required to derive a more robust quantitative value for L_{disk} since at large R_c the jet overwhelms the disk emission and at very small R_c the torus obscures it.

Given the unclear results of the model-fitting for the FRII population, we carry the procedure a bit further by contrasting the behaviour of the AIC for the FRIs and FRIIs in the 'Jet+Torus' model case. Figure 6.7 shows that the family of AIC plots for each population differ systematically from each other. The plots can be broadly divided into two parts. Below $\theta_c \approx 30°$ the AIC drops for both the FRI and FRII population (shaded region in Figure 6.7). This formally implies that the fit gets better for opening angles of the torus that are smaller than $\theta_c \approx 30°$, but clearly is the result of the algorithm trying to fit the *entire* variation in L_o by torus obscuration *alone*. Above $\theta_c \approx 35°$ the AIC declines again and reaches a minimum at angles close to $90°$ for the FRIs, consistent with there being no torus. For the FRIIs, the AIC does not decline appreciably above $\theta_c \approx 35°$. In addition it shows a conspicuous minimum at $\theta_c \approx 37°$.

Thus although simple model-fitting using the LM alogorithm yielded ambiguous results for the FRIIs on the face of it, by rejecting the possibility that the entire variation in L_o is due to obscuration by a torus, we obtain model parameters that are broadly consistent with the predictions of the Unified Scheme. The model-fitting resulted in the best θ_c roughly coinciding with the angle where the upper limits start appearing in FRII galaxies. The best A_{V_0} turned out to ≈ 3 mag for the FRIIs at the best θ_c while for the FRIs, A_{V_0} turned out to be ≈ 0. We point out that the A_{V_0} that we infer here is in the nature of a lower limit, since detection limits would exclude measured data points corresponding to higher values of A_{V_0}. We find that the behaviour of FRI and FRII optical nuclei are distinctly different in that the model-fitting results are unambiguous for the FRIs while they are not so for the FRIIs, hinting at intrinsic differences between FRIs and FRIIs.

It maybe recalled that the BL Lac objects taken by themselves show a flatter logarithmic distribution of L_o against R_c than would be expected from beaming alone, and indeed model fitting just the BL Lacs gives the 'Jet+Disk' model to be the best one for them, with an implied L_{disk} of 3.3×10^{22} W Hz^{-1} (See Table 6.6). As was stated in § 6.3.3, this is most likely to be due to the contaminating host galaxy luminosity mimicking emission from a disk. We note however, that unless values for their optical nuclei that are uncontaminated by the host galaxy are used, we cannot totally rule out an accretion disk in the BL Lacs alone, and therefore the implication that they may not be intrinsically similar to the FRI radio galaxies.

For the *smaller* matched subsamples of FRIs and FRIIs, the variation of AIC with
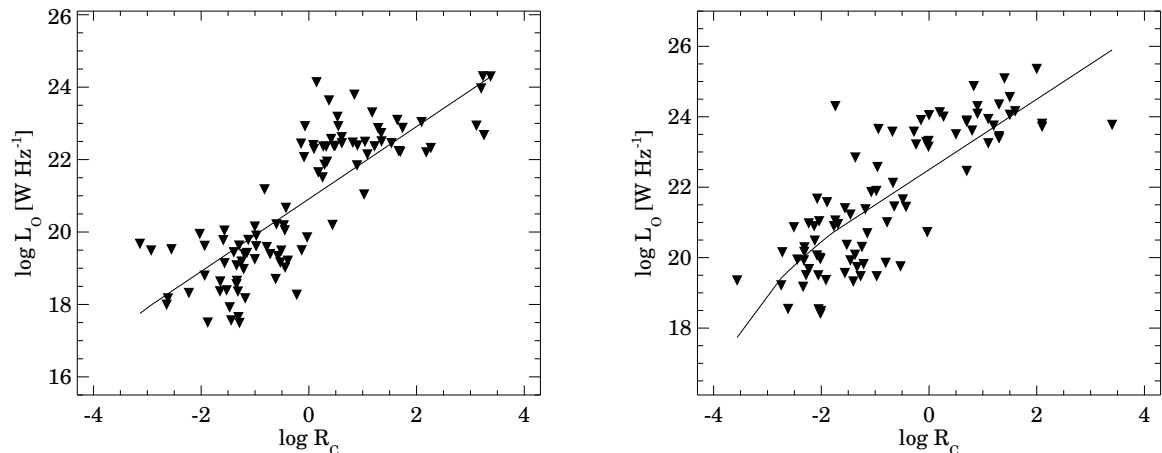
Figure 6.6: Best fits to the FRI (left) and FRII (right) populations using only a 'Jet+Torus' model. Table 6.6 lists the model parameters.

θ_c (see Figure 6.8) is broadly similar to that of their respective unrestricted samples. The only discernible difference for the 'matched' FRIIs is that the 'AIC minimum' observed at $\theta_c \approx 37°$ for the whole sample, is now no longer prominent. However, this is not surprising in view of the fact that the 'matched' FRII objects are much fewer, especially at low radio core prominence values.

We considered the residuals for the model-fit on the R_c versus L_o data and examined them for any correlations with R_c and L_o. For both FRIs and FRIIs we find no correlation of the residuals with R_c and L_o. However, there seems to be a weak correlation for the BL Lacs considered alone. This may be reflective of the effects of ignoring the host galaxy luminosity when taking the optical core luminosity.

We note that while reliable quantitative results cannot be obtained using the current data because of the drawbacks with the sample, the approach and the results indicate that it is a good approach to derive various parameters if data for a rigorous and large sample are available. Better data would allow more parameters to be incorporated and controlled.

6.4   Discussion

We have investigated the nature of the newly discovered parsec-scale optical nuclei in radio galaxies in the context of the Fanaroff-Riley divide and the simple Unified Scheme. We have used the radio core-prominence parameter R_c as a statistical indicator of orientation with respect to our line of sight. We use a total of 54 FRI radio galaxies,
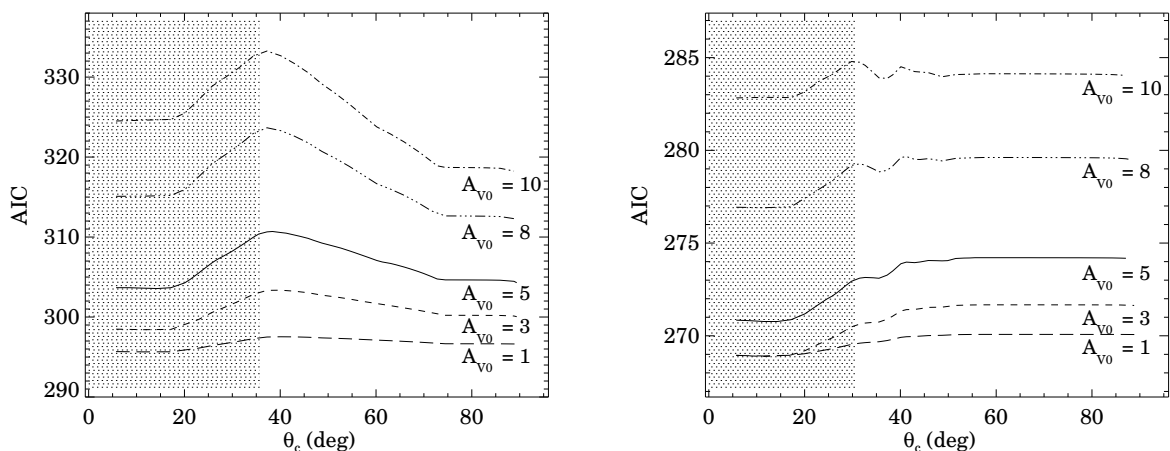
Figure 6.7: AIC values for different initial A_{V_0} plotted against torus opening angles θ_c (in degrees) for the FRI (left) and the FRII (right) populations for the 'Jet+Torus' model. For a given A_{V_0}, AIC was estimated at $2°$ intervals of θ_c. The shaded area denotes the region where the model becomes unphysical; we disregard this regime in our discussion. In the physical regime, AIC is minimum at around $90°$ for the FRIs and $37°$ for the FRIIs.

55 FRII radio galaxies, and further, 44 BL Lac objects (of FRI morphology) and 34 radio-loud quasars in the analysis, which includes statistical analysis and simple model-fitting.

We find that the optical core luminosity shows a strong correlation with radio core prominence R_c, or equivalently, orientation, for the 54 FRI radio galaxies but not for the 42 narrow-line FRII radio galaxies, which is confirmed by both non-parametric and parametric statistical tests. The strong correlation for the FRI radio galaxies suggests that their optical cores are orientation-dependent in the same way as the radio jets, and are likely to be of a similar non-thermal origin. The lack of correlation for the narrow-line FRII radio galaxies is suggestive of the presence of some obscuration (probably in the form of a dusty torus) of L_o which spoils any intrinsic correlation with R_c. We also note that there are more upper limits than detections of optical cores in the FRIIs.

Although the above correlation is very significant for the FRI galaxies, there is a significant amount of scatter that remains. A linear regression suggests that R_c accounts for $\sim 60\%$ of the variation of the logarithmic L_o. Using the extended (*i.e.,* kpc-scale) luminosity of the Hα+[NII] line as a proxy for the intrinsic AGN power for the 23 FRI radio galaxies for which this measurement is available, we find that variation in intrinsic power could contribute to the above residual scatter. On the other hand, several FRI galaxies have been found to have extended (kpc-scale) dusty disks. For the 18 FRI galaxies studied here for which such disks have been seen, the nuclear optical
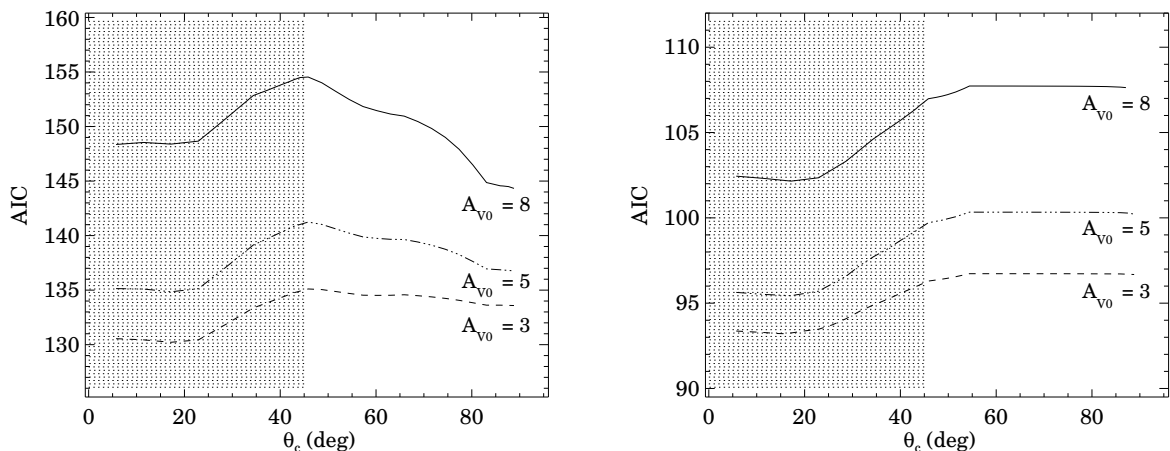
Figure 6.8: AIC values for different initial A_{V_0} plotted against torus opening angles θ_c (in degrees) for the matched subsamples of FRI (left) and the FRII (right) populations for the 'Jet+Torus' model. The shaded area denotes the region where the model becomes unphysical; we disregard this regime in our discussion. In the physical regime, AIC is minimum at around $90°$ for the FRIs while the case is not clear for FRIIs.

luminosity significantly correlates with the orientation of this disk as measured by its apparent ellipticity. The orientation of these disks appear to bear no clear relation to the orientation of the AGN axis, however, as evidenced by the lack of any correlation with the core prominence R_c. We note that a similar misalignment between the AGN axis and the host galaxy disk has previously been reported for Seyfert galaxies by, for example, Kinney *et al.* (2000).

We find that the optical core luminosity of FRI and FRII radio galaxies taken along with 44 BL Lacs of FRI morphology and 34 radio-loud quasars respectively is strongly correlated with radio core prominence. We note that while the FRII radio galaxies alone did not show such a correlation, the broad-line FRIIs, *viz.,* the BLRGs and quasars taken together show a significant correlation of L_o with R_c, consistent with the idea that their obscuring tori is no longer attenuating the optical nuclei in them. A multiple linear regression test with radio core prominence, redshift and extended radio luminosity shows that the $L_o – R_c$ correlation is the most significant for both the FR populations.

In order to understand the seemingly different functional forms obeyed by the data, we tried to fit some simple models to them. The most general model comprises of a relativistic optical synchrotron jet, an orientation-dependent thin accretion disk and an obscuring torus. We did not incorporate intrinsic variation in any of these components, nor the obscuring effects of an *extended* dusty disk. From the minimum and maximum values of R_c we derived the Lorentz factor γ to be ≈ 9 for the FRI population and $\approx$

11.5 for the FRIIs, consistent with other inferences in the literature. The primary result from the model-fitting is that a relativistic beamed jet alone is a good fit to the variation in the optical cores of the FRI population. Although formally the 'Jet+Torus' model is also a good fit, the values of the opening angle and extinction derived are virtually equivalent to there being no torus ($A_V \approx 0$ and $\theta_c \approx 90°$). For the FRII population, model-fitting indicates that formally the best fit is again a beamed synchrotron jet. But a beamed jet obscured by a torus with an inferred opening angle of $\approx 37°$ is a comparable fit. Model-fitting the broad-line FRII sources by themselves implies that an optically luminous accretion disk contributes significantly along with the relativistic beamed jet.

These results are tentative to the extent that the objects that we have used constitute an eclectic sample. A more rigorous analysis requires construction of samples where the objects of a given FR population are chosen to be intrinsically similar in the framework of the Unified Scheme and from the same volume of space. Further, for the highly beamed objects, *viz.,* the quasars and much more so, the BL Lacs, measurements of their nuclei uncontaminated by the host galaxy should be used.

For the *smaller* matched subsamples of FRIs and FRIIs, where the extended radio luminosity and redshift are confined to a narrow range, a multiple linear regression test with the variables, R_c, z, L_{ext} shows that $L_o - R_c$ is still the strongest correlation while L_{ext} is no longer significant. The variation of AIC with θ_c is *broadly* similar to that for the unrestricted sample, validating our procedure and the *qualitative results* for the whole sample regarding the differences between FRIs and FRIIs. The only discernible difference for the matched FRIIs is that the 'AIC minimum' seen at $\theta_c \approx 37°$ for the unrestricted sample, is now no longer prominent. However, this is probably due to much fewer 'matched' FRIIs, especially at low R_c.

The quantitative results of the model-fitting, on the other hand, can clearly be useful only when applied to a larger sample that is rigorously selected.

6.5   Conclusions

We use the radio core prominence R_c as a statistical indicator of orientation and find that the systematic differences between radio-loud AGN of the two Fanaroff-Riley types appear to also extend to their optical nuclei, in a manner that is consistent with the predictions of the simple Unified Scheme. We find that the behaviour of FRI and FRII optical nuclei are qualitatively different. We find that,

1. The luminosity of the parsec-scale optical nuclei in the FRI radio galaxies is orientation-dependent, while that in the FRII radio galaxies is not. This result is consistent with

the idea that FRIIs contain an obscuring torus, (as required by the simple US) whereas there is no torus in the FRIs.

2. For the FRI radio galaxies, though the correlation with orientation is very significant, a significant amount of residual scatter remains. This may be due to obscuration from an *extended kpc-scale* dusty disk. The axis of this disk appears unrelated to the AGN axis. The residual scatter may also be due to intrinsic variation in the optical luminosity.

3. The optical core luminosity correlates significantly with R_c, or equivalently, orientation, for the FRI radio galaxies and BL Lacs of FRI morphology taken together – the FRI population. Our model-fitting suggests that a relativistically beamed optical jet gives the best fit.

4. For the FRII radio galaxies and radio-loud quasars taken together – the FRII population, the optical core luminosity again correlates significantly with R_c. Our model-fitting indicates that formally the best fit is again a beamed synchrotron jet. But a beamed jet obscured by a torus with an inferred opening angle close to 40° is a comparable fit, and is able to explain the contrasting behaviour of the FRI and FRII data.

5. The scatter in the L_o – R_c correlation is likely to be a result of the spread in intrinsic AGN power.

6. Our model-fitting suggests that the luminosity of the intrinsic (*i.e.,* unbeamed) jet in the FRIIs is approximately an order of magnitude larger than for the FRIs, although this result needs to be confirmed using a rigorous sample.

7. The data for the broad-line FRIIs alone are best fit by a model that comprises of a relativistic jet and a thin optically thick disk, consistent with the presence of the 'big blue bump' in them.

The robustness of the above results are limited by the facts that (a) the "samples" used are eclectic, (b) the luminosity of the optical nuclei in the highly beamed objects is contaminated by the contribution of the host galaxy, and (c) there could be variability between the epochs of the optical and radio measurements. A robust analysis requires rigorous measurement of the optical luminosity as well as samples that are rigorously selected, with the objects of a given FR population chosen to be intrinsically similar in the framework of the Unified Scheme and from the same volume of space.

Table 6.5: Statistics of correlations.

Type	N (l_x, l_y)	X	Y	Spearman	Kendall	Schmitt(slope, intercept)
FRI galaxies	54 (5,17)	$\log R_c$	$\log L_o$	0.0001	0.0001	0.52(0.17) 19.40(0.25)
BL Lacs	44 (6,0)	$\log R_c$	$\log L_o$	0.0295	0.0323	0.17(0.14) 22.45(0.16)
FRI & BL Lacs	98 (11,17)	$\log R_c$	$\log L_o$	<0.0001	<0.0001	1.15(0.10) 20.72(0.14)
FRI-BL sample	57 (1,2)	$\log R_c$	$\log L_o$	<0.0001	<0.0001	1.20(0.17) 20.72(0.16)
FRII galaxies	42 (1,20)	$\log R_c$	$\log L_o$	0.2175	0.2392	0.32(0.23) 20.12(0.38)
BLRGs & QSRs	47 (5,0)	$\log R_c$	$\log L_o$	<0.0001	<0.0001	0.60(0.12) 23.15(0.12)
FRII & QSRs	89 (6,20)	$\log R_c$	$\log L_o$	<0.0001	<0.0001	1.18(0.11) 22.26(0.17)
FRII-QS sample	38 (0,3)	$\log R_c$	$\log L_o$	<0.0001	<0.0001	1.12(0.11) 22.71(0.15)
FRI galaxies	23 (3,6)	$\log L_{line}$	$\log L_o$	0.0324[a]	0.0131	0.56(0.15) 0.05(5.09)
FRII galaxies	27 (3,10)	$\log L_{line}$	$\log L_o$	0.0017[a]	0.0014	0.65(0.20) –3.28(7.00)
FRII & BLRGs	35 (3,10)	$\log L_{line}$	$\log L_o$	0.0003	0.0002	0.76(0.24) –6.69(8.56)
FRI galaxies[V]	9 (0,2)	b/a (d)	$\log L_o$	0.2499[a]	0.2310	1.83(1.22) 17.67(0.89)
"	14 (0,5)	b/a ($d+l$)	$\log L_o$	0.0928[a]	0.0399	1.91(0.61) 17.54(0.37)
"	9 (0,0)	b/a (d)	$\log R_c$	0.0732[a]	0.0953	–1.09(0.47) –0.19(0.37)
"	14 (0,0)	b/a ($d+l$)	$\log R_c$	0.6065[a]	0.5200	–0.37(0.40) –0.80(0.23)
FRI galaxies[D]	6 (0,0)	b/a (d)	$\log L_o$	0.0845[a]	0.0909	2.24(0.82) 17.62(0.48)
"	7 (0,0)	b/a ($d+l$)	$\log L_o$	0.0543[a]	0.0509	2.33(0.76) 17.63(0.54)
"	7* (0,0)	b/a (d)	$\log R_c$	0.0802[a]	0.0985	1.39(0.53) –2.30(0.29)
"	8* (0,0)	b/a ($d+l$)	$\log R_c$	0.0588[a]	0.0833	1.51(0.48) –2.30(0.29)
FRI galaxies[V+D]	12 (0,2)	b/a (d)	$\log L_o$	0.1855[a]	0.1531	1.53(0.70) 17.95(0.44)
"	18 (0,5)	b/a ($d+l$)	$\log L_o$	0.0353[a]	0.0248	1.90(0.60) 17.66(0.33)
"	12 (0,0)	b/a (d)	$\log R_c$	0.7630[a]	0.6808	–0.06(0.69) –1.06(0.49)
"	18 (0,0)	b/a ($d+l$)	$\log R_c$	0.9085[a]	0.9698	0.02(0.48) –1.12(0.28)

Statistical significance of various correlations (of X and Y) and linear regression fits. All the results are derived using ASURV as implemented in IRAF. Col. (1): the subclass of objects under consideration, 'FRII galaxies' refer to narrow-line FRIIs alone, 'QSRs' refer to quasars, 'FRI-BL' and 'FRII-QS samples' refer to the matched subsamples of FRIs and FRIIs as described in § 6.3.4; FRI galaxies with superscripts V, D, $V+D$ refer to FRI sources from Verdoes Kleijn *et al.* (1999), de Koff *et al.* (2000) and from both papers, respectively; $\star$ an additional FRI source – 3C 430 with a disk of $b/a = 0.15$ and $\log R_c = -2.5$ was included in the $b/a - \log R_c$ correlation; Col. (2): the number of data points and those with limits in X and Y respectively, in paranthesis; Col. (3) & (4): the independent and dependent variable respectively; b/a being the ratio of the minor-to-major axis of the extended dust feature seen in the *HST* images of radio galaxies, 'd' and 'l' standing for a dust disk and a lane respectively, '$d+l$' refers to our jointly considering disks and lanes in the correlations; Col. (5) & (6): probability that no correlation exists between X and Y from Spearman's ρ and Kendall's τ correlation tests respectively; 'a' - Spearman Rank test is not accurate as no. of objects, N < 30; Col. (7): slope and intercept with standard deviation in parantheses from Schmitt's linear regression test, bootstrap approximation using 200 iterations, X bins = 10, Y bins = 10.

Table 6.6: Parameters from the different model-fits for the FR populations.

| | Model | A_{V_0} | θ_c | L_{jet}^{int} | σ | L_{disk} | σ | AIC |
				Model	Outputs			
FRI	Jet only	...	...	2.7e+20	1.3e+19	...	...	295.2
	Jet+Disk	...	...	2.6e+20	1.4e+19	8.5e+17	1.1e+18	297.1
	Jet+Disk+Torus	3.0	45	2.7e+20	1.5e+19	3.5e+18	1.6e+18	304.5
	Jet+Torus	3.0	45	2.9e+20	1.4e+19	...	...	303.1
	Best fit	0.1	90	2.6e+20	1.3e+19	...	...	295.3
FRI^M	Jet only	...	...	3.8e+20	2.5e+19	...	...	132.3
	Jet+Disk	...	...	4.1e+20	2.9e+19	−7.9e+18	2.0e+18	133.4
	Jet+Disk+Torus	3.0	45	4.4e+20	3.3e+19	−1.4e+18	4.1e+18	137.0
	Jet+Torus	3.0	45	4.4e+20	2.9e+19	...	...	135.0
FRII	Jet only	...	...	5.8e+21	3.0e+20	...	...	269.6
	Jet+Disk	...	...	6.5e+21	3.7e+20	−6.7e+19	1.2e+19	270.7
	Jet+Disk+Torus	3.0	45	6.7e+21	3.9e+20	−5.8e+19	1.5e+19	272.9
	Jet+Torus	3.0	45	6.1e+21	3.2e+20	...	...	271.5
	Best fit	3.0	37	6.5e+21	3.4e+20	...	...	270.8
$FRII^M$	Jet only	...	...	1.6e+21	1.3e+20	...	...	94.3
	Jet+Disk	...	...	1.8e+21	1.5e+20	−1.9e+20	2.1e+19	93.4
	Jet+Disk+Torus	3.0	45	2.0e+21	1.7e+20	−2.1e+20	2.5e+19	95.9
	Jet+Torus	3.0	45	1.8e+21	1.4e+20	...	...	96.2
BL FRII	Jet only	...	...	2.2e+22	1.6e+21	...	...	127.3
	Jet+Disk	...	...	1.3e+22	1.2e+21	1.5e+22	2.7e+21	123.3
BL Lacs*	Jet only	...	...	1.2e+21	9.0e+19	...	...	118.4
	Jet+Disk	...	...	6.2e+19	1.4e+19	3.3e+22	3.0e+21	78.6

$\star$ See § 6.3.5 in the text. In Col.(1) FRI/FRII and FRI^M/$FRII^M$ stand for the FRI/FRII population and its matched subsample as discussed in § 6.3.4, BL FRII stand for the broad-line FRIIs *viz.*, BLRGs and quasars. A_{V_0} and θ_c (in degrees) are the fixed initial parameters for the models where a torus is incorporated. σ is the standard deviation for the variable on the left. A lower AIC (Akaike's Information Criterion) value indicates a better model fit. The 'Best fit' model is the 'Jet+Torus' model for FRIs and FRIIs for which AIC is the minimum (see § 6.3.5), the A_{V_0} and θ_c (in degrees) are the parameters corresponding to this fit.

Chapter 7

Synthesis, conclusions and future work

7.1 Synthesis of our observations

7.1.1 Comparison of parsec-scale polarization of FRI and FRII radio galaxies

We have observed four FRI radio galaxies for parsec-scale polarization using VLBP and detected polarization in all of them. We find that the detection of polarization and the relatively high fractional polarization in the cores of FRI radio galaxies ($m_c \sim 0.4 - 1\%$) is in contrast to the results obtained for FRII radio galaxies, where typically polarization is not detected in parsec-scale cores or it is very low ($m_c \sim 0.2 - 0.4\%$) (Taylor *et al.*, 2001; Pollack *et al.*, 2003; Middelberg *et al.*, 2003). Keeping in mind the Doppler boosting effects, we expect the jets in FRI radio galaxies to be relatively less boosted in total intensity, due to their slower speeds, compared to the FRII radio galaxies. If we assume that the inner jets in FRI and FRII radio galaxies are only a few percent polarized, the polarized flux density may fall below the detection limit in FRIIs. This could then account for the polarization trends seen in FRIs and FRIIs.

Rusk (1988) and Rudnick *et al.* (1986) find that the kpc-scale cores in FRII radio galaxies are typically $< 0.6\%$ polarized while the cores in quasars have $2 - 5\%$ polarization, suggesting the presence of orientation-dependent, depolarizing circumnuclear matter in FRIIs. There may be a larger amount of circumnuclear matter in FRIIs as compared to FRIs (where the US does not require an obscuring torus), in the form

of a molecular torus with an ionized inner edge, corona of an accretion disk, clouds that make the narrow-line and broad-line region. This would lead to high and spatially variable RM around the central engines in radio galaxies which would lead to beam depolarization (e.g., Zavala & Taylor, 2002). However, there may also be the question of differences in instrumental detection limits. Most of the FRIIs observed for pc-scale polarization in the literature, have been observed with VLBA alone, while the four FRIs studied by us have been observed with global VLBI.

If we assume that the 'shock-in-jet' model of Wardle (1998) is correct for the BL Lac jets and the AGN orientation does not influence the B-field orientation much and the RM correction to the observed polarization electric vectors (χ) vectors in FRIs is small ($\leq 10°$), then our finding of BL Lac-like B-field geometry in three out of four FRIs is consistent with the predictions of the Unified Scheme. The 'shock-in-jet' model also predicts that the FRII jets would primarily have longitudinal magnetic-fields, similar to that observed in quasars, which is consistent with the observations of a few FRII radio galaxies with detected polarization, e.g., 1010+350 (Pollack *et al.*, 2003), 3C 111 (our observations).

7.1.2 Comparison of parsec-scale polarization of BL Lacs and radio-loud quasars

In radio-loud quasars, the fractional polarization of the VLBI core, m_c, is typically $< 2\%$, while it is typically $2 - 5\%$ in BL Lac objects, although some sources may show upto 10% fractional polarization (Cawthorne *et al.*, 1993; Gabuzda, 1997; Pollack *et al.*, 2003). The orientation of the polarization electric vectors in the VLBI cores of quasars had not shown a systematic trend until the recent work of Pollack *et al.* (2003), which shows quasar cores to preferentially have χ's which are transverse to the jet direction. The observations of BL Lac cores by Gabuzda *et al.* (2000) have demonstrated a bimodal χ distribution, with χ either aligned with or perpendicular to the VLBI jet; it has recently been suggested that this bimodality may be associated with bimodality in the optical depth of the polarized regions within the observed VLBI core (Gabuzda, 2003).

There are no systematic differences in the fractional polarization of the VLBI jets in quasars and BL Lacs. Fractional polarization of the VLBI jets, m_j, range from $0 - 65\%$ in both quasars and BL Lacs (Cawthorne *et al.*, 1993; Gabuzda, 1997). There is also a systematic difference seen in the orientation of the polarization electric vector with respect to the position of the local VLBI jet direction – χ vectors are predominantly transverse to the jet directions in core-dominated quasars while they are predominantly longitudinal in the primarily low-energy peaked BL Lac jets (Cawthorne *et al.*, 1993;

Gabuzda, 1997). We find however, that the high-energy peaked BL Lac jets tend to have predominantly transverse χ vectors, similar to quasars.

It is now known that the RM in the parsec-scale cores of quasars is of the order of a few 1000 rad m^{-2} while it is only a few 100 rad m^{-2} in the cores of BL Lacs (Zavala & Taylor, 2002). Therefore, there are fewer thermal electrons to Faraday rotate the EVPA of polarized emission in BL Lacs. This has implications for greater depolarization in quasar cores and the cores of FRII radio galaxies, when compared to BL Lacs and FRI radio galaxies.

7.1.3   Optical nuclei in FRIs and FRIIs

We have attempted to fit simple model-fits to the optical nuclear data obtained from the *HST* observations of FRI and FRII radio galaxies (Chapter 6). Our model-fitting results point to intrinsic differences between FRI and FRII radio galaxies, on parsec-scales. An obscuring torus is required to explain the behaviour of the optical nuclei in FRIIs, but not in the FRIs. This result would then be consistent with the detection of polarization in all the FRI radio galaxies observed by us.
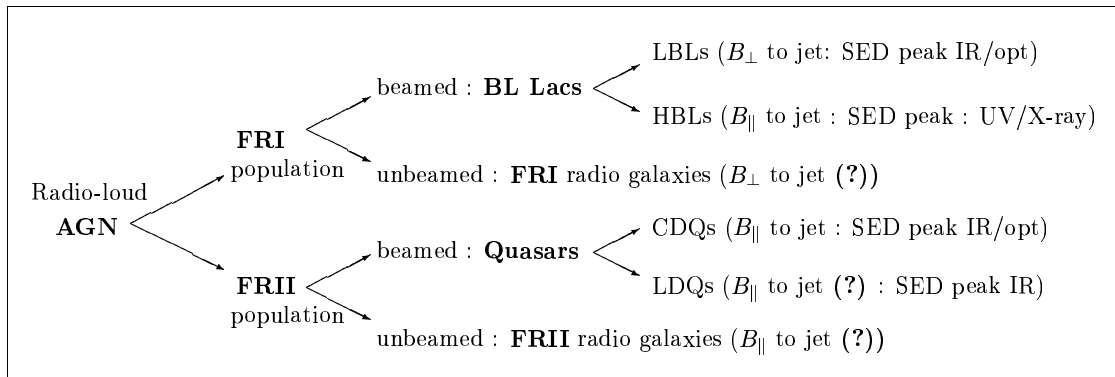
Figure 7.1: This figure summarises our present knowledge of the B-field orientations and SED peaks for the various AGN subclasses, after incorporating the results of our VLBP observations of BL Lac objects, FRI and FRII (3C 111) radio galaxies.

7.2   Conclusions of the thesis

1. We have constructed a sample of radio galaxies to meaningfully compare the nuclear properties of those of type FRI and FRII. In the context of the Fanaroff-Riley divide, VLBP and *HST* observations of this sample probe the conditions in the

centres of radio galaxies in terms of the presence of ordered B-fields, depolarizing ionized circumnuclear material which could be associated with an accretion disk or be present as gas in the broad-line region, and dusty obscuring tori which could hide the optical emission as well depolarize radio emission from it's inner ionized edge.

2. We detect parsec-scale polarization in all four FRI radio galaxies observed as part of a pilot study to investigate the B-field geometry in our sample of radio galaxies.

3. Extensive parsec-scale radio structure has been detected for the first time in the FRI radio galaxy 3C 78.

4. Comparison of our VLBI map of the FRI radio galaxy 3C 66B with others from literature suggests that the motion of the jet components in 3C 66B is subluminal $(v \simeq 0.22c)$.

5. Detection of polarization in the core of the FRI 3C 270, which is suggested to have free-free absorption in a nuclear gas disk, implies that the nuclear disk is probably thin and fails to significantly depolarise the emission from the base of the radio jet.

6. The FRI radio galaxy 3C 264, shows evidence of a 'sheath-layer' with longitudinal B-field, consistent with the 'spine-shear' geometry seen in radio galaxies on kiloparsec-scales.

7. The FRI radio galaxy 3C 270, shows the lowest jet-to-counter-jet ratio and the highest inferred angle to line-of-sight θ. Its lowest relative proper motion is consistent with its plane-of-sky orientation, where Doppler beaming effects are the least.

8. B-field geometry in FRIs is similar to that observed in BL Lac objects in three out of four sources. As Gabuzda *et al.* (1994) postulate, the BL Lac jets and by implication, the "parent" FRI radio galaxies, have lower velocities and weaker longitudinal magnetic fields which allow shocks to form easily, gively rise to a predominantly transverse B-field configuration. Alternatively as Gabuzda *et al.* (2003) suggest, in the slower BL Lac (and by implication FRIs) jets, the toroidal component of the magnetic field may dominate. If so, then the B-field geometry in FRIs is consistent with the predictions of this picture in the framework of the radio-loud Unified Scheme.

9. The detection of polarization in all the FRI radio galaxies observed suggests the possible absence of circumnuclear ionised matter, possibly in the form of a dusty obscuring torus, in FRIs, which could depolarize the synchrotron emission.

10. The parsec-scale radio structure and the corresponding magnetic field in the Broad line radio galaxy 3C 111, observed at six different epochs at 8 and 43 GHz, five months after a large millimeter outburst, is rapidly evolving.

11. The comparison of 43 and 8 GHz images at three epochs separated by a few months shows that Faraday and/or optical depth effects were important at $r \simeq 0.5$ mas from the core in epoch 1996.52, but appear to be less important near the inner-jet/core regions. It is possible that the core was optically thick at 8 GHz but optically thin at 43 GHz in epoch 1997.78, but further analysis is required to confirm this. Thus, the Faraday and optical depth effects are seen to evolve along the jet.

12. The 43 GHz images point to the dominant B-field being longitudinal in the inner and outermost jet of the FRII 3C 111.

13. Assuming that the 43 GHz emission is optically thin, the B-field is primarily longitudinal in both the innermost and outermost parts of the jet. In the region of substantial bending at 1–2 mas from the core, however, the B-field structure is complex presumably due to a combination of bending (possibly giving rise to shocks) and interaction of the jet with its surrounding medium.

14. The jet motion is mildly superluminal. A preliminary analysis suggests speeds of $v \simeq 1.6c$, but this must be verified by more detailed modeling of the jet structure at 43 GHz.

15. VLBP observations of low–energy peaked BL Lacs (LBLs) and high–energy peaked BL Lacs (HBLs) reveal differences in the core fractional polarizations, similar to the trend observed on arcsecond-scales – LBLs have higher core fractional polarizations compared to HBLs.

16. The jet fractional polarizations do not show systematic differences in LBLs and HBLs.

17. The ordered component of the B-fields in the parsec-scale jets of HBLs tend to be parallel to the local jet direction. This contrasts with the tendency for the B-fields in the parsec-scale jets of LBLs which are perpendicular to the local jet direction.

18. The systematics of the magnetic-field geometry do not reflect the sequence in the SED peaks of CDQs, LBLs and HBLs : the B-field orientation goes from longitudinal to transverse to longitudinal while the SED peaks form a sequence of increasing frequency.

19. The VLBI-core EVPAs do not show any systematic differences between HBLs and LBLs. In both cases, there is a clear tendency for the core polarization electric vectors to lie either parallel or perpendicular to the jet direction (e.g., Gabuzda *et al.*, 2000).

20. Several of the observed HBLs show evidence for a "spine-sheath" magnetic-field structure, with transverse B-field in the inner region of the jet and longitudinal B-field at the edges. This result may point in the direction of a helical magnetic field threading the jets of these objects, in turn having implications for mechanisms for the production of circular polarization in them.

21. Currently available circular polarization measurements in the literature suggest that quasars may be more likely to show detectable circular polarization than BL Lacs. However, the situation is not clear, since the largest difference in detection rates are found in the VLBI measurements, and the low detection rate for the BL Lac objects in this case may be due to the fact that the observed quasars happen to have brighter VLBI cores on average than the BL Lacs.

22. Given the recent advances in circular polarization measurement techniques on both arcsecond (ATCA) and milliarcsecond (VLBI) scales, which have made detections possible in at least a minority of BL Lacs (and quasars) with relatively faint compact cores, it is beginning to become feasible to obtain circular polarization measurements of well-defined samples on various scales. This would then enable *rigorous* tests of the predictions of various scenarios for the physical differences between different types of object.

23. We use the radio core prominence R_c as a statistical indicator of orientation and find that the systematic differences between radio-loud AGN of the two Fanaroff-Riley types appear to also extend to their optical nuclei, in a manner that is consistent with the predictions of the simple Unified Scheme.

24. The luminosity of the parsec-scale optical nuclei in the FRI radio galaxies is orientation-dependent, while that in the FRII radio galaxies is not. This result is consistent with the idea that FRIIs contain an obscuring torus, (as required by the simple US) whereas there is no torus in the FRIs.

25. For the FRI radio galaxies, though the correlation with orientation is very significant, a significant amount of residual scatter remains. This may be due to obscuration from an *extended kpc-scale* dusty disk, known to exist in some of these objects. The data available on these disks indicate that the axis of this disk is unrelated to the AGN axis. The residual scatter may also be due to intrinsic variation in the optical luminosity.

26. The optical core luminosity correlates significantly with R_c, or equivalently, orientation, for the FRI radio galaxies and BL Lacs of FRI morphology taken together – the FRI population. Our model-fitting suggests that a relativistically beamed optical jet gives the best fit.

27. For the FRII radio galaxies and radio-loud quasars taken together – the FRII population, the optical core luminosity again correlates significantly with R_c. Our model-fitting indicates that formally the best fit is again a beamed synchrotron jet. But a beamed jet obscured by a torus with an inferred opening angle close to $40°$ is a comparable fit, and is able to explain the contrasting behaviour of the FRI and FRII data.

28. Assuming the extended radio luminosity L_{ext} to be a proxy of AGN power, the observed correlation between the optical core luminosity L_o and L_{ext} suggests that the scatter in the L_o – R_c correlation is likely to be a result of the spread in intrinsic AGN power.

29. Our model-fitting suggests that the luminosity of the intrinsic (*i.e.,* unbeamed) jet in the FRIIs is approximately an order of magnitude larger than for the FRIs, although this result needs to be confirmed using a rigorous sample.

30. The data for the broad-line FRIIs alone are best fit by a model that comprises of a relativistic jet and a thin optically thick disk, consistent with the presence of the 'big blue bump' in them.

31. From our work we arrive at the general conclusion that the FRI and FRII radio galaxies seem to be intrinsically different on parsec-scales.

7.3   Future work

There are some outstanding issues which need to be settled for a full understanding of radio-loud AGNs. Observations suggest that the Fanaroff-Riley dichotomy in radio galaxies is indeed a dichotomy and there exist intrinsic differences between FRI and

FRII radio galaxies. The issue gets clouded however with the detection of radio sources which show both FRI and FRII characteristics, *viz.*, narrow jets and "hot spots" along with diffuse large-scale radio lobes (e.g., Capetti *et al.*, 1995). One question that needs to be pursued in the future is if and when an FRI radio galaxy turns into an FRII, and if this is a continuous process so that at the extreme ends of the luminosity ranges, there are classical FRIs and FRIIs and in the intermediate luminosity range the radio morphologies are more mixed.

The pc-scale B-field-orientation dichotomy which is observed in core-dominated quasars and low-energy peaked BL Lacs, does not extend to the high-energy peaked BL Lacs, which have B-field orientation similar to quasars. This is in disagreement with the simple 'shock-in-jet' model for BL Lacs and quasars. The Unified Scheme postulates that FRI and FRII radio galaxies are the 'parent' population of BL Lac objects and radio-loud quasars, respectively. However, there exists a small subset of BL Lac objects which have radio morphologies more consistent with FRIIs than FRIs (e.g., Kollgaard *et al.*, 1992). It is still not clear if the optical emission in the centres of radio galaxies which has been detected with the HST is indeed optical synchrotron radiation, as suggested by Capetti & Celotti (1999); Chiaberge *et al.* (1999, 2002); Verdoes Kleijn *et al.* (2002). To address some of these issues, we describe below some projects which need to be done in the future.

7.3.1 Pc-scale B-field geometry for a selected sample of FRIs and FRIIs

The comparison of the parsec-scale magnetic-field geometry in a sample of rigorously selected FRIs and FRIIs using VLBP, is required to ascertain if the B-field dichotomy observed in the beamed AGNs (BL Lacs and quasars) is also present in their unbeamed counterparts *viz.*, FRI and FRII radio galaxies. We have constructed such a sample of radio galaxies and observed four FRIs with VLBP as a pilot study. We plan to observe the complete sample in the near future.

7.3.2 Multiwavelength high resolution study

The synchrotron peaks of the Spectral Energy Distributions of CDQs, LBLs and HBLs form a sequence of increasing frequency (e.g., Maraschi & Tavecchio, 2001). We find that the systematics of the jet B-field geometry in CDQs, LBLs and HBLs, which tend to be longitudinal, transverse and longitudinal respectively, does not reflect the sequence in the SED peaks. In order to examine a possible connection between the B-field

geometry inferred from VLBP and the synchrotron peak frequency in the SEDs (which is related to B-field strengths and/or electron Lorentz factors (Sambruna *et al.*, 1996)) for the radio galaxies (SED information is not complete for radio galaxies – as shown in Figure 7.1), the VLBP results must be combined with the SEDs of the radio galaxy cores. Unlike the cores of 'beamed' objects where the AGN dominates the emission at all wavelengths, host galaxy contribution becomes significant in radio galaxy cores. High spatial resolution observations that delineate the weak nuclei from the host galaxy are therefore required. The SEDs can be derived using VLA, *HST* and *Chandra* data for their nuclei. If the US holds true, then the SEDs of the radio galaxies should be dimmed, redshifted versions of their beamed counterparts. This hypothesis can easily be tested by comparing the (well known) SED peaks of BL Lacs and CDQs with the FR radio galaxies.

7.3.3 Optical nuclei in radio galaxies

Optical polarimetry and a spectral index study of the optical nuclei with the *HST* could determine if the optical nuclear emission in radio galaxies is synchrotron emission with a power-law spectrum and a high degree of polarization or thermal emission from stars or an accretion disk.

Our work on the model-fitting of optical nuclear emission must be extended to a comparable set of beamed counterparts of FRI and FRII radio galaxies *i.e.*, BL Lacs and quasars, chosen from similar volumes in space and having optical nuclear luminosities from which host galaxy contributions have been subtracted.

Bibliography

Akaike, H. (1974). A New Look at the Statistical Model Identification. *IEEE Transactions on Automatic Control*, **19**, 716–723.

Alef, W., Preuss, E., Kellermann, K.I. & Gabuzda, D. (1998). Sub-milliarcsec Structure of 3C 111 at 0.7 and 3.6 CM. In *ASP Conf. Ser. 144: IAU Colloq. 164: Radio Emission from Galactic and Extragalactic Compact Sources*, 129–+.

Aller, H.D., Aller, M.F., Latimer, G.E. & Hodge, P.E. (1985). Spectra and linear polarizations of extragalactic variable sources at centimeter wavelengths. *ApJS*, **59**, 513–768.

Antonucci, R. (1993). Unified models for active galactic nuclei and quasars. *ARA&A*, **31**, 473–521.

Antonucci, R. & Barvainis, R. (1990). Narrow-line radio galaxies as quasars in the sky plane. *ApJ*, **363**, L17–L20.

Antonucci, R.R.J. (1984). Optical spectropolarimetry of radio galaxies. *ApJ*, **278**, 499–520.

Antonucci, R.R.J. & Miller, J.S. (1985). Spectropolarimetry and the nature of NGC 1068. *ApJ*, **297**, 621–632.

Antonucci, R.R.J. & Ulvestad, J.S. (1985). Extended radio emission and the nature of blazars. *ApJ*, **294**, 158–182.

Asada, K., Inoue, M., Uchida, Y., Kameno, S., Fujisawa, K., Iguchi, S. & Mutoh, M. (2002). A Helical Magnetic Field in the Jet of 3C 273. *PASJ*, **54**, L39–L43.

Attridge, J.M., Roberts, D.H. & Wardle, J.F.C. (1999). Radio Jet-Ambient Medium Interactions on Parsec Scales in the Blazar 1055+018. *ApJ*, **518**, L87–L90.

Baade, W. & Minkowski, R. (1954). Identification of the Radio Sources in Cassiopeia, Cygnus a, and Puppis a. *ApJ*, **119**, 206–+.

Bahcall, J.N., Kirhakos, S., Saxe, D.H. & Schneider, D.P. (1997). Hubble Space Telescope Images of a Sample of 20 Nearby Luminous Quasars. *ApJ*, **479**, 642–+.

Bailey, J., Sparks, W.B., Hough, J.H. & Axon, D.J. (1986). Infrared polarimetry of the nucleus of Centaurus A - The nearest blazar? *Nature*, **322**, 150–+.

Baker, J.C., Hunstead, R.W., Kapahi, V.K. & Subrahmanya, C.R. (1994). Evidence for a Beamed Optical Continuum in Radio Quasars. In *The First Stromlo Symposium: The Physics of Active Galaxies. ASP Conference Series, Vol. 54, 1994, G.V. Bicknell, M.A. Dopita, and P.J. Quinn, Eds., p.195*, 195–+.

Barthel, P.D. (1989). Is every quasar beamed? *ApJ*, **336**, 606–611.

Baum, S.A., Heckman, T.M., Bridle, A., van Breugel, W.J.M. & Miley, G.K. (1988). Extended optical-line-emitting gas in radio galaxies - Broad-band optical, narrow-band optical, and radio imaging of a representative sample. *ApJS*, **68**, 643–714.

Baum, S.A., Zirbel, E.L. & O'Dea, C.P. (1995). Toward Understanding the Fanaroff-Riley Dichotomy in Radio Source Morphology and Power. *ApJ*, **451**, 88–+.

Becker, R.H., White, R.L. & Edwards, A.L. (1991). A new catalog of 53,522 4.85 GHz sources. *ApJS*, **75**, 1–229.

Begelman, M.C. (2001). MHD mechanisms for jet formation. In *ASP Conf. Ser. 250: Particles and Fields in Radio Galaxies Conference*, 1–58381.

Bicknell, G.V. (1995). Relativistic Jets and the Fanaroff-Riley Classification of Radio Galaxies. *ApJS*, **101**, 29–+.

Bicknell, G.V. & Henriksen, R.N. (1980). The dynamical importance of magnetic fields in beam models of radio galaxies. *Astrophys. Lett.*, **21**, 29–34.

Bicknell, G.V., de Ruiter, H.R., Parma, P., Morganti, R. & Fanti, R. (1990). Physical properties of jets in low-luminosity radio sources. *ApJ*, **354**, 98–115.

Binette, L., Magris, C.G., Stasinska, G. & Bruzual, A.G. (1994). Photoionization in elliptical galaxies by old stars. *A&A*, **292**, 13–19.

Birkinshaw, M. & Davies, R.L. (1985). The orientations of the rotation axes of radio galaxies. I - Radio morphologies of bright elliptical galaxies. *ApJ*, **291**, 32–44.

Blandford, R.D. & Begelman, M.C. (1999). On the fate of gas accreting at a low rate on to a black hole. *MNRAS*, **303**, L1–L5.

Blandford, R.D. & Konigl, A. (1979). Relativistic jets as compact radio sources. *ApJ*, **232**, 34–48.

Blandford, R.D. & Levinson, A. (1995). Pair cascades in extragalactic jets. 1: Gamma rays. *ApJ*, **441**, 79–95.

Blandford, R.D. & Payne, D.G. (1982). Hydromagnetic flows from accretion discs and the production of radio jets. *MNRAS*, **199**, 883–903.

Blandford, R.D. & Rees, M.J. (1974). A 'twin-exhaust' model for double radio sources. *MNRAS*, **169**, 395–415.

Blandford, R.D. & Znajek, R.L. (1977). Electromagnetic extraction of energy from Kerr black holes. *MNRAS*, **179**, 433–456.

Bridle, A.H. & Perley, R.A. (1984). Extragalactic Radio Jets. *ARA&A*, **22**, 319–358.

Burbidge, G. & Hewitt, A. (1987). An updated list of BL Lac objects, and their relation to galaxies and quasistellar objects. *AJ*, **93**, 1–5.

Burn, B.J. (1966). On the depolarization of discrete radio sources by Faraday dispersion. *MNRAS*, **133**, 67–+.

Burnham, K.P. & Anderson, D.R. (2002). *Model selection and multimodel inference: a practical information-theoretic approach.*. Springer-Verlag, New York, NY.

Butcher, H.R., van Breugel, W. & Miley, G.K. (1980). Optical observations of radio jets. *ApJ*, **235**, 749–754.

Capetti, A. & Celotti, A. (1999). Testing the FR I/BL Lac unifying model with HST observations. *MNRAS*, **304**, 434–442.

Capetti, A., Fanti, R. & Parma, P. (1995). Radio galaxies of intermediate radio luminosity: a discussion of the radio properties of B2 0836+29, B2 0844+31 and B2 1521+28. *A&A*, **300**, 643–+.

Capetti, A., Celotti, A., Chiaberge, M., de Ruiter, H.R., Fanti, R., Morganti, R. & Parma, P. (2002). The HST survey of the B2 sample of radio-galaxies: Optical nuclei and the FR I/BL Lac unified scheme. *A&A*, **383**, 104–111.

Cassaro, P., Stanghellini, C., Bondi, M., Dallacasa, D., della Ceca, R. & Zappalà, R.A. (1999). Extended radio emission in BL Lac objects. I. The images. *A&AS*, **139**, 601–616.

Cawthorne, T.V., Wardle, J.F.C., Roberts, D.H. & Gabuzda, D.C. (1993). Milliarc-second Polarization Structure of 24 Objects from the Pearson-Readhead Sample of Bright Extragalactic Radio Sources. II. Discussion. *ApJ*, **416**, 519–+.

Celotti, A. (1997). What Are Jets Made of? Some Clues. In *Relativistic Jets in AGNs*, 270–278.

Celotti, A., Padovani, P. & Ghisellini, G. (1997). Jets and accretion processes in active galactic nuclei: further clues. *MNRAS*, **286**, 415–424.

Chen, X. (1995). Hot accretion discs with advection. *MNRAS*, **275**, 641–648.

Chiaberge, M., Capetti, A. & Celotti, A. (1999). The HST view of FR I radio galaxies: evidence for non-thermal nuclear sources. *A&A*, **349**, 77–87.

Chiaberge, M., Capetti, A. & Celotti, A. (2002). Understanding the nature of FR II optical nuclei: A new diagnostic plane for radio galaxies. *A&A*, **394**, 791–800.

Clark, B.G. (1980). An efficient implementation of the algorithm 'CLEAN'. *A&A*, **89**, 377–+.

Cohen, M.H., Cannon, W., Purcell, G.H., Shaffer, D.B., Broderick, J.J., Kellermann, K.I. & Jauncey, D.L. (1971). The Small-Scale Structure of Radio Galaxies and Quasi-Stellar Sources at 3.8 Centimeters. *ApJ*, **170**, 207–+.

Cornwell, T. (1982). Self-Calibration. In *Synthesis Mapping*, 13–+.

Cornwell, T.J. & Evans, K.F. (1985). A simple maximum entropy deconvolution algorithm. *A&A*, **143**, 77–83.

Costamante, L. & Ghisellini, G. (2002). TeV candidate BL Lac objects. *A&A*, **384**, 56–71.

Cotton, W.D. (1989). Very Long Baseline Interferometry, Techniques and Applications. *eds. M. Fellini & R.E. Spencer (Dordrecht :Kluwer)*, 275.

Crane, P., Peletier, R., Baxter, D., Sparks, W.B., Albrecht, R., Barbieri, C., Blades, J.C., Boksenberg, A., Deharveng, J.M., Disney, M.J., Jakobsen, P., Kamperman, T.M., King, I.R., Macchetto, F., Mackay, C.D., Paresce, F., Weigelt, G., Greenfield, P., Jedrzejewski, R. & Nota, A. (1993). Discovery of an optical synchrotron jet in 3C 264. *ApJ*, **402**, L37–L40.

Davidson, K. & Netzer, H. (1979). The emission lines of quasars and similar objects. *Reviews of Modern Physics*, **51**, 715–766.

de Koff, S., Best, P., Baum, S.A., Sparks, W., Röttgering, H., Miley, G., Golombek, D., Macchetto, F. & Martel, A. (2000). The Dust-Radio Connection in 3CR Radio Galaxies. *ApJS*, **129**, 33–59.

di Serego Alighieri, S., Cimatti, A. & Fosbury, R.A.E. (1994). Misdirected quasars and evolved stars in distant radio galaxies. *ApJ*, **431**, 123–136.

Dondi, L. & Ghisellini, G. (1995). Gamma-ray-loud blazars and beaming. *MNRAS*, **273**, 583–595.

Eilek, J.A., Melrose, D.B. & Walker, M.A. (1997). Synchrotron Aging in Filamented Magnetic Fields. *ApJ*, **483**, 282–+.

Elvis, M., Schreier, E.J., Tonry, J., Davis, M. & Huchra, J.P. (1981). Two optically dull galaxies with strong nuclear X-ray sources. *ApJ*, **246**, 20–27.

Fabbiano, G., Willner, S.P., Carleton, N.P. & Elvis, M. (1986). The highly obscured nucleus of 3C 219. *ApJ*, **304**, L37–L40.

Falomo, R., Scarpa, R. & Bersanelli, M. (1994). Optical spectrophotometry of blazars. *ApJS*, **93**, 125–143.

Fanaroff, B.L. & Riley, J.M. (1974). The morphology of extragalactic radio sources of high and low luminosity. *MNRAS*, **167**, 31P–36P.

Feretti, L., Comoretto, G., Giovannini, G., Venturi, T. & Wehrle, A.E. (1993). VLBI observations of a complete sample of radio galaxies. III - The two-sided milliarcsecond structure of 3C 338. *ApJ*, **408**, 446–451.

Ferrarese, L. & Merritt, D. (2000). A Fundamental Relation between Supermassive Black Holes and Their Host Galaxies. *ApJ*, **539**, L9–L12.

Ferrarese, L., Ford, H.C. & Jaffe, W. (1996). Evidence for a Massive Black Hole in the Active Galaxy NGC 4261 from Hubble Space Telescope Images and Spectra. *ApJ*, **470**, 444–+.

Filippenko, A.V. (1992). The Central Engine of AGN / Active Galactic Nuclei - Starbursts Versus Black-Holes. In *Physics of Active Galactic Nuclei*, 345–+.

Fomalont, E.B. & Bridle, A.H. (1978). Extended radio sources and elliptical galaxies. II. A search for radio cores using the VLA. *AJ*, **83**, 725–731.

Fossati, G., Celotti, A., Ghisellini, G. & Maraschi, L. (1997). Unifying models for X-ray-selected and radio-selected BL Lac objects. *MNRAS*, **289**, 136–150.

Fossati, G., Maraschi, L., Celotti, A., Comastri, A. & Ghisellini, G. (1998). A unifying view of the spectral energy distributions of blazars. *MNRAS*, **299**, 433–448.

Fraix-Burnet, D., Nieto, J.L. & Poulain, P. (1989). Detection of optical polarization in the 3C 66B jet. *A&A*, **221**, L1+.

Fraix-Burnet, D., Golombek, D. & Macchetto, F.D. (1991). An optical study of 3C 31, 3C 66B, 3C 120, and their jets. *AJ*, **102**, 562–571.

Gabuzda, D.C. (1997). The Parsec-Scale Total Intensity and Polarization Structure of Relativistic Jets in AGN. In *Relativistic Jets in AGNs*, 30–37.

Gabuzda, D.C. (2003). VLBI Polarisation Properties of a Complete Sample of Radio-Loud BL Lacs. *Ap&SS*, **288**, 39–50.

Gabuzda, D.C., Cawthorne, T.V., Roberts, D.H. & Wardle, J.F.C. (1992). A survey of the milliarcsecond polarization properties of BL Lacertae objects at 5 GHz. *ApJ*, **388**, 40–54.

Gabuzda, D.C., Mullan, C.M., Cawthorne, T.V., Wardle, J.F.C. & Roberts, D.H. (1994). Evolution of the milliarcsecond total intensity and polarization structures of BL Lacertae objects. *ApJ*, **435**, 140–161.

Gabuzda, D.C., Mioduszewski, A.J., Roberts, D.H. & Wardle, J.F.C. (1999). The very long baseline interferometric polarization structure of 3C 345 at lambda=2.8 CM. *MNRAS*, **303**, 515–520.

Gabuzda, D.C., Pushkarev, A.B. & Cawthorne, T.V. (2000). Analysis of λ=6cm VLBI polarization observations of a complete sample of northern BL Lacertae objects. *MNRAS*, **319**, 1109–1124.

Gabuzda, D.C., Pushkarev, A.B. & Garnich, N.N. (2001). Unusual radio properties of the BL Lac object 0820+225. *MNRAS*, **327**, 1–9.

Gabuzda, D.C., Murray, E. & Cronin, P. (2003). Evidence for Toroidal B-Field Structures in BL Lac Objects . In *the Symposium "Radio Astronomy at 70: from Karl Jansky to microjansky" (astro-ph/0311504)*.

Garrington, S.T., Leahy, J.P., Conway, R.G. & Laing, R.A. (1988). A systematic asymmetry in the polarization properties of double radio sources with one jet. *Nature*, **331**, 147–149.

Gavazzi, G., Perola, G.C. & Jaffe, W. (1981). Observations of the head-tail radio galaxy NGC 3862 /3C 264/ at 0.6, 1.4, and 5.0 GHz. *A&A*, **103**, 35–43.

Gebhardt, K., Bender, R., Bower, G., Dressler, A., Faber, S.M., Filippenko, A.V., Green, R., Grillmair, C., Ho, L.C., Kormendy, J., Lauer, T.R., Magorrian, J., Pinkney, J., Richstone, D. & Tremaine, S. (2000). A Relationship between Nuclear Black Hole Mass and Galaxy Velocity Dispersion. *ApJ*, **539**, L13–L16.

Genzel, R., Eckart, A., Ott, T. & Eisenhauer, F. (1997). On the nature of the dark mass in the centre of the Milky Way. *MNRAS*, **291**, 219–234.

Georganopoulos, M. (2000). Blue Quasars and Blazar Unification Schemes. *ApJ*, **543**, L15–L18.

George, I.M., Warwick, R.S. & Bromage, G.E. (1988). X-ray and ultraviolet observations of Markarian 421. *MNRAS*, **232**, 793–808.

Ghez, A.M., Morris, M., Becklin, E.E., Tanner, A. & Kremenek, T. (2000). The accelerations of stars orbiting the Milky Way's central black hole. *Nature*, **407**, 349–351.

Ghisellini, G. & Celotti, A. (2001). The dividing line between FR I and FR II radiogalaxies. *A&A*, **379**, L1–L4.

Ghisellini, G. & Maraschi, L. (1989). Bulk acceleration in relativistic jets and the spectral properties of blazars. *ApJ*, **340**, 181–189.

Ghisellini, G., Celotti, A., Fossati, G., Maraschi, L. & Comastri, A. (1998). A theoretical unifying scheme for gamma-ray bright blazars. *MNRAS*, **301**, 451–468.

Giommi, P. & Padovani, P. (1994). Bl-Lacertae Reunification. *MNRAS*, **268**, L51+.

Giommi, P., Tagliaferri, G., Beuermann, K., Raymont, G.B., Brissenden, R., Graser, U., Mason, K.O., Murdin, P., Pooley, G., Thomas, H.C. & Tuohy, I. (1989). Bl-Lacertae Objects from the EXOSAT High Galactic Latitude Survey - Constraints on the Logn-Logs and on the Cosmological Evolution. In *BL Lac Objects*, 231–+.

Giovannini, G., Feretti, L., Gregorini, L. & Parma, P. (1988). Radio nuclei in elliptical galaxies. *A&A*, **199**, 73–84.

Giovannini, G., Feretti, L. & Comoretto, G. (1990). VLBI observations of a complete sample of radio galaxies. I - Snapshot data. *ApJ*, **358**, 159–163.

Giovannini, G., Cotton, W.D., Feretti, L., Lara, L. & Venturi, T. (2001). VLBI Observations of a Complete Sample of Radio Galaxies: 10 Years Later. *ApJ*, **552**, 508–526.

Goetz, M.M.A., Preuss, E., Alef, W. & Kellermann, K.I. (1987). Strong structural variability in the lobe-dominated radio galaxy 3 C 111. *A&A*, **176**, 171–174.

Goodrich, R.W. (1992). Polarization in the narrow forbidden O III lines in Seyfert 2 galaxies. *ApJ*, **399**, 50–56.

Gopal-Krishna & Wiita, P.J. (2001). The Fanaroff-Riley transition and the optical luminosity of the host elliptical galaxy. *A&A*, **373**, 100–105.

Gregory, P.C. & Condon, J.J. (1991). The 87GB catalog of radio sources covering delta between O and + 75 deg at 4.85 GHz. *ApJS*, **75**, 1011–1291.

Gregory, P.C., Scott, W.K., Douglas, K. & Condon, J.J. (1996). The GB6 Catalog of Radio Sources. *ApJS*, **103**, 427–+.

Högbom, J.A. (1974). Aperture Synthesis with a Non-Regular Distribution of Interferometer Baselines. *A&AS*, **15**, 417–+.

Hardcastle, M.J. & Worrall, D.M. (1999). ROSAT X-ray observations of 3CRR radio sources. *MNRAS*, **309**, 969–990.

Hardcastle, M.J. & Worrall, D.M. (2000). Radio, optical and X-ray nuclei in nearby 3CRR radio galaxies. *MNRAS*, **314**, 359–363.

Hardcastle, M.J., Alexander, P., Pooley, G.G. & Riley, J.M. (1996). The jets in 3C 66B. *MNRAS*, **278**, 273–284.

Hardcastle, M.J., Birkinshaw, M. & Worrall, D.M. (2001). Chandra observations of the X-ray jet in 3C 66B. *MNRAS*, **326**, 1499–1507.

Heckman, T.M., Miley, G.K., Lehnert, M.D. & van Breugel, W. (1991). Spatially resolved optical images of high-redshift quasi-stellar objects. *ApJ*, **370**, 78–101.

Hes, R., Barthel, P.D. & Fosbury, R.A.E. (1996). Emission line imaging of 3CR quasars and radio galaxies. *A&A*, **313**, 423–438.

Ho, L. (1999). Supermassive Black Holes in Galactic Nuclei: Observational Evidence and Astrophysical Consequences. In *ASSL Vol. 234: Observational Evidence for the Black Holes in the Universe*, 157–+.

Homan, D.C. & Wardle, J.F.C. (1999). Detection and Measurement of Parsec-Scale Circular Polarization in Four AGNS. *AJ*, **118**, 1942–1962.

Homan, D.C., Attridge, J.M. & Wardle, J.F.C. (2001). Parsec-Scale Circular Polarization Observations of 40 Blazars. *ApJ*, **556**, 113–120.

Homan, D.C., Ojha, R., Wardle, J.F.C., Roberts, D.H., Aller, M.F., Aller, H.D. & Hughes, P.A. (2002). Parsec-Scale Blazar Monitoring: Flux and Polarization Variability. *ApJ*, **568**, 99–119.

Hough, D.H., Vermeulen, R.C. & Readhead, A.C.S. (1998). First VLBA Images of the Nuclei in 3CR Lobe-dominated Quasars. In *ASP Conf. Ser. 144: IAU Colloq. 164: Radio Emission from Galactic and Extragalactic Compact Sources*, 83–+.

Hughes, P.A., Aller, H.D. & Aller, M.F. (1985). Polarized Radio Outbursts in Bl-Lacertae - Part Two - the Flux and Polarization of a Piston-Driven Shock. *ApJ*, **298**, 301–+.

Hutchings, J.B., Janson, T. & Neff, S.G. (1989). What is the difference between radio-loud and radio-quiet quasi-stellar objects? *ApJ*, **342**, 660–665.

Hutchings, J.B., Frenette, D., Hanisch, R., Mo, J., Dumont, P.J., Redding, D.C. & Neff, S.G. (2002). Imaging of z~2 QSO Host Galaxies with the Hubble Space Telescope. *AJ*, **123**, 2936–2944.

Hutter, D.J. & Mufson, S.L. (1980). Detection of X-Ray Emission from Markarian 180. *BAAS*, **12**, 486–+.

Impey, C.D. & Tapia, S. (1990). The optical polarization properties of quasars. *ApJ*, **354**, 124–139.

Inglis, M.D., Brindle, C., Hough, J.H., Young, S., Axon, D.J., Bailey, J.A. & Ward, M.J. (1993). Evidence for an Obscured Broadline Region in the Early Type Radio Galaxy IC5063. *MNRAS*, **263**, 895–+.

Jackson, C.A. & Wall, J.V. (1999). Extragalactic radio-source evolution under the dual-population unification scheme. *MNRAS*, **304**, 160–174.

Jackson, N. & Browne, I.W.A. (1990). Spectral differences between radio galaxies and quasars. *Nature*, **343**, 43–45.

Jackson, N., Sparks, W.B., Miley, G.K. & Macchetto, F. (1993). The radio and optical structure of 3C 66B. *A&A*, **269**, 128–134.

Jaffe, W., Ford, H.C., Ferrarese, L., van den Bosch, F. & O'Connell, R.W. (1993). A large nuclear accretion disk in the active galaxy NGC4261. *Nature*, **364**, 213–215.

Jannuzi, B.T., Smith, P.S. & Elston, R. (1994). The optical polarization properties of X-ray-selected BL Lacertae objects. *ApJ*, **428**, 130–142.

Jannuzi, B.T., Yanny, B. & Impey, C. (1997). Hubble Space Telescope Imaging of the Host Galaxies of Three X-Ray-selected BL Lacertae Objects. *ApJ*, **491**, 146–+.

Jenkins, C.R. (1982). Radio observations of early-type galaxies. *MNRAS*, **200**, 705–731.

Jones, D.L. (1984). A search for changing structure in low-luminosity compact radio sources. *ApJ*, **287**, 33–40.

Jones, D.L. & Wehrle, A.E. (1997). VLBA Imaging of NGC 4261: Symmetric Parsec-Scale Jets and the Inner Accretion Region. *ApJ*, **484**, 186–+.

Jones, D.L., Terzian, Y. & Sramek, R.A. (1981). VLBI observations of galactic nuclei. *ApJ*, **246**, 28–37.

Jones, T.W., O'dell, S.L. & Stein, W.A. (1974). Physics of Compact Nonthermal Sources. Theory of Radiation Processes. *ApJ*, **188**, 353–368.

Junor, W., Biretta, J.A. & Wardle, J.F.C. (2001). VLBA lambda lambda 6, 4 cm polarimetry of Vir A. In *IAU Symposium*, 136–+.

Kapahi, V.K. & Saikia, D.J. (1982). Relativistic beaming in the central components of double radio quasars. *Journal of Astrophysics and Astronomy (ISSN 0250-6335), vol. 3, Dec. 1982, p. 465-483.*, **3**, 465–483.

Kapahi, V.K. & Shastri, P. (1987). Optically induced orientation bias in B2 radio quasars. *MNRAS*, **224**, 17P–+.

Kellermann, K.I. & Pauliny-Toth, I.I.K. (1969). The Spectra of Opaque Radio Sources. *ApJ*, **155**, L71+.

Kellermann, K.I., Sramek, R., Schmidt, M., Shaffer, D.B. & Green, R. (1989). VLA observations of objects in the Palomar Bright Quasar Survey. *AJ*, **98**, 1195–1207.

Kinney, A.L., Schmitt, H.R., Clarke, C.J., Pringle, J.E., Ulvestad, J.S. & Antonucci, R.R.J. (2000). Jet Directions in Seyfert Galaxies. *ApJ*, **537**, 152–177.

Kollgaard, R.I., Wardle, J.F.C., Roberts, D.H. & Gabuzda, D.C. (1992). Radio constraints on the nature of BL Lacertae objects and their parent population. *AJ*, **104**, 1687–1705.

Kollgaard, R.I., Gabuzda, D.C. & Feigelson, E.D. (1996). Parsec-Scale Radio Structure of Four X-Ray–selected BL Lacertae Objects. *ApJ*, **460**, 174–+.

Komesaroff, M.M., Roberts, J.A., Milne, D.K., Rayner, P.T. & Cooke, D.J. (1984). Circular and linear polarization variations of compact radio sources. *MNRAS*, **208**, 409–425.

Komissarov, S.S. (1990). Relativistic beaming of jets with boundary layers. *Pis ma Astronomicheskii Zhurnal*, **16**, 661–664.

Kormendy, J. (1988). Evidence for a supermassive black hole in the nucleus of M31. *ApJ*, **325**, 128–141.

Kormendy, J. & Gebhardt, K. (2001). Supermassive Black Holes in Galactic Nuclei (Plenary Talk). In *AIP Conf. Proc. 586: 20th Texas Symposium on relativistic astrophysics*, 363–+.

Kormendy, J. & Richstone, D. (1995). Inward Bound—The Search For Supermassive Black Holes In Galactic Nuclei. *ARA&A*, **33**, 581–+.

Kotilainen, J.K., Falomo, R. & Scarpa, R. (1998). The host galaxies of BL Lac objects in the near-infrared. *A&A*, **336**, 479–489.

Kuehr, H. & Schmidt, G.D. (1990). Complete samples of radio-selected BL Lac objects. *AJ*, **99**, 1–6.

Kuehr, H., Nauber, U. & Pauliny-Toth, I.I.K. (1979). *A Catalogue of radio sources*. Bonn: Max-Planck-Institut (MPI) fuer Radioastronomie, 1979.

Kuehr, H., Pauliny-Toth, I.I.K., Witzel, A. & Schmidt, J. (1981). The 5-GHz strong source surveys. V - Survey of the area between declinations 70 and 90 deg. *AJ*, **86**, 854–863.

Laing, R.A. (1980). A model for the magnetic-field structure in extended radio sources. *MNRAS*, **193**, 439–449.

Laing, R.A. (1981). Multifrequency observations of 40 powerful extragalactic sources with the 5-km telescope. *MNRAS*, **195**, 261–324.

Laing, R.A. (1988). The sidedness of jets and depolarization in powerful extragalactic radio sources. *Nature*, **331**, 149–151.

Laing, R.A. (1994). Decelerating Relativistic Jets in FRI Radio Sources. In *The First Stromlo Symposium: The Physics of Active Galaxies. ASP Conference Series, Vol. 54, 1994, G.V. Bicknell, M.A. Dopita, and P.J. Quinn, Eds., p.227*, 227–+.

Laing, R.A., Riley, J.M. & Longair, M.S. (1983). Bright radio sources at 178 MHz - Flux densities, optical identifications and the cosmological evolution of powerful radio galaxies. *MNRAS*, **204**, 151–187.

Laing, R.A., Parma, P., de Ruiter, H.R. & Fanti, R. (1999). Asymmetries in the jets of weak radio galaxies. *MNRAS*, **306**, 513–530.

Lara, L., Cotton, W.D., Feretti, L., Giovannini, G., Venturi, T. & Marcaide, J.M. (1997). VLBI Observations of a Complete Sample of Radio Galaxies. VII. Study of the FR I Sources 3C 31, 4C 35.03, and 3C 264. *ApJ*, **474**, 179–+.

Laurent-Muehleisen, S.A., Kollgaard, R.I., Moellenbrock, G.A. & Feigelson, E.D. (1993). Radio morphology and parent population of X-ray selected BL Lacertae objects. *AJ*, **106**, 875–898.

Laurent-Muehleisen, S.A., Kollgaard, R.I., Ryan, P.J., Feigelson, E.D., Brinkmann, W. & Siebert, J. (1997). Radio-loud active galaxies in the northern ROSAT All-Sky Survey. I. Radio identifications. *A&AS*, **122**, 235–247.

Laurent-Muehleisen, S.A., Kollgaard, R.I., Feigelson, E.D., Brinkmann, W. & Siebert, J. (1999). The RGB Sample of Intermediate BL Lacertae Objects. *ApJ*, **525**, 127–143.

Le Roux, E. (1961). Étude théorique du rayonnement synchrotron des radiosources. *Annales d'Astrophysique*, **24**, 71–+.

Leahy, J.P., Pooley, G.G. & Jagers, W.J. (1986). A multi-frequency polarization study of 3 C 66 B. *A&A*, **156**, 234–251.

Ledden, J.E. & Odell, S.L. (1985). The radio-optical-X-ray spectral flux distributions of blazars. *ApJ*, **298**, 630–643.

Ledlow, M.J. & Owen, F.N. (1996). 20 CM VLA Survey of Abell Clusters of Galaxies. VI. Radio/Optical Luminosity Functions. *AJ*, **112**, 9–+.

Lee, J.C., Ogle, P.M., Canizares, C.R., Marshall, H.L., Schulz, N.S., Morales, R., Fabian, A.C. & Iwasawa, K. (2001). Revealing the Dusty Warm Absorber in MCG -6-30-15 with the Chandra High-Energy Transmission Grating. *ApJ*, **554**, L13–L17.

Linfield, R. (1981). VLBI observations of jets in double radio galaxies. *ApJ*, **244**, 436–446.

Linfield, R. (1987). VLBI observations of the 3C 111 jet. *ApJ*, **317**, 121–127.

Linfield, R. & Perley, R. (1984). 3C 111 - A luminous radio galaxy with a highly collimated jet. *ApJ*, **279**, 60–73.

Lister, M. (2003). The MOJAVE Program: Investigating the Parsec-Scale Evolution of Relativistic Jets in Active Galaxies. *American Astronomical Society Meeting*, **203**, –+.

Lister, M.L. (2001). Parsec-Scale Jet Polarization Properties of a Complete Sample of Active Galactic Nuclei at 43 GHz. *ApJ*, **562**, 208–232.

Livio, M., Ogilvie, G.I. & Pringle, J.E. (1999). Extracting Energy from Black Holes: The Relative Importance of the Blandford-Znajek Mechanism. *ApJ*, **512**, 100–104.

Livio, M., Pringle, J.E. & King, A.R. (2003). The Disk-Jet Connection in Microquasars and Active Galactic Nuclei. *ApJ*, **593**, 184–188.

Longair, M.S. & Gunn, J.E. (1975). An investigation of the optical fields of 35 3CR radio sources to faint limiting optical magnitudes. *MNRAS*, **170**, 121–138.

Macchetto, F., Albrecht, R., Barbieri, C., Blades, J.C., Boksenberg, A., Crane, P., Deharveng, J.M., Disney, M.J., Jakobsen, P., Kamperman, T.M., King, I.R., Mackay, C.D., Paresce, F., Weigelt, G., Baxter, D., Greenfield, P., Jedrzejewski, R., Nota, A., Sparks, W.B. & Miley, G.K. (1991). HST observations of 3C 66B - A double-stranded optical jet. *ApJ*, **373**, L55–L58.

Macchetto, F., Marconi, A., Axon, D.J., Capetti, A., Sparks, W. & Crane, P. (1997). The Supermassive Black Hole of M87 and the Kinematics of Its Associated Gaseous Disk. *ApJ*, **489**, 579–+.

Magorrian, J., Tremaine, S., Richstone, D., Bender, R., Bower, G., Dressler, A., Faber, S.M., Gebhardt, K., Green, R., Grillmair, C., Kormendy, J. & Lauer, T. (1998). The Demography of Massive Dark Objects in Galaxy Centers. *AJ*, **115**, 2285–2305.

Malkan, M.A. (1983). The ultraviolet excess of luminous quasars. II - Evidence for massive accretion disks. *ApJ*, **268**, 582–590.

Maltby, P., Matthews, T.A. & Moffet, A.T. (1963). Brightness Distribution in Discrete Radio Sources.IV. a Discussion of 24 Identified Sources. *ApJ*, **137**, 153–+.

Maraschi, L. & Rovetti, F. (1994). A unified relativistic beaming model for BL Lacertae objects and flat spectrum radio quasars. *ApJ*, **436**, 79–88.

Maraschi, L. & Tavecchio, F. (2001). Spectral Energy Distributions of Blazars: Facts and Speculations. In *ASP Conf. Ser. 227: Blazar Demographics and Physics*, 40–+.

Marscher, A.P. & Gear, W.K. (1985). Models for high-frequency radio outbursts in extragalactic sources, with application to the early 1983 millimeter-to-infrared flare of 3C 273. *ApJ*, **298**, 114–127.

Marscher, A.P., Marshall, F.E., Mushotzky, R.F., Dent, W.A., Balonek, T.J. & Hartman, M.F. (1979). Search for X-ray emission from bursting radio sources. *ApJ*, **233**, 498–503.

Marshall, F.E., Mushotzky, R.F., Boldt, E.A., Holt, S.S., Rothschild, R.E. & Serlemitsos, P.J. (1978). N galaxies - A new class of X-ray sources. *Nature*, **275**, 624–+.

Matthews, T.A., Morgan, W.W. & Schmidt, M. (1964). A Discussion of Galaxies Indentified with Radio Sources. *ApJ*, **140**, 35–+.

McLure, R.J., Kukula, M.J., Dunlop, J.S., Baum, S.A., O'Dea, C.P. & Hughes, D.H. (1999). A comparative HST imaging study of the host galaxies of radio-quiet quasars, radio-loud quasars and radio galaxies - I. *MNRAS*, **308**, 377–404.

Meier, D.L. (1999). A Magnetically Switched, Rotating Black Hole Model for the Production of Extragalactic Radio Jets and the Fanaroff and Riley Class Division. *ApJ*, **522**, 753–766.

Middelberg, E., Roy, A.L., Bach, U., Gabuzda, D.C. & Beckert, T. (2003). Where has all the polarization gone? In *Proceedings of conference "Future Directions in High Resolution Astronomy", ASP Conf. Series*, (astro–ph/0309385).

Miller, J.S., Goodrich, R.W. & Mathews, W.G. (1991). Multidirectional views of the active nucleus of NGC 1068. *ApJ*, **378**, 47–64.

Minkowski, R. (1960). A New Distant Cluster of Galaxies. *ApJ*, **132**, 908–910.

Mirabel, I.F. & Rodriguez, L.F. (1994). A Superluminal Source in the Galaxy. *Nature*, **371**, 46–+.

Miyoshi, M., Moran, J., Herrnstein, J., Greenhill, L., Nakai, N., Diamond, P. & Inoue, M. (1995). Evidence for a Black-Hole from High Rotation Velocities in a Sub-Parsec Region of NGC4258. *Nature*, **373**, 127–+.

Morganti, R., Parma, P., Capetti, A., Fanti, R., de Ruiter, H.R. & Prandoni, I. (1997). Polarization of low-luminosity radio galaxies: The 6 CM data. *A&AS*, **126**, 335–355.

Morris, S.L., Stocke, J.T., Gioia, I.M., Schild, R.E., Wolter, A., Maccacaro, T. & della Ceca, R. (1991). The luminosity function and cosmological evolution of X-ray-selected BL Lacertae objects. *ApJ*, **380**, 49–65.

Murphy, D.W., Browne, I.W.A. & Perley, R.A. (1993). VLA Observations of a Complete Sample of Core-Dominated Radio Sources. *MNRAS*, **264**, 298–+.

Mutel, R.L., Su, B., Bucciferro, R.R. & Phillips, R.B. (1990). Superluminal motion of the radio core of BL Lacertae - 1980.4-1988.3. *ApJ*, **352**, 81–95.

Narayan, R. & Nityananda, R. (1986). Maximum entropy image restoration in astronomy. *ARA&A*, **24**, 127–170.

Narayan, R. & Yi, I. (1994). Advection-dominated accretion: A self-similar solution. *ApJ*, **428**, L13–L16.

Narayan, R., Igumenshchev, I.V. & Abramowicz, M.A. (2000). Self-similar Accretion Flows with Convection. *ApJ*, **539**, 798–808.

Netzer, H. & Maoz, D. (1990). On the emission-line response to continuum variations in the Seyfert galaxy NGC 5548. *ApJ*, **365**, L5–L7.

Nolthenius, R. (1993). A revised catalog of CfA1 galaxy groups in the Virgo/Great Attractor flow field. *ApJS*, **85**, 1–25.

Northover, K.J.E. (1973). The radio galaxy 3C 66. *MNRAS*, **165**, 369–+.

O'Dea, C.P., Dent, W.A. & Balonek, T.J. (1985). *Broadband spectral evolution of outbursts in extragalactic radio sources*, 63–67. Active galactic nuclei (A86-36901 16-90). Manchester, England and Dover, NH, Manchester University Press, 1985, p. 63-67.

O'Dea, C.P., Barvainis, R. & Challis, P.M. (1988). Subarcsecond-resolution radio observations of sixteen core-dominated quasars and active galactic nuclei. *AJ*, **96**, 435–454.

O'Dea, C.P., Heckman, T.M., Baum, S.A. & Laurikainen, E. (1994). A Comparison of the Infrared Properties of Radio Loud Active Galaxies. In *The First Stromlo Symposium: The Physics of Active Galaxies. ASP Conference Series, Vol. 54, 1994, G.V. Bicknell, M.A. Dopita, and P.J. Quinn, Eds., p.209*, 209–+.

Orr, M.J.L. & Browne, I.W.A. (1982). Relativistic beaming and quasar statistics. *MNRAS*, **200**, 1067–1080.

Owen, F.N. & Ledlow, M.J. (1994). The FRI/Il Break and the Bivariate Luminosity Function in Abell Clusters of Galaxies. In *The First Stromlo Symposium: The Physics of Active Galaxies. ASP Conference Series, Vol. 54, 1994, G.V. Bicknell, M.A. Dopita, and P.J. Quinn, Eds., p.319*, 319–+.

Pacholczyk, A.G. (1970). *Radio astrophysics. Nonthermal processes in galactic and extragalactic sources*. Series of Books in Astronomy and Astrophysics, San Francisco: Freeman, 1970.

Padovani, P. & Giommi, P. (1995a). A Sample-Oriented Catalogue of Bl-Lacertae Objects. *MNRAS*, **277**, 1477–+.

Padovani, P. & Giommi, P. (1995b). The connection between x-ray- and radio-selected BL Lacertae objects. *ApJ*, **444**, 567–581.

Padovani, P. & Urry, C.M. (1990). Fanaroff-Riley I galaxies as the parent population of BL Lacertae objects. I - X-ray constraints. *ApJ*, **356**, 75–82.

Parma, P., Morganti, R., Capetti, A., Fanti, R. & de Ruiter, H.R. (1993). Polarization properties at 1.4 GHz of low luminosity radio galaxies. *A&A*, **267**, 31–38.

Parma, P., de Ruiter, H.R., Fanti, R. & Laing, R. (1994). Brightness Asymmetries and Velocities of Jets in Low Luminosity Radio Galaxies. In *The First Stromlo Symposium: The Physics of Active Galaxies. ASP Conference Series, Vol. 54, 1994, G.V. Bicknell, M.A. Dopita, and P.J. Quinn, Eds., p.241*, 241–+.

Pauliny-Toth, I.I.K., Preuss, E., Witzel, A., Kellermann, K.I. & Shaffer, D.B. (1976). The Structure of the Radio Nucleus of 3 Clii. *A&A*, **52**, 471–+.

Perley, R.A., Schwab, F.R. & Bridle, A.H. (1989). *Synthesis Imaging in Radio Astronomy*. ASP Conferences Series, Volume 6.

Perlman, E.S. & Stocke, J.T. (1993). The radio structure source of X-ray-selected BL Lacertae objects. *ApJ*, **406**, 430–446.

Perlman, E.S., Sparks, W.B., Radomski, J., Packham, C., Fisher, R.S., Piña, R. & Biretta, J.A. (2001). Deep 10 Micron Imaging of M87. *ApJ*, **561**, L51–L54.

Pica, A.J., Smith, A.G., Webb, J.R., Leacock, R.J., Clements, S. & Gombola, P.P. (1988). Long-term optical behavior of 144 compact extragalactic objects - 1969-1988. *AJ*, **96**, 1215–1226.

Pollack, L.K., Taylor, G.B. & Zavala, R.T. (2003). VLBI Polarimetry of 177 Sources from the Caltech-Jodrell Bank Flat-Spectrum Survey. *ApJ*, **589**, 733–751.

Press, W.H., Flannery, B.P., Teukolsky, S.A. & Vetterling, W.T. (1992). *Numerical Recipes in Fortran.*. Cambridge University Press.

Prestage, R.M. & Peacock, J.A. (1988). The cluster environments of powerful radio galaxies. *MNRAS*, **230**, 131–160.

Preuss, E., Alef, W. & Kellermann, K.I. (1988). Superluminal Behavior of the Double-Lobed Radio Galaxy 3C111. In *IAU Symp. 129: The Impact of VLBI on Astrophysics and Geophysics*, 105–+.

Preuss, E., Alef, W., Shengyin, W., Yuhai, Q., Zhihan, Q., Kellermann, K.I., Matveenko, L. & Götz, M.M.A. (1990). 3C 111 and 3C 390.3: Beaming in Nearby Radio Galaxies. In *Parsec-scale radio jets*, 120–+.

Price, D.J., Pringle, J.E. & King, A.R. (2003). A comparison of the acceleration mechanisms in young stellar objects and active galactic nuclei jets. *MNRAS*, **339**, 1223–1236.

Punch, M., Akerlof, C.W., Cawley, M.F., Chantell, M., Fegan, D.J., Fennell, S., Gaidos, J.A., Hagan, J., Hillas, A.M., Jiang, Y., Kerrick, A.D., Lamb, R.C., Lawrence, M.A., Lewis, D.A., Meyer, D.I., Mohanty, G., O'Flaherty, K.S., Reynolds, P.T., Rovero, A.C., Schubnell, M.S., Sembroski, G., Weekes, T.C. & Wilson, C. (1992). Detection of TeV photons from the active galaxy Markarian 421. *Nature*, **358**, 477–+.

Pushkarev, A.B. & Gabuzda, D.C. (2001). Evidence for Interaction with a Surrounding Medium in Several BL Lacertae Objects. In *ASP Conf. Ser. 250: Particles and Fields in Radio Galaxies Conference*, 200–+.

Quataert, E. & Gruzinov, A. (2000). Convection-dominated Accretion Flows. *ApJ*, **539**, 809–814.

Quillen, A.C., Almog, J. & Yukita, M. (2003). 870 Micron Observations of Nearby 3CRR Radio Galaxies. *AJ*, **126**, 2677–2686.

Quirrenbach, A. (1992). Variability and VLBI Observations of Extragalactic Radio Surces. *Reviews of Modern Astronomy*, **5**, 214–228.

Rayner, D.P., Norris, R.P. & Sault, R.J. (2000). Radio circular polarization of active galaxies. *MNRAS*, **319**, 484–496.

Readhead, A.C.S., Walker, R.C., Pearson, T.J. & Cohen, M.H. (1980). Mapping radio sources with uncalibrated visibility data. *Nature*, **285**, 137–140.

Rector, T.A. & Stocke, J.T. (2001). The Properties of the Radio-Selected 1 Jy Sample of BL Lacertae Objects. *AJ*, **122**, 565–584.

Rees, M.J. (1967). Studies in radio source structure-I. A relativistically expanding model for variable quasi-stellar radio sources. *MNRAS*, **135**, 345–+.

Rees, M.J., Phinney, E.S., Begelman, M.C. & Blandford, R.D. (1982). Ion-supported tori and the origin of radio jets. *Nature*, **295**, 17–21.

Rowan-Robinson, M. (1977). On the unity of activity in galaxies. *ApJ*, **213**, 635–647.

Rudnick, L., Jones, T.W. & Fiedler, R. (1986). Weak nuclei of powerful radio sources - Spectra and polarizations. *AJ*, **91**, 1011–1018.

Rusk, R. (1988). The Brightness and Polarization Structure of Compact Radio Sources. In *IAU Symp. 129: The Impact of VLBI on Astrophysics and Geophysics*, 161–+.

Rusk, R. & Seaquist, E.R. (1985). Alignment of radio and optical polarization with VLBI structure. *AJ*, **90**, 30–38.

Rybicki, G.B. & Lightman, A.P. (1979). *Radiative processes in astrophysics*. New York, Wiley-Interscience, 1979. 393 p.

Saikia, D.J., Subrahmanya, C.R., Patnaik, A.R., Unger, S.W., Cornwell, T.J., Graham, D.A. & Prabhu, T.P. (1986). Radio observations of the S0 galaxy NGC 1218 (3C 78). *MNRAS*, **219**, 545–553.

Sambruna, R. (1994). Ph.D. thesis, SISSA, Trieste.

Sambruna, R.M., Maraschi, L. & Urry, C.M. (1996). On the Spectral Energy Distributions of Blazars. *ApJ*, **463**, 444–+.

Sargent, W.L.W. (1977). Redshifts for six 3CR radio galaxies and the spectrum of 3C 111. *ApJ*, **212**, L105+.

Scarpa, R. & Falomo, R. (1997). Are high polarization quasars and BL Lacertae objects really different? A study of the optical spectral properties. *A&A*, **325**, 109–123.

Scarpa, R. & Urry, C.M. (2001). On The Parent Population of Radio Galaxies and the FR I-FR II Dichotomy. *ApJ*, **556**, 749–755.

Schilizzi, R.T. (1986). Very long baseline interferometry. *Radio Science*, **21**, 665–679.

Schmidt, M. (1963). 3C 273: a star-like object with large red-shift. *Nature*, **197**, 1040–1040.

Schmidt, M. (1965). Optical Spectra and Redshifts of 31 Radio Galaxies. *ApJ*, **141**, 1–+.

Schwab, F.R. (1984). Relaxing the isoplanatism assumption in self-calibration; applications to low-frequency radio interferometry. *AJ*, **89**, 1076–1081.

Schwab, F.R. & Cotton, W.D. (1983). Global fringe search techniques for VLBI. *AJ*, **88**, 688–694.

Schwartz, D.A., Brissenden, R.J.V., Tuohy, T.R., Feigelson, E.D., Hertz, P.L. & Remillard, R.A. (1989). Bl-Lacertae Objects Detected in the HEAO-1 all Sky X-Ray Survey. In *BL Lac Objects*, 209–+.

Schwinger, J. (1949). On the Classical Radiation of Accelerated Electrons. *Physical Review*, **75**, 1912–1925.

Shakura, N.I. & Sunyaev, R.A. (1973). Black holes in binary systems. Observational appearance. *A&A*, **24**, 337–355.

Shapiro, S.L. & Teukolsky, S.A. (1993). Relativistic Stellar Systems with Rotation. *ApJ*, **419**, 636–+.

Shields, G.A. (1978). Thermal continuum from acretion disks in quasars. *Nature*, **272**, 706–708.

Shklovsky, I.S. (1958). On the Nature of the Emission from the Galaxy NGC 4486. In *IAU Symp. 6: Electromagnetic Phenomena in Cosmical Physics*, 517–+.

Shlosman, I., Begelman, M.C. & Frank, J. (1990). The fuelling of active galactic nuclei. *Nature*, **345**, 679–686.

Simard-Normandin, M. & Kronberg, P.P. (1980). Rotation measures and the galactic magnetic field. *ApJ*, **242**, 74–94.

Simard-Normandin, M., Kronberg, P.P. & Button, S. (1981). The Faraday rotation measures of extragalactic radio sources. *ApJS*, **45**, 97–111.

Simpson, C. (1996). A method of probing the torus geometry? *Vistas in Astronomy*, **40**, 57–61.

Singal, A.K. (1986). Magnetization effects in an incoherent synchrotron source. *A&A*, **155**, 242–246.

Singal, A.K. (1993). Evidence against the unified scheme for powerful radio galaxies and quasars. *MNRAS*, **262**, L27–L30.

Slee, O.B., Siegman, B.C. & Perley, R.A. (1989). A VLA survey of rich clusters of galaxies. I - Whole-cluster maps, source list and source statistics. *Australian Journal of Physics*, **42**, 633–733.

Smith, E.P. & Heckman, T.M. (1986). Morphological and environmental clues to the origin of powerful radio galaxies. In *Radio Continuum Processes in Clusters of Galaxies*, 305–311.

Smith, E.P. & Heckman, T.M. (1990). The local environments of low-redshift quasars and powerful radio galaxies. *ApJ*, **348**, 38–47.

Spangler, S.R. & Sakurai, T. (1985). Limits on thermal plasma in the lobes of the radio galaxies 3C 79 and 3C 379.1. *ApJ*, **297**, 84–89.

Sparks, W.B., Biretta, J.A. & Macchetto, F. (1994). Hubble Space Telescope observations of synchrotron jets. *ApJS*, **90**, 909–916.

Sparks, W.B., Golombek, D., Baum, S.A., Biretta, J., de Koff, S., Macchetto, F., McCarthy, P. & Miley, G.K. (1995). Discovery of an Optical Synchrotron Jet in 3C 78. *ApJ*, **450**, L55+.

Steer, D.G., Dewdney, P.E. & Ito, M.R. (1984). Enhancements to the deconvolution algorithm 'CLEAN'. *A&A*, **137**, 159–165.

Stickel, M., Fried, J.W. & Kuehr, H. (1989). Optical spectroscopy of 1 Jy BL Lacertae objects and flat spectrum radio sources. *A&AS*, **80**, 103–114.

Stickel, M., Fried, J.W., Kuehr, H., Padovani, P. & Urry, C.M. (1991). The complete sample of 1 Jansky BL Lacertae objects. I - Summary properties. *ApJ*, **374**, 431–439.

Stickel, M., Fried, J.W. & Kuehr, H. (1993). The complete sample of 1 Jy BL Lac objects. II - Observational data. *A&AS*, **98**, 393–442.

Stocke, J.T., Liebert, J., Schmidt, G., Gioia, I.M., Maccacaro, T., Schild, R.E., Maccagni, D. & Arp, H.C. (1985). Optical and radio properties of X-ray selected BL Lacertae objects. *ApJ*, **298**, 619–629.

Stocke, J.T., Morris, S.L., Gioia, I.M., Maccacaro, T., Schild, R.E. & Wolter, A. (1989). The Optical and Radio Properties of X-Ray Selected Bl-Lacertae Objects. In *BL Lac Objects*, 242–+.

Strittmatter, P.A., Serkowski, K., Carswell, R., Stein, W.A., Merrill, K.M. & Burbidge, E.M. (1972). Compact Extragalactic Nonthermal Sources. *ApJ*, **175**, L7+.

Stull, M.A. (1971). Flux densities of radio galaxies at 8000 MHz. *AJ*, **76**, 1–4.

Tadhunter, C.N., Morganti, R., di Serego-Alighieri, S., Fosbury, R.A.E. & Danziger, I.J. (1993). Optical Spectroscopy of a Complete Sample of Southern 2-JY Radio Sources. *MNRAS*, **263**, 999–+.

Tanaka, Y., Nandra, K., Fabian, A.C., Inoue, H., Otani, C., Dotani, T., Hayashida, K., Iwasawa, K., Kii, T., Kunieda, H., Makino, F. & Matsuoka, M. (1995). Gravitationally Redshifted Emission Implying an Accretion Disk and Massive Black-Hole in the Active Galaxy MCG:-6-30-15. *Nature*, **375**, 659–+.

Tansley, D., Birkinshaw, M., Hardcastle, M.J. & Worrall, D.M. (2000). The infrared jet in 3C 66B. *MNRAS*, **317**, 623–629.

Taylor, G.B. (1998). Magnetic Fields in Quasar Cores. *ApJ*, **506**, 637–646.

Taylor, G.B. (2000). Magnetic Fields in Quasar Cores. II. *ApJ*, **533**, 95–105.

Taylor, G.B., Hough, D.H. & Venturi, T. (2001). Very Long Baseline Array Polarimetry of Three Powerful Radio Galaxy Cores. *ApJ*, **559**, 703–709.

Taylor, G.L., Dunlop, J.S., Hughes, D.H. & Robson, E.I. (1996). A near-IR study of the host galaxies of radio-quiet quasars, radio-loud quasars and radio galaxies. *MNRAS*, **283**, 930–968.

Terlevich, R. & Melnick, J. (1985). Warmers - The missing link between Starburst and Seyfert galaxies. *MNRAS*, **213**, 841–856.

Ulrich, M.H. (1978). Spectra of the stellar population in three objects related to BL Lacertae. *ApJ*, **222**, L3–L6.

Unger, S.W., Booler, R.V. & Pedlar, A. (1984). A kiloparsec radio jet in the nucleus of the S0 galaxy NGC 1218 (3C78). *MNRAS*, **207**, 679–684.

Urry, C.M. & Padovani, P. (1995). Unified Schemes for Radio-Loud Active Galactic Nuclei. *PASP*, **107**, 803–+.

Urry, C.M., Padovani, P. & Stickel, M. (1991). Fanaroff-Riley I galaxies as the parent populations of BL Lacertae objects. III - Radio constraints. *ApJ*, **382**, 501–507.

Urry, C.M., Scarpa, R., O'Dowd, M., Falomo, R., Pesce, J.E. & Treves, A. (2000). The Hubble Space Telescope Survey of BL Lacertae Objects. II. Host Galaxies. *ApJ*, **532**, 816–829.

Urry, C.M., Woo, J. & O'Dowd, M. (2002). Black Hole Masses in AGN and Galaxies. *APS Meeting Abstracts*, 17096–+.

Urry, M. (2003). The AGN Paradigm for Radio-Loud Objects. In *ASP Conf. Ser. 290: Active Galactic Nuclei: From Central Engine to Host Galaxy*, 3–27.

Ustyugova, G.V., Lovelace, R.V.E., Romanova, M.M., Li, H. & Colgate, S.A. (2000). Poynting Jets from Accretion Disks: Magnetohydrodynamic Simulations. *ApJ*, **541**, L21–L24.

van Breugel, W. (1982). Multifrequency comparison of the total intensity and polarization distributions for 3C 31, 3C 66B, and 3C 129. *A&A*, **110**, 225–237.

van Breugel, W. & Jagers, W. (1982). Multifrequency observations of extended radio galaxies V - 3C 31, 3C 33.1, 3C 35, 3C 66B, 3C 129, 3C 130, 3C 223, 3C 310, 3C 390.3 and 4C 48.29. *A&AS*, **49**, 529–559.

Venturi, T., Giovannini, G., Feretti, L., Comoretto, G. & Wehrle, A.E. (1993). VLBI observations of a complete sample of radio galaxies. II - The parsec-scale structure of NGC 315. *ApJ*, **408**, 81–91.

Verdoes Kleijn, G.A., Baum, S.A., de Zeeuw, P.T. & O'Dea, C.P. (1999). Hubble Space Telescope Observations of Nearby Radio-Loud Early-Type Galaxies. *AJ*, **118**, 2592–2617.

Verdoes Kleijn, G.A., Baum, S.A., de Zeeuw, P.T. & O'Dea, C.P. (2002). Core Radio and Optical Emission in the Nuclei of nearby FR I Radio Galaxies. *AJ*, **123**, 1334–1356.

Vermeulen, R.C. (2002). Associated HI in Absorbers at High Redshift. In *IAU Symposium*, 91–+.

Vermeulen, R.C. & Cohen, M.H. (1994). Superluminal motion statistics and cosmology. *ApJ*, **430**, 467–494.

Vermeulen, R.C., Ogle, P.M., Tran, H.D., Browne, I.W.A., Cohen, M.H., Readhead, A.C.S., Taylor, G.B. & Goodrich, R.W. (1995). When Is BL Lac Not a BL Lac? *ApJ*, **452**, L5+.

Veron-Cetty, M.P. & Veron, P. (1998). Quasars and Active Galactic Nuclei (8th Ed.) (Veron+ 1998). *VizieR Online Data Catalog*, **7207**, 0–+.

Waggett, P.C., Warner, P.J. & Baldwin, J.E. (1977). NGC 6251, a very large radio galaxy with an exceptional jet. *MNRAS*, **181**, 465–474.

Wang, J., Staubert, R. & Ho, L.C. (2002). The Accretion Rates and Spectral Energy Distributions of BL Lacertae Objects. *ApJ*, **579**, 554–559.

Wang, J.M., Ho, L.C. & Staubert, R. (2003). The central engines of radio-loud quasars. *A&A*, **409**, 887–898.

Ward, M.J., Blanco, P.R., Wilson, A.S. & Nishida, M. (1991). Infrared spectroscopy of a Cygnus A - Implications for the obscured active nucleus. *ApJ*, **382**, 115–120.

Wardle, J.F.C. (1998). Magnetic Fields in AGN. In *ASP Conf. Ser. 144: IAU Colloq. 164: Radio Emission from Galactic and Extragalactic Compact Sources*, 97–+.

Wardle, J.F.C., Moore, R.L. & Angel, J.R.P. (1984). The radio morphology of blazars and relationships to optical polarization and to normal radio galaxies. *ApJ*, **279**, 93–98.

Wardle, J.F.C., Homan, D.C., Ojha, R. & Roberts, D.H. (1998). Electron-positron jets associated with the quasar 3C 279. *Nature*, **395**, 457–461.

Webb, J.R., Smith, A.G., Leacock, R.J., Fitzgibbons, G.L., Gombola, P.P. & Shepherd, D.W. (1988). Optical observations of 22 violently variable extragalactic sources - 1968-1986. *AJ*, **95**, 374–397.

Weiler, K.W. & de Pater, I. (1983). A catalog of high accuracy circular polarization measurements. *ApJS*, **52**, 293–327.

Whitney, A.R., Shapiro, I.I., Rogers, A.E.E., Robertson, D.S., Knight, C.A., Clark, T.A., Marandino, G.E., Vandenberg, N.R. & Goldstein, R.M. (1971). High-Accuracy Determination of 3C273-3C279 Position Difference from Long-Baseline Interferometer Fringe Phase Measurements. *BAAS*, **3**, 465–+.

Wiita, P.J. (1978). Twin-beam models for double radio sources. I - Steady-state configurations. *ApJ*, **221**, 41–50.

Wills, B.J. (1975). A strong millimeter wave component in the radio galaxy 3C 111. *ApJ*, **202**, L59–L62.

Wills, B.J., Wills, D., Breger, M., Antonucci, R.R.J. & Barvainis, R. (1992). A survey for high optical polarization in quasars with core-dominant radio structure - Is there a beamed optical continuum? *ApJ*, **398**, 454–475.

Wilson, A.S. & Colbert, E.J.M. (1995). The difference between radio-loud and radio-quiet active galaxies. *ApJ*, **438**, 62–71.

Woo, J., Urry, C.M., Lira, P., van der Marel, R.P. & Maza, J. (2004). The Fundamental Plane Evolution of Active Galactic Nucleus Host Galaxies. *ApJ*, **617**, 903–914.

Wood, K.S., Meekins, J.F., Yentis, D.J., Smathers, H.W., McNutt, D.P., Bleach, R.D., Friedman, H., Byram, E.T., Chubb, T.A. & Meidav, M. (1984). The HEAO A-1 X-ray source catalog. *ApJS*, **56**, 507–649.

Wu, X., Liu, F.K. & Zhang, T.Z. (2002). Supermassive black hole masses of AGNs with elliptical hosts. *A&A*, **389**, 742–751.

Xie, G.Z., Liang, E.W., Xie, Z.H. & Dai, B.Z. (2002). Supermassive Black Holes in BL Lacertae Objects: Estimated Masses and Their Relation to Nuclear Luminosity. *AJ*, **123**, 2352–2357.

Xu, C., Baum, S.A., O'Dea, C.P., Wrobel, J.M. & Condon, J.J. (2000). VLBA Observations of a Sample of Nearby FR I Radio Galaxies. *AJ*, **120**, 2950–2964.

Zavala, R.T. & Taylor, G.B. (2002). Faraday Rotation Measures in the Parsec-Scale Jets of the Radio Galaxies M87, 3C 111, and 3C 120. *ApJ*, **566**, L9–L12.

Zavala, R.T. & Taylor, G.B. (2003). Faraday rotation as a probe of the physical conditions near relativistic jets. *New Astronomy Review*, **47**, 589–592.

Zirbel, E.L. & Baum, S.A. (1995). On the FR I/FR II Dichotomy in Powerful Radio Sources: Analysis of Their Emission-Line and Radio Luminosities. *ApJ*, **448**, 521–+.

Zirm, A., Dey, A., Dickinson, M., McCarthy, P.J., Eisenhardt, P., Djorgovski, S.G., Spinrad, H., Stanford, A. & van Breugel, W. (1998). NICMOS Imaging of High-Redshift Radio Galaxies. *Bulletin of the American Astronomical Society*, **30**, 1412–+.

List of Publications

[1] Kharb, P. & Shastri, P. 2003, OPTICAL NUCLEI OF RADIO-LOUD AGN AND THE FANAROFF-RILEY DIVIDE, submitted to *Astronomy & Astrophysics*, (astroph/0401042)

[2] Kharb, P., Gabuzda, D., & Shastri, P. 2003, MAGNETIC FIELD GEOMETRY OF 3C111 ON PC-SCALES, *Bulletin of the Astronomical Society of India*, **31**, 433–435

[3] Kharb, P., Gabuzda, D., & Shastri, P. 2003, MAGNETIC FIELD GEOMETRY IN "RED" AND "BLUE" BL LACS, Proceedings of the Amsterdam workshop on 'Circular polarisation from relativistic jet sources', *Astrophysics and Space Science*, **288**, 51–61

[4] Kharb, P., Gabuzda, D., Alef, W., Preuss, E., & Shastri, P. 2003, MAGNETIC FIELD GEOMETRY OF THE BROAD LINE RADIO GALAXY 3C111, *New Astronomy Review*, **47**, 621–624

[5] Kharb, P., Shastri, P., & Gabuzda, D. C. 2003, PC-SCALE STUDY OF RADIO GALAXIES & BL LACS, *New Astronomy Review*, **47**, 431–434

[6] Kharb, P., Gabuzda, D., & Shastri, P. 2002, POLARIZATION STUDY OF BL LACERTAE OBJECTS ON PC-SCALES, *Bulletin of the Astronomical Society of India*, **30**, 761–764

[7] Kharb, P. & Shastri, P. 2001, RELATIVISTIC BEAMING AND CENTRAL COMPONENTS OF RADIO GALAXIES, *Bulletin of the Astronomical Society of India*, **29**, 425–427

[8] Kharb, P. & Shastri, P. 2001, THE PARSEC-SCALE CENTRAL COMPONENTS OF FR I RADIO GALAXIES, *IAU Symp. 205 :* Galaxies and their Constituents at the Highest Angular Resolutions, 74–75

[9] Kharb, P. & Shastri, P. 2001, THE PARSEC-SCALE CENTRAL COMPONENTS OF FRI RADIO GALAXIES, *ASP Conf. Ser. 250*: Particles and Fields in Radio Galaxies Conference, 100–103